

Doctoral Dissertation

博士論文

**Dynamics in Jupiter's inner magnetosphere
revealed by EUV spectroscopic observations**

(極端紫外域の分光観測から明らかにする
木星の内部磁気圏におけるダイナミクス)

A Dissertation Submitted for the Degree of Doctor of Science

December 2019

令和元年12月博士(理学)申請

Department of Earth and Planetary Science,

Graduate School of Science,

The University of Tokyo

東京大学大学院理学系研究科地球惑星科学専攻

Reina (Hikida) Kuroda

黒田(疋田) 伶奈

Abstract

Jupiter rotates with a period of ~ 10 hours and has the strongest intrinsic magnetic field in the solar system. Furthermore, the magnetic field and dynamic pressure of solar wind at Jupiter are weaker than they are at Earth. Therefore, plasma flow in Jupiter's magnetosphere is predominantly in the direction of its rotation, confirmed up to the greatest distance covered by the Galileo spacecraft ($\sim 150 R_J$ [R_J : the radius of Jupiter]). In the inner magnetosphere of Jupiter ($< \sim 10 R_J$), the satellite Io orbits with a period of 42 hours and has active volcanoes that have been monitored via infrared observations with ground-based telescopes. Io's atmosphere mainly contains sulfur dioxide and is sustained by a set of volcanic outgassing and sublimation. The sulfur dioxide is dissociated into sulfur and oxygen atoms via electron impact or photodissociation. The atoms which obtain sufficient energy to escape form a neutral cloud around Io. They are ionized by electron impact, charge exchange, or recombination and picked up by Jupiter's magnetic field. The ions are then accelerated to a nearly corotational flow of ambient plasma and form a torus-like structure called the Io plasma torus (IPT). The plasma in the torus is transported outward in the radial direction by centrifugal force on a timescale of several tens of days. The ions are excited by electron impacts and emit radiation mainly in the ultraviolet (UV) wavelength range.

The electron environment in Jupiter's magnetosphere was surveyed by past missions. An in-situ observation between 6 to 13 R_J was made by the Voyager spacecraft within an energy range of 10 to 5950 eV. The Galileo spacecraft provided further information between 6 to 8 R_J in an energy range of 0.9 to 5200 eV. These observations showed that the electron velocity distribution in the above region had a hot tail. There is a trend that at larger distances from Jupiter, there is a greater fraction of hot electrons to the total electron density. The Cassini spacecraft was able to detect temporal variation in the hot electron density. Cassini observed IPT radiation from several tens of days after a volcanic eruption on Io in 2000 and recorded a trend in which luminosity decreased with time. The Cassini observation indicated that temporal variation in the observed UV radiation can be reproduced assuming an increase in the density of hot electrons after the volcanic eruption in addition to an increase in the plasma supply rate to the IPT.

There is controversy over whether the hot electrons in the IPT are transported from outside the torus or generated locally in the torus. The interchange motion of magnetic flux tube and an Earth-like injection whose signatures were captured by the Galileo spacecraft have been proposed as candidate carriers of hot electrons from outside the torus. However, from the viewpoint of magnetohydrodynamics, it is difficult to transport plasma inward in the radial direction to the inner magnetosphere, where the intrinsic magnetic field is strong, and it has not been clarified whether inward transport contributes to the presence of the hot electrons in the IPT. Meanwhile, three possible mechanisms of heating inside the IPT have been proposed. The first is the interaction with Alfvén waves generated by the radial motion of the magnetic flux

tubes. The other two, which are heating mechanisms near Io, are the interaction with Alfvén waves generated by Io’s passage through Jupiter’s magnetosphere or the interaction with ion cyclotron waves excited by pickup molecular ions. No conclusion has been reached as to which mechanism is the dominant reason for the temporal variation in the hot electron density. This is mainly because there has been no observation that includes a time series from a volcanic activation to a return to initial state. One of the purposes of this study is to explore the mechanism behind the temporal variation in the hot electron density.

By clarifying the mechanism of the temporal variation in the hot electron density, how plasma transport or heating changes occur during a volcanically active period can be understood; therefore, there is a possibility that the response of Jupiter’s magnetospheric dynamics to volcanic activation can be explored. It can be expected that volcanic activation would cause the following changes in Jupiter’s magnetospheric dynamics: (1) increases in the plasma density in the IPT; (2) enhanced mass loading; and (3) increases in the efficiency of radial transport due to increases in the magnetic flux tube content. The other purpose of this study is to validate this hypothesis on the response of Jupiter’s magnetospheric dynamics to volcanic activation.

To clarify the temporal variation in the plasma density and temperature in the IPT associated with volcanic activation using the spectral data from the Hisaki satellite is an effective way to tackle the above topics. Hisaki has been observing IPT radiation intermittently from its launch at the end of 2013 to the present day. It has been performing imaging spectroscopy of planetary atmosphere/plasma in the extreme UV wavelength range from Earth orbit. Spectroscopic remote sensing is a powerful tool for deriving the density and temperature of plasma. The method of exploring the condition of plasma in emission regions using spectral data is called plasma diagnosis and has been used mainly in the fields of astronomy and nuclear fusion. In this study, the method was applied to data from Hisaki.

This study investigated the temporal variation in the density and temperature of plasma in the IPT associated with volcanic activation for the longest period to date. The periods of observation used in this study are December 2013 to April 2014, November 2014 to May 2015, and January 2016 to December 2016. From the observations of Io by ground-based telescopes, five volcanic events are indicated to occur before and during these periods. The temporal variation in radiation from the IPT showed that, of the five volcanic events, the one that occurred in 2015 had the greatest impact on the IPT. The findings of this study are described below.

The temporal variation in the hot electron density in the IPT was researched for the longest period. The dawn-dusk asymmetries of the hot electron density were found for the first time. After two volcanic events, including the one in 2015, the increases in the hot electron density were confirmed only on the dusk side. After two other volcanic events, the hot electron density increased on both the dusk and the dawn sides. After the other event, no increase was confirmed on either the dusk or the dawn side, though this might be due to the insufficiency of the

observation period.

The temporal variation in the radial distribution of mass density in the IPT, whose radial gradient can be considered an indicator of the amount of plasma transported outward, was clarified in this study. As a result, in the period after the greatest volcanic event in 2015, the time taken from volcanic activation to a decrease in the mass density gradient was found to be ~ 30 days. In comparison, the time taken to increase the hot electron density on the dusk side was found to be ~ 40 days during the same period. This meant that it took approximately ten days from the increase in the amount of plasma transported outward, that is to say, from the enhancement of the radial motion of flux tubes, to increase the density of hot electrons. Based on the estimation that the growth time of the interchange instability is approximately one hour, local heating associated with the radial motion of the flux tubes was revealed not to be the dominant mechanism by which the hot electron density increased and its dawn-dusk asymmetry occurred during this specific period that involved the greatest volcanic event.

The dependence of the hot electron density on the Io phase angle was also investigated. It was clarified that when the hot electron density near Io increased, the hot electron density far from Io also increased. Moreover, it was revealed that the dawn-dusk asymmetries of the hot electron density occurred regardless of the location of Io. These results indicate that heating near Io is not the mechanism responsible for the increases in the hot electron density and the dawn-dusk asymmetries.

The local heating was revealed not to be the dominant mechanism responsible for the increase in the hot electron density and its dawn-dusk asymmetry for a period involving the greatest volcanic event, as indicated above. Therefore, it can be concluded that transport is the cause of the increase in the hot electron density after the greatest volcanic event. As for the periods involving other volcanic events, though they could not be fully verified due to data discontinuities, there is no contradiction in considering that the transport is responsible for the increase in the hot electron density. As the cause of the dawn-dusk asymmetry of the hot electron density, both loss and transport can be listed, and future direct observations would be useful to identify it.

As mentioned above, as for the period involving the greatest volcanic event, it was revealed that inward plasma transport developed after the increase in the plasma supply rate to the inner magnetosphere. This suggests that increased mass loading increased the efficiency of radial transport. Based on the lengths of the periods from the occurrence of volcanic eruptions to the increases in hot electron density, the timescale of plasma transport associated with volcanic activation was suggested to be 20–80 days.

Contents

Abstract	i
Acknowledgments	vii
1. General introduction	1
1.1. Jovian magnetosphere	1
1.1.1. Basic information	1
1.1.2. Plasma flow in Jupiter’s magnetosphere	3
1.1.2.1. Azimuthal flow	3
1.1.2.2. Radial flows	4
1.1.2.2.1. Interchange motions	5
1.1.2.2.2. Injections	7
1.1.2.2.3. Reconnection jet	11
1.2. The Io plasma torus (IPT)	12
1.2.1. Basic information	12
1.2.2. Similar systems	13
1.2.3. Io’s volcanism	15
1.2.4. Observations of the IPT with remote sensing	19
1.2.4.1. Ultraviolet spectroscopic observations of the IPT	20
1.2.4.2. Derivation of plasma densities and temperature with plasma diagnosis method	22
1.2.5. Hot electron component	25
1.2.5.1. Direct observations	25
1.2.5.2. Mechanisms considered to be responsible for the presence of hot electrons	27
1.2.5.3. Time variability	29
1.2.6. Energy budget of the IPT	31
1.3. The goal and layout of this thesis	32
2. Dataset and methods	35
2.1. Dataset	35
2.2. Methods	39
2.2.1. Introduction: plasma diagnosis method	39
2.2.2. Data reduction	41
2.2.2.1. Creating spectra	42
2.2.2.2. Calculation of line brightness	44
2.2.2.3. Determination of density and temperature	46
3. Temporal variation in plasma densities and temperature in the IPT	48
3.1. Tendency of temporal variation in plasma densities and temperature in the IPT	54

3.2. Comparison with other works	57
3.3. Discussion	65
3.4. Conclusion	66
4. Temporal variation in radial distribution of mass density	67
4.1. Data analysis	67
4.2. Results	68
4.3. Discussion	73
4.4. Conclusion	73
5. Dawn-dusk asymmetry and dependence on the Io phase angle of hot electron density	74
5.1. Dawn-dusk asymmetry	74
5.2. Io phase dependence of hot electron density	78
5.2.1. Data analysis	78
5.2.2. Results and discussion	79
5.3. Discussion on the cause of the dawn-dusk asymmetry of hot electron density	81
5.3.1. Evaluation of loss effects	81
5.3.1.1. Estimation of thermal relaxation time via Coulomb collision	81
5.3.1.2. Estimation of the minimum value of timescale of loss via pitch angle scattering of hot electrons inside the IPT	84
5.3.2. Evaluation of the effect of local heating	85
5.3.3. Possibility for transport to be asymmetric	86
5.3.4. Future work	88
5.4. Conclusion	89
6. General conclusion	90
Appendix	93
A. Identification of emission lines	93
A1. Methods	93
A2. Results	93
B. Evaluation of the effect of satellite inversion	103
B1. Evaluation of spatial dependence of sensitivity	103
B2. Evaluation of variation in the field of view	105
C. How to convert light intensity to brightness	107
C1. Estimation of torus emission width	107
C2. Conversion factor to brightness	110
D. Verifying the validity of assumptions	112
D1. Verification of solution dependence on the hot electron temperature and the mixing ratios of proton and doubly ionized oxygen	112

D2. Verification of the validity of the assumption of the mixing ratio of singly ionized oxygen in the third season	123
E. Parameter determination uncertainties	124
E1. Comparison of line intensities and results of plasma diagnosis	124
E2. Dependences of confidence intervals and chi-square values on electron parameters	125
E3. Verification of solution plausibility in a multidimensional space	128
F. Shift of streamlines due to dawn-to-dusk electric field	130
References	131

Acknowledgments

I wish to express my sincere appreciation to my supervisor, Prof. Ichiro Yoshikawa, for his kind guidance during my doctoral and master's courses. The conversations with him have been very stimulating.

I am grateful to Prof. Yuto Kato, Prof. Yoshifumi Saito, Assoc. prof. Satoshi Kasahara, Prof. Kanako Seki, Assoc. prof. Takanobu Amano, for their very sincere and constructive comments on my thesis.

Discussions with Prof. Takeshi Imamura, Asst. Prof. Kunihiro Keika, Dr. Naomoto Iwagami have been illuminating.

I wish to thank all group members who contributed to the Hisaki project. I especially wish to thank Lect. Kazuo Yoshioka, Assoc. Prof. Fuminori Tsuchiya, Asst. Prof. Masato Kagitani, Asst. Prof. Tomoki Kimura, Asst. Prof. Go Murakami, Asst. Prof. Atsushi Yamazaki, Prof. Nick Schneider, Prof. Emer. Fran Bagenal, Lect. Hajime Kita, Dr. Chihiro Tao, Mr. Eddie Nerney, Dr. Ryoichi Koga, and Ms. Mika Shishido.

I express my deep gratitude to Dr. Masaki Kuwabara, Dr. Yusuke Nara, Mr. Fumiharu Suzuki, Mr. Tianxu Zhang, Mr. Seiya Nishimura, Mr. Junya Fukuba, Mr. Yudai Suzuki, Mr. Riku Katsuse, Mr. Shutaro Sato, Mr. Syuhei Yonemoto, Mr. Shogo Arao, Ms. Minori Narita, and all the colleagues who have been concerned with Yoshikawa and Yoshioka Laboratory at the University of Tokyo.

CHIANTI is a collaborative project involving George Mason University, the University of Michigan (USA), and the University of Cambridge (UK). Science data of the Hisaki satellite was obtained from the ISAS/JAXA Data Archives and Transmission System (DARTS) (<https://www.darts.isas.jaxa.jp/pub/hisaki/>).

My greatest acknowledgment is sent to my family, Naoyuki, Masako, Norikazu, Mitsuko, and Sachiko. They have supported me all my life. I am also grateful to family-in-law, Yoshihiro, Satoko, and Hiroyuki, for their encouragement. Finally, I would like to express my special thanks to my husband, Takahiro. This work could not be accomplished without his sincere support for many years.

1. General introduction

1. 1. Jovian magnetosphere

1. 1. 1. Basic information

The main features of Jupiter's magnetosphere are as follows: (1) a strong intrinsic magnetic field, (2) a large amount of plasma within the magnetosphere, and (3) a high rotation speed. The main parameters that determine the properties of the Earth's magnetosphere, Jupiter's magnetosphere, and Saturn's magnetosphere are summarized in Table 1.1. The magnetic moment of Jupiter, which was estimated from direct observation by the Voyager spacecraft, is ~18000 times that of Earth (Connerney et al., 1982). While the main plasma source in the Earth's magnetosphere is the ionosphere, that in Jupiter's magnetosphere is the volcanic satellite Io, and the plasma supply rate is as high as 260–1400 kg/s, which was estimated from the physical chemistry model with the observed plasma densities. See Subsection 1.2.6 for details (Bagenal and Delamere, 2011). Furthermore, the rotation period of Jupiter is ~9.9 hours, which was obtained by ground-based radio observations, and is faster than that of the Earth's magnetosphere (May et al., 1979). Regarding Saturn, the magnetic moment estimated from direct observation by the Pioneer 11, Voyager 1, and Voyager 2 spacecraft is ~550 times that of Earth (Acuna et al., 1983). The water-related ions supplied from the Enceladus satellite are estimated to be 12–250 kg/s, which was estimated by the same method as Jupiter's case (Bagenal and Delamere, 2011). The rotation period of Saturn is ~10.5 hours, which was estimated from the gravitational, radio occultation, and wind data by the Pioneer 11, Voyager 1, and Cassini spacecraft (Anderson and Schubert, 2007). From these characteristics, Saturn's magnetosphere is expected to be intermediate between the Earth's magnetosphere and Jupiter's magnetosphere.

From the features described above, the main properties of the shape of Jupiter's magnetosphere are as follows: (1) a large size and (2) a disk-like structure. Schematic diagrams of the magnetospheres of Mercury, Earth, Jupiter, and Saturn are shown in Figure 1.1. The magnetic field lines are stretched outward from the planet to form a disk-like shape in the equatorial region. The magnetospheres of Earth and Saturn have a shape closer to a dipole than that of Jupiter. As for Mercury's magnetosphere, the subsolar magnetopause is close to the surface, and the shape differs greatly from the other three magnetospheres.

Table 1.1. Properties of magnetospheres of Earth, Jupiter, Saturn.

M_{Earth} represents the magnetic moment of Earth.

	Earth	Jupiter	Saturn
Magnetic moment / M_{Earth}	1	$\sim 18000^{\text{a}}$	$\sim 550^{\text{b}}$
Planetary field direction at equator	N	S	S
Plasma source [kg/s]	$\sim 5^{\text{c}}$	$\sim 260\text{--}1400^{\text{d}}$	$\sim 12\text{--}250^{\text{d}}$
Planetary radius (R_{P}) [km]	$\sim 6400^{\text{c}}$	$\sim 72000^{\text{c}}$	$\sim 60000^{\text{c}}$
Subsolar magnetopause distance [R_{P}]	$\sim 10^{\text{c}}$	$\sim 60\text{--}90^{\text{c}}$	$\sim 22\text{--}27^{\text{c}}$
Rotational period [hours]	24	$\sim 9.9^{\text{e}}$	$\sim 10.5^{\text{f}}$
Solar wind P_{dyn} [nPa]	$\sim 2^{\text{c}}$	$\sim 0.08^{\text{c}}$	$\sim 0.03^{\text{c}}$

^a Connerney et al., 1982; ^b Acuna et al., 1983; ^c Jackman et al., 2014;

^d Bagenal and Delamere, 2011; ^e May et al., 1979; ^f Anderson and Schubert, 2007

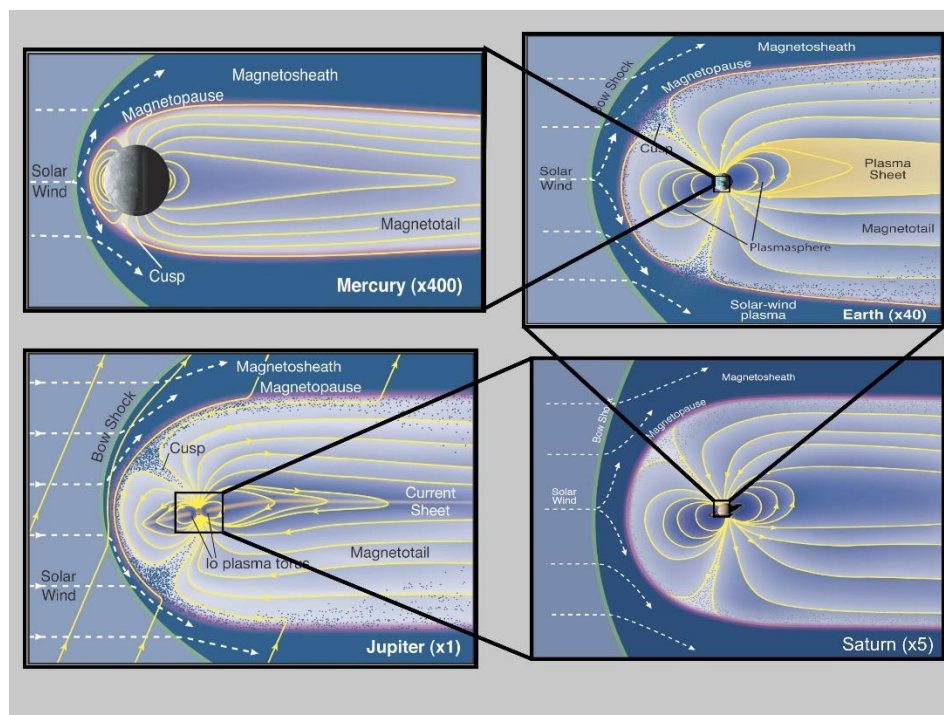


Figure 1.1. Configurations of magnetospheres of Mercury, Earth, Saturn, and Jupiter (© Fran Bagenal and Steve Bartlett).

1. 1. 2. Plasma flow in Jupiter's magnetosphere

From the results of direct observations by the Voyager, Galileo, and Cassini spacecraft, the following properties are known: (1) plasma flow in Jupiter's magnetosphere is predominantly in the direction of its rotation, which is confirmed up to the greatest distance covered by the Galileo spacecraft ($\sim 150 R_J$ [R_J : the radius of Jupiter]; Krupp et al., 2005); (2) at distances of $6\text{--}9 R_J$ from Jupiter, the signatures interpreted as the interchange motions are observed; (3) injection events are observed at a distance of $\sim 9\text{--}25 R_J$ from Jupiter; (4) burst events interpreted as signatures of reconnections occur between the night side to the dawn side at distances of $80\text{--}115 R_J$ from Jupiter. A schematic diagram of plasma flow in Jupiter's magnetosphere as viewed from above the north pole is shown in Figure 1.2. The details will be presented in this subsection. Regions within distances of $\sim 10 R_J$, from ~ 10 to $30\text{--}50 R_J$, and outside $30\text{--}50 R_J$ are called the inner, middle, and outer magnetospheres, respectively (Acuna et al., 1983).

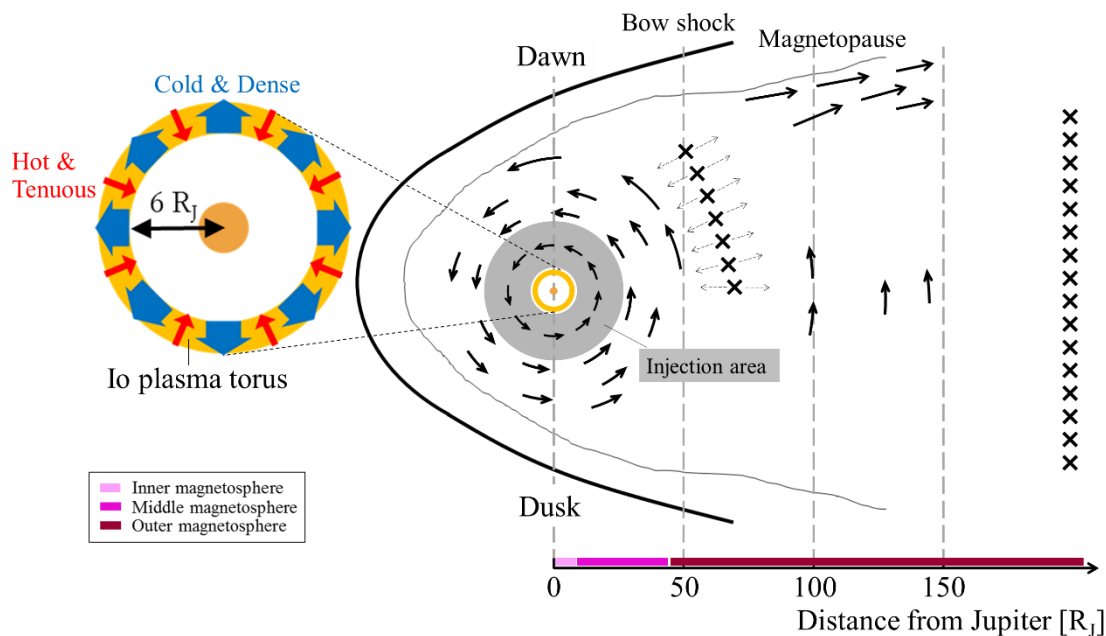


Figure 1.2. Schematic diagram of plasma flow in Jupiter's magnetosphere as viewed from above the north pole inferred from direct observations. The X-symbols show the location of a magnetic x-line.

1. 1. 2. 1. Azimuthal flow

Plasma flow in Jupiter's magnetosphere is predominantly in the direction of its rotation. The observation result of azimuthal plasma speed obtained by PLS (Plasma science experiment) on the Voyager spacecraft is shown in Figure 1.3 (Khurana et al., 2004). In the middle and outer magnetospheres, the azimuth speed is delayed from the corotation speed. The plasma speeds

in the azimuth direction obtained by EPD (Energetic Particles Detector) on the Galileo satellite are shown in Figure 1.4 (Khurana et al., 2004). Outside $\sim 30 R_J$, the delay from the corotation is significant, and the azimuthal speed is $\sim 200\text{--}400$ km/s.

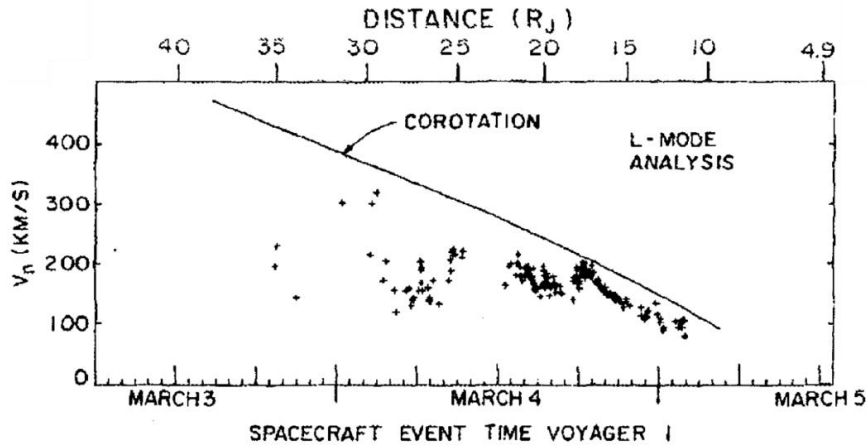


Figure 1.3. Corotational motion of plasmas in the middle magnetosphere observed by Voyager/PLS (adopted from Khurana et al. [2004]). The curve represents the corotational speed.

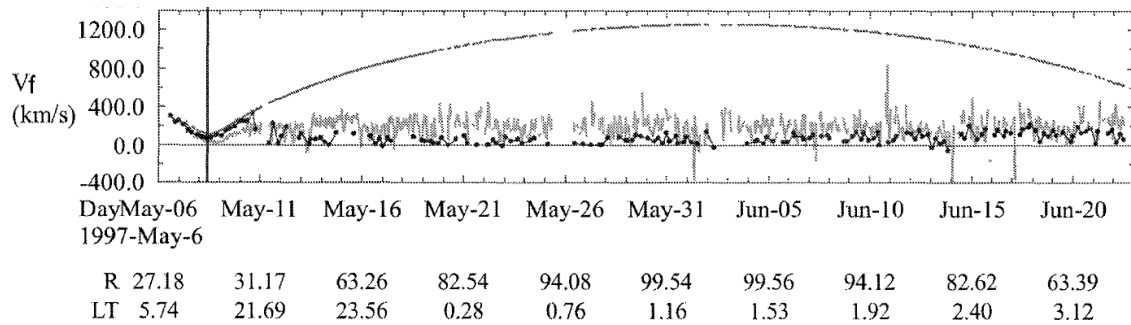


Figure 1.4. Ion flow velocity in the corotational direction observed by the Galileo satellite (adopted from Khurana et al. [2004]). The black and gray polygonal lines indicate results obtained by the PLS instrument and the EPD instrument, respectively. The curve is the corotational speed. The vertical line shows the timing of the closest approach of Galileo to Jupiter.

1. 1. 2. 2. Radial flows

The plasma in the inner magnetosphere is transported outward in the radial direction by centrifugal force on a timescale of several tens of days, as shown by blue arrows in Figure 1.2. Though, from the viewpoint of magnetohydrodynamics (MHD), it is difficult to transport plasma inward in the radial direction to the inner magnetosphere, where the intrinsic magnetic field is strong, the signatures of the inward transport has been captured. In the following, I will introduce them.

1. 1. 2. 2. 1. Interchange motions

Since a large amount of plasma is supplied to the inner magnetosphere and the rotation speed is high, it has been expected that the interchange motions, as shown on the left side of Figure 1.2, exist in Jupiter's magnetosphere. Hill (1976) obtained the interchange stability condition by a theoretical approach. He showed that the system is unstable if there is an inward gradient in the plasma mass content inside a flux tube, as expressed below.

$$\frac{\partial}{\partial r_e} \left(\frac{\rho_e r_e g}{B_e} \right) < 0. \quad (1.1)$$

Here, ρ_e , r_e , and B_e are the mass density, radial distance, and magnetic field strength in the equatorial plane, respectively. g is given in Equation (1.2).

$$g = \int \frac{ds}{r} \quad (1.2)$$

, where r and s represent the radial distance and length of the magnetic flux tube along the magnetic field line, respectively.

The observations by the Galileo satellite captured indirect evidence for the existence of inward-moving magnetic flux tubes. Abrupt changes in plasma characteristics over several seconds were captured at 17:34 during passing in the inner magnetosphere, as shown in Figure 1.5 (Thorne et al., 1997). The following three signatures were simultaneously observed: a sudden increase in magnetic field strength, an increase in the flux of high-energy particles, and a decrease in the upper hybrid frequency, which indicates the decrease in the electron density. These are interpreted as the signature of the inward magnetic flux tube. According to the statistical analysis of 29 events captured by MAG (magnetometer) on the Galileo satellite, the occupancy ratio of the magnetic flux tube with a higher magnetic field strength compared to the ambient flux tube is 0.32%. No event is observed inside the Io's orbit (Russell et al., 2005). Also, the signatures of interchange motions were observed in Saturn's magnetosphere by the Cassini satellite. In Saturn's magnetosphere, it has revealed that interchange events occur more frequently than in Jupiter's magnetosphere; the occurrence rate is 5–10% (Azari et al., 2018; Azari et al., 2019).

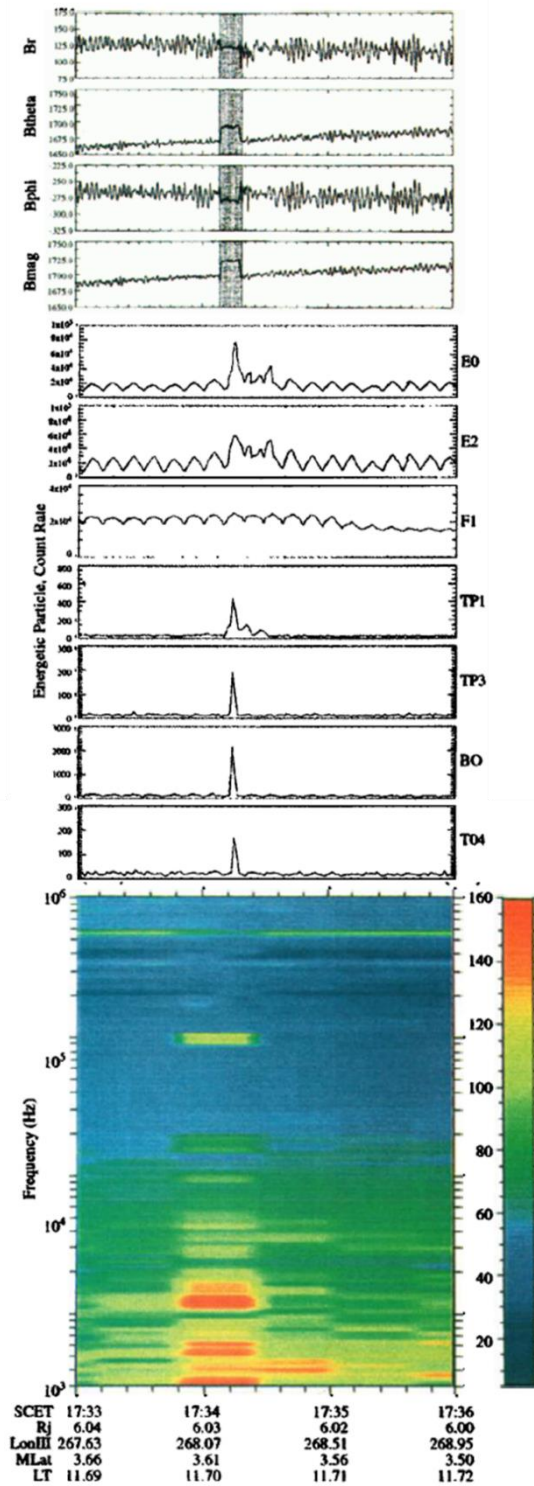


Figure 1.5. Signature obtained by the Galileo satellite suggesting radial inward motion of flux tube in Jupiter's magnetosphere (Thorne et al., 1997). The upper four panels are magnetic field strength by the MAG instrument, the lower seven panels are particle observations by the EPD instrument (see Table 1.2 for details), and the lower is the electromagnetic field observation by the PWS (Plasma Wave Spectrometer) instrument.

Table 1.2. Galileo/EPD channels (Thorne et al., 1997).

Channel	Species	Energy [MeV]
E0	electron	0.015–0.029
E2	electron	0.042–0.055
F1	electron	0.174–0.304
TP1	proton	0.08–0.22
TP3	proton	0.54–1.25
B0	proton	3.2–10.1
TO4	oxygen	1.8–9.0

The approaches using MHD simulations have been taken. Hiraki et al. (2012) simulated the interchange motions using a two-dimensional reduced MHD simulation. It was found that the timescale of the outward transport associated with the interchange motions is from ~ 2 to ~ 72 days, though the result largely depends on the assumptions in their calculation.

1. 1. 2. 2. 2. Injections

The signature of injections is observed at ~ 9 to $\sim 25 R_J$ (Mauk et al., 1999). An energetic plasma injection of ions and electrons captured by Galileo is shown in Figure 1.6. The electron intensifications near 13:00, 16:00, 17:30, and 19:20 UT can be seen with energy dispersed. The electrons with low energy arrived at the spacecraft before the arrival of the electrons with high energy. This is interpreted as the results of the energy-dependent magnetic gradient and curvature drifts.

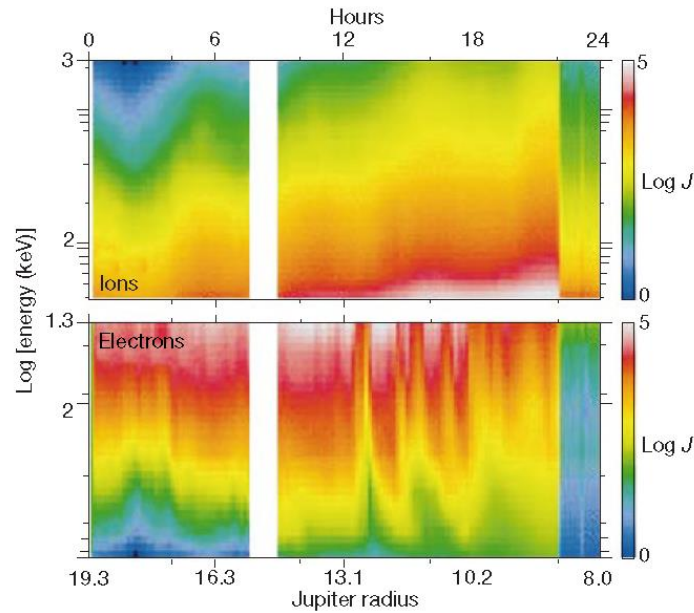


Figure 1.6. Measurements of energetic plasma injection of ions (top) and electrons (bottom) in Jupiter’s magnetosphere by Galileo (Mauk et al., 2002).

Also, the Hisaki satellite, which has been observing IPT radiation intermittently from its launch at the end of 2013 to the present day, captured the sign of the injection of plasma from outside the IPT. The transient IPT brightening of the IPT was observed ~ 10 hours after the brightening of Jupiter’s aurora. A schematic view of the interpretation of this phenomenon is shown in Figure 1.7. The auroral brightenings are caused by an increase in energetic (100–200 keV [Tao et al., 2018]) electron precipitation along the magnetic field line from the middle magnetosphere (time = t_1), while the IPT brightenings are interpreted as the results of the inward transport of hot electrons (energy of several tens eV to ~ 1000 eV) (time = t_2).

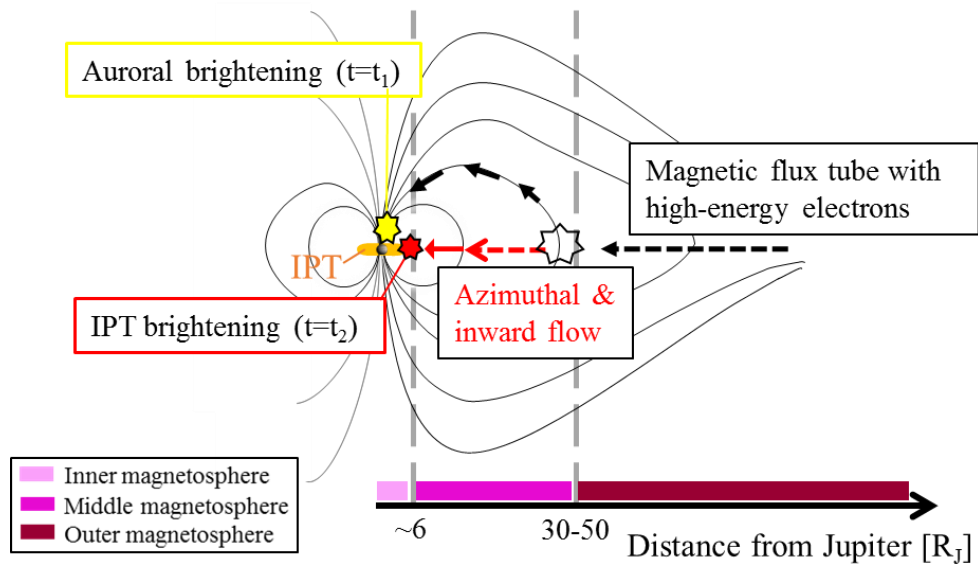


Figure 1.7. Interpretation of the transient brightening events of the aurora and the IPT.

The transient brightening events of the aurora and the IPT between DOY (day of year) 1–14 in 2014 are shown in Figure 1.8 (Yoshikawa et al., 2016). The auroral radiation and the fitted sine function with ~ 10 hours are represented by black dots and a red line in Figure 1.8 (A). The deviations from the fitted function are shown in Figure 1.8 (B), and the timings of brightening are indicated by the black lines in Figure 1.8 (C). In Figure 1.8 (D), the IPT radiation and its 20-hour running averaged value are indicated by red dots and a black line, while the timings of the brightening are indicated by red lines in Figure 1.8 (C). Overall, four IPT brightening events are observed after the auroral brightening in this period. Details about the analysis method to detect the brightening events are summarized in Yoshikawa et al. (2016) and Suzuki et al. (2018).

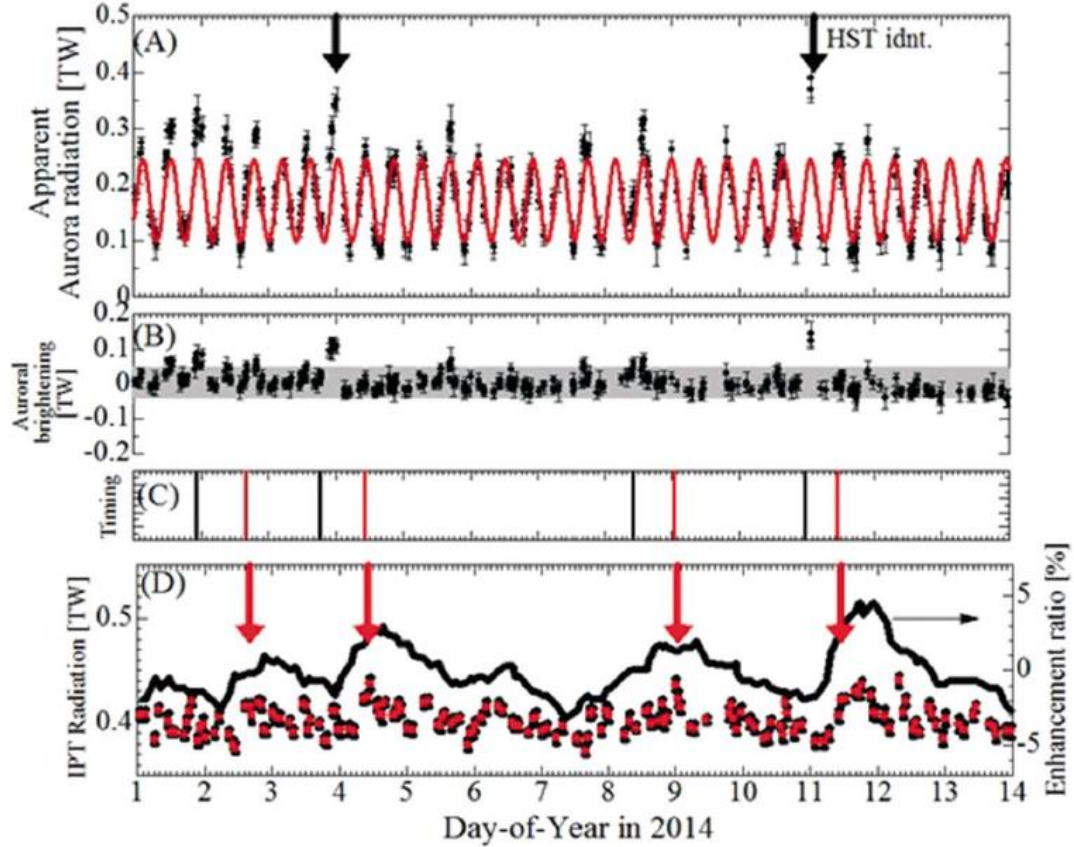


Figure 1.8. Transient brightening events of Jupiter’s aurora and the IPT between DOY 1–14 in 2014 (Yoshikawa et al., 2016). (A) Temporal variations in auroral radiation. The red line indicates a ~ 10 -h periodic sinusoidal fitted curve. (B) Deviations of the observations from the sinusoidal curve. (C) Timings of the transient enhancements. The black and red lines indicate the brightening timings of the aurora and IPT, respectively. (D) Temporal variations in the IPT radiation in the wavelength range of 65–78 nm. The red dots indicate 40-min averaged values. The black line shows 20-h running averaged values, which exclude known periodic variations in the IPT radiation.

Observations by the Hubble Space Telescope revealed that the auroral brightenings on DOY 4 and DOY 11 in 2014 occur mostly in the main oval and low-latitude regions (Badman et al., 2016). The auroral radiation obtained by the HST and the solar wind dynamic pressure at Jupiter estimated by a 1-D MHD model (Tao et al., 2005) for the period between DOY 1–16 in 2014 is shown in Figure 1.9. The low-latitude and main oval regions are interpreted to be mapped to the middle magnetosphere, at distances of ~ 10 – $25 R_J$ and ~ 15 – $40 R_J$, respectively (Grodent et al., 2015). Therefore, the IPT brightenings with the auroral brightenings may indicate the inflow of plasma from the middle to the inner magnetosphere.

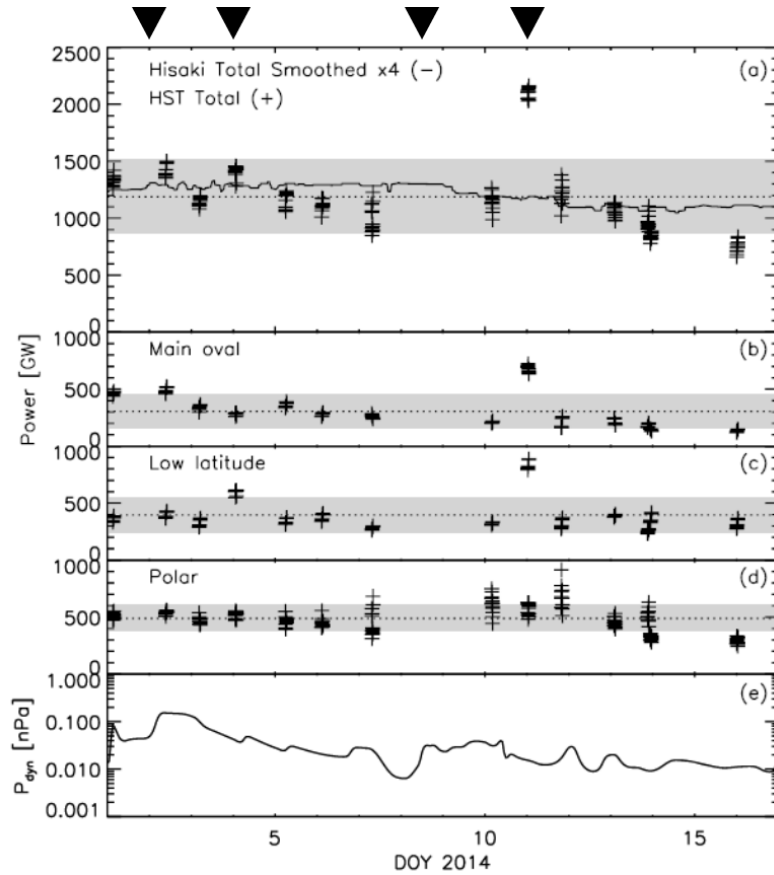


Figure 1.9. Auroral power obtained by the HST and solar wind dynamic pressure between DOY 1–16 in 2014 (modified from Badman et al. [2016]). The timings of the transient brightenings detected by Hisaki are indicated by black triangles. (a) The total FUV auroral power, mean values, and correspondent standard deviations are indicated by crosses, a dotted line, and shading, respectively. The solid line shows the total EUV auroral power observed by Hisaki, smoothed by a running median with a window of 39.7 hours (four Jovian rotations), and scaled by a factor of 4. (b)–(d) Radiation from the main oval, low-latitude, and polar regions. (e) Solar wind dynamic pressure at Jupiter propagated using a 1-D MHD model (Tao et al., 2005).

1. 1. 2. 2. 3.Reconnection jet

In Jupiter’s magnetosphere, unlike the solar-wind-driven Dungey cycle in the Earth’s magnetosphere, the Vasyliunas cycle shown in Figure 1.10, driven by the plasma supply from the satellite Io in the inner magnetosphere and its corotation, is thought to be dominant (Vasyliunas, 1983). It is thought that reconnections occur from midnight to the dawn side as indicated by X-symbols, which is caused by the stretched magnetic field lines with mass loading. The reconnection from midnight to the dawn side is also suggested from observations of the burst event by the Galileo satellite and the Cassini spacecraft (Woch et al., 2002; Kasahara et al., 2013).

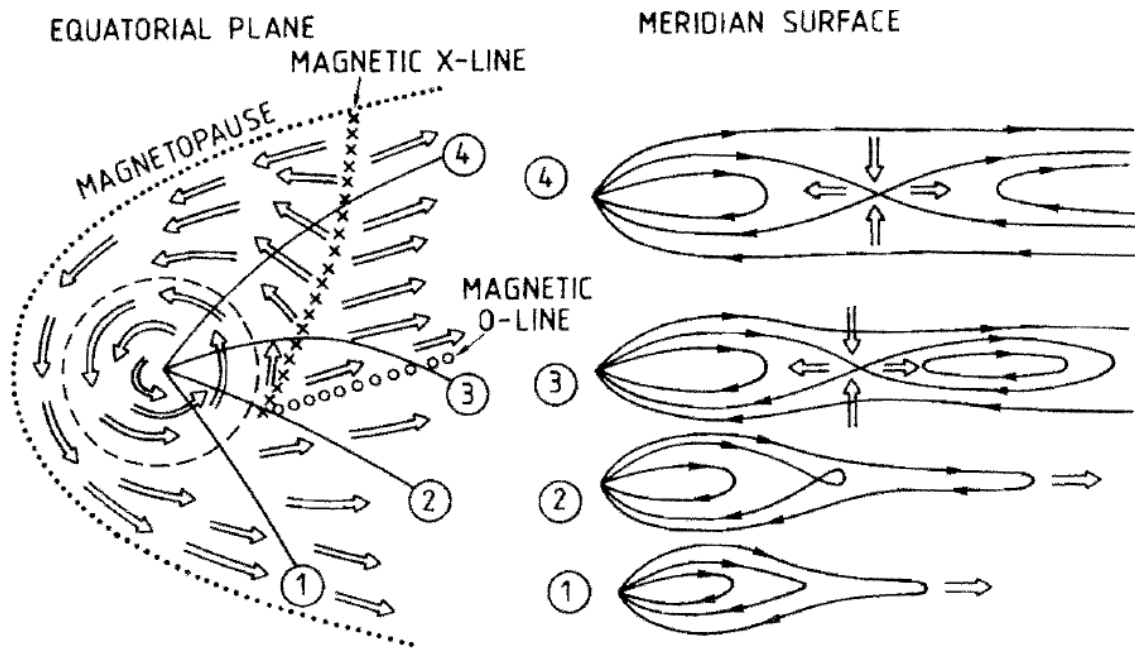


Figure 1.10. Schematic diagram of plasma flow in Jupiter's magnetosphere (Vasyliunas, 1983) in the equatorial plane (left). Schematic diagram of plasma flow and magnetic field in a sequence of meridian surfaces (right). The X-symbols and O-symbols show the location of a magnetic x-line and o-line, respectively.

1. 2. The Io plasma torus (IPT)

1. 2. 1. Basic information

The satellite Io orbits at a distance of $5.91 R_J$ from Jupiter with a period of 42 hours and has active volcanoes. The surface image is shown in Figure 1.11. Io's atmosphere mainly contains sulfur dioxide and is sustained by a set of volcanic outgassing and sublimation. The sulfur dioxide is dissociated into sulfur and oxygen atoms via electron impact or photodissociation. The atoms which obtain sufficient energy to escape form a neutral cloud around Io (Thomas et al., 2004). They are ionized by electron impact, charge exchange, or recombination and picked up by Jupiter's magnetic field. The ions are then accelerated to a nearly corotational flow of ambient plasma and form a torus-like structure called the Io plasma torus (IPT), as shown in Figure 1.12. The main components of ions in the IPT are S^+ , S^{2+} , S^{3+} , O^+ , O^{2+} , and H^+ (Bagenal, 1994). The sulfur and oxygen ions are excited by electron impacts and emit radiation mainly in the ultraviolet (UV) wavelength range.

The electron velocity distribution has a hot tail in addition to the core component of several eV (Sittler and Strobel, 1987). The core electron temperature can be reproduced by considering Coulomb interaction with ions and hot electrons. Meanwhile, there is still controversy over

whether the hot electrons are generated locally in the torus or transported from outside the torus, as shown in Subsubsection 1.2.5.2.

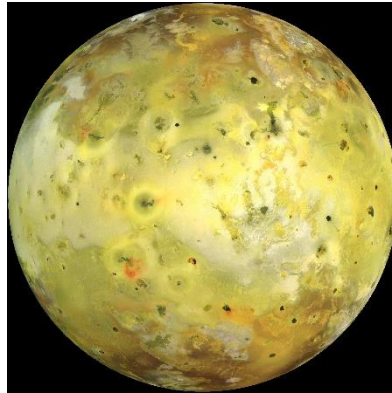


Figure 1.11. Global image of the Io satellite in true color obtained by the Galileo satellite on Jul. 3, 1999 (© NASA/JPL/University of Arizona). Multiple hot spots can be seen on the surface.

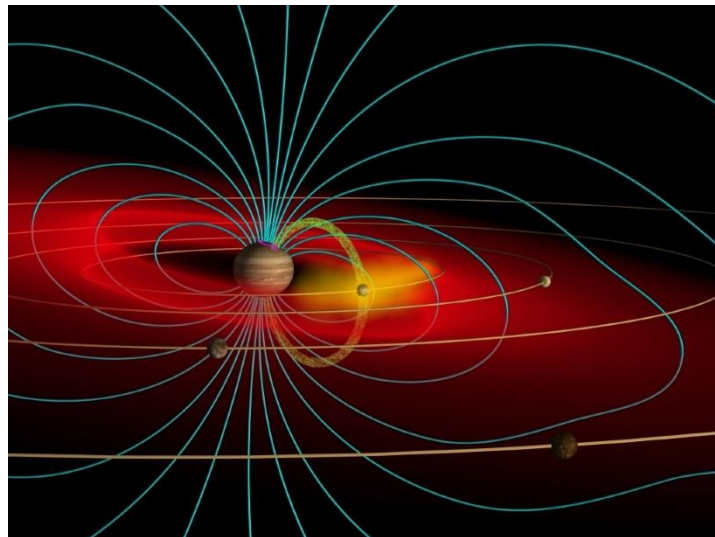


Figure 1.12. Schematic diagram of the Io plasma torus (© John Spencer). The innermost Galilean satellite, Io, supplies volcanic materials to Jupiter's magnetosphere.

1. 2. 2. Similar systems

The situation that the torus-like structure exists in the magnetosphere is not unusual in the universe. For example, the torus structures in Saturn's magnetosphere are shown in Figure 1.13. There is the Enceladus torus consisting of water-related molecular ions from the Enceladus satellite and E-ring torus mainly composed of the OH neutral (Arridge et al., 2011). Also, the transit observations suggested that a torus-like system exists near the exoplanet WASP 49-b, as shown in Figure 1.14 (Oza et al., 2019).

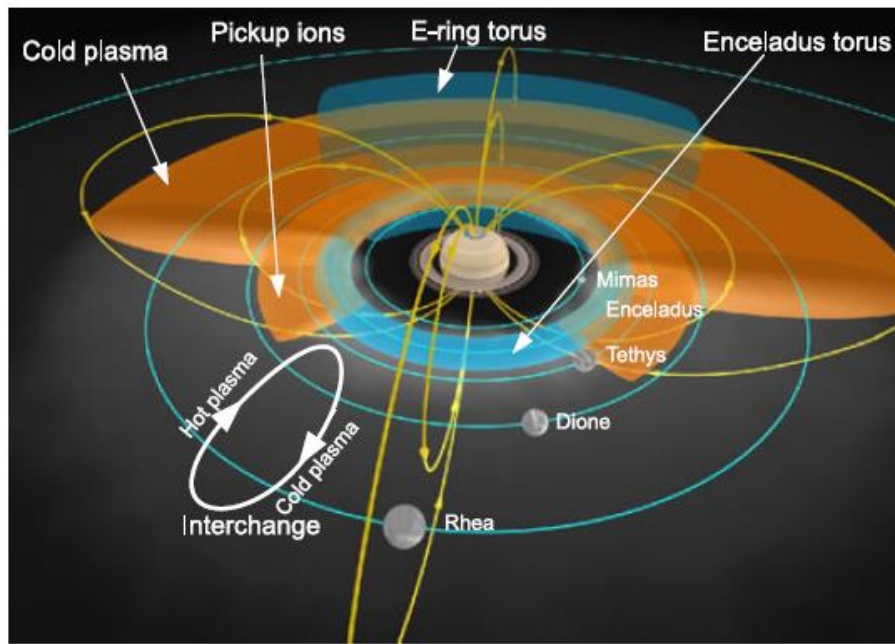


Figure 1.13. Schematic of Saturn's magnetosphere (Arridge et al., 2011).

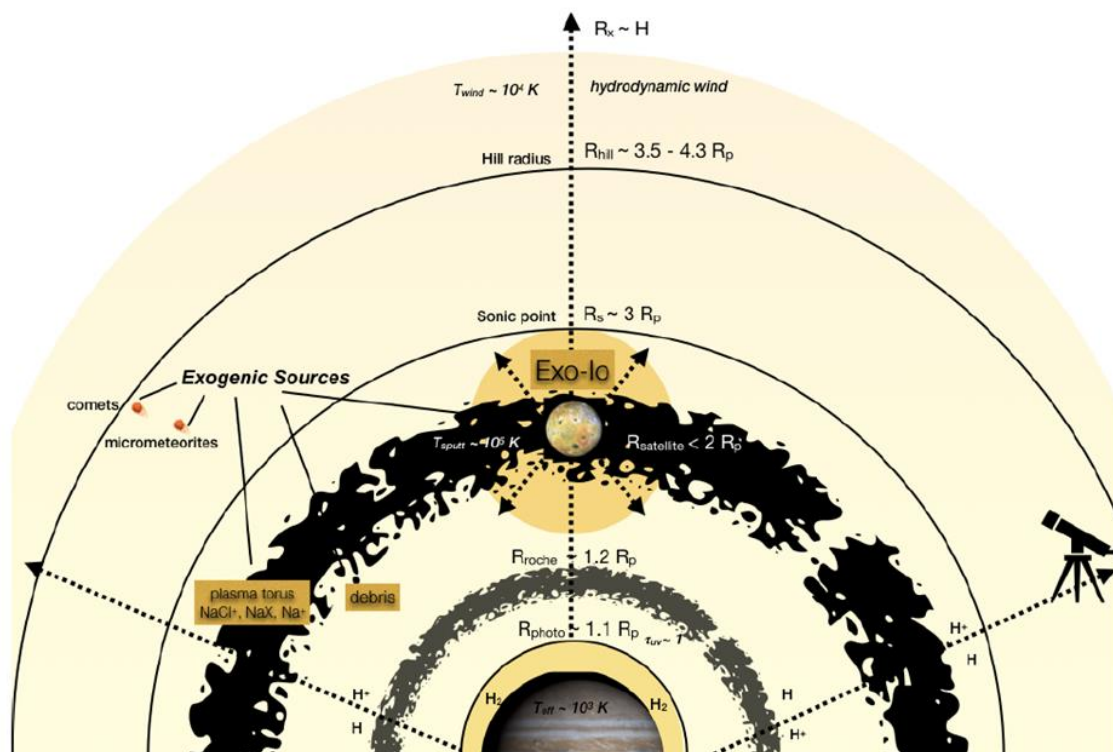


Figure 1.14. Imaginary picture of the torus with a giant gas planet outside the solar system (Oza et al., 2019). An exo-Io sodium cloud is shown at $2 R_p$ (R_p : planetary radius) around exo-Io by the yellow shade. If the planet is magnetic, plasma torus carrying ejected material shown in black shade should be present.

1. 2. 3. Io's volcanism

Io's locked eccentric orbit results in high internal heating with tidal forcing from Jupiter (Peale et al., 1979). This high heat flow causes volcanic activity on Io, which exhibits a high degree of spatial and temporal variability. Thermal signatures are easily detected from the Earth in the infrared wavelength range generated by hundreds of active volcanoes (Marchis et al., 2010). In this subsection, a volcanic eruption that occurred during the Jupiter flyby of the Cassini spacecraft from 1999 to 2000 and five volcanic events, which are indicated to occur before and during the periods used in this study, will be introduced.

In 2000, the DDS instrument (Dust Detector System) on the Galileo satellite captured the significant increase in the dust flux associated with the volcanic activity (Kruger et al., 2003), by which surface change at Tvashtar (63° N, 123° W) was confirmed by the Galileo spacecraft (Geissler et al., 2004). Temporal variation in the dust emission rate of Io obtained by Galileo/DDS is shown in Figure 1.15. Cassini observed IPT radiation from Sep. 2000, which is several tens of days after the volcanic eruption and recorded a trend in which luminosity decreased with time. The Cassini/UVIS (Ultraviolet Imaging Spectrograph) observations revealed a dramatic change in the mixing ratio of ions, as shown in Figure 1.16.

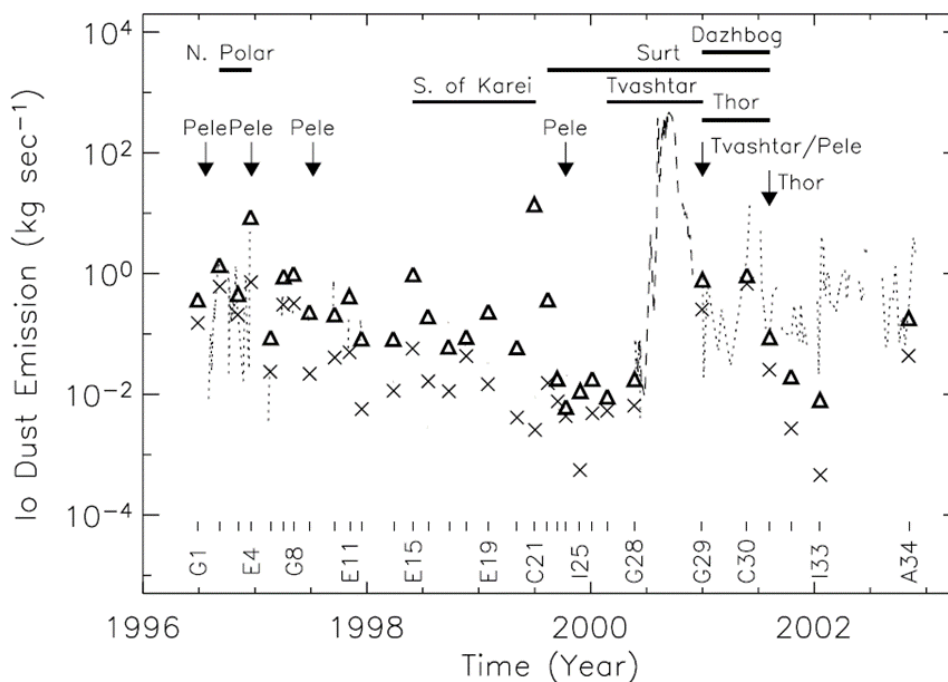


Figure 1.15. Temporal variation in the dust emission rate of Io obtained by Galileo/DDS (Kruger et al., 2003). The triangles and crosses represent the maxima and minima in the distance range $13\text{--}30 R_J$, respectively. The dashed line is in the range of $30\text{--}280 R_J$. Dotted lines show the remaining orbits with $30\text{--}400 R_J$. The horizontal bars indicate periods when surface changes on Io were confirmed (Geissler et al., 2004). Galileo perijove passages are labeled at the bottom.

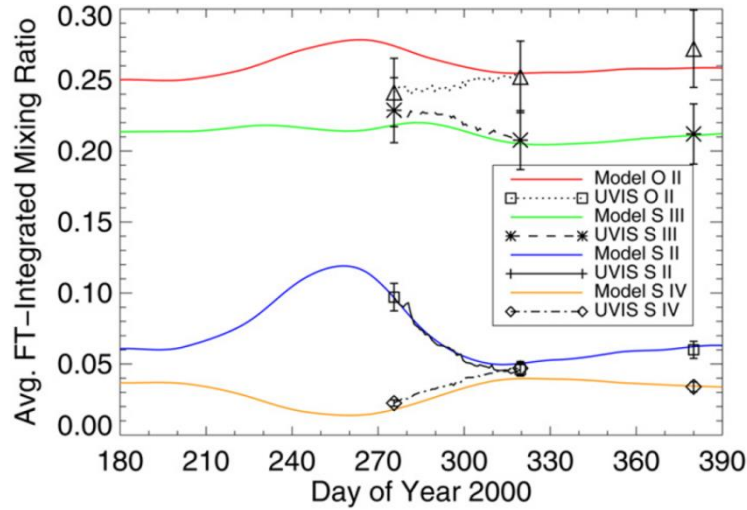


Figure 1.16. Ion mixing ratios in the IPT obtained by Cassini/UVIS (Steffl et al., 2008). Black lines and dots indicate observation. Colorful lines indicate reproduced mixing ratios with the model. Uncertainties of the UVIS mixing ratios are approximately 10%, as shown by error bars.

Temporal variation in the IPT radiation associated with the volcanic activity on Io has been also observed by the Hisaki satellite (Yoshikawa et al., 2017; Kimura et al., 2018; Tsuchiya et al., 2018). The time series of the IPT radiation obtained by the Hisaki satellite and the main volcanic activity captured by ground-based telescopes from Nov. 2013 to Jun. 2018 is summarized in Figure 1.17. The approximate start timings of volcanic activation indicated by ground-based telescopes are labeled in the magenta dotted lines (Yoneda et al., 2015; de Kleer et al., 2019; Morgenthaler et al., 2019). This study focused on the behavior of temporal variation from DOY -374 to DOY -255, from DOY -32 to DOY 132, and from DOY 388 to DOY 728 (from Dec. 2013 to Apr. 2014, from Nov. 2014 to May 2015, from Jan. 2016 to Dec. 2016), as shown by purple horizontal lines in Figure 1.17. From the observation of the Io satellite by the ground-based telescopes, five volcanic events are indicated to occur before and during the above periods. The reason why the above periods were adopted will be described in Chapter 2. Then, I will introduce the characteristics of the five volcanic events. Table 1.3 summarizes the volcanic events. In this study, these events were labeled as Events 1–5, as shown in Figure 1.17 and indicated by triangles in magenta.

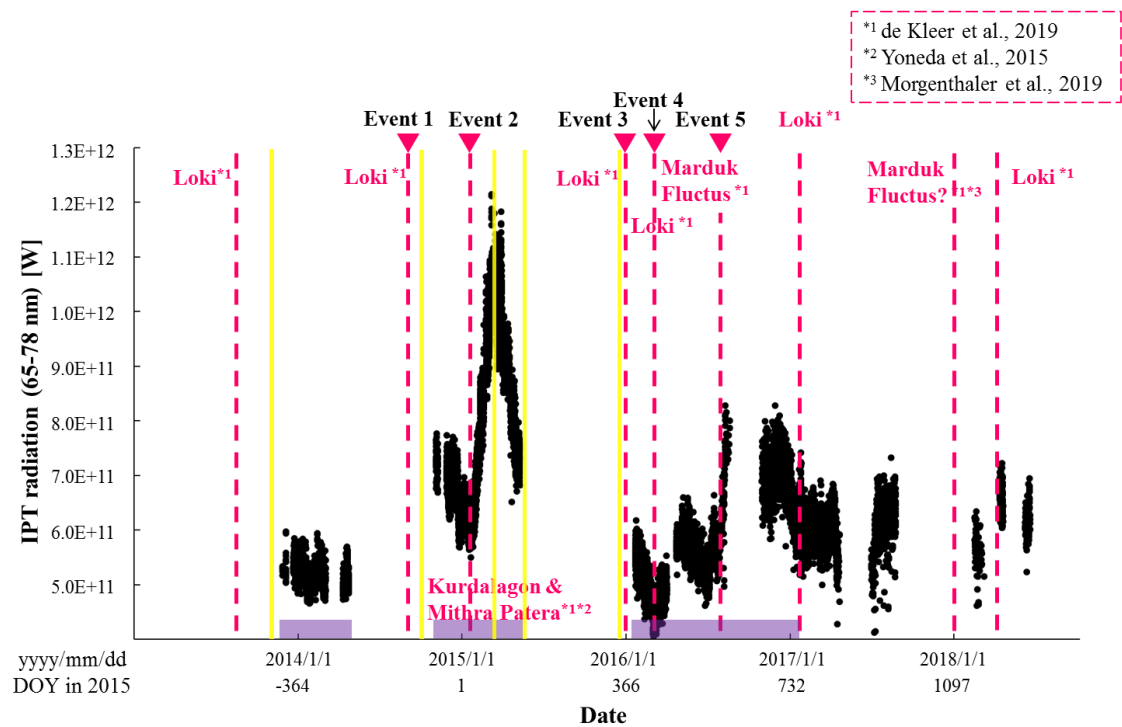


Figure 1.17. Temporal variation in the IPT radiation from 65 nm to 78 nm, which includes the bright lines of S II, S III, and S IV obtained by the Hisaki satellite from Nov. 2013 to Jun. 2018. Approximate start timings of volcanic activations are labeled in magenta dotted lines. Timings of the observation by the narrowest slit are shown in yellow lines. Periods of interest in this study are indicated by purple lines.

Table 1.3. Summary of volcanic events of interest in this study

Event number	Active volcanoes	Approximate timings of activation	References
1	Loki Patera	Aug. 1, 2014 (DOY -138 in 2015)	de Kleer et al., 2019
2	Kurdalagon Patera and Mithra Patera	Jan. 10, 2015 (DOY 10 in 2015)	de Kleer et al., 2019; Yoneda et al., 2015
3	Loki Patera	Jan. 1, 2016 (DOY 365 in 2015)	de Kleer et al., 2019
4	Loki Patera	Mar. 3, 2016 (DOY 427 in 2015)	de Kleer et al., 2019
5	Marduk Fluctus	Jul. 24, 2016 (DOY 570 in 2015)	de Kleer et al., 2019

As for a period involving Event 2, which had the greatest impact on the IPT of the five events, as shown in Figure 1.17, two kinds of observations were conducted by ground-based

telescopes. One was the infrared observation of the volcanoes on Io by de Kleer et al. (2019). It was shown that Kurdalagon Patera (-49° N, 217° W) and Mithra Patera (-58° N, 266° W) had high activities in early 2015. The time series of infrared images of Io obtained by Keck and Gemini N telescopes are shown in Figure 1.18. The other was the D line emission from the sodium atmosphere in Jupiter's magnetosphere (Yoneda et al., 2015). It started to brighten from around Jan. 10, 2015, and reached its peak on Feb. 15, 2015, as shown in Figure 1.19. Therefore, Jan. 10, 2015 (DOY 10) is shown as the timing of volcanic activation in Figure 1.17.

In contrast, for Events 1 and 3–5, the timings of volcanic activations were not clear because there were discontinuities of the Hisaki observation and because as volcanic monitoring, the only infrared observation by de Kleer et al. (2019) was conducted. Regarding Event 1, they showed that the flux density of 3.8- μ m emission from Loki Patera (13° N, 309° W) decreased from Aug. 2014, and it settled down in Jan. 2015, as shown in Figure 1.20. Then, in Figure 1.17, Aug. 2014 was labeled as the activation timing, but it is possible that activation occurred earlier. Also, the emission from Loki Patera started to increase in Jan. 2016. Then, it reached two maxima at the end of Jan. 2016 and Mar. 2016 and settled down in Jun. 2016, as shown in Figure 1.20. Then, for Event 3, Jan. 1, 2016 (DOY \sim 365) was set to the timing of volcanic activation. For Event 4, the timing at which the IPT radiation observed by the Hisaki satellite began to rise (DOY \sim 427) was set to the timing of volcanic activation. Regarding Marduk Fluctus (28° S, 209° W), as shown in Figure 1.20, the emission was higher than the previous year at the start of the observation around Feb. 2016 and gradually increased. Then, it reached the maximum value around May 2016. Similar to Event 4, the timing when the IPT radiation observed by Hisaki began to rise (DOY \sim 570) was set to the timing of volcanic activation.

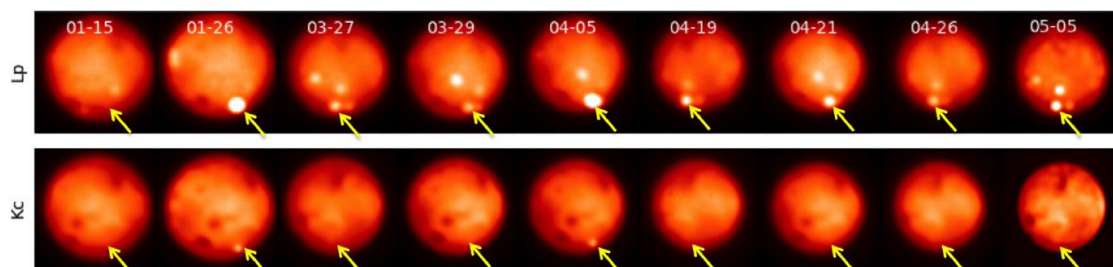


Figure 1.18. Infrared observation of the progression of eruptions at Kurdalagon Patera indicated by yellow arrows in 2015 obtained by the Keck and Gemini N telescopes (de Kleer and de Pater, 2016b). Images are labeled with filter name and central wavelength: Lp and Kc are 3.78 μ m and 2.27 μ m, respectively). The Kurdalagon Patera brightened dramatically on Jan. 26 and Apr. 5.

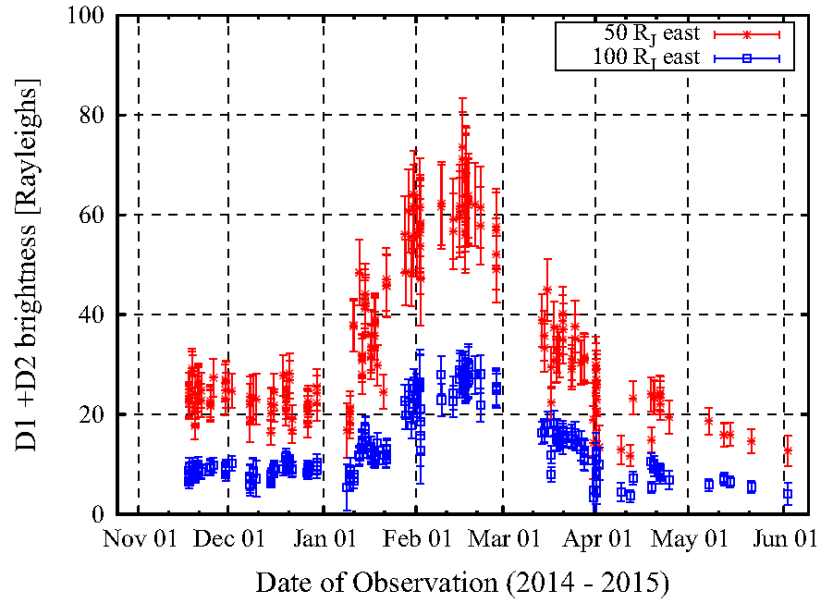


Figure 1.19. D1+D2 brightness of Jupiter’s sodium nebula at 50 R_J and 100 R_J distance on the east side from Nov. 2014 to Jun. 2015 obtained by the ground-based telescope (Yoneda et al., 2015).

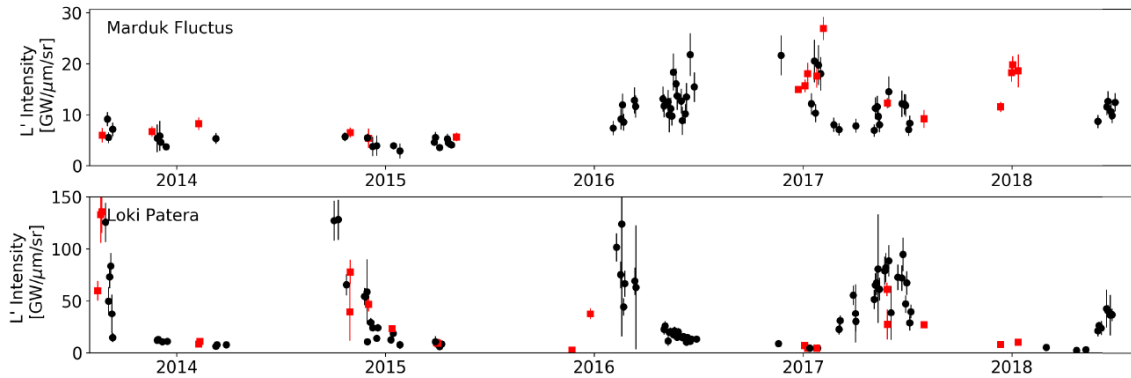


Figure 1.20. Activity timelines of Marduk Fluctus and Loki Patera (de Kleer et al., 2019). The black and red dots indicate detection with Gemini N and Keck telescopes, respectively.

1. 2. 4. Observations of the IPT with remote sensing

Remote sensing is a useful tool to capture time-varying phenomena. Also, spatial information can be obtained by remote observations. The remote sensing of Jupiter’s magnetosphere has been carried out by the spectroscopic observation, the ENA (Energetic neutral atom) observation (Mauk et al., 2004), and radio wave instrument (Clarke et al., 2005). In this study, I used the UV spectroscopic data obtained by the Hisaki satellite. I will introduce the UV spectroscopic observations of the IPT and studies using them.

1. 2. 4. 1. Ultraviolet spectroscopic observations of the IPT

The IPT emission in the UV wavelength range, which is mostly absorbed by the terrestrial atmosphere, has been observed by various instruments. A UV glow near Io was detected for the first time by Pioneer 10 (Judge and Carlson, 1974). In Jan. 1979, UVS (Ultraviolet Spectrometer) on the Voyager spacecraft observed the IPT and detected several emission features near 68.5 and 83.3 nm. Sulfur and oxygen ions were identified from the spectral shape, as shown in Figure 1.21 (Broadfoot et al., 1979). In 1979 and 1980, the spectrograph on the International Ultraviolet Explorer (IUE) obtained spectra of the IPT from 117.5 to 195.0 nm (Moos and Clarke, 1981). The spectral resolution of the IUE was 1.1 nm, which was three times better than that of the Voyager instrument. In 1981, the spectrograph on a sounding rocket detected emissions from the IPT in the wavelength range 115.0–175.0 nm. The spectral resolution was 1.2 nm (Durrance et al., 1983). The Hopkins Ultraviolet Telescope (HUT) obtained the spectrum at 83.0–186.4 nm in the first order and 41.5–93.2 nm in second order with a limiting spectral resolution of ~0.3 nm and ~0.15 nm, respectively (Moos et al., 1991). In 1993, the spectrograph on the Extreme Ultraviolet Explorer (EUVE) detected emission lines between 37.0 and 75.0 nm with a resolution of 0.25–0.35 nm (Hall et al., 1994b). In 2001, the spectrum of the IPT from 90.5 to 118.7 nm was obtained with a resolution of 0.026 nm by the Far Ultraviolet Spectroscopic Explorer (FUSE) (Feldman et al., 2004). Hubble Space Telescope's Space Telescope Imaging Spectrograph observed the IPT from 115.0 to 172.0 nm (Herbert et al., 2003). During the Cassini spacecraft's flyby of Jupiter from 2000 to 2001, several emission lines from 56.1 to 191.2 nm were identified, as shown in Figure 1.22 (Steffl et al., 2004a, 2004b). The spectral resolution, which was measured by the point-spread function, was 0.3 nm.

Extreme Ultraviolet Spectroscope for Exospheric Dynamics (EXCEED) on the Hisaki satellite has obtained the IPT spectrum in the wavelength range from 52.0 to 148.0 nm. Since 2013, EXCEED has obtained the extreme ultraviolet (EUV) spectra of the atmospheres/magnetospheres of planets from Earth orbit. EXCEED consists of an entrance mirror, slits, a grating, and a photon detector. It has three slits of different widths: 10, 60, and 140 arc seconds. The narrowest and widest slits are typically used for the IPT observations. If the widest slit (140 arc seconds) is used, the entire IPT can be imaged, albeit at low spectral resolution. If the narrowest slit (10 arc seconds) is used, an IPT spectrum can be obtained at 0.3–0.4 nm spectral resolution. Details of the instrument and its performance are given by Yoshioka et al. (2013), Yamazaki et al. (2014), and Yoshikawa et al. (2014).

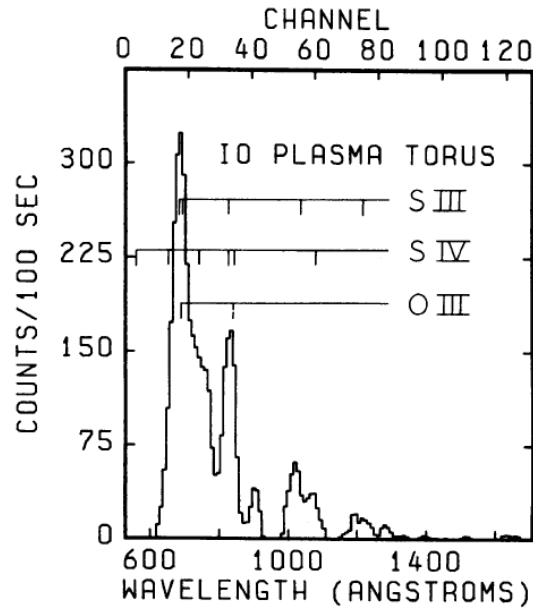


Figure 1.21. Spectrum of the IPT obtained by Voyager/UVS (Broadfoot et al., 1979). Lines of S III, S IV, and O III are indicated by labels.

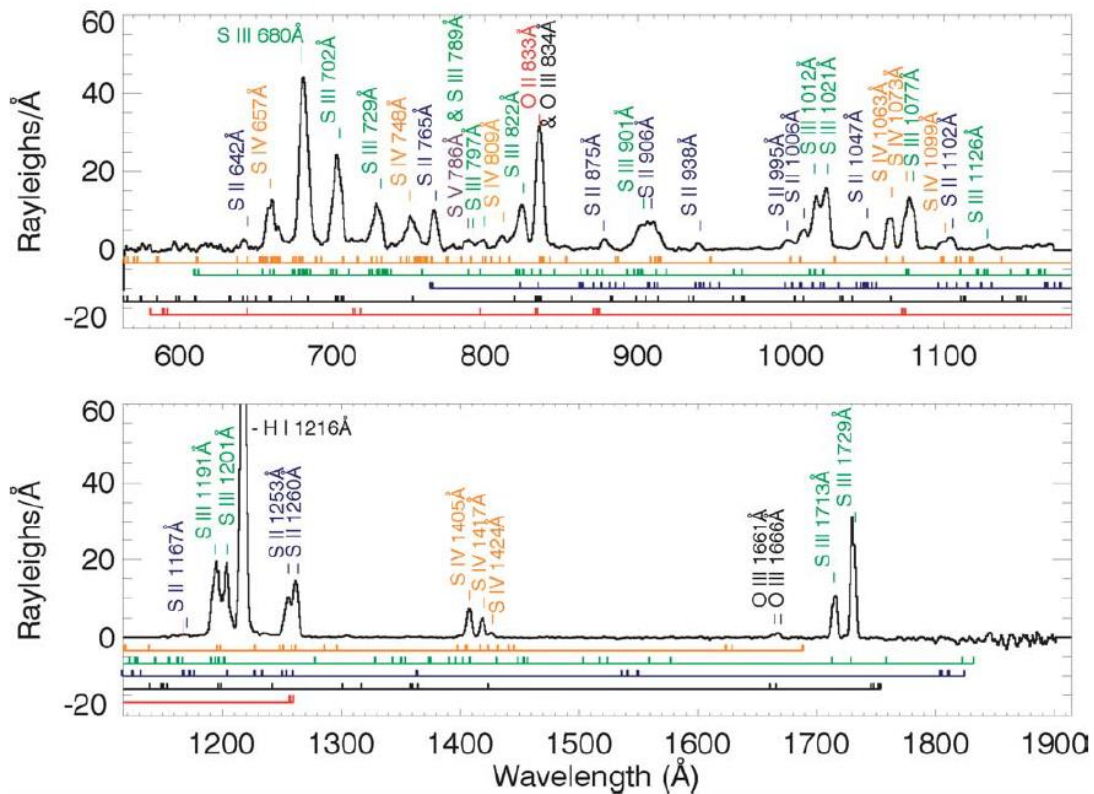


Figure 1.22. Spectrum of the IPT from 56.1–191.3 nm obtained by Cassini/UVIS (Steffl et al., 2004b). The 1-D spectra of the torus covering a radial range of 4–8 R_J are averaged.

1. 2. 4. 2. Derivation of plasma densities and temperature with plasma diagnosis method

The plasma diagnosis, estimating plasma density and/or temperature from two or more line intensities, has been widely used (Mason and Monsignori Fossi, 1994). For example, this method has been used in stellar physics, solar physics, and magnetospheric physics (Mewe, 1991; Watanabe et al., 2007; Yoshioka et al., 2018). In this subsection, the studies applying the plasma diagnosis method for the UV spectroscopic data of IPT will be introduced. The main researches are listed in Table 1.4. The details are described below.

Table 1.4. List of main studies applying the plasma diagnosis method for the UV spectroscopic data of IPT.

Reference	Used data	Observation periods	Wavelength resolution [nm]
Strobel and Davis, 1980	Voyager/UVS	Oct. 1978–Mar. 1979	~3
Shemansky and Smith, 1981	Voyager/UVS	Oct. 1978–Mar. 1979	~3
Hall et al., 1994a	HUT	Dec. 1990	~0.3
Hall et al., 1994b	EUVE	Mar. 30, 1993–Apr. 1, 1993	0.25–0.35
Feldman et al., 2001	FUSE, HUT	Jan. 20, 2000	0.026
Steffl et al., 2004b	Cassini/UVIS	Jan. 14, 2001	0.3
Steffl et al., 2008	Cassini/UVIS	Oct. 2000–Nov. 2000, Jan. 2001	0.3
Yoshioka et al., 2011	Cassini/UVIS	Oct. 4, 2000–Oct. 9, 2000	0.3
Yoshioka et al., 2014	Hisaki/EXCEED	Nov. 27, 2013	0.3–0.4
Yoshioka et al., 2017	Hisaki/EXCEED	Nov. 27, 2013	0.3–0.4
Nerney et al., 2017	Voyager/UVS, Galileo/EUV, Cassini/UVIS	Mar. 15, 1979–Apr. 13, 1979, Jun. 19, 1996–Jun. 22, 1996, Jan. 14, 2001 Nov. 27, 2013	N/A
Yoshioka et al., 2018	Hisaki/EXCEED	Feb. 18, 2015–Feb. 23, 2015 Dec. 20, 2013–Apr. 20, 2014, Nov. 30, 2014–May 12, 2015,	0.3–0.4
This study	Hisaki/EXCEED (with the 140 arcseconds slit)	Jan. 23, 2016–Mar. 14, 2016, May 7, 2016–Aug. 27, 2016, Oct. 31, 2016–Dec. 28, 2016	> 1

By Strobel and Davis (1980) and Shemansky and Smith (1981), the plasma densities and temperature inside the IPT from the UV spectroscopic observation by Voyager/UVS was derived. Feldman et al. (2001) determined the ion mixing ratios using the FUSE data. Utilizing observations with high wavelength resolution, they detected the emission of Cl ions and discussed its mixing ratio. The Cassini spacecraft captured the long-term fluctuation in the UV radiation from the IPT for the first time. Steffl et al. (2004b) derived the radial distribution of column densities and temperature of plasmas from the Cassini/UVIS data. They found that when the kappa distribution is assumed as the electron velocity distribution, the spectrum fits slightly better than when the Maxwell distribution is assumed. The kappa values were obtained, as shown in Figure 1.23. The kappa value is smaller at the outer side, that is, the gradient of the electron velocity distribution is gentler: there are more hot components in the outer region. The derived kappa values are consistent with the value by Mayer-Vernet et al. (1995) using the data obtained by the Ulysses spacecraft. Steffl et al. (2008) showed the fluctuations in the ion mixing ratios over two months associated with the volcanic activity. Yoshioka et al. (2011) assumed that the electron velocity distribution is composed of two components, a core component of several eV and a hot component of several dozens of eV to ~ 1000 eV and derived the hot electron fraction from the Cassini data. Yoshioka et al. (2014), Yoshioka et al. (2017), and Yoshioka et al. (2018) revealed the radial distribution of plasma densities and temperature in the volcanically quiet and active periods using the Hisaki data with high wavelength resolution mode with the 10 arcseconds slit. Nerney et al. (2017) reanalyzed the data obtained by Voyager/UVS, Galileo/EUV, and Cassini/UVIS using the latest version of the CHIANTI atomic database (version 8.0.7) (Dere et al., 1997; Del Zanna et al., 2015). The differences between database versions are not noticeable.

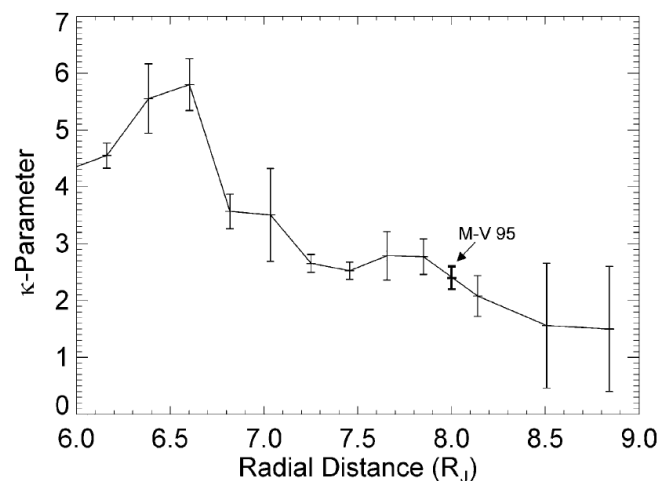


Figure 1.23. Derived kappa parameters versus radial distance by the Cassini data and kappa values by the Ulysses data (Steffl et al., 2004b). The solid line is obtained by the Cassini data. The labeled M-V 95 is obtained by the Ulysses spacecraft.

1. 2. 5. Hot electron component

In this subsection, the direct observation of the hot electron component in Jupiter's magnetosphere and researches on mechanisms which have been considered responsible for the presence of the hot electrons will be presented. Moreover, the temporal variation in the hot electron component, which is associated with the volcanic activity of the Io satellite, will be introduced.

1. 2. 5. 1. Direct observations

The electron environment in Jupiter's magnetosphere was surveyed by past missions. An in-situ observation between 6 to 13 R_J was made by the Voyager spacecraft within an energy range of 10 to 5950 eV (Sittler and Strobel, 1987). The Galileo spacecraft provided further information between 6 to 8 R_J in an energy range of 0.9 to 5200 eV (Frank and Paterson, 2000a). These observations showed that the electron velocity distribution in the above region had a core component of several eV and a hot tail. The electron velocity distribution in the IPT obtained by the Voyager spacecraft is shown in Figure 1.24. For convenience, most of the studies have adopted the two-Maxwellian approximation for the electron population.

The hot electron temperature is thought of as several dozens of eV to ~1000 eV (Bagenal, 1994; Delamere and Bagenal, 2003). The radial distribution of hot electron temperature obtained by the Voyager spacecraft is shown in Figure 1.25 (Bagenal, 1994). It can be seen that the hot electron temperature from 5 R_J to 10 R_J is ~100–300 eV. However, its stationarity is unknown due to the nature of direct observation. Also, the hot electron temperature was estimated to be 40–600 eV from the physical chemistry model, which will be introduced in Subsection 1.2.6; however, in this model, it is difficult to separate information on temperature and density, and it should be mentioned that there is large uncertainty.

Note that the Voyager observation indicated that there is a trend that at larger distances from Jupiter, there is a greater fraction of hot electrons to the total electron density (Scudder et al., 1981).

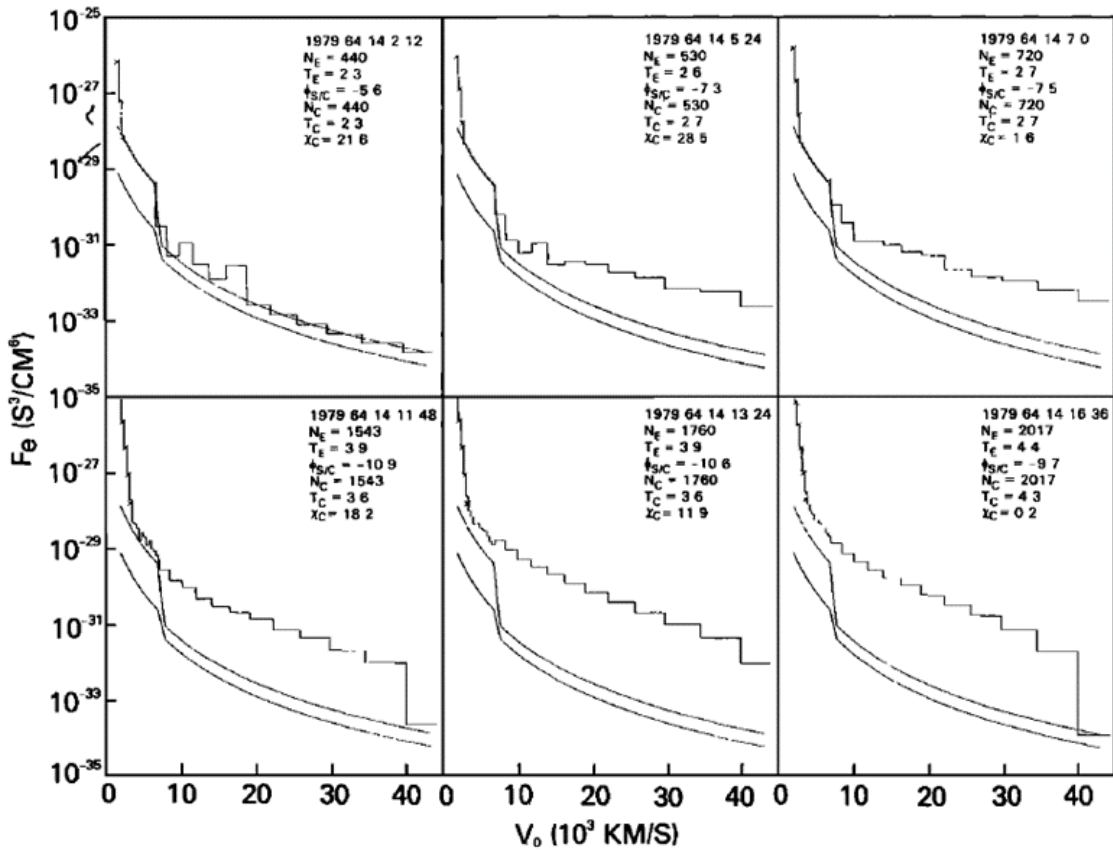


Figure 1.24. Electron distribution function in the IPT obtained by the Voyager spacecraft (Sittler and Strobel, 1987), which is shown by the top line in each panel. The fitting to the core component is shown in the middle line. The zero-count level is indicated by the lowest line. Measurement time, moment estimated total electron density and temperature, spacecraft potential, cold electron density and temperature, and chi-square value of cold component fit are indicated in the upper right-hand corner of each panel.

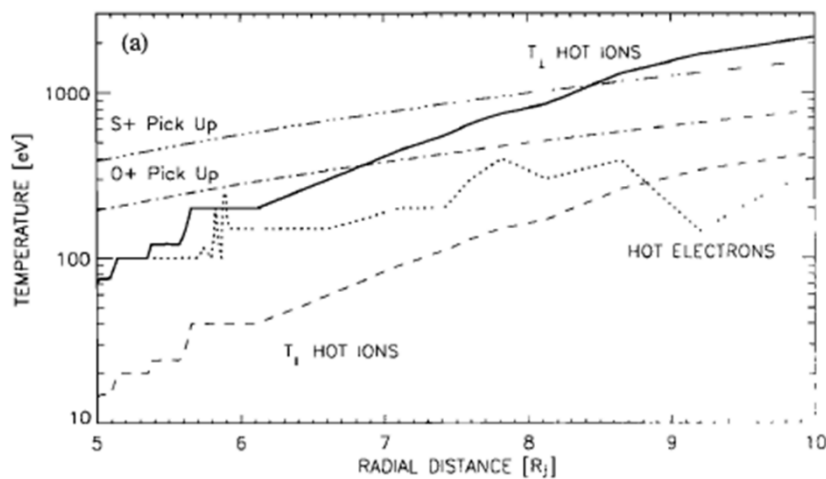


Figure 1.25. Perpendicular temperature of hot electrons (dotted line) by the Voyager/PLS instrument (Bagenal, 1994).

1. 2. 5. 2. Mechanisms considered to be responsible for the presence of hot electrons

There is still controversy over whether the hot electrons in the IPT are transported from outside the torus or generated locally in the torus. Details will be described as follows.

As candidate carriers of hot electrons from outside the torus, the interchange motion of magnetic flux tube and an Earth-like injection whose signatures were captured by the Galileo spacecraft, as described in Subsubsection 1.1.2.2, have been proposed. From Nov. 2013, the observation of the IPT radiation has been made by the Hisaki satellite for the longest period in the UV wavelength range. Yoshioka et al. (2014) obtained the radial distributions of plasma densities and temperature using the Hisaki data with high wavelength resolution on 29, Nov. 2013, as shown in Figure 1.26. They showed that there is an outward gradient of hot electron fraction as an average picture for 550 min of the integration time, which is interpreted as the existence of continuous hot electron transport from outside the IPT that balances with collisional loss. However, the possibility that local heating is responsible for the presence of hot electrons has not been rejected, and it has not been clarified whether inward transport contributes to the presence of the hot electrons in the IPT.

Note that the origin of the transported hot electrons remains an open research problem. It was revealed by the Voyager observation that there are hot tails in the velocity distributions in both the magnetosheath and the outer magnetosphere (Scudder et al., 1981). Therefore, it is expected that there is energy transport between them in some way, including the wave-induced transport (Delamere and Bagenal, 2010).

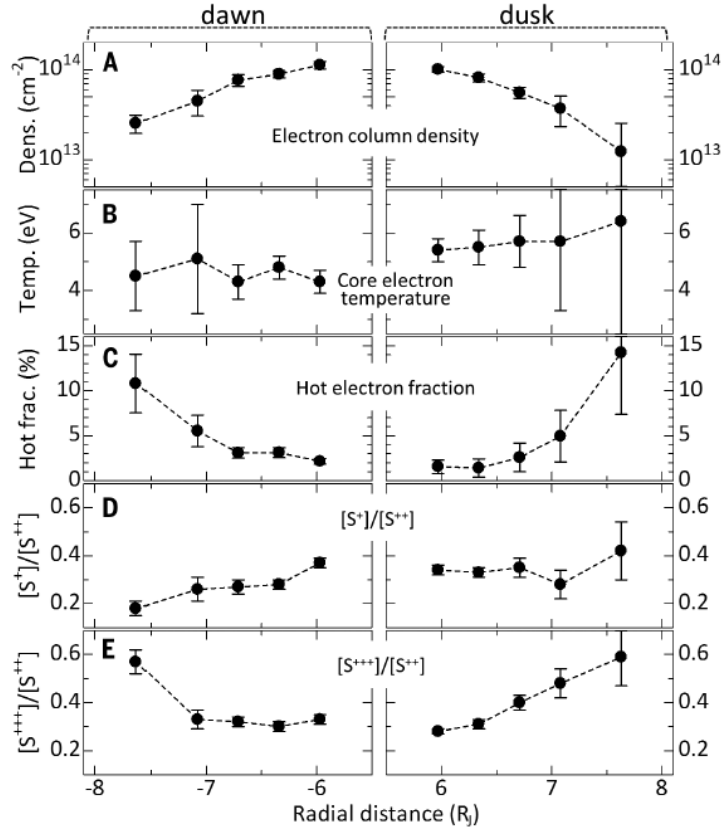


Figure 1.26. Radial distribution of plasma parameters derived from spectroscopic observation by the Hisaki satellite (Yoshioka et al., 2014). (A) Electron column density. (B) Core electron temperature. (C) Hot electron fraction. (D) Ratio of S^+ density to S^{2+} density. (E) Ratio of S^{3+} density to S^{2+} density. The error bars represent the one-sigma values.

Meanwhile, three possible mechanisms of heating inside the IPT have been proposed. The first is the interaction with Alfvén waves generated by the radial motion of magnetic flux tubes (Hess et al., 2011; Copper et al., 2016). The other two, which are heating mechanisms near Io, are the interaction with Alfvén waves generated by Io’s passage through Jupiter’s magnetosphere (Hess et al., 2011) or the interaction with ion cyclotron waves excited by pickup molecular ions (Russell et al., 2001). In fact, past observations confirmed the dependence of the IPT radiation on the Io phase angle, which is interpreted as the existence of electron heating near Io (Sandel and Broadfoot, 1982a; Steffl et al., 2006; Tsuchiya et al., 2015). For instance, the analysis using the Hisaki data from Dec. 31, 2013 to Jan. 13, 2014 revealed that the line intensities at short wavelength range near Io are brighter than those far from Io, as shown in Figure 1.27. As the wavelength dependence of line intensities reflect the electron energy, the above result is interpreted as the existence of the local heating near Io (Tsuchiya et al., 2015).

However, there is no quantitative evaluation of the contribution of each mechanism to the presence of the hot electrons. Therefore, the mechanism responsible for the presence of the hot electrons, the transport or the local heating, remains an open research problem.

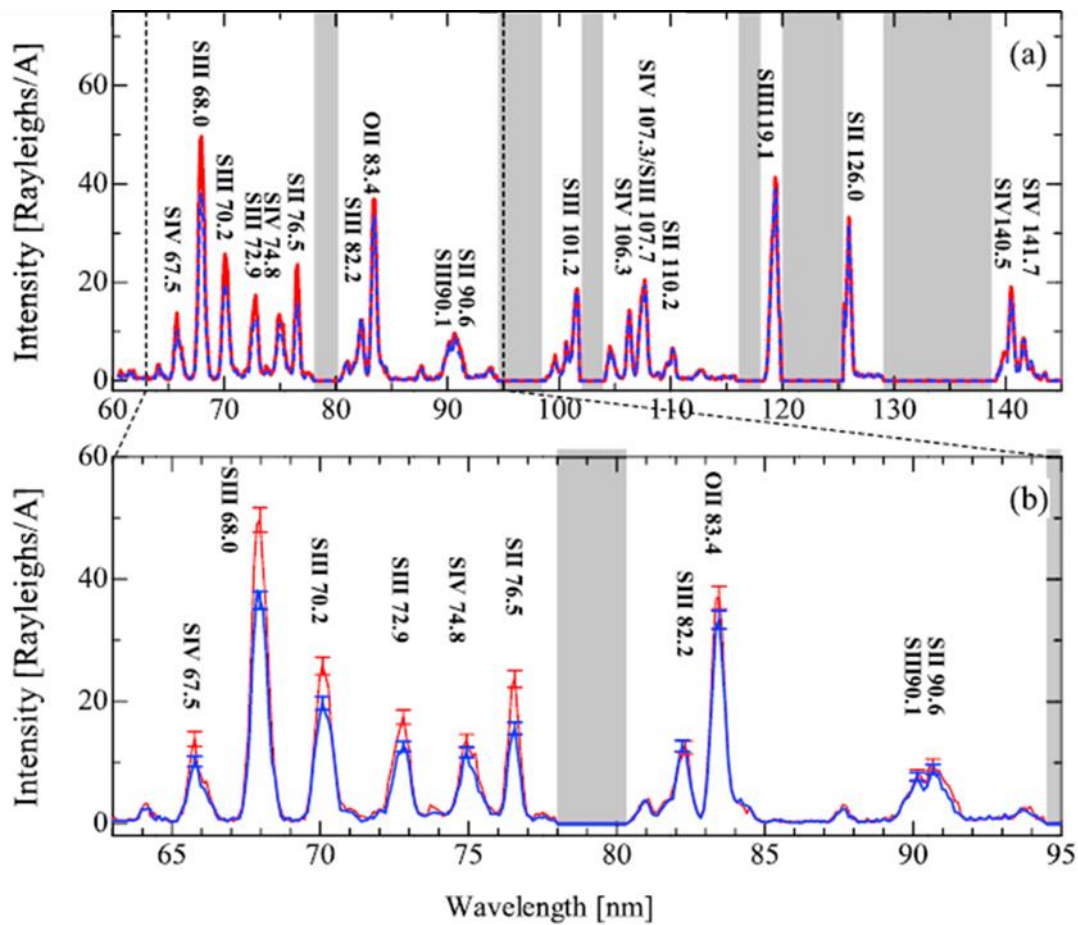


Figure 1.27. (a) IPT spectra near Io (red solid line) and far from Io (blue broken line) obtained by the Hisaki satellite. Areas including geocoronal emissions, which are removed in this figure, are indicated by gray shades. Integrated period is Dec. 31, 2013 to Jan. 13, 2014. (b) Same as (a) except for the wavelength range from 63 to 95 nm (Tsuchiya et al., 2015).

1. 2. 5. 3. Time variability

There are few opportunities for direct observations. Besides, direct observations suffer from limited spatial and temporal coverage. From remote observations by the Cassini spacecraft and the Hisaki satellite, the temporal variation in the density and fraction of the hot electron has been discussed, as described below.

Cassini observed IPT radiation from several tens of days after a volcanic eruption on Io in 2000, which is introduced in Subsection 1.2.3, and recorded a trend in which luminosity decreased with time, as shown in Figure 1.28. The Cassini observation indicated that temporal variation in the observed UV radiation can be reproduced assuming an increase in the density of hot electrons after the volcanic eruption in addition to an increase in the plasma supply rate

to the IPT (Steffl et al., 2008). Please note that only the trend of decreasing luminosity of the IPT with time was observed, and the Cassini observation was not able to capture a time series of the IPT radiation from the volcanic activation to return to the initial state.

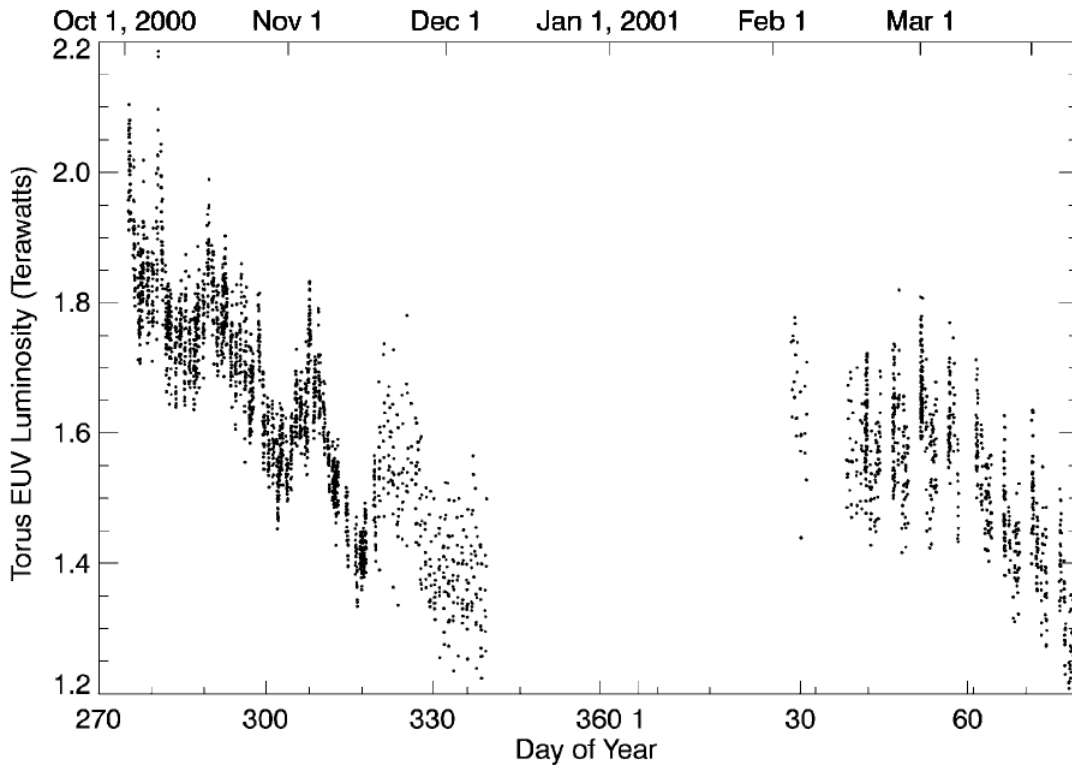


Figure 1.28. Torus EUV luminosity obtained by the Cassini observation (Steffl et al., 2004a)

Besides, the analysis using the Hisaki data revealed that the hot electron density increased during another volcanic active period in Feb. 2015 (Yoshioka et al., 2018). Yoshioka et al. (2018) obtained the radial distribution of plasma densities and temperature, as shown in Figure 1.29. Yoshioka et al. (2018) used the high spectral resolution data in Feb. 2015, when the volcanic activity was high, in addition to Nov. 2013, when the volcanic activity was low. During the volcanic event, the hot electron density increased in the inner region of the torus.

As the mechanism of the temporal variation in the hot electron density, either the transport and the local heating are possible, and no conclusion has been reached as to which is dominant.

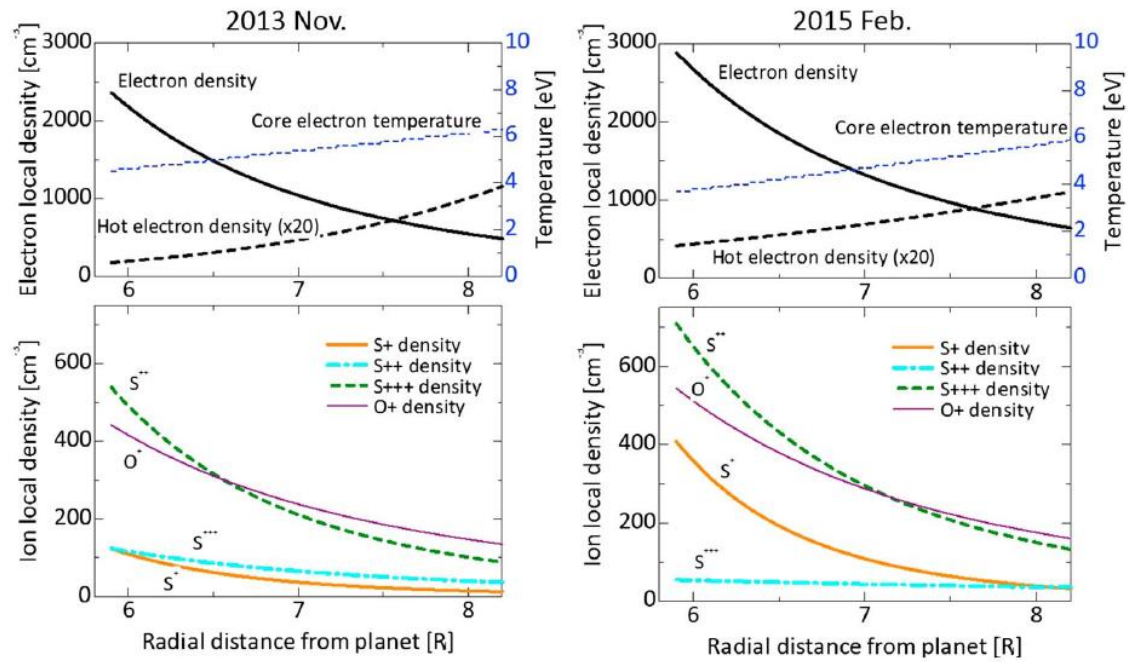


Figure 1.29. Radial variation in plasma densities and temperature in the volcanically quiet (left) and active (right) periods (Yoshioka et al., 2018). The top panels show the local electron densities and core temperature. The bottom panels show the local ion densities. Power-law distribution is assumed.

1. 2. 6. Energy budget of the IPT

The hot electron fraction inside the IPT is only a few percent at most, but its roles in energy balance and ion mixing ratios are significant. Delamere and Bagenal (2003) clarified the mass and energy balance, assuming the IPT as one system in a steady state. They determined five parameters (source rates of sulfur and oxygen atoms, loss timescale, and temperature and fraction of hot electrons) that reproduce the plasma densities obtained by the Voyager and Cassini spacecraft. The electron impact ionization, deionization, and charge exchange reactions were considered as chemical reactions inside the IPT. The outward transport and escaping fast neutrals were assumed as escape mechanisms from the system. This model is called the physical chemistry model. Regarding the energy balance, heat transfers via chemical reactions, Coulomb collision, and radiation were considered. As a result, as shown in Figure 1.30, it was found that the ratio of hot-electron energy to the whole IPT energy input is between 11% and 61%. Also, it can be seen that the contribution of hot electron energy to the UV emission is 26–66%: that is, the pickup energy can only fuel 34–74% of the radiation. Note that during the Cassini observation, which was conducted after the volcanic activation as described in Subsection 1.2.3, the contribution of hot electron energy tends to be larger than that in the Voyager observation period. This is consistent with the tendency as described in Subsubsection 1.2.5.3: the hot electron density increases after the volcanic activation.

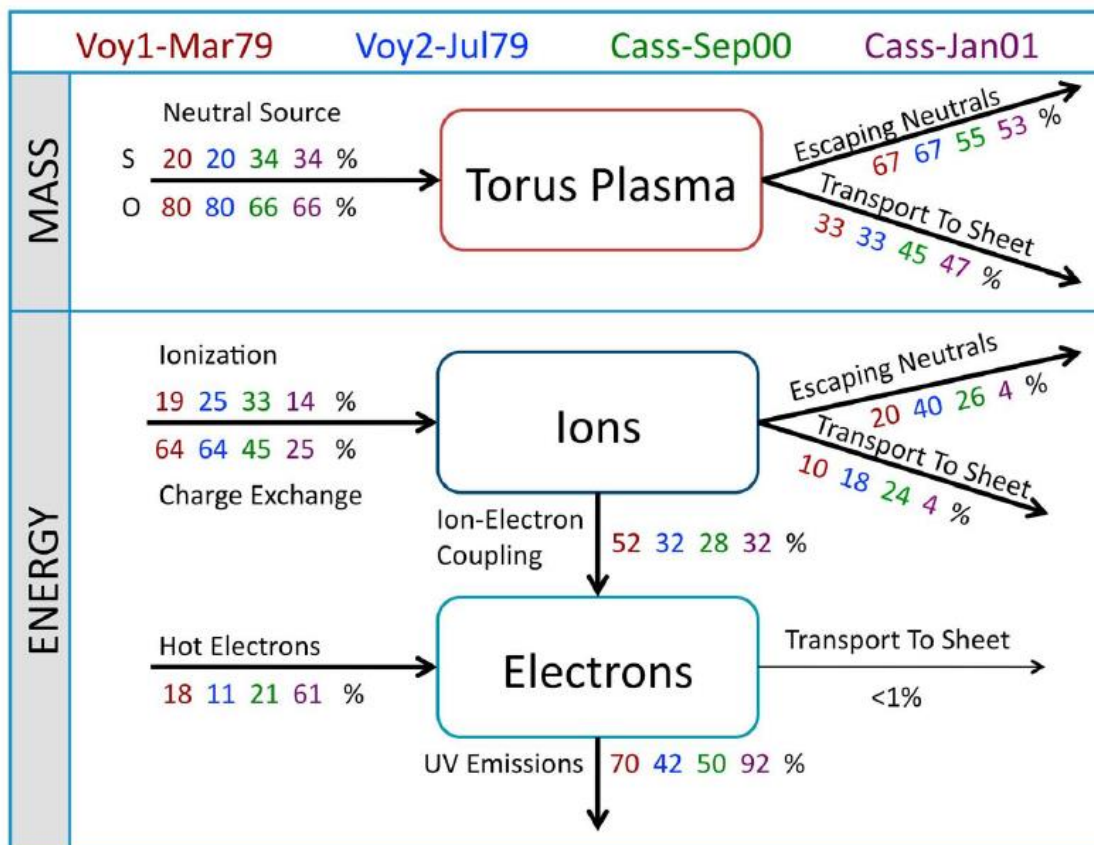


Figure 1.30. Schematic diagram of the mass and energy flow through the IPT during the Voyager and Cassini flybys: Mar. 1979, Jul. 1979, Sep. 2000, and Jan. 2001 (Bagenal and Delamere, 2011).

1. 3.The goal and layout of this thesis

As described in Subsection 1.2.5, the mechanism responsible for the temporal variation in the hot electron density in the IPT associated with the volcanic eruption is an open question. Either the local heating and the transport is possible, and no conclusion has been reached as to which is dominant. This is mainly because before the Hisaki observation, there was no observation that includes a time series from a volcanic activation to a return to initial state. One of the purposes of this study is to explore the mechanism behind the temporal variation in the hot electron density.

By clarifying the mechanism of the temporal variation in the hot electron density, how plasma transport or heating changes occur during a volcanically active period can be understood; therefore, there is a possibility that the response of Jupiter's magnetospheric dynamics to volcanic activation can be explored. It can be expected that volcanic activation would cause the following changes in Jupiter's magnetospheric dynamics: (1) increases in the

plasma density in the IPT; (2) enhanced mass loading; and (3) increases in the efficiency of radial transport due to increases in the magnetic flux tube content. The other purpose of this study is to validate this hypothesis on the response of Jupiter’s magnetospheric dynamics to volcanic activation.

To clarify the temporal variation in the plasma density and temperature in the IPT associated with volcanic activation using the spectral data from the Hisaki satellite is an effective way to tackle the above topics. Then, in this study, the analysis method for applying plasma diagnosis to the data with the 140 arcseconds slit, which are regularly acquired by the Hisaki satellite, was developed. As shown in Table 1.4, the observation of the IPT by the Hisaki satellite with the widest slit, which is used in this study, is the most continuous and longest observation to date. With the 140 arcseconds slit, the entire image of the IPT is captured in the field of view, and the total radiation from the IPT can be observed. Therefore, this slit is used for most of the observation period. However, due to this characteristic, with the data with the 140 arcseconds slit, the wavelength dispersion information is contaminated by the spatial structure of the IPT in the north-south direction, which will be explained in detail in Section 2.2. Therefore, the line brightness could not be derived, and the application of plasma diagnosis to data by the Hisaki satellite has so far been limited to data obtained by observations with the 10 arcseconds slit, which have been performed only for several days (e.g., Yoshioka et al., 2018). In this study, the analysis method for applying plasma diagnosis to the data with the 140 arcseconds slit was developed, and the temporal variation in plasma densities and temperature was clarified. The characteristics of observations with the 10 arcseconds slit and 140 arcseconds slit are summarized in Table 1.5.

Table 1.5. Characteristics of observations with the 10 arcseconds slit and 140 arcseconds slit

	Spectral resolution	Time continuity	Derivation of the total radiation	Derivation of line brightness (Application of plasma diagnosis)
Observation with the slit of 10 arc seconds	⊙	×	×	○
Observation with the slit of 140 arc seconds (This study)	△	⊙	○	△

In this paper, the dataset and method of analysis will be shown in Chapter 2. The temporal variation in plasma densities and temperature in the IPT will be shown in Chapter 3. In Chapter 4, the temporal variation in the radial distribution of mass density will be shown. In Chapter 5, the dawn-dusk asymmetry of the hot electron density will be described. The cause of the dawn-dusk asymmetry will be discussed. Finally, a general conclusion will be given, and the response of the dynamics of Jupiter's magnetosphere to the volcanic activation will be argued in Chapter 6.

2. Dataset and methods

2. 1.Dataset

I used the UV spectroscopic data obtained by EXCEED mounted on the Hisaki satellite. Hisaki has been observing IPT radiation intermittently from its launch at the end of 2013 to the present day. It has been performing imaging spectroscopy of planetary atmosphere/plasma in the EUV wavelength range from Earth orbit with its inclination angle of 29.7 degrees. The orbital period is 105 min. EXCEED counts photons for ~40 min of continuous exposure, which is conducted in every orbit. The observation geometry is shown in Figure 2.1. The specifications of EXCEED are listed in Table 2.1. EXCEED mainly consists of a parabolic mirror with a diameter of 200 mm entrance mirror, slits, a reflective diffraction grating with a scored area of 60 mm in diameter, and a two-dimensional photodetector. EXCEED covers a wavelength range of 52.0 to 148.0 nm. The optical design and ray path are shown in Figure 2.2. The surface of the mirror is chemically vapor-deposited with silicon carbide (CVD-SiC) to increase the reflectivity of EUV light. The reflected light passes through the slit and enters the diffraction grating whose surface is toroidal. The diffracted light is focused on the detector, and a two-dimensional spectrum is obtained, with one axis representing wavelength and the other axis representing spatial information. CVD-SiC is also applied to the surface of the diffraction grating. Details of the instrument and its performance are given by Yoshioka et al. (2013), Yamazaki et al. (2014), and Yoshikawa et al. (2014).

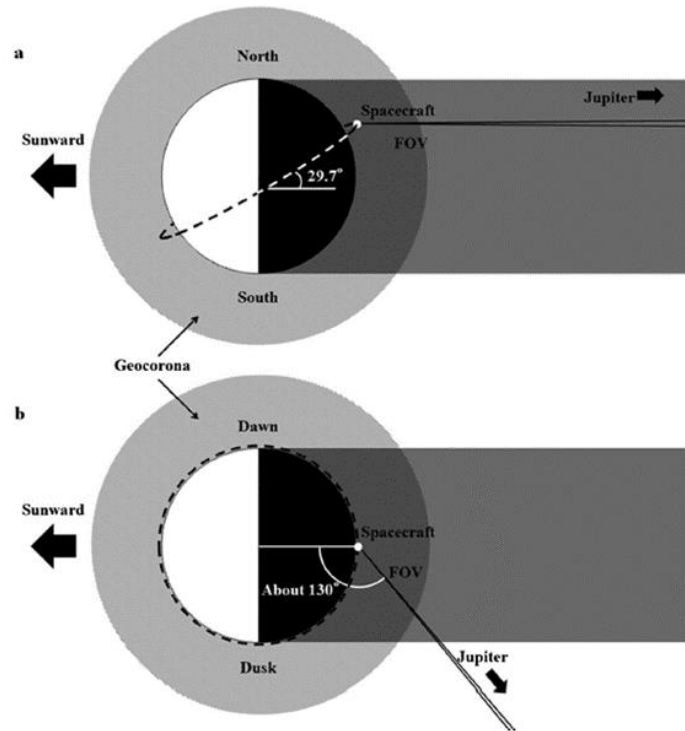


Figure 2.1. Observation geometry of Hisaki satellite during Jupiter observation as viewed from (a) the side and (b) above the north pole of the Earth in Feb. 2014 (Kuwabara et al., 2017). Orbital inclination is 29.7 degrees. Satellite orbit is shown in the dashed line. The field of view of the EXCEED is represented in solid lines.

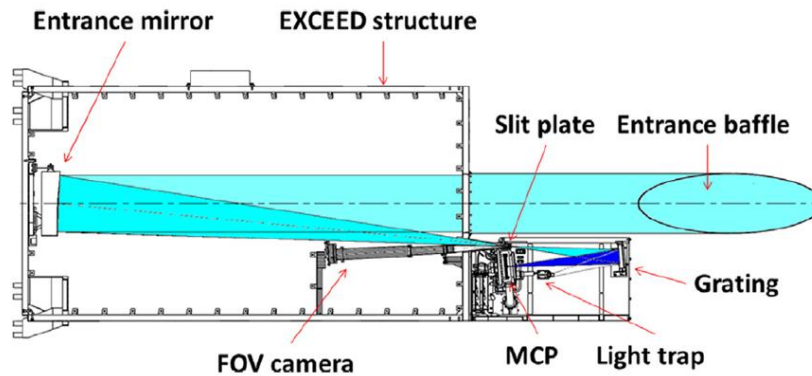


Figure 2.2. Optical design of EXCEED (Yoshioka et al., 2013). Photons are incident on the entrance mirror and collected onto the slit. FOV guiding camera monitors the reflected light from the slit plate. Light passing through the slit is diffracted by the grating and converted to the electrons by an MCP detector.

Table 2.1. Specifications of EXCEED (modified from Yoshioka et al. [2013])

Entrance mirror	Shape	Off-axis (5.4°) parabolic
	Effective diameter	203 mm
	Reflecting surface	CVD-SiC
	Focal length	1600 mm
Slits	Widths	10", 60", 140"
	Wavelength resolution	~0.3–0.4 nm (10"), ~0.9 nm (60"), >1.0 nm (140") (FWHM)
Grating	Shape	Toroidal (Rh = 400 mm, Rv = 393 mm)
	Effective diameter	50 mm
	Surface	CVD-SiC
	Groove lines	Laminar, 1800 mm ⁻¹
Detector		Micro Channel Plate (MCP) with CsI and Resistive Anode Encoder (RAE)
Field of view		400" × (10", 60", 140")
Wavelength range		52.0–148.0 nm

EXCEED has three slits of different widths: 10, 60, and 140 arc seconds. The narrowest and widest slits are typically used for the IPT observations. If the narrowest slit (10 arc seconds) is used, an IPT spectrum can be obtained at ~0.3 nm spectral resolution. If the widest slit (140 arc seconds) is used, the entire IPT can be imaged, albeit at low spectral resolution. Examples of spectral images of the Jupiter observation taken by Hisaki are shown in Figure 2.3(a) and Figure 2.3(b), which were obtained with the narrowest slit and widest slit, respectively. The horizontal and vertical axes represent the wavelength and distance from the center of Jupiter, respectively. The example of the 1-D spectrum on the dusk side is shown in Figure 2.3(c). The data in the orange dotted line in Figure 2.3(b) were integrated. Emission from the IPT, Jovian aurora, and geocorona appear in the spectra. The IPT is seen on both sides of Jupiter. The Jovian aurora is seen on the disk and above 90.0 nm in the spectral axis. The geocoronal emissions at He I 58.4 nm, O II 83.4 nm, H I 97.3 nm, H I 102.6 nm, H I 121.6 nm, O I 130.2 nm, and O II 135.6 nm illuminate in the entire area of slits. The Hisaki satellite orbits around the Earth with an apogee (perigee) altitude of 954 km (1156 km). Then, the spectrum includes contributions from not only the IPT emission but also foreground geocoronal emission. The detailed discussions of line identification using the Hisaki data with the best spectral resolution mode will be shown in Appendix A.

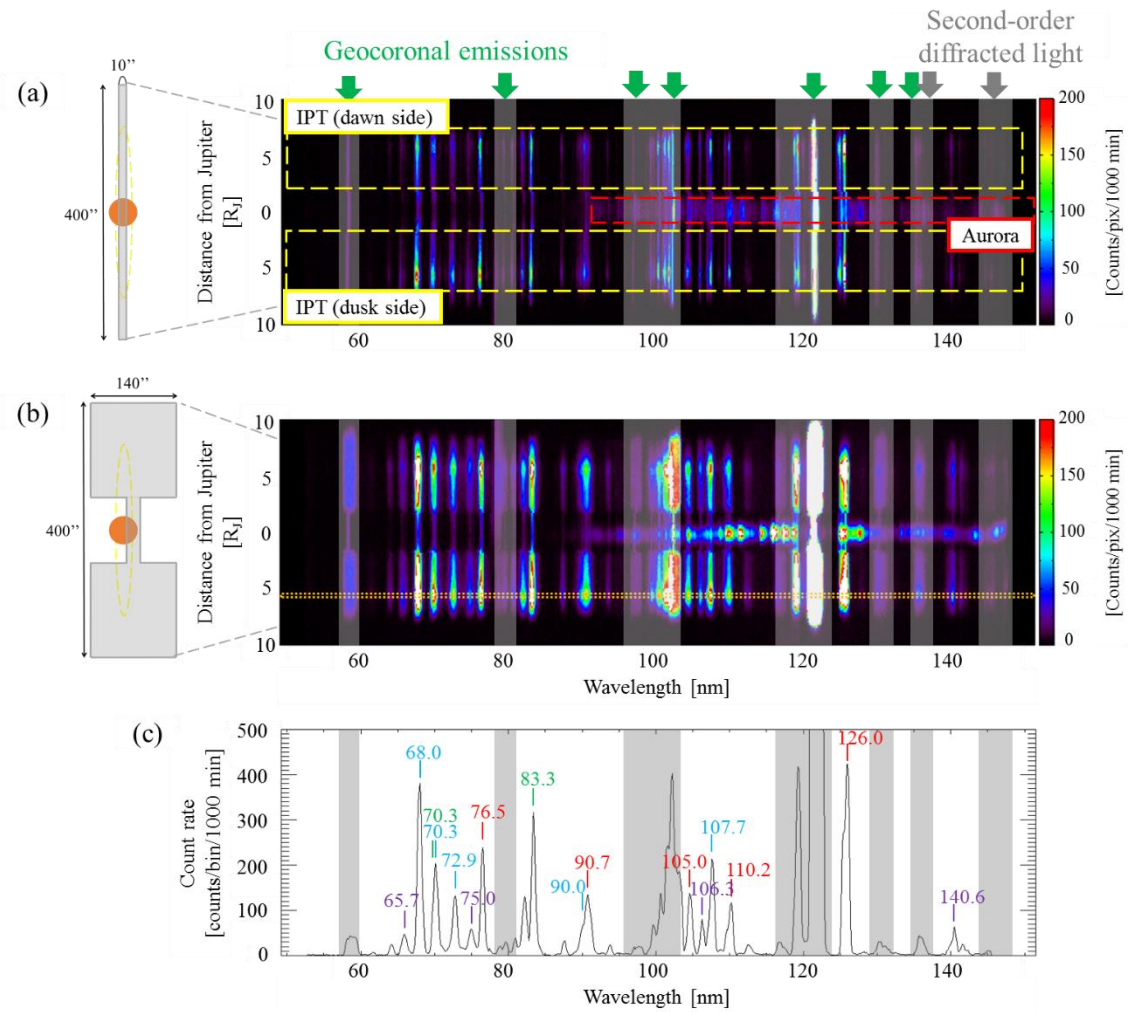


Figure 2.3. (a) Example of the spectral image obtained by Hisaki/EXCEED with the narrowest slit. Data from Feb. 18, 2015 to Feb. 22, 2015 are integrated. The total integration time is 2439 min. Wavelength ranges, including geocoronal emission lines, secondary diffracted light, and ghost, are shown in gray. (b) Example of spectral image with the widest slit. Data from Feb. 5, 2015 to Feb. 9, 2015 are integrated. The total integration time is 2817 min. (c) Example of 1-D spectrum obtained from the integrated data at a distance from Jupiter of 5.9–6.2 R_J on the dusk side (indicated by the orange dotted line in [b]). Main emission lines are labeled in red, blue, purple, and green, which indicates S II, S III, SIV, and O II and O III, respectively.

The time series of the IPT radiation obtained by Hisaki/EXCEED with the slit of 140 arc seconds and the main volcanic activities indicated by ground-based telescopes from Nov. 2013 to Jun. 2018 are summarized in Figure 2.4. The timing when the Field-Of-View (FOV) guiding camera broke down is shown by the blue dotted line. It should be noted that the failure of the FOV guiding camera prevents us from using data after 2017. Currently, the Hisaki project is developing a method for data selection after 2017, but it is difficult to obtain continuous information as before 2016. After the FOV guiding camera broke down, the pointing accuracy

was degraded, and it is necessary to select the data carefully. The IPT radiation after the failure of the FOV guiding camera shown in Figure 2.4 was obtained by selecting data with certain conditions for the aurora and IPT positions along the spatial axis (the vertical axis in Figure 2.3[b]). As can be seen in Figure 2.4, after the failure of the guiding camera, the scattering of the data is larger than before the failure, and to improve the data selection method is a future issue. Then, this study focused on the behavior of temporal variation in plasma densities and temperature from DOY -374 to DOY -255 , from DOY -32 to DOY 132, and from DOY 388 to DOY 728 (from Dec. 2013 to Apr. 2014, from Nov. 2014 to May 2015, from Jan. 2016 to Dec. 2016). In this study, the above observation periods were labeled as the first season, second season, and third season, as shown in the top of Figure 2.4.

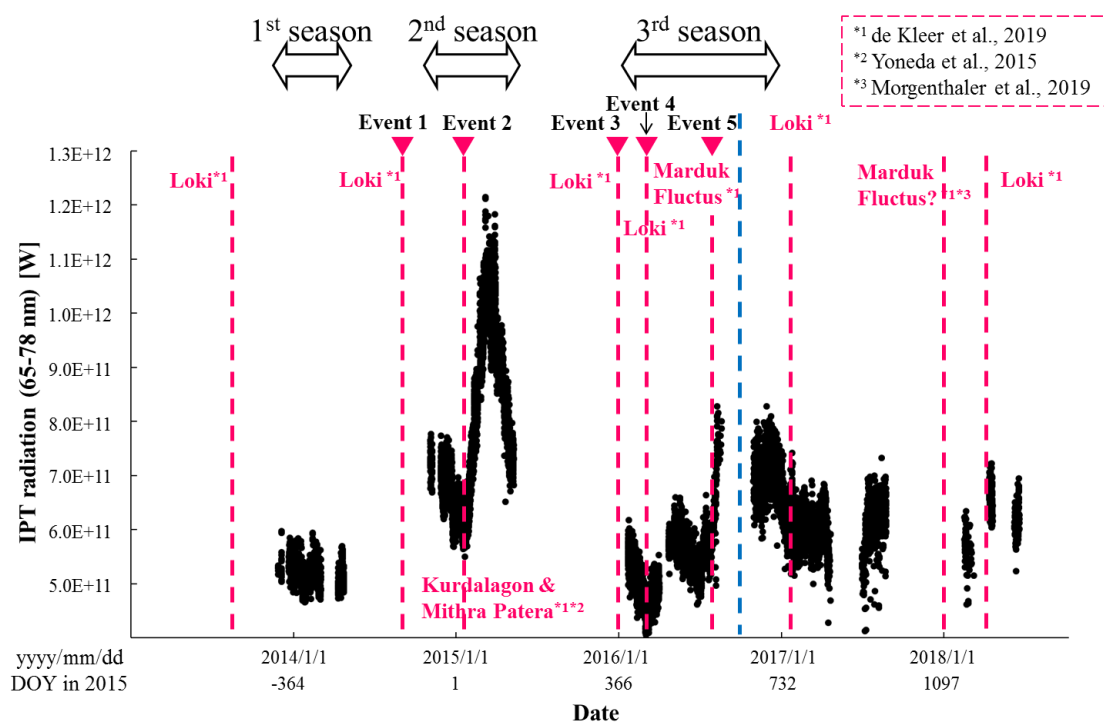


Figure 2.4. Same as Figure 1.17, except for the blue dotted line, which indicates timing when the FOV guiding camera broke down.

2. 2.Methods

2. 2. 1. Introduction: plasma diagnosis method

Spectroscopic remote sensing is a powerful tool for deriving the density and temperature of plasma. The method of exploring the condition of plasma in emission regions using spectral data is called plasma diagnosis, which has been widely used (Osterbrock, 1989; Mason and Monsignor Fossi, 1994). In this study, this method was applied to the Hisaki data. The main

components of ions in the IPT are S^+ , S^{2+} , S^{3+} , O^+ , O^{2+} , and H^+ . The sulfur and oxygen ions emit radiation mainly via the electron impact excitation. By observing the radiation with a spectroscope, the plasma density and temperature in the IPT can be derived. In this subsection, the details on the plasma diagnosis method will be introduced.

Note that the typical transition rate between energy levels in the IPT is $\sim 10^9 \text{ cm}^3\text{s}^{-1}$ (Kramida et al., 2017). As the typical density of heavy ions is the order of 10^2 cm^{-3} , the typical timescale is roughly calculated as 10^{-11} s . The typical transitions of sulfur ions confirmed by observations of the IPT emission will be shown in Figures A.5–A.7 in Appendix A. Meanwhile, the reaction rate of the main ionization and charge exchange reaction of atoms and ions of sulfur and oxygen in the IPT is $10^{-7} \text{ cm}^3\text{s}^{-1}$ (Delamere and Bagenal, 2003). As the typical electron density is the order of 10^3 cm^{-3} , the typical timescale is roughly calculated as 10^4 s .

Let N_j be the ion density of energy state j , A_{ji} be the natural transition probability from state j to state i , and l be the length in the line of sight direction. The emission intensity of line via electron collision excitation is given by Equation (2.1). Here, the ion density of the energy state j , N_j , is given by solving Equation (2.2). α_{ij} in Equation (2.2) is expressed as Equation (2.3).

$$I(\lambda_{ji}) = 10^{-6} \int N_j A_{ji} dl \text{ [Rayleigh]}. \quad (2.1)$$

$$\begin{pmatrix} \alpha_{11} & \alpha_{21} \\ \alpha_{12} & \ddots \end{pmatrix} \begin{pmatrix} N_1 \\ \vdots \end{pmatrix} = 0. \quad (2.2)$$

$$\alpha_{ij} = A_{ij} + N_e \int_0^\infty \widehat{g}_e v \sigma_e dv. \quad (2.3)$$

N_e , \widehat{g}_e , v , and σ_e represent the electron density, the normalized electron velocity distribution, the electron velocity, and the collisional cross-section. By using these equations, the column density and temperature inside the IPT can be obtained from the intensities of emission lines. In this study, I used the CHIANTI atomic database version 8.0.7 for the natural transition probability and collisional cross-section (Dere et al., 1997; Del Zanna et al., 2015).

To understand the nature of plasma diagnosis, let me consider the dependence of emissivity on the electron parameters. I assumed the electron velocity distribution as the sum of two Maxwellian distributions, core and hot components. Figure 2.5 represents the dependence of volume emissivities of lines used in this study on electron parameters calculated by using the CHIANTI atomic database ver. 8.0.7. It is clear from Figure 2.5 that emissivity dependence on core electron density and core electron temperature is less dependent on wavelength. In contrast, the emissivity dependence to hot electron fraction is more dependent on wavelength. Thanks to the difference of emissivity dependence of electron parameters, one can derive them by line intensities. It should be noted that emissivity dependence to hot electron temperature is less than other electron parameters.

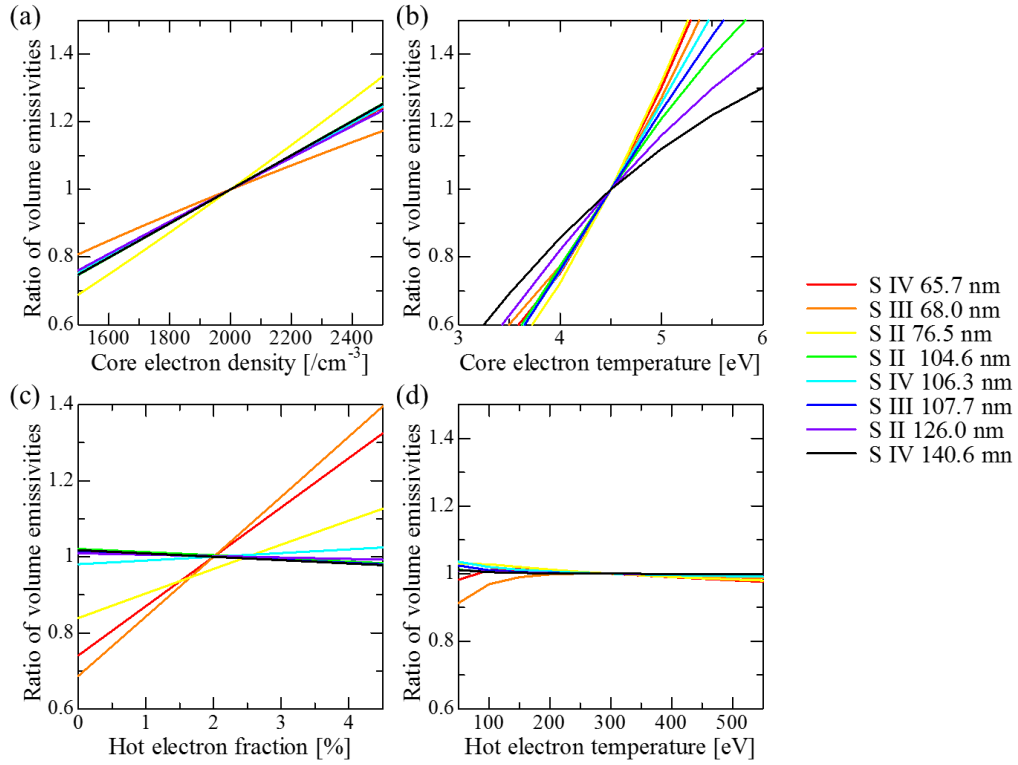


Figure 2.5. Dependence of volume emissivities of main lines used for plasma diagnosis on electron parameters. I used the CHIANTI atomic database ver. 8.0.7. The other parameters were fixed to typical values in the IPT to calculate dependence on a parameter: Core electron density, core electron temperature, hot electron fraction, and hot electron temperature are fixed to 2000 cm^{-3} , 5 eV , 2% , and 300 eV , respectively. (a) Dependence on core electron density. (b) Dependence on core electron temperature. (c) Dependence on hot electron fraction. (d) Dependence on hot electron temperature.

2. 2. 2. Data reduction

The main procedure of the plasma diagnosis analysis is shown in Figure 2.6. Details of each procedure will be introduced in the following subsections.

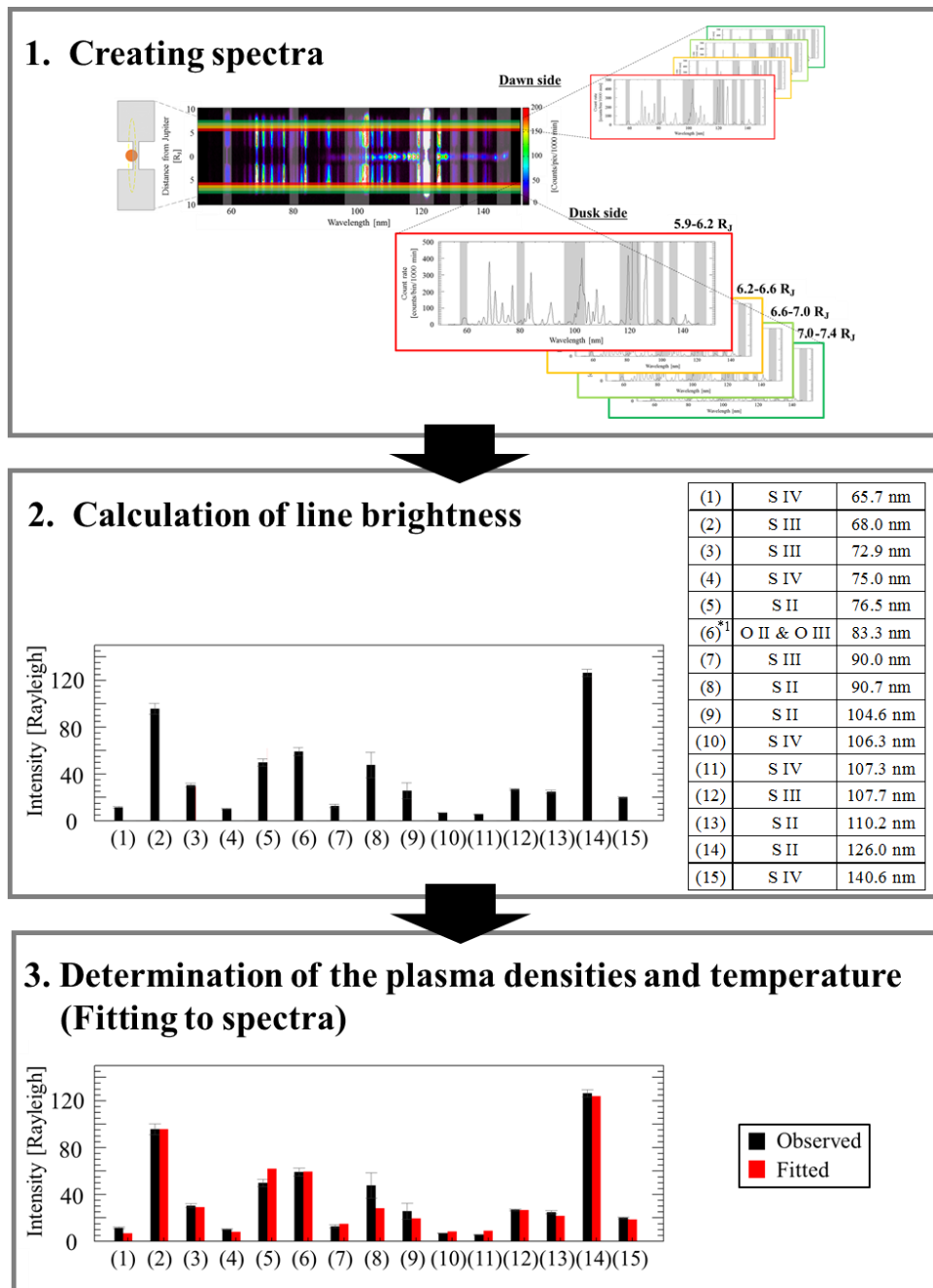


Figure 2.6. Schematic diagram of the plasma diagnosis procedure.

*¹ O II & O III 83.3 nm is used only for the first and second seasons.

2. 2. 2. 1. Creating spectra

“The level-2 data” with the 140 arcseconds slit in the first season and the second season provided by the data pipeline system were used. See Kimura et al. (2019) for information on the data level. As for the analysis of the data in the third season, “the level-2 prime data” with

the 140 arcseconds slit, which include the information on the spatial blurring, were used to select data properly. To increase in signal-to-noise ratio and explore the long-term modulation of the timescale of several tens of days in response to volcanic activity, the data were integrated every five days. The spectra were extracted from 5.9–6.2 R_J , 6.2–6.6 R_J , 6.6–7.0 R_J , and 7.0–7.4 R_J in the projected radial distance at dusk and dawn sides as shown in Figure 2.7.

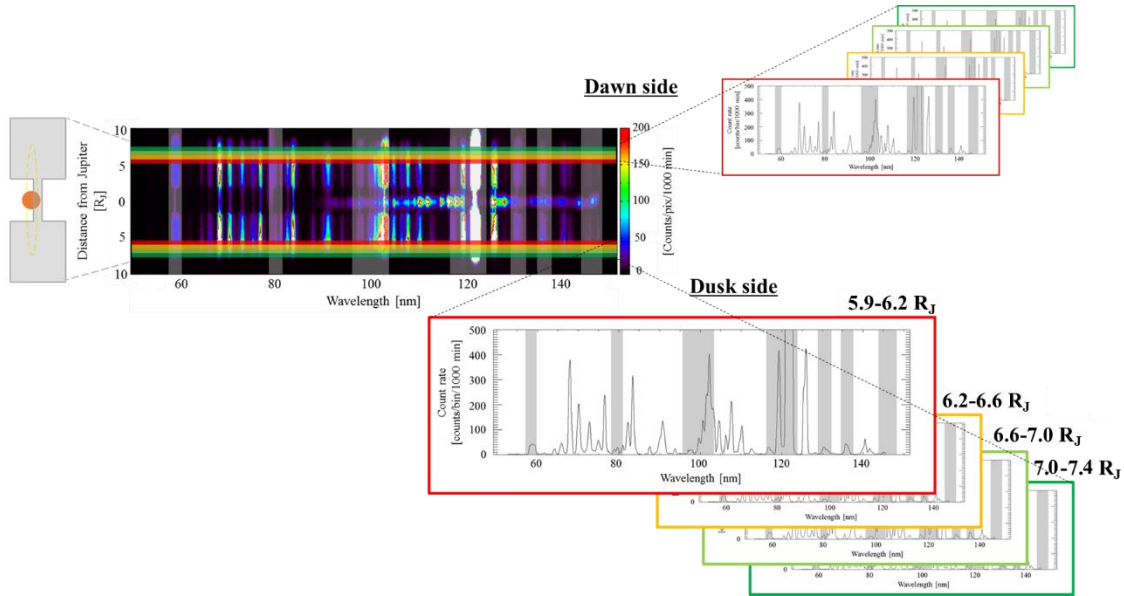


Figure 2.7. Schematic diagram of the extraction of spectra from 5.9–6.2 R_J , 6.2–6.6 R_J , 6.6–7.0 R_J , and 7.0–7.4 R_J at dusk and dawn sides.

The spatial calibration along the radial direction was performed by estimating Jupiter’s center position from the position of auroral emission obtained by Hisaki/EXCEED (Tsuchiya et al., 2018). It should be noted that, to avoid the incidence of sunlight, the satellite inversion around the equatorial plane occurred at the timings shown in Table 2.2, mainly when the observation target was changed or when the planetary opposition occurred. The position of Jupiter’s center in the field of view slightly changed before and after the inversion. As for the radial variation in the field of view, which corresponds to the variation in the vertical axis of the spectral image as shown in Figure 2.3(b), was evaluated by detecting Jupiter’s radial position using the auroral emission, and the influence was minimized by changing pixels to integrate. Meanwhile, the influence of variation in the horizontal axis in the field of view, in the north-south direction, cannot be reduced. It was evaluated as $\sim 0.4 R_J$, which will be shown in Appendix B, and was sufficiently small compared to the width of the slit in the north-south direction, but it may have a slight effect on the results of the analysis.

Table 2.2. List of the satellite inversion timing in the IPT observation.

Jan. 17, 2014
Jan. 20, 2014
Jan. 28, 2014
Nov. 3, 2014
Feb. 13, 2015
Dec. 3, 2015
Mar. 18, 2016
Oct. 24, 2016

2. 2. 2. 2. Calculation of line brightness

The lines adopted in this research are listed in Table 2.3. The lines affected by bright geocoronal emission lines at the close wavelength (e.g., S II 100.6 nm, S III 102.1 nm, and S III 120.1 nm) were excluded. Also, blended lines (e.g., S III 70.3 nm and O III 70.3 nm) were excluded.

Table 2.3. Lines used in plasma diagnosis.

(1)	S IV	65.7 nm
(2)	S III	68.0 nm
(3)	S III	72.9 nm
(4)	S IV	75.0 nm
(5)	S II	76.5 nm
(6) ^{*1}	O II & O III	83.3 nm
(7)	S III	90.0 nm
(8)	S II	90.7 nm
(9)	S II	104.6 nm
(10)	S IV	106.3 nm
(11)	S IV	107.3 nm
(12)	S III	107.7 nm
(13)	S II	110.2 nm
(14)	S II	126.0 nm
(15)	S IV	140.6 nm

^{*1} O II & O III 83.3 nm is used only for the first and second seasons.

In studies which use line brightness obtained by Hisaki/EXCEED, the data with the slit of 10 arc seconds which is narrower than the spatial scale of the target have been used (Yoshioka et al., 2014; Yoshioka et al., 2017; Yoshioka et al., 2018; Hikida et al., 2018). In those cases, from the count rates per pixel, they derived the absolute line brightness that is projected onto

unit pixel by using the sensitivity calibration function, which is determined by experiments in the laboratory and observations of EUV stars in orbit. However, when using data taken with the widest slit, the above method is not applicable. This is because the slit width (140 arc seconds) is wider than the typical latitudinal scale of plasma torus. Also, the spectral resolution with the widest slit is lower. Thus, the following procedure was used to determine the absolute line brightness in the equatorial region of the torus, as described in Figure 2.8. (1) By assuming the distribution along the north-south direction to be described by the Gaussian function, the equivalent widths of emission region (σ) at each point were estimated. The equivalent widths of the typical lines of each ion species (S II 76.5 nm, S III 68.0 nm, S IV 65.7 nm, and O II & O III 83.3 nm) were determined. It was assumed that the emission profiles of the same ion species at different wavelengths are the same. In this procedure, the optical aberration and blending effects were excluded. Details will be discussed in Appendix C.1. (2) Using Equation (2.4), I calculated β , the ratio of emission from the equatorial region, whose thickness, φ , is projected to unit pixel, to total emission at the wavelength. x means the distance from the center of emission region along the north-south direction. λ_1 represents 76.5 nm, 68.0 nm, 65.7 nm, or 83.3 nm depending on the ion species. (3) The count rate at the wavelength was determined for each line by the Gaussian fitting and multiplied by β and ε , the sensitivity calibration function, as shown in Equation (2.5). I_{λ_2} is the brightness to be evaluated. The estimated β values will be shown in Appendix C.2.

$$\beta_{\lambda_1} = \frac{\int_{-\frac{\varphi}{2}}^{+\frac{\varphi}{2}} \exp\left(-\frac{x^2}{2\sigma_{\lambda_1}^2}\right) dx}{\int_{-\infty}^{\infty} \exp\left(-\frac{x^2}{2\sigma_{\lambda_1}^2}\right) dx} \quad . \quad (2.4)$$

$$I_{\lambda_2} = \beta_{\lambda_1} \varepsilon_{\lambda_2} \int_{-\infty}^{\infty} \exp\left(-\frac{x^2}{2\sigma_{\lambda_2}^2}\right) dx \quad . \quad (2.5)$$

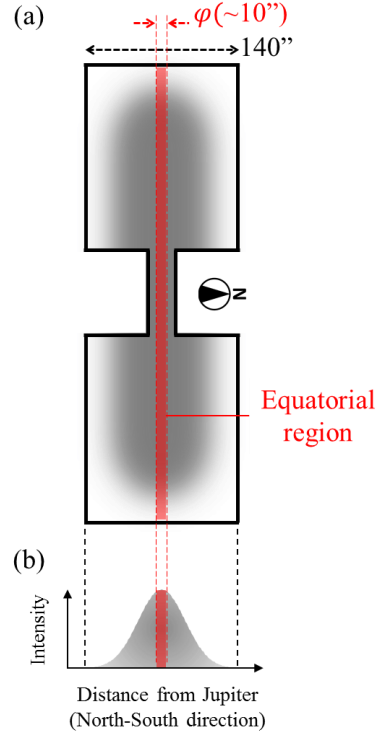


Figure 2.8. (a) Schematic diagram of observation of emission from IPT. (b) Schematic diagram of emission profile. The ratio of the red-shaded area to Gaussian integral corresponds to β in Equation (2.4).

2. 2. 2. 3. Determination of density and temperature

In this study, plasma densities and temperatures were determined by chi-square fitting with CHIANTI atomic database version 8.0.7 (Dere et al., 1997; Del Zanna et al., 2015).

The following assumptions were made. (1) The IPT consists of S^+ , S^{2+} , S^{3+} , O^+ , O^{2+} , H^+ , and e^- . The ratio of H^+ density to the total ion density was fixed to 10% of the total ion density (Bagenal, 1994). Besides, $[O^{2+}]/[O^+]$ was fixed to 0.1 (Shemansky, 1987; Steffl et al., 2004b; Yoshioka et al., 2011; Nerney et al., 2017). This is because all of O III lines in the wavelength range of EXCEED are blended with other lines, and O^{2+} density cannot be determined accurately. For the determination of O^+ density in the first and second seasons, the data were screened out with the satellite local time to eliminate the geocoronal contamination in the same way as Yoshioka et al. (2017). As to the third season when the FOV guiding camera had broken, $[O^+]/[S^{2+}]$ was fixed to 1.0 (Steffl et al., 2004b; Nerney et al., 2017) as the data were not screened out with the satellite local time to increase in signal-to-noise ratio. (2) The electron velocity distribution was assumed as the sum of two Maxwellian distributions of cold and hot components (Sittler and Strobel., 1987). The hot electron temperature was fixed to 200 eV. This assumption hardly affects the result because line intensities have low sensitivity to hot electron temperature, as shown in Figure 2.5. (3) The plasma in the IPT was assumed as quasi-charge

neutral. (4) The column densities and temperature were assumed as uniform in the integral regions. The validity of assumptions of (1) and (2) will be discussed in Appendix D.

By assuming the local density to be represented by the power-law distribution as described by Equation (2.6) and defining the inner and outer edges of the IPT emission, the column density was also described by r , n_0 , r_0 , and γ . r represents the distance from Jupiter. n_0 is the number density at the Io's orbit ($r_0 = 5.91 R_J$). The inner and outer edges were assumed to be at the $5.9 R_J$ and $8.2 R_J$ distance from Jupiter, respectively. n_0 and γ can be determined from the chi-square fitting to the column-integrated values obtained by the plasma diagnosis.

$$n(r) = n_0 \left(\frac{r}{r_0} \right)^\gamma. \quad (2.6)$$

3. Temporal variation in plasma densities and temperature in the IPT

This study investigated the temporal variation in the density and temperature of plasma in the IPT associated with volcanic activation for the longest period to date. The temporal variation in parameters obtained by plasma diagnosis on the dusk and dawn sides from the first season to the third season, which is from DOY -374 in 2015 to DOY 728 in 2015, is shown in Figure 3.1(1) and 3.1(2), respectively. The temporal variation in the core electron density, hot electron density, core electron temperature, and ion densities are shown in (i)–(vii). The temporal variation in parameters in the first, second, and third seasons, which correspond to from DOY -374 to DOY -255, from DOY -32 to DOY 132, and from DOY 388 to DOY 728 are shown in Figure 3.2, Figure 3.3, and Figure 3.4, respectively.

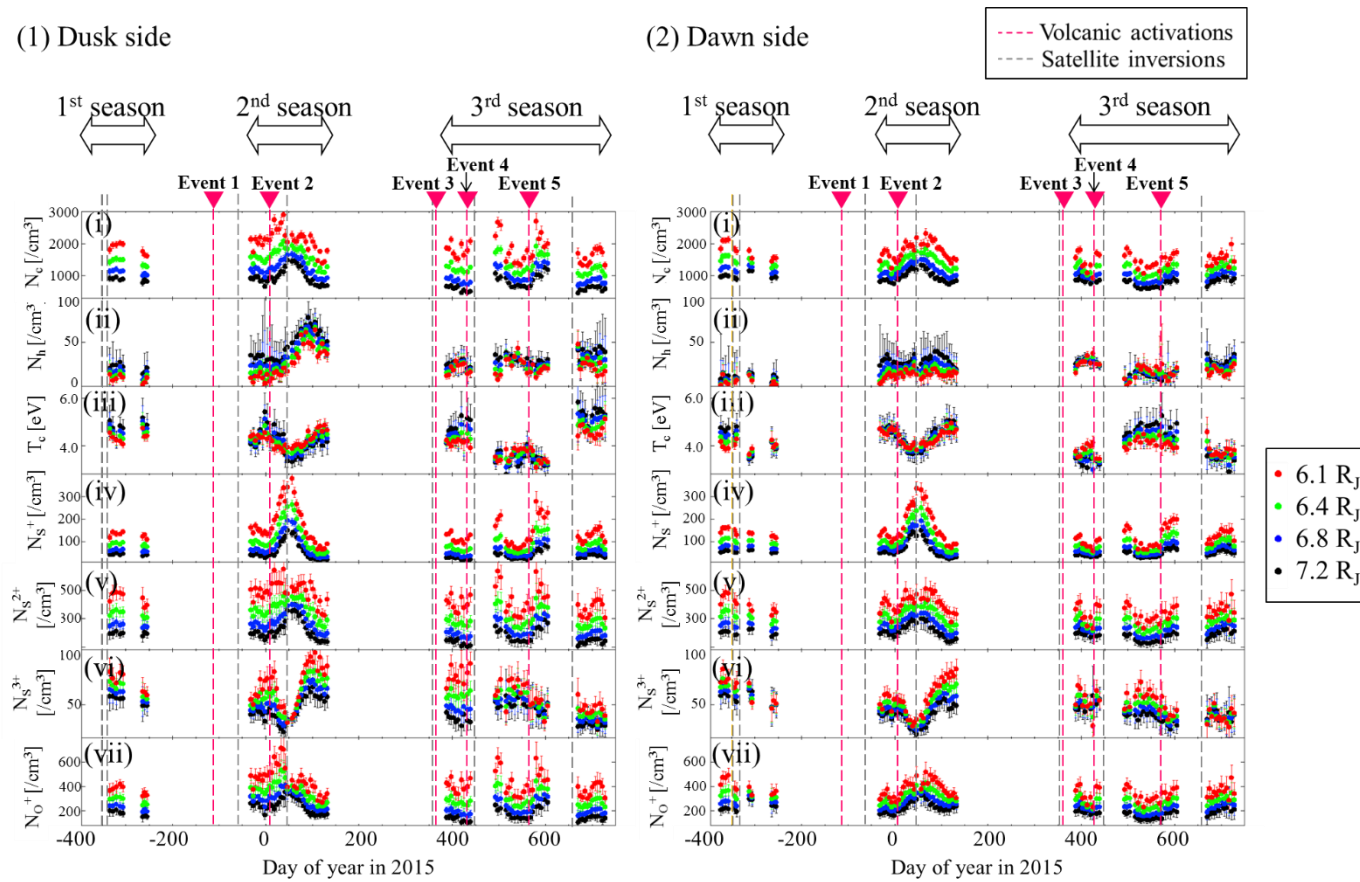


Figure 3.1. (1) Temporal variation in parameters in the Io plasma torus on the dusk side. (i)–(vii) Results of plasma diagnosis (temporal variation in core electron density (N_c), hot electron density (N_h), core electron temperature (T_c), and ion mixing densities (N_{S^+} , $N_{S^{2+}}$, $N_{S^{3+}}$, and N_{O^+})). The red, green, blue, and black points represent Event local values of $6.1 R_J$, $6.4 R_J$, $6.8 R_J$, and $7.2 R_J$, respectively. The error bars represent the one-sigma values. (2) The same as (1) on the dawn side. Approximate timings of volcanic activation indicated by the ground-based observations are indicated by the magenta dotted lines and triangles. Timings of satellite inversion are shown in gray dotted lines.

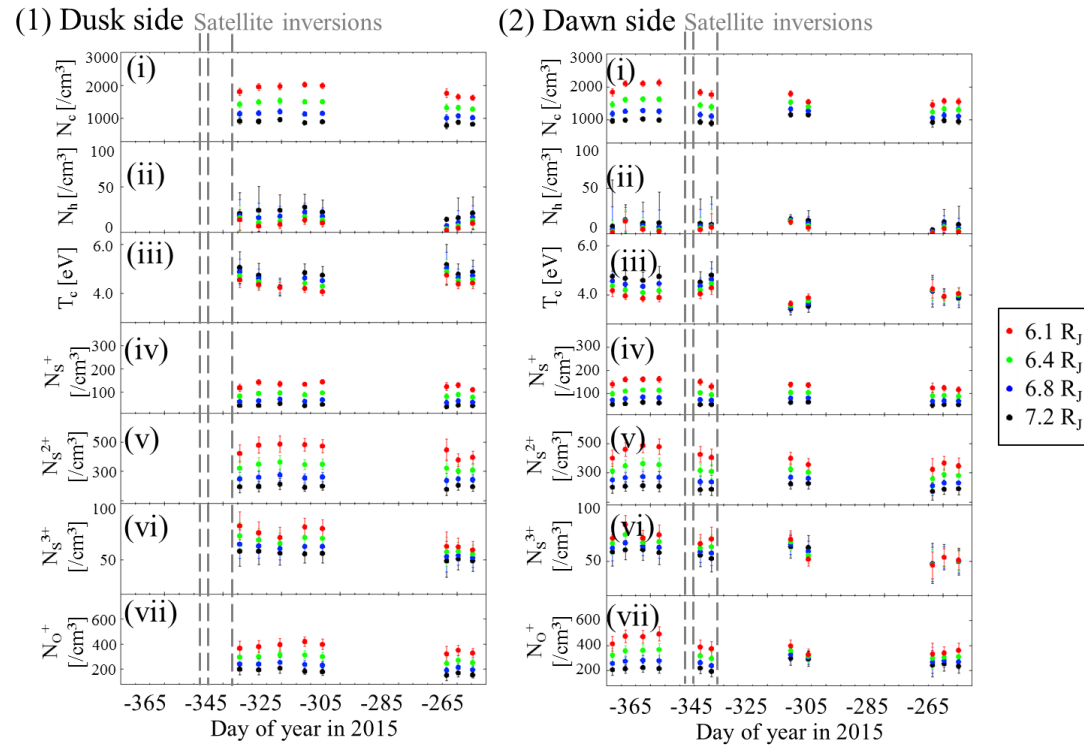


Figure 3.2. (1) Temporal variation in parameters in the Io plasma torus on the dusk side from DOY -374 to DOY -255 (from Dec. 2013 to Apr. 2014). (i)–(vii) Same as Figure 3.1. The integration time was ~ 560 – 3300 min at each point. (2) Same as (1) on the dawn side.

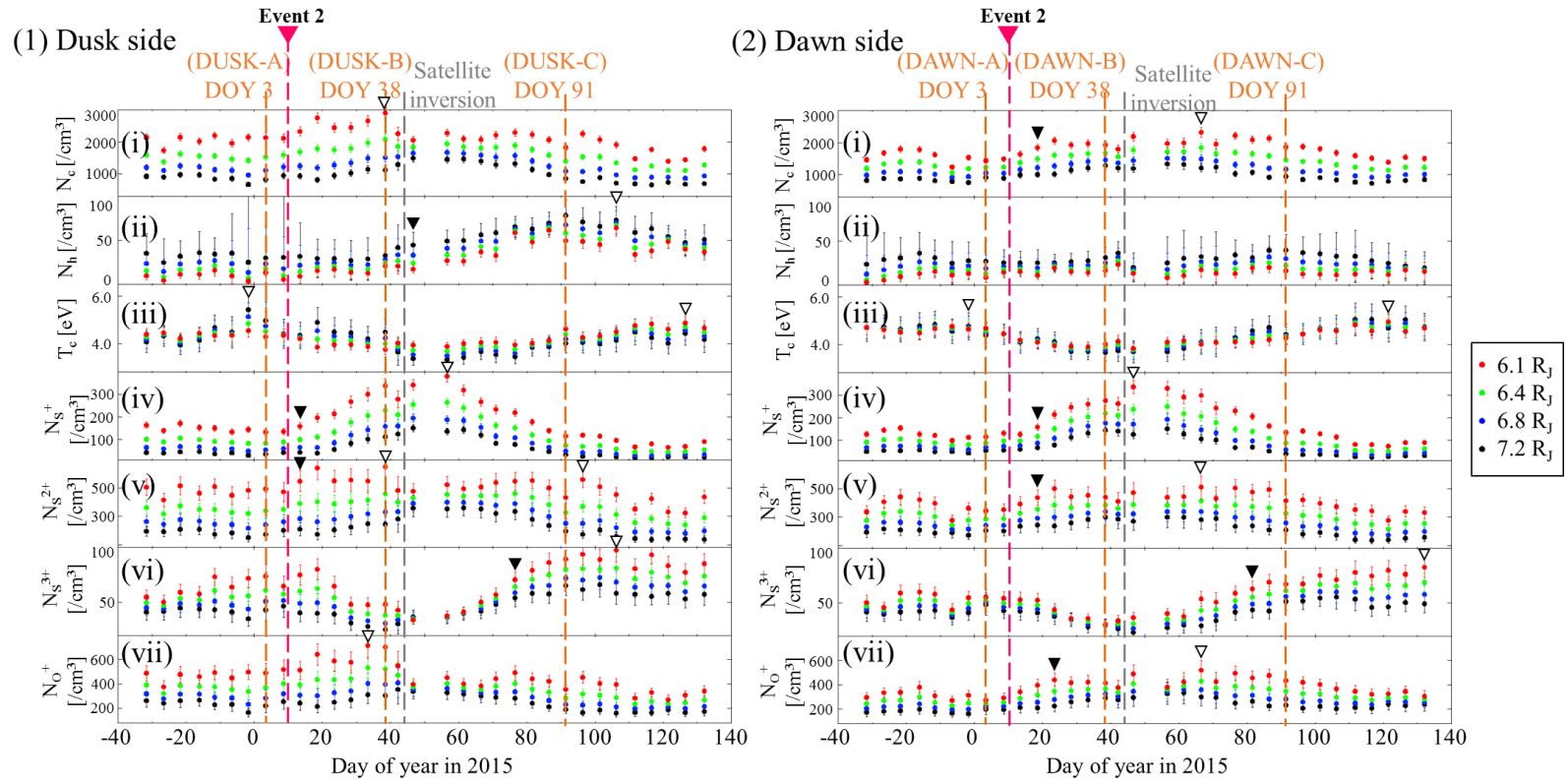


Figure 3.3. (1) Temporal variation in parameters in the Io plasma torus on the dusk side from DOY -32 to DOY 132 (from Nov. 2014 to May 2015). (i)–(vii) Same as Figure 3.1. The integration time was ~ 1400 – 3100 min at each point. Black triangles show the start of significant increase. White-filled triangles indicate the reaching of the local maximum value. (2) Same as (1) on the dawn side.

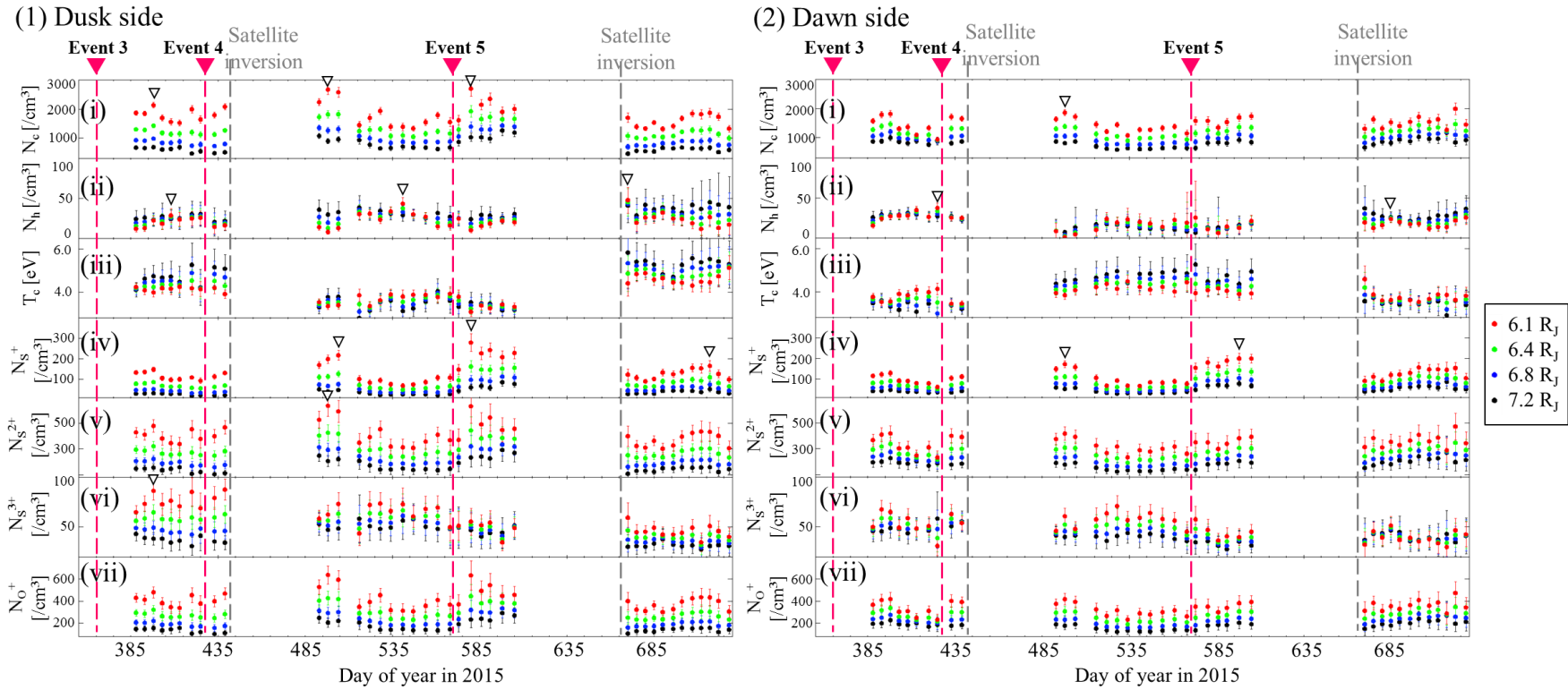


Figure 3.4. (1) Temporal variation in parameters in the Io plasma torus on the dusk side from DOY 388 to DOY 728 (from Jan. 2016 to Dec. 2016). (i)–(vii) Same as Figure 3.1. The integration time was ~ 780 – 3000 min at each point. (2) Same as (1) on the dawn side. Note that the single-ionized oxygen ratio to double-ionized sulfur was fixed to 1.0 in this period.

As for the results from DOY -374 to DOY -255 shown in Figure 3.2, note that there is a difference in timing of data point between dusk and dawn sides. This is because the data at the timing when the spatial coverage was not enough cannot be used in the analysis. During the period shown in Figure 3.2, no remarkable volcanic activation was detected by the ground-based observations. As mentioned in Subsection 1.2.3, the brightening signature of Loki Patera was observed around Aug. 2013, but it settled down in Dec. 2013 (de Kleer et al., 2019). On the dawn side, it can be seen that the core electron density decreases slightly, which might be the influence of the volcanic activity.

The results from DOY -32 to DOY 132 are shown in Figure 3.3. The ground-based observation showed that two volcanic activation events, which are labeled as Events 1–2 occurred before and during this period, as introduced in Subsection 1.2.3 (Yoneda et al., 2015; de Kleer et al., 2019). The black triangles show the approximate timings of the start of the parameter increase. The criterion will be described in Section 3.1. The white-filled triangles indicate the reaching of the local maximum value. In the inner region (at a $6.1 R_J$ distance from Jupiter), the core electron density starts to increase after the volcanic activation on DOY ~ 10 , which is labeled as Event 2. It reaches a peak on DOY 38 on the dusk side, which is labeled by the triangle in Figure 3.3(1)(i). Also, on the dawn side, it increases from DOY 19 and has a peak on DOY 66, as shown in Figure 3.3(2)(i). In the inner region, the hot electron density increases from DOY 47 on the dusk side as labeled by the triangle in Figure 3.3(1)(ii), but on the dawn side, such a significant increase is not confirmed. The core electron temperature decreases to DOY 47 and increases on both sides, as indicated by triangles in Figure 3.3(iii). This pattern can be interpreted as a result of the preceding increase in the plasma density and the following increase in the hot electron density. Although the value is within the ± 1 sigma range, there is a slight increase from the beginning of the observation period, and it reaches a local maximum near DOY -2 . Such behavior could be the influence of the small-scale volcanic activity that occurred in the middle of 2014, which is labeled as Event 1 in Figure 3.1. Also, the ion densities fluctuate dynamically. It is evident that the sulfur ion densities have peaks at different timing, as can be seen in Figure 3.3(iv)–(vii); specifically, the S^{3+} density decreases once and has a local minimum on DOY 47. This tendency is consistent with the temporal variation captured by the Cassini spacecraft (Delamere et al., 2004) and can be interpreted as follows: at the beginning of the increase in plasma supply rate, the ionization of neutrals and deionization of S^{3+} by charge exchange is promoted. Afterward, the S^{3+} density gradually increases as the ionization of neutrals are promoted and/or the hot electron density increases.

The results from DOY 388 to DOY 728 are shown in Figure 3.4. The ground-based observation showed that three volcanic activation events, which are labeled as Events 3–5, occurred before and during this period, as introduced in Subsection 1.2.3 (de Kleer et al., 2019). The responses of the parameters to the volcanic events are somewhat similar to the response to Event 2 in 2015: several tens of days after the volcanic activation, the core electron density

takes a local maximum, and the hot electron density starts to increase. Let me follow the temporal variation in each parameter specifically. During the period shown in Figure 3.4, the core electron density at a distance of 6.1 R_J has local maxima on DOY 398, DOY 498, and DOY 580 on the dusk side, and on DOY 498 on the dawn side shown by the white-filled triangles. As for the hot electron density at a distance of 6.1 R_J , it reaches local maxima on DOY 408, DOY 541, and DOY 670 on the dusk side, and DOY 425 and DOY 685 on the dawn side. The core electron temperature does not have a significant local maximum. The S^+ density at a distance of 6.1 R_J reaches a local maximum on DOY 504, DOY 580, and DOY 717 on the dusk side, and DOY 498 and DOY 598 on the dawn side. The S^{2+} density at a distance of 6.1 R_J reaches a local maximum on DOY 498 on the dusk side. The S^{3+} density at a distance of 6.1 R_J reaches a local maximum on DOY 398 on the dusk side. Note that the analysis in this period was performed with $[O^+]/[S^{2+}]$ fixed to 1.0. This is because the data type in this period was different from other periods as described in Subsection 2.2, and the data were not screened out with the satellite local time.

3. 1. Tendency of temporal variation in plasma densities and temperature in the IPT

This section will summarize the trend of temporal variation in the plasma densities and temperature. Note that the trend of O^+ and O^{2+} will not be mentioned below as their mixing ratios are fixed for the third season and all seasons, respectively.

To make it easier to understand the trend of each parameter, the period in which parameter exceeds the average value in the quiet period more/less than one sigma for three continuous points was defined as an “increasing period”/“decreasing period.” Regarding the hot electron density, the average value during the first season (from DOY -374 to DOY -255) and the first half of the second season (from DOY -32 to DOY 9) was used as the threshold. For the other parameters, the average value during only the quieter period (DOY -263 to DOY -255 in the first season) was used as the threshold to make the trends easy to understand.

Also, regarding the hot electron density, “maximum period,” which was defined as the period from the start of taking a value within the range of ± 1 sigma from the maximum value to the end, was indicated. Figure 3.5 shows an example of determining the periods for the hot electron density in the second season.

Figure 3.6 schematically shows the temporal variation in each parameter during the whole period. As mentioned in Subsection 1.2.3, there are uncertainties in the timings of volcanic activations of Events 1, 3, 4, and 5. Also, there is a difference in the scale of volcanic activity, as inferred from the IPT radiation shown in Figure 1.17. Therefore, it should be noted that the interpretation of these events might be more difficult than that of Event 2.

Figure 3.6 shows that core electron density tends to increase after the volcanic event.

Besides, the hot electron density tends to increase tens of days after the volcanic activation. Figure 3.7 summarizes the relationship between volcanic activations and increases in the hot electron density. On the dusk side, it was 4 out of 5 events that the hot electron density increased tens of days after volcanic activation. Also, the volcanic activation occurred tens of days before all four events of the increase in hot electron density on the dusk side. Therefore, the correlation between the volcanic activation and the increase of hot electron density on the dusk side is expected. Interpretations will be shown in Chapter 5.

No tendency for the core electron temperature common to multiple events can be confirmed in Figure 3.6. It decreases after the greatest event (Event 2). This can be interpreted as the promotion of the thermal relaxation via the Coulomb collision due to the increase in the core electron density. The trends of S^+ and S^{2+} densities are similar to the trend of the core electron density. In contrast, the S^{3+} density does not show a tendency common to multiple events. In Event 2, there is an increasing period after the decreasing period, which was interpreted in the previous section.

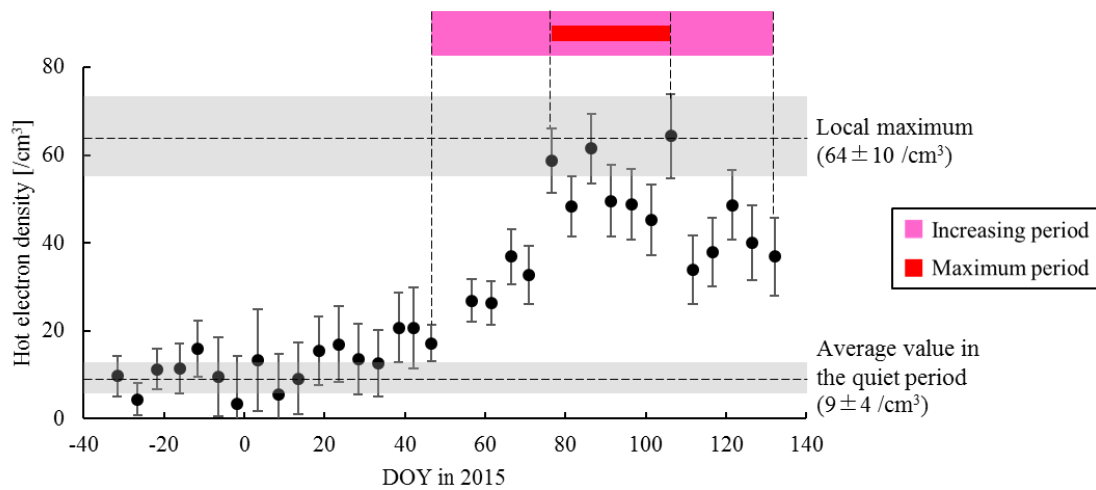


Figure 3.5. Example of determining the increasing period and maximum period. The case for hot electron density in the second season is shown.

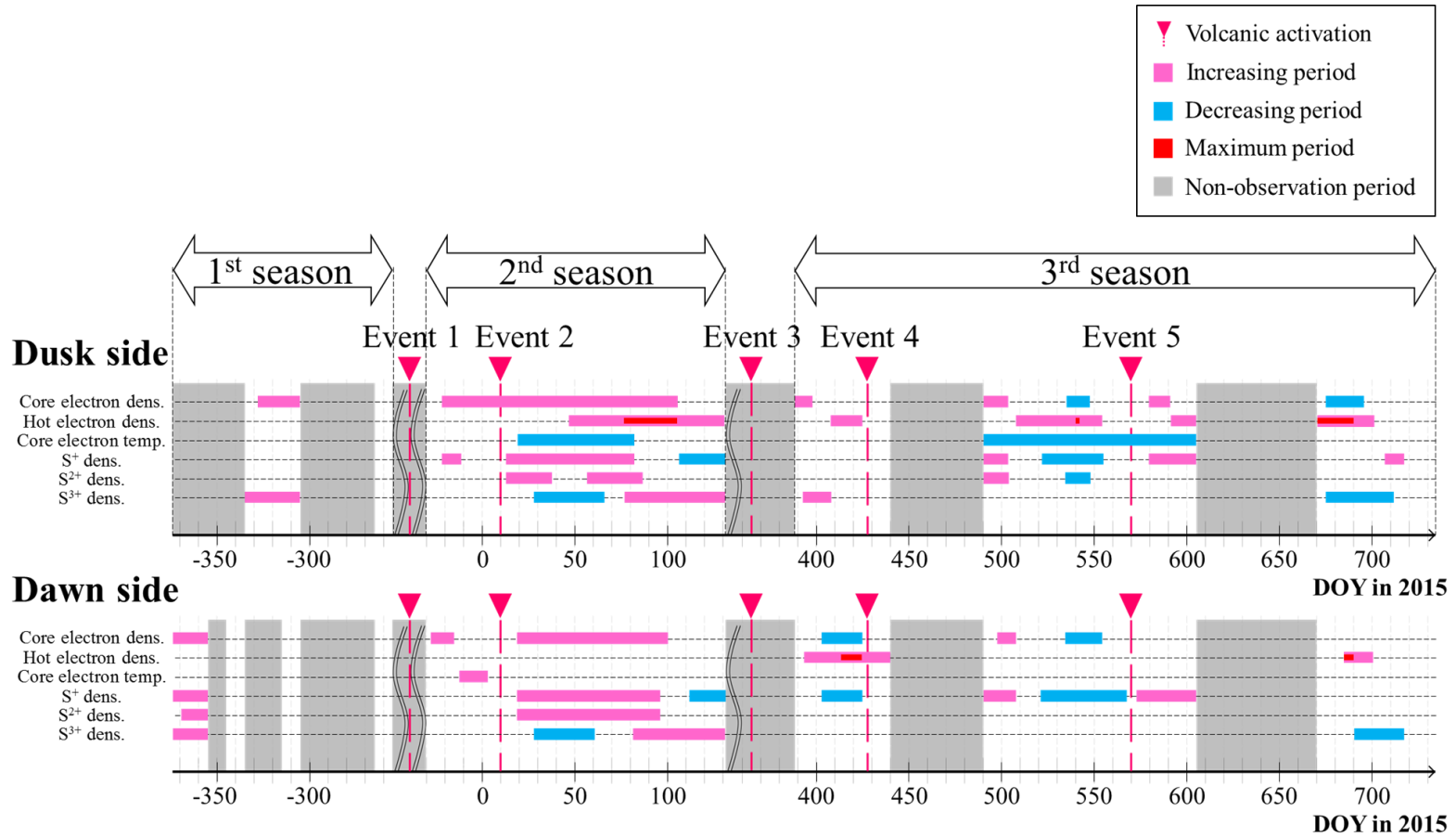


Figure 3.6. Schematic view of temporal variation in each parameter in the whole period. From the top, the vertical axes indicate core electron density, hot electron density, core electron temperature, S⁺ density, S²⁺ density, and S³⁺ density. The increasing period, decreasing period, and maximum period are shown in pink, blue, and red, respectively. The timings of volcanic activation are indicated by magenta dotted lines and triangles. The non-observation periods are shaded in gray.

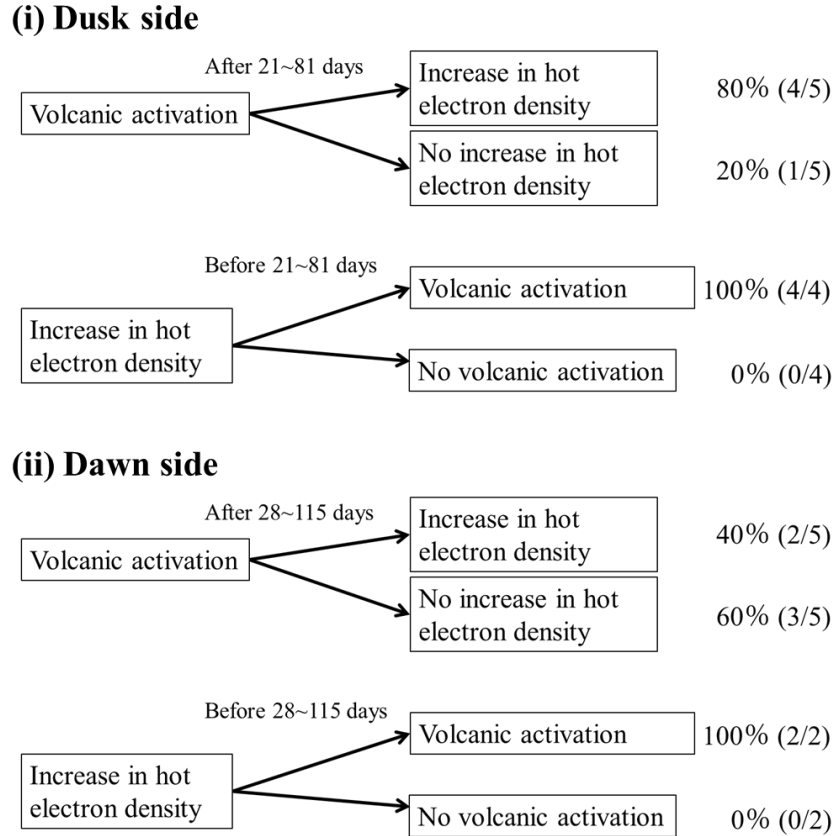


Figure 3.7. Relationship between volcanic activation and increase in hot electron density.

3. 2.Comparison with other works

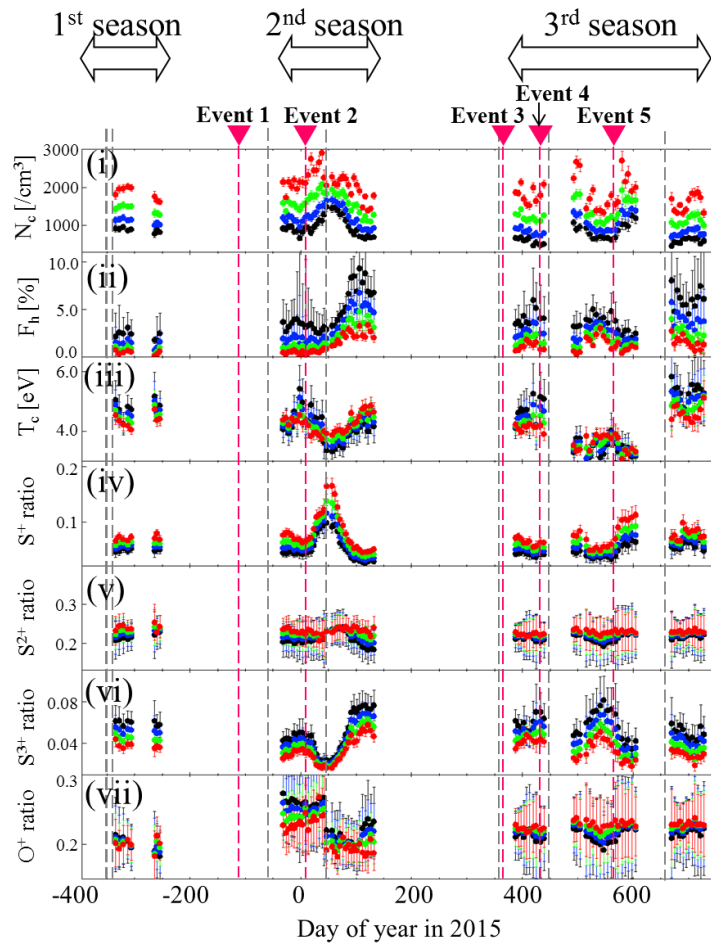
In this section, as for the hot electron and ions, the mixing ratio to the total electron density will be used to compare with other studies. The temporal variations in these mixing ratios are shown in Figures 3.8–11 (corresponding to the results in the whole season, first season, second season, and third season, respectively).

Let me compare the characteristics of plasmas at a distance of $\sim 6 R_J$ from Jupiter obtained in this study with other studies, which are listed in Table 3.1. The averaged values of parameters derived in this study for the dusk and dawn sides on DOY -312 , DOY 3, DOY 38, DOY 91, and DOY 388 to 728 are shown in Table 3.2. Let me review the information on volcanic activity. In the Voyager/PLS observation period, the IPT is thought little affected by volcanic eruption compared to the other periods (Delamere and Bagenal, 2003). Meanwhile, it should be mentioned that the eruption of Tvashtar Catena occurred in 2000 before the observation period of Cassini (Geissler et al., 2004), and the temporal variation in plasma parameters was confirmed (Delamere et al., 2004; Steffl et al., 2008) as introduced in Subsection 1.2.3. No volcanic activation was confirmed during the Hisaki observation at the end of 2013 and the

beginning of 2014, though there might be a little influence by volcanic activation in the middle of 2013. In contrast, as mentioned above, the volcanic activations were indicated by the ground-based observations in 2015 and 2016.

According to results in this study in Table 3.2, with the volcanic activities, the core electron density rises to about twice the minimum density (1200 cm^{-3}). The electron density obtained by Voyager ($\sim 2000 \text{ cm}^{-3}$) is roughly at the middle value of the above modulations, as shown in Table 3.1. As for the hot electron fraction, the minimum value in this study ($\sim 0.2\%$), which is associated with the volcanically quiet situation, is consistent with the value obtained by the Voyager data ($\sim 0.23\%$). In contrast, in the volcanically active period, Steffl et al. (2008) indicated that the amplitude of the increase in the hot electron fraction was about 30% of that in the quiet period; there is a quantitative difference between my results, which claims the rise to 1.8% and 2.7% in the second and third season respectively, and them. One of the reasons could be the differences in conditions such as the scale of volcanic activity and/or the amount of supplied plasma to the magnetosphere. For more detailed discussions, it is necessary to explore the mass and energy budget in the same way as Steffl et al. (2008), which is introduced in Subsection 1.2.6. As for the core electron temperature and mixing ratios of S^+ , S^{2+} , S^{3+} , and O^+ , the results of this study and other studies under similar conditions of volcanic activity are almost the same values. As is evident from Table 3.1 and Table 3.2, the result in this study in Feb. 2015 is consistent with the value in Feb. 2015 by Yoshioka et al. (2018), which used the narrowest slit data.

(1) Dusk side



(2) Dawn side

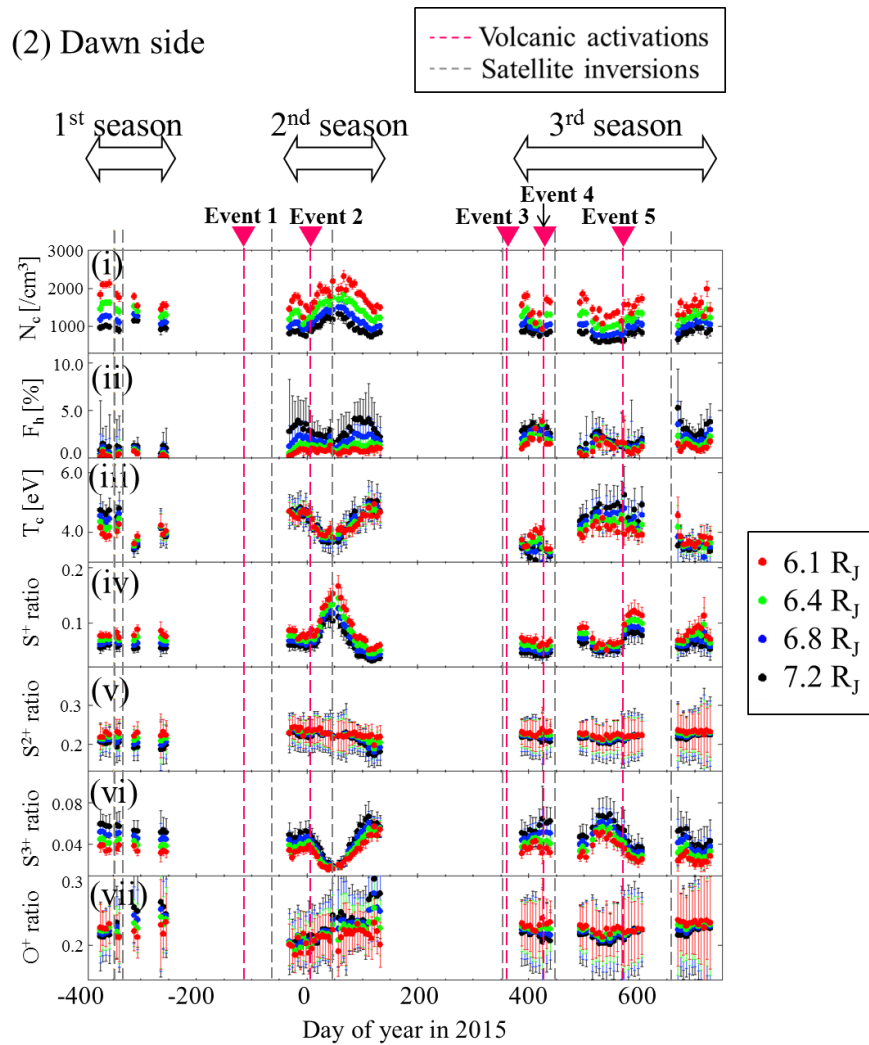


Figure 3.8. Same as Figure 3.1, except for hot electron fraction (F_h) and ion mixing ratios.

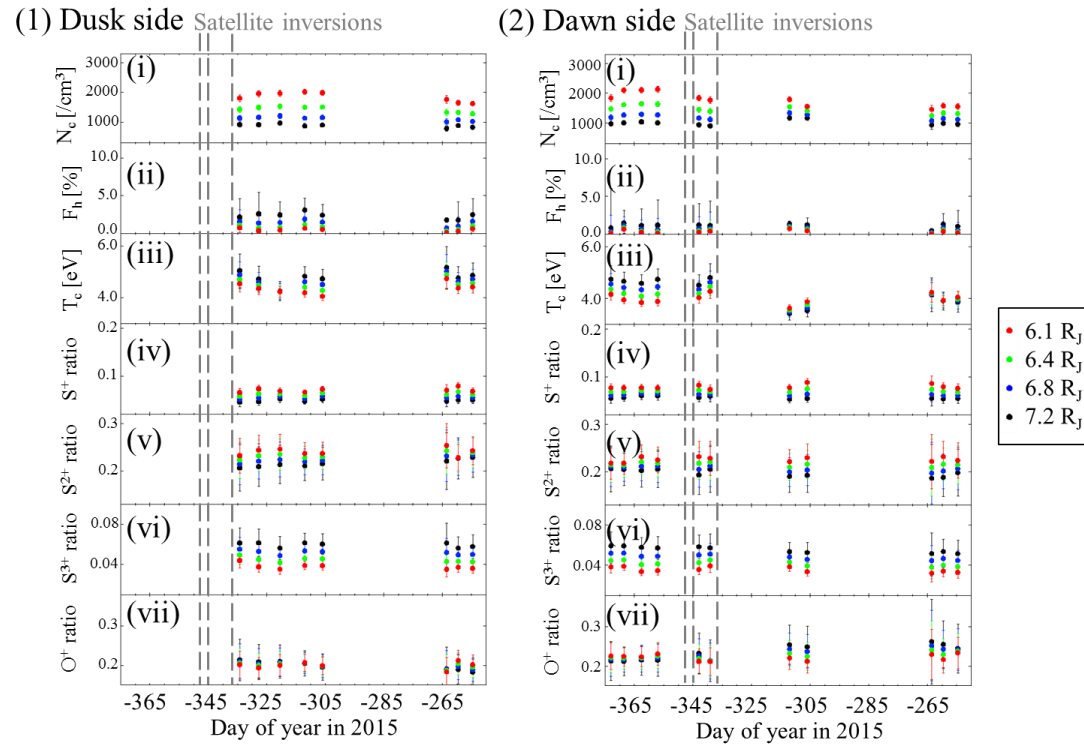


Figure 3.9. Same as Figure 3.2, except for hot electron fraction (F_h) and ion mixing ratios.

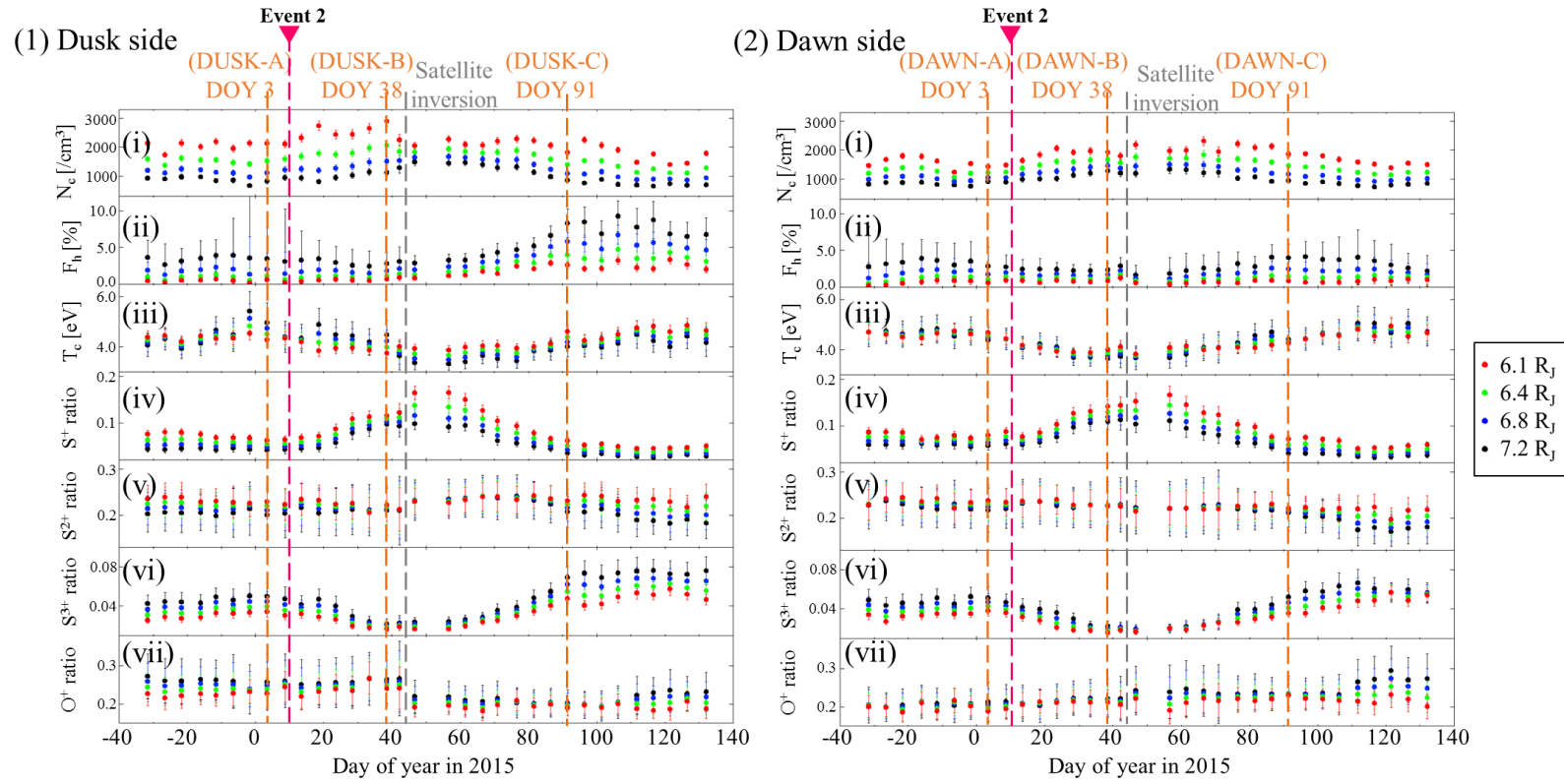
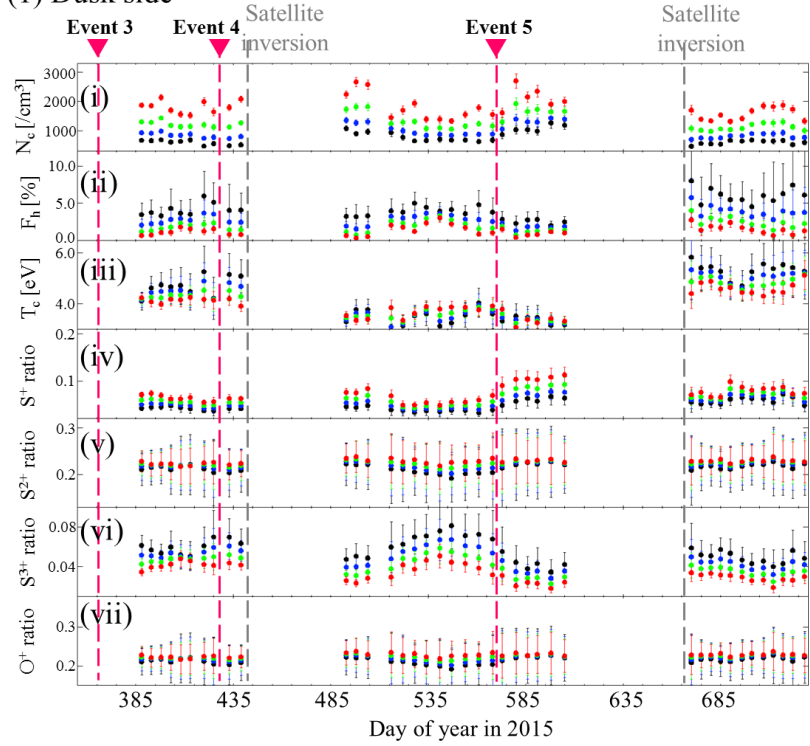


Figure 3.10. Same as Figure 3.3, except for hot electron fraction (F_h) and ion mixing ratios.

(1) Dusk side



(2) Dawn side

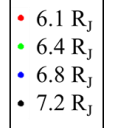
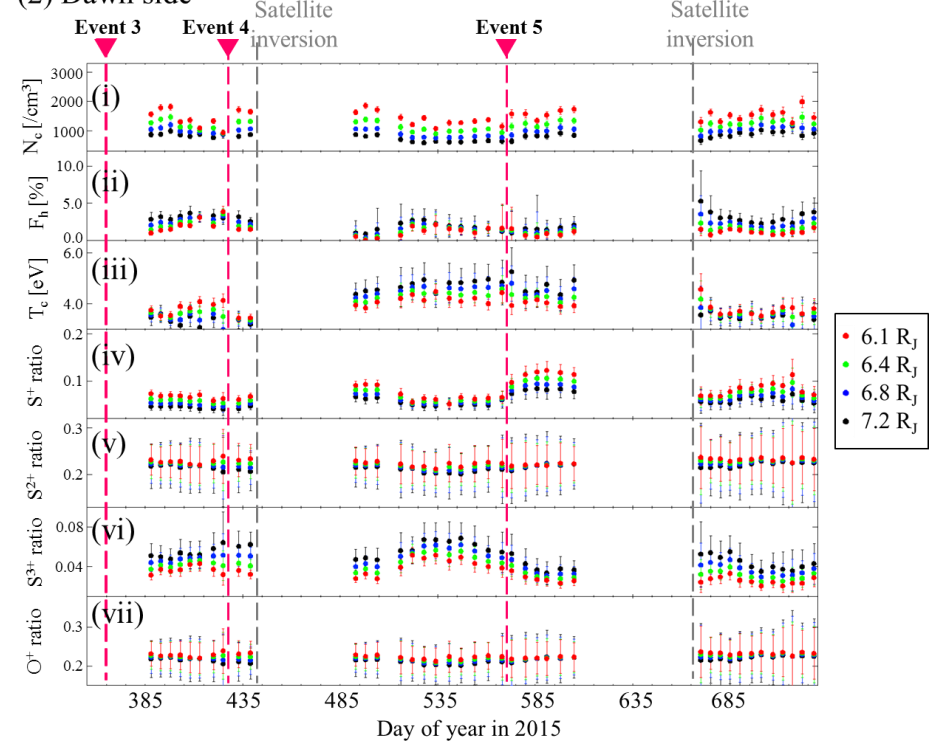


Figure 3.11. Same as Figure 3.4, except for hot electron fraction (F_h) and ion mixing ratios.

Table 3.1. Parameters at a distance of $\sim 6 R_J$ from Jupiter by other studies.

	Voyager/PLS	Cassini/UVIS		Hisaki/EXCEED		
Period	Mar. 1979	Oct. 2000 to Jan. 2001		Nov. 2013	Feb. 2015 (DOY 52)	
Volcanic activation ^{*1}	×	○		△	○	
Electron density [cm^{-3}]	~ 2000	N/A		2100 ± 300	2600 ± 200	
Hot electron fraction [%]	~ 0.23	~ 0.2	–	~ 0.3	0.5 ± 0.4	0.9 ± 0.3
Core electron temperature [eV]	~ 4	N/A		4.6 ± 0.9	3.8 ± 0.6	
S ⁺ mixing ratio	~ 0.06	~ 0.05	–	~ 0.10	0.05 ± 0.01	0.13 ± 0.02
S ²⁺ mixing ratio	~ 0.2	~ 0.20	–	~ 0.22	0.22 ± 0.05	0.24 ± 0.03
S ³⁺ mixing ratio	~ 0.03	~ 0.02	–	~ 0.05	0.05 ± 0.01	0.02 ± 0.01
O ⁺ mixing ratio	~ 0.22	~ 0.26	–	~ 0.28	0.19 ± 0.05	0.19 ± 0.03
References	Bagenal, 1994; Delamere and Bagenal, 2003; Nerney et al., 2017	Delamere et al., 2004; Steffl et al., 2008		Yoshioka et al., 2018	Yoshioka et al., 2018	

^{*1} The periods in which the IPT is expected to be greatly affected by volcanic activations are denoted as ○. The periods in which is expected to be a little affected by volcanic activations are denoted as △. The period in which the IPT is expected to be little affected by volcanic activations is denoted as ×.

Table 3.2. Parameters at a distance of $\sim 6 R_J$ from Jupiter obtained in this study.

Period	Feb.2014 (DOY -312)	Jan. 2015 (DOY 3)	Feb. 2015 (DOY 38)	Apr. 2015 (DOY 91)	Jan. 2016 to Dec. 2016 (DOY 388 to 728)	
Volcanic activation ^{*1}	\triangle	\triangle	\circ	\circ	\circ	
Electron density [cm^{-3}]	1700 ± 50	1790 ± 80	2400 ± 100	1850 ± 60	1240	– 2260
Hot electron fraction [%]	0.5 ± 0.2	0.6 ± 0.3	0.8 ± 0.2	1.8 ± 0.3	0.2	– 2.7
Core electron temperature [eV]	4.3 ± 0.1	4.5 ± 0.2	3.9 ± 0.2	4.4 ± 0.2	3.6	– 4.5
S ⁺ mixing ratio	0.090 ± 0.005	0.071 ± 0.006	0.13 ± 0.01	0.067 ± 0.004	0.05	– 0.11
S ²⁺ mixing ratio	0.24 ± 0.02	0.23 ± 0.03	0.22 ± 0.02	0.23 ± 0.02	0.22	– 0.24
S ³⁺ mixing ratio	0.033 ± 0.002	0.036 ± 0.004	0.016 ± 0.002	0.042 ± 0.003	0.02	– 0.05
O ⁺ mixing ratio	0.19 ± 0.02	0.21 ± 0.03	0.23 ± 0.03	0.21 ± 0.02	N/A	

^{*1} Same as Table 3.1.

3.3. Discussion

Figure 3.12 shows the increasing periods of the hot electron density. Table 3.3 shows the timings of the increasing periods as shown by pink bars in Figure 3.12. The period from the volcanic activation to the start timing of an increasing period of hot electron density is shown by black arrows in Figure 3.12. The lengths of the period indicated by the arrows are summarized in Table 3.4. After Event 1, unlike the other events, no increase in the hot electron density was confirmed on either the dusk or dawn side. This might be due to the insufficiency of the observation period. As for Event 1, the timing of volcanic activation is thought to be before DOY -138 as introduced in Subsection 1.2.3. As Hisaki started observation from DOY -32 , there is a timing gap of 106 days or more between the timings of the volcanic activation and the start of observation. Therefore, if the change in the hot electron density occurred on the same timescale (21–81 days) as Events 2–5, it is natural that no increase was confirmed in the observation after Event 1. After Events 2 and 4, the increases in hot electron density were confirmed only on the dusk side; the significant dawn-dusk asymmetries were confirmed. After Events 3 and 5, the hot electron density increased on both the dusk and dawn sides.

The shortest time of the increase in hot electron density on either dusk or dawn side was ~ 21 days, and the longest was ~ 81 days. It can be suggested that the timescales of plasma transport associated with volcanic events are 20 to 80 days. Though the cause of the timescale difference for each event could not be investigated in this study, one of the candidates is the scale of volcanic activity. Note that “the timescale of plasma transport associated with volcanic event” means “the timescale from volcanic activation to the reaching of inward transport to the IPT.” The interpretation of this timescale will be given in Subsection 5.3.3.

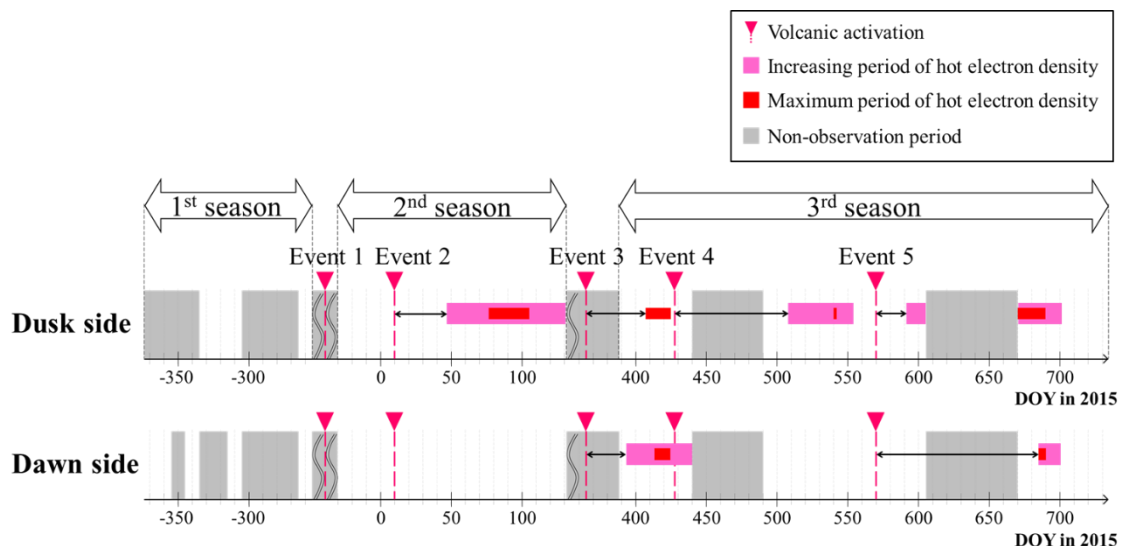


Figure 3.12. The schematic diagram showing periods from the volcanic activation to the start timing of an increasing period of hot electron density by black arrows.

Table 3.3. List of the increasing period of hot electron density.

Event number	Increasing period of hot electron density (DOY in 2015)	
	Dusk	Dawn
1		
2	47–132	
3	408–425	393–439
4	508–554	
5	591–701	685–701

Table 3.4. List of the days from the volcanic activation to the start timing of an increasing period of hot electron density. Error was set to half the time interval of the results of plasma diagnosis shown in Figure 3.1.

Event number	Days from the volcanic activation to the start timing of increase period of hot electron density [days]	
	Dusk	Dawn
1		
2	37 ± 3	
3	43 ± 3	28 ± 3
4	81 ± 3	
5	21 ± 3	115 ± 3

3. 4.Conclusion

By applying the plasma diagnosis method to the spectroscopic data obtained by the HISAKI satellite, the long-term plasma densities and temperature in the IPT was revealed for the longest period to date. As a result, the increases in the hot electron density were confirmed after four of the five volcanic activation events (Events 2–5). Based on the lengths of the periods from the occurrence of volcanic eruptions to the increases in hot electron density, the timescale of plasma transport associated with volcanic activation was suggested to be 20–80 days.

4. Temporal variation in radial distribution of mass density

By using the results of the plasma diagnosis shown in Chapter 3, the temporal variation in the radial distribution of mass density in the IPT was clarified for the first time.

4. 1. Data analysis

The mass density, $\rho(r)$, was derived by multiplying the derived densities of S^+ , S^{2+} , S^{3+} , O^+ , O^{2+} , H^+ , and e^- for their masses and, then, by summing them up as follows.

$$\begin{aligned} \rho(r) = & m_S n_{S^+}(r) + m_{S^{2+}} n_{S^{2+}}(r) + m_{S^{3+}} n_{S^{3+}}(r) + m_{O^+} n_{O^+}(r) + m_{O^{2+}} n_{O^{2+}}(r) \\ & + m_{H^+} n_{H^+}(r) + m_{e^-} n_{e^-}(r). \end{aligned} \quad (4.1)$$

m_α represents the mass for species of α . $n_\alpha(r)$ represents the power-law distribution of the local density for species of α , which was obtained in Chapter 3 and represented by the radial distance r . The H^+ density, $n_{H^+}(r)$, was assumed to be 0.1 times the total electron density, as assumed in Section 2.2. When discussing the temporal variation in mass density in the next section, I will show the average mass density, ρ_{ave} , which is the average value of 6.1 R_J , 6.4 R_J , 6.8 R_J , and 7.2 R_J , as defined below.

$$\rho_{ave} = \frac{1}{4} \{ \rho(r = 6.1 R_J) + \rho(r = 6.4 R_J) + \rho(r = 6.8 R_J) + \rho(r = 7.2 R_J) \}. \quad (4.2)$$

Also, the radial gradient of mass density, which can be considered an indicator of the amount of outward transport of plasmas, was derived by performing a linear regression of the derived radial distribution of mass density. Figure 4.1 shows an example of the determination of the radial gradient of mass density. In this study, the absolute value of the slope of the red line ($1.53 \times 10^{-33} \text{ kg/cm}^4$ in Figure 4.1) was called the mass density gradient.

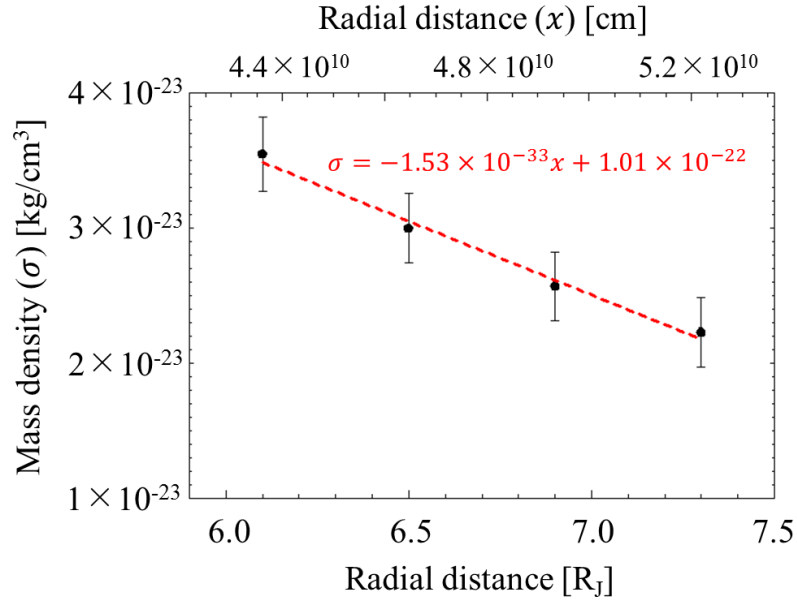


Figure 4.1. Derivation of mass density gradient on DOY 9 in 2015 on the dawn side. The black dots indicate the mass densities derived from Equation (4.1). Error bars indicate one sigma values determined in consideration of error propagation. The red dotted line is the result of linear regression and corresponds to the formula in red.

4.2. Results

The averaged mass density and the radial gradient of mass density obtained for the whole period are shown in Figure 4.2. The results for the second and third seasons, when the volcanic activations are indicated to occur, are shown in Figures 4.3 and 4.4.

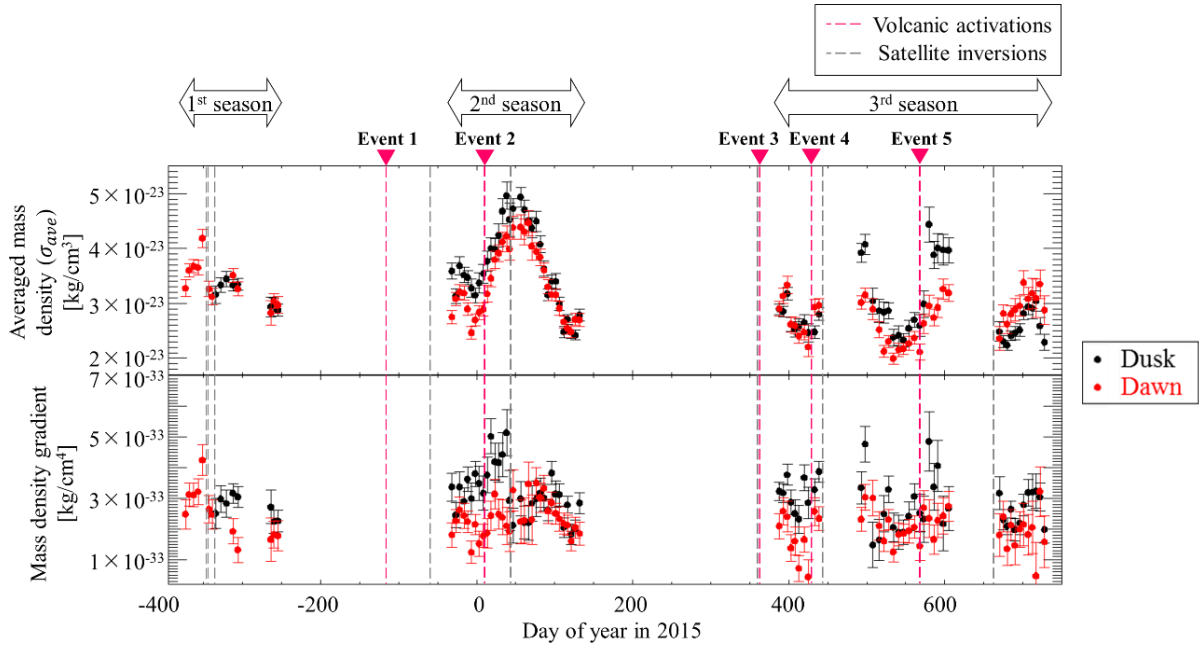


Figure 4.2. Temporal variations in the averaged mass density and the mass density gradient for the period between DOY -374 in 2015 and DOY 728 in 2015. The black and red points indicate the values obtained for the dusk and dawn sides, respectively. The error bars represent the one-sigma values. The approximate timings of volcanic activation indicated by ground-based observations are indicated by the magenta dotted lines and triangles.

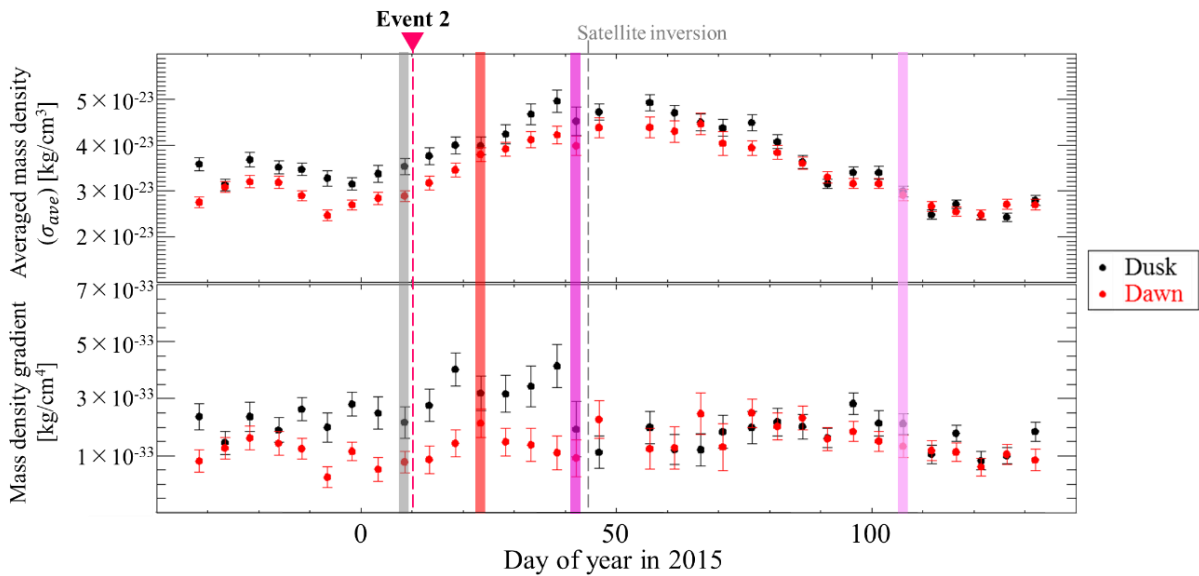


Figure 4.3. Same as Figure 4.2 except for the period between DOY -32 in 2015 and DOY 132 in 2015. Radial distributions of mass density at the timings indicated by the black, red, magenta, and light pink lines (on DOY 8 , DOY 24 , DOY 42 , and DOY 106 , respectively) are shown in Figure 4.5.

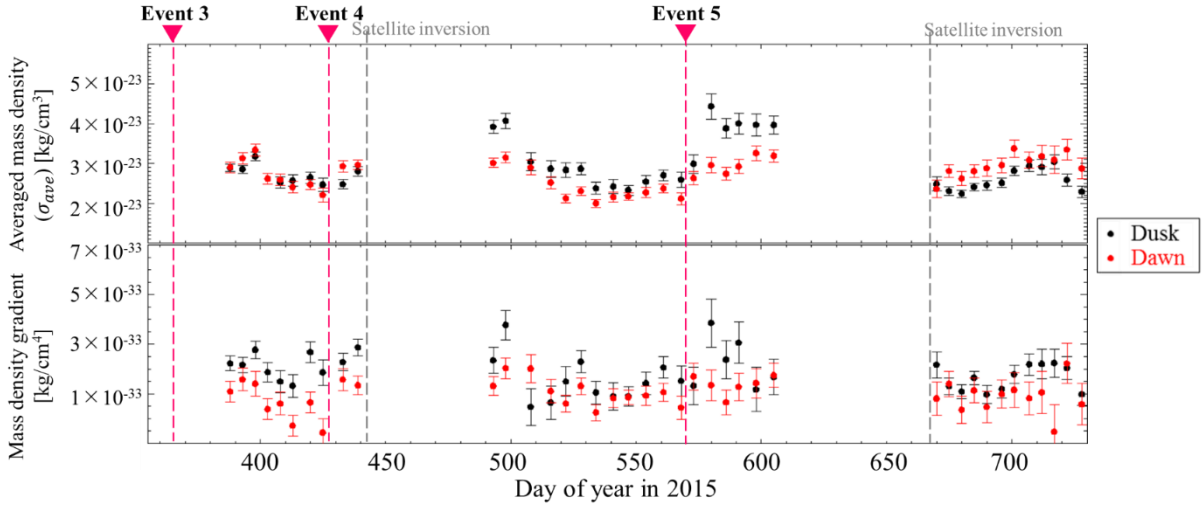


Figure 4.4. Same as Figure 4.2 except for the period between DOY 388 in 2015 and DOY 728 in 2015.

As can be seen from Figure 4.2, the temporal variation in the mass density is similar to that in core electron density shown in Figure 3.8.

During the first season, when the volcanic activity is relatively quiet, the mass density gradient is steeper on the dusk side than on the dawn side (Figure 4.2). This trend is observed during the entire period, and not just during the quiet period. The cause of the mass density gradient asymmetry on the dawn and dusk sides is unknown, but probably due to the dawn-dusk asymmetry of core electron density, which will be mentioned in Section 5.1.

During the second season, the trend of temporal variation in the mass density gradient after Event 1 could not be evaluated due to the insufficiency of the observation period. In comparison, it was captured that the mass density gradient fluctuated drastically after Event 2, especially on the dusk side, as shown in Figure 4.3. It rises slightly after volcanic activation; then, it decreases from DOY 42. Though this start timing of the decrease (DOY 42) is almost the same time as the satellite inversion (DOY 43), the decrease is not considered to be a trend due to the artificial effects since the decrease started before the satellite inversion. Afterward, it gradually reverts to its initial state. The radial gradient of mass density can be regarded as an indicator of the amount of outward transport of plasmas. Therefore, the temporal variation in the mass density gradient indicated above is interpreted as follows: the outward mass transport increases from DOY 42, and gradually returns to its initial state. To make this trend easier to understand, the radial distributions of mass density at the timings marked in black, red, magenta, and light pink lines in Figure 4.3 (corresponding to DOY 8, DOY 24, DOY 42, and DOY 106, respectively) are shown in Figure 4.5. Immediately after volcanic activation (on DOY 24), the mass density in the inner torus becomes higher than that observed during the quiet period. On DOY 42, the mass density in the outer torus increases, and the gradient slope decreases; the outward motion develops. On DOY 106, the mass density distribution returns to its initial state. Figure 4.6 shows the temporal variation in the mass density radial distribution on the dusk side with error,

which is one sigma calculated by error propagation. For clarity, the radial distributions at two timings are drawn in each panel. From Figure 4.6 (1), it can be said that the increase in density on DOY 24 in the inner region ($\sim 6 R_J$) is significant. From Figure 4.6 (2), it can be seen that the increase in density on DOY 42 in the outer region ($\sim 8 R_J$) is significant. The validity of assumptions in the plasma diagnosis analysis will be discussed in Appendix D.

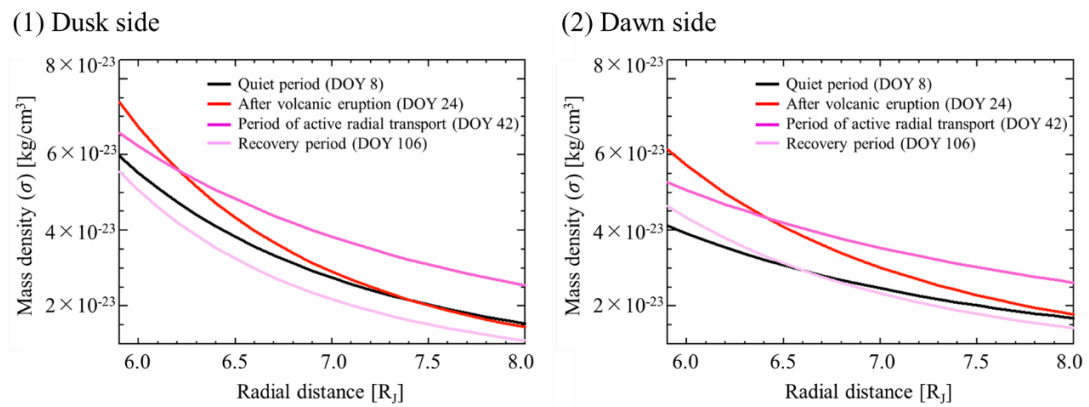
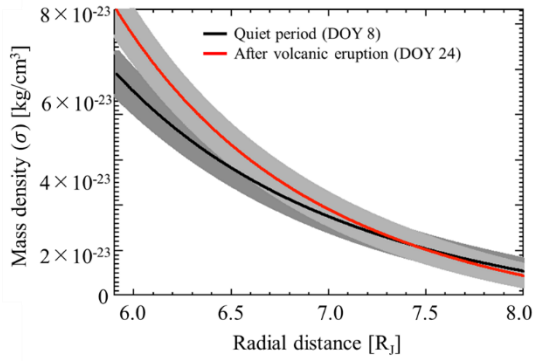
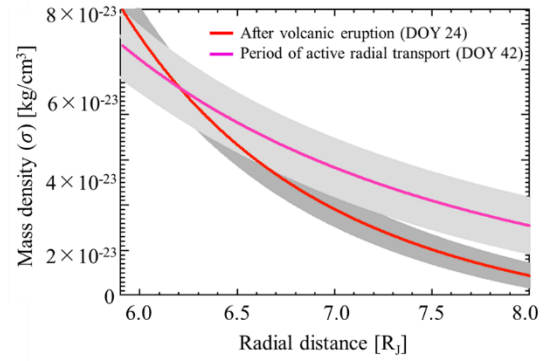


Figure 4.5. Temporal variations in the radial distribution of mass density on the dusk and dawn sides. The black, red, magenta, and light pink lines indicate the radial distributions on DOY 8, DOY 24, DOY 42, and DOY 106, respectively.

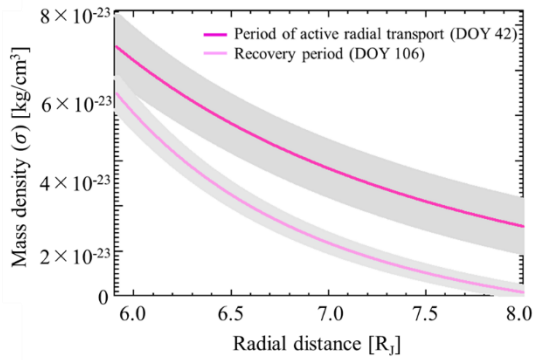
(1) DOY 8 and DOY 24



(2) DOY 24 and DOY 42



(3) DOY 42 and DOY 106



(4) DOY 8 and DOY 106

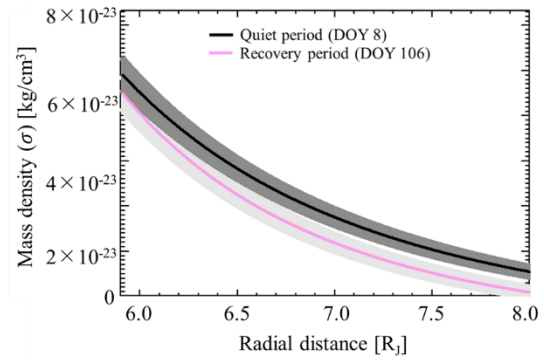


Figure 4.6. Temporal variation in the radial distribution of mass density with error, which is one sigma calculated by error propagation, on the dusk side.

During the third season, changes in the mass density gradient are observed, but their tendencies of the response to the volcanic events are not clear (Figure 4.4). It should be noted that it might be more difficult to capture the temporal variation in the mass density gradient after Events 3, 4, and 5 than after Event 2 due to the timing gaps of the observation periods and the difference in the scale of volcanic activity, as inferred from the IPT radiation shown in Figure 1.17. The start timing of observation was ~ 23 days after Event 3. Also, the observation was interrupted ~ 12 days after Event 4. Therefore, if there were changes in the mass density gradient after Events 3 and 4 on the same timescale as Event 2 (~ 30 days), they could not be captured by the Hisaki observation. Also, for Event 5, the time difference from the event to the interruption of observation was ~ 35 days, which is close to the timescale of ~ 30 days, and it is highly possible that the significant temporal variation could not be captured due to the timing gap of the observation period.

4. 3.Discussion

As described above, after Event 2, a remarkable temporal variation in the mass density gradient was observed, indicating that the outward plasma transport rate increases from DOY 42, which is ~30 days after the volcanic activation (Event 2 on DOY ~10). This ~30 days is interpreted as a timescale for outward plasma transport from the inner part of the IPT to the outer part. There are mainly two types of studies on outward transport timescales in the IPT. One is the MHD simulation of interchange motions. As introduced in Subsubsection 1.1.2.2, it was claimed that the timescale is ~2 to ~72 days, although the solution varies greatly depending on the assumption of the nonlinear effect and ionospheric conductivity (Hiraki et al., 2012). The other is the mass-energy balance analysis introduced in Subsection 1.2.6. It was claimed that the timescale of plasma loss from the IPT system is ~23 to ~50 days (Delamere and Bagenal, 2003). Therefore, the timescale of ~30 days derived in this study, which is regarded as the timescale for the loss by the outward transport, is compatible with the other studies. It is future work to make the same calculation as the other studies and to make a detailed comparison with this study under the same conditions, such as the plasma supply rate.

4. 4.Conclusion

Using the results of the plasma diagnosis shown in Chapter 3, the temporal variation in the radial distribution of mass density in the IPT was clarified for the first time. Although only during the second season when the greatest volcanic activation (Event 2) occurred, there was a noticeable temporal change in the mass density gradient, and it was revealed that ~30 days after the volcanic activation, the amount of outward plasma transport increases.

5. Dawn-dusk asymmetry and dependence on the Io phase angle of hot electron density

In Section 5.1, the dawn-dusk asymmetry of the density and temperature of plasma will be indicated. In Section 5.2, the dependence on the Io phase angle of the hot electron density will be shown in order to discuss the possibility that local heating near Io is responsible for the temporal variation in the hot electron density and its dawn-dusk asymmetry. In Section 5.3, the cause of the dawn-dusk asymmetry of the hot electron density will be discussed.

5.1. Dawn-dusk asymmetry

Let me review studies on the dawn-dusk asymmetry of plasma parameters. According to the analysis by Herbert and Sandel (2000), which used the Voyager/UVS data, the electron density profile peaked between dusk and local midnight, and the maximum value was ~ 1.2 times the minimum value. They attributed this trend to the torus shift due to the dawn-dusk electric field (Barbosa and Kivelson, 1983), which may cause the streamlines on the dusk side to converge (Thomas et al. 2004). This process will be explained in Appendix F. As for the core electron temperature, it was indicated that the temperature on the dusk side is higher than that on the dawn side by 20–30% because of the shift of torus position (Barbosa and Kivelson, 1983; Herbert and Sandel, 2000; Murakami et al., 2016). As for the hot electron fraction and ion mixing ratios, the dawn-dusk asymmetry has not been confirmed in past observations (Yoshioka et al., 2014).

To focus on the values in the volcanically quiet period, the averaged parameters at a distance of $6.1 R_J$ from Jupiter in the first season (from DOY -374 to DOY -255) and at the beginning of the second season (from DOY -32 to DOY 3), when the volcanic activities were comparatively quiet, are listed in Table 5.1. As for the ions, the mixing ratios to the total electron density are listed to compare with other studies. As for the parameters except for the core electron density at the beginning of the second season, the dawn-dusk asymmetry is not confirmed. At the beginning of the second season, the core electron density on the dusk side is ~ 1.25 times higher than that on the dawn side. This tendency is qualitatively consistent with results by Herbert and Sandel (2000). In contrast, the core electron temperature difference between the dusk and dawn sides is within ± 1 sigma range, which is not consistent with the other studies indicated above. One should note that with the plasma diagnosis method, it is difficult to separate the information on the core electron temperature and hot electron density compared to the other parameter combinations. Figure 5.1 shows the comparison of observed intensities on DOY 91 at $6.1 R_J$ on the dusk side and fitted intensities with electron parameters free and fixed. Yellow bars represent the fitted intensities with hot electron column density fixed to $1.8 \times 10^{12} \text{ cm}^{-2}$, which is the derived column density on DOY 3 and selected as a typical value in a volcanic quiet period, and with core electron temperature fixed to 7 eV, which

is warmer than the typical value in a quiet period. It can be said that several intensities, particularly (2) S III 68.0 nm, (14) S II 126.0 nm, and (15) S IV 141.6 nm, are fitted to the observed intensities much better in the case with colder temperature and higher hot electron density (with electron parameters free) than in the other case (with electron parameters fixed), but the difference between the fitted intensities with and without them fixed is slight. The analysis combining other methods, such as the physical chemistry model, is a future task. A detailed discussion on the validity of parameter derivation will be supplied in Appendix E. As for the ion mixing ratios, the significant dawn-dusk asymmetry is not confirmed.

Table 5.1. List of derived parameters at a distance of 6.1 R_J from Jupiter in the volcanically quiet period.

	First season		Second season (from DOY -32 to DOY 3)	
	Dusk	Dawn	Dusk	Dawn
Electron density [cm ⁻³]	1600 ± 100	1500 ± 100	2000 ± 100	1600 ± 200
Hot electron density [cm ⁻³]	6.4 ± 3.2	6.0 ± 4.5	10.0 ± 4.0	9.6 ± 4.8
Core electron temperature [eV]	4.7 ± 0.1	4.5 ± 0.3	4.4 ± 0.1	4.6 ± 0.1
S ⁺ mixing ratio	0.089 ± 0.007	0.088 ± 0.009	0.072 ± 0.006	0.079 ± 0.006
S ²⁺ mixing ratio	0.25 ± 0.01	0.23 ± 0.01	0.23 ± 0.01	0.24 ± 0.01
S ³⁺ mixing ratio	0.033 ± 0.005	0.037 ± 0.006	0.031 ± 0.003	0.034 ± 0.003
O ⁺ mixing ratio	0.18 ± 0.01	0.20 ± 0.01	0.23 ± 0.01	0.20 ± 0.01

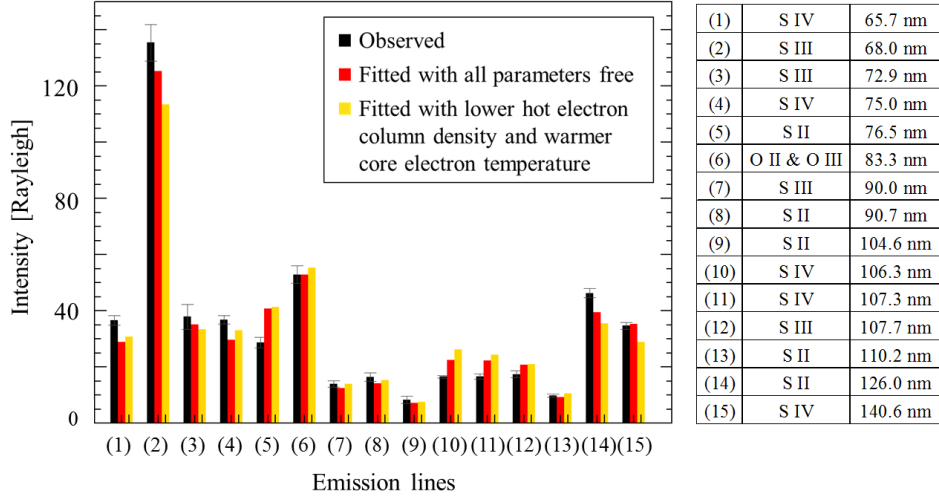


Figure 5.1. Comparison of observed line intensities and fitted intensities with electron parameters free and fixed. The 15 numbered emission lines are listed in the right panel. The black bars indicate the observed line intensities on DOY 91 at 6.1 R_J on the dusk side. The red bars show the fitted intensities with hot electron column density and core electron temperature free. The yellow bars represent the fitted intensities with them fixed to $1.8 \times 10^{12} \text{ cm}^{-2}$ which is the derived column density on DOY 3 at 6.1 R_J on the dusk side and selected as a typical value in a volcanic quiet period, and 7 eV, which is warmer than the typical temperature in the quiet period.

Then, to focus on the variation with the volcanic activity, the derived parameters on DOY 3, DOY 38, and DOY 91 in the second season on the dusk and dawn sides are listed in Table 5.2. The derived parameters in the third season on the dusk and dawn sides are listed in Table 5.3. The significant dawn-dusk asymmetries are confirmed in the core electron density, the hot electron density, and the S³⁺ mixing ratio. The asymmetries of the hot electron density and the S³⁺ mixing ratio were confirmed for the first time. As shown in Section 3.3, the increases in the hot electron density were confirmed after four of the five volcanic activation events (Events 2–5). After two of them (Events 2 and 4), the increases were confirmed only on the dusk side. Notably, after Event 2, the asymmetry was significant. The mixing ratio of S³⁺ after Event 2 on the dusk side is higher than that on the dawn side on DOY 91 as shown in Table 5.2. This tendency is consistent with the higher hot electron fraction on the dusk side: the ionization rates increase with the electron temperature. Note that it is expected that the dawn-dusk asymmetry of core electron temperature appears along with the asymmetry of hot electron density by the energy transfer via Coulomb collision, but it was not confirmed in this study. This is probably because it is difficult to separate the information on the core electron temperature and hot electron density with the plasma diagnosis method, as mentioned earlier in this section. The analysis to confirm the validity of the increase in hot electron density claimed in this study will be shown in Appendix E.

Table 5.2. List of derived parameters at a distance of 6.1 R_J from Jupiter on dusk and dawn sides in the second season.

	Jan. 2015 (DOY 3)		Feb. 2015 (DOY 38)		Apr. 2015 (DOY 91)	
	Dusk	Dawn	Dusk	Dawn	Dusk	Dawn
Electron density [cm ⁻³]	2100 ± 100	1440 ± 90	2900 ± 200	1900 ± 100	1820 ± 80	1870 ± 90
Hot electron density [cm ⁻³]	13 ± 11	8.6 ± 5.8	20 ± 6.0	15 ± 3.8	49 ± 9.1	17 ± 5.6
Core electron temperature [eV]	4.3 ± 0.3	4.7 ± 0.3	3.8 ± 0.2	4.0 ± 0.2	4.6 ± 0.2	4.3 ± 0.2
S ⁺ mixing ratio	0.062 ± 0.008	0.080 ± 0.009	0.12 ± 0.01	0.14 ± 0.02	0.061 ± 0.005	0.072 ± 0.007
S ²⁺ mixing ratio	0.23 ± 0.04	0.24 ± 0.03	0.22 ± 0.04	0.23 ± 0.03	0.23 ± 0.02	0.22 ± 0.03
S ³⁺ mixing ratio	0.034 ± 0.005	0.038 ± 0.006	0.017 ± 0.002	0.016 ± 0.002	0.048 ± 0.005	0.036 ± 0.004
O ⁺ mixing ratio	0.23 ± 0.04	0.19 ± 0.03	0.24 ± 0.04	0.21 ± 0.03	0.19 ± 0.02	0.23 ± 0.03

Table 5.3. List of derived parameters at a distance of 6.1 R_J from Jupiter on dusk and dawn sides in the third season.

	Dusk			Dawn		
	Electron density [cm ⁻³]	1300 ± 100	–	2700 ± 300	940 ± 90	–
Hot electron density [cm ⁻³]	8.0 ± 3.0	–	42 ± 8.0	0.8 ± 0.1	–	36 ± 7.0
Core electron temperature [eV]	3.1 ± 0.2	–	5.1 ± 0.6	3.4 ± 0.2	–	4.6 ± 0.6
S ⁺ mixing ratio	0.05 ± 0.01	–	0.11 ± 0.02	0.051 ± 0.008	–	0.12 ± 0.02
S ²⁺ mixing ratio	0.22 ± 0.04	–	0.24 ± 0.05	0.21 ± 0.04	–	0.24 ± 0.06
S ³⁺ mixing ratio	0.018 ± 0.005	–	0.05 ± 0.01	0.020 ± 0.007	–	0.052 ± 0.008

5. 2.Io-phase dependence of hot electron density

5. 2. 1. Data analysis

The plasma diagnosis was performed to investigate the dependence of the hot electron density on the Io phase angle. The data were selected according to whether Io exists on the dusk side (Io phase angle of 180–360 deg, the gray area in Figure 5.2) or the dawn side (Io phase angle of 0–180 deg, the red area in Figure 5.2), and integrated every ~10 days. The analysis method and assumptions were the same as shown in Section 2.2 except for the integration area. The data from 5.9 to 7.1 R_J , which is wider than the area used for the analysis shown in Section 2.2, were integrated to increase in signal-to-noise ratio. Note that to calculate the column density, the path length in the line-of-sight direction was assumed the length of the red line in Figure 5.3. The inner and outer edges of the IPT were assumed to be at the 5.9 R_J and 8.2 R_J distances from Jupiter, respectively.

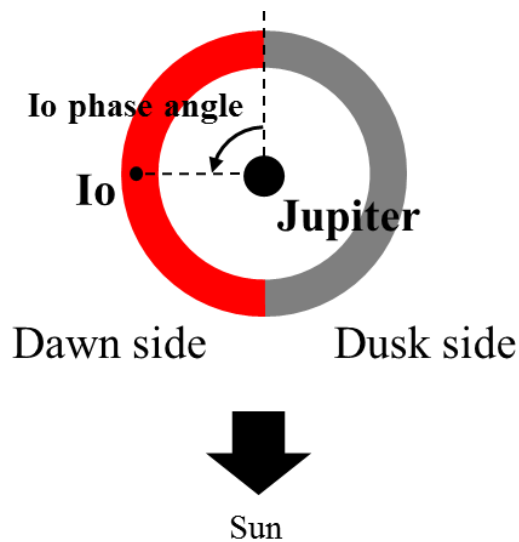


Figure 5.2. Schematic diagram of the Io phase angle from above the north pole.

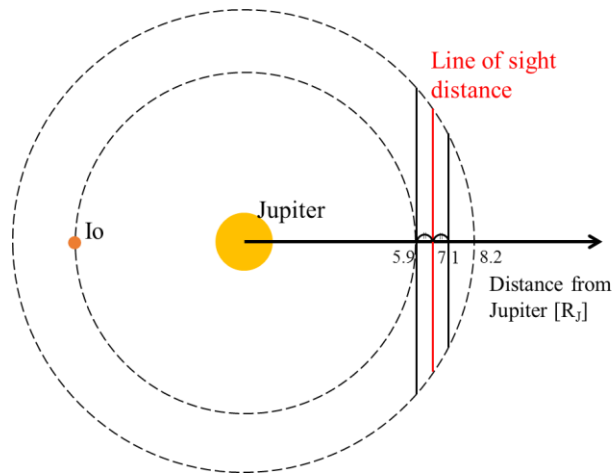


Figure 5.3. Schematic diagram about the assumption of the path length along the line-of-sight direction from above the north pole.

5. 2. 2. Results and discussion

Figure 5.4 shows the column densities of the hot electron on the dusk and dawn sides (i) when Io is close to the interested area and (ii) when Io is far from it. It can be seen that when the hot electron density near Io increases, the hot electron density far from Io also increases. Therefore, the cause of the increase in the hot electron density is not the increase in the heating associated with Io. Moreover, the dawn-dusk asymmetry of the hot electron density associated with the volcanic event occurs regardless of the location of Io. It can be seen that the dawn-dusk asymmetry of the hot electron density is confirmed both near and far from Io when there is a significant dawn-dusk asymmetry, as shown in Figure 5.4 by the orange shades (DOY 47–132 after Event 2 and DOY 508–554 after Event 4). To make it easier to see the trend, the ratio of hot electron densities on the dusk and dawn sides is shown in Figure 5.5. When the ratio of hot electron densities on the dusk and dawn sides increases near Io, it also increases far from Io. Then, it can be said that the dawn-dusk asymmetry of the hot electron density occurs regardless of the position of Io. Therefore, the local heating near Io was not the dominant mechanism of the increase in the hot electron density and its dawn-dusk asymmetry.

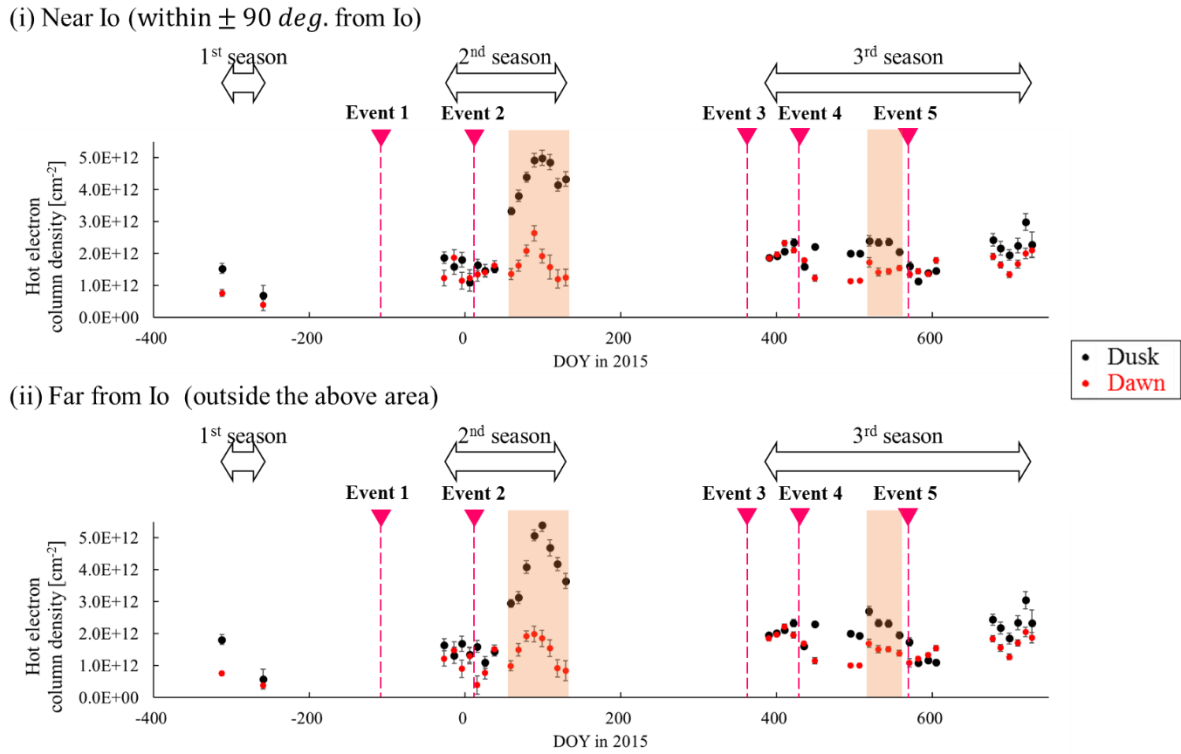


Figure 5.4. Temporal variations in the hot electron column density (i) near Io and (ii) far from Io. Black and red points indicate the values for the dusk and dawn sides, respectively, while the error bars represent the one-sigma values. The areas shaded in orange indicate periods when there are significant dawn-dusk asymmetries.

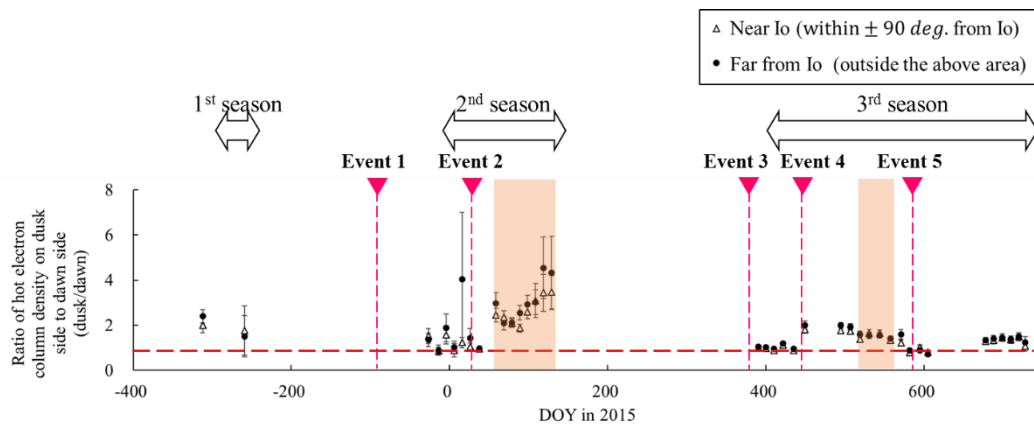


Figure 5.5. Temporal variations in the ratio of hot electron column density on the dusk side to that on the dawn side. White triangles and black circles represent results near Io and far from Io, respectively. The red dotted line represents the case where the ratio is one. The error bars represent the one-sigma values.

It should be noted that a significant difference between results near Io and far from Io was not confirmed for both dusk and dawn sides. In other words, significant local heating near Io was not confirmed in this study. Note that this result does not deny the presence of local heating near Io, which was evaluated by Tsuchiya et al. (2015) by using the Hisaki data, as introduced in Subsubsection 1.2.5.2. There are two caveats. Firstly, Tsuchiya et al. (2015) and this study differ in the amplitude of the fluctuation of interest in addition to the analysis method. The plasma density and temperature were derived from the spectrum in this study, while only spectral information was used in Tsuchiya et al. (2015); therefore, it was possible to detect finer-scale changes in Tsuchiya et al. (2015). The ratio of fluctuation amplitude near Io, which was focused in Tsuchiya et al. (2015), to a steady-state value was at most 10%. On the contrary, the ratio of fluctuation amplitude in the volcanically active period after Event 2 to a steady-state value was 277% as the hot electron densities on the dusk side in the volcanically quiet and active periods were $\sim 13 \text{ cm}^{-3}$ and $\sim 49 \text{ cm}^{-3}$, as shown in Table 5.2. Therefore, it is natural that the heating near Io confirmed in Tsuchiya et al. (2015) was not confirmed in this study. Secondly, the analysis period is different between Tsuchiya et al. (2015) and this study. The period used for analysis in Tsuchiya et al. (2015), which is from Dec. 31, 2013 to Jan. 13, 2014, could not be used for this study due to the lack of signal-to-noise ratio. Therefore, this study does not deny the presence of local heating near Io proposed by Tsuchiya et al. (2015), and it is considered that it may always exist in a steady state.

5. 3. Discussion on the cause of the dawn-dusk asymmetry of hot electron density

5. 3. 1. Evaluation of loss effects

As the main candidates for the loss mechanism, thermal relaxation due to the Coulomb collision and loss to Jupiter's atmosphere due to the pitch angle scattering via wave-particle interaction can be listed. In the following sections, their loss timescales will be estimated. Also, the possibility that the loss timescales were shorter on the dawn side than on the dusk side, which leads to the dawn-dusk asymmetry of the hot electron density, will be discussed.

5. 3. 1. 1. Estimation of thermal relaxation time via Coulomb collision

One of the possible mechanisms of loss of the hot electrons supplied to the IPT is the thermal relaxation due to the Coulomb collision with the core electrons. The typical thermal relaxation time will be estimated in this section.

While the discussion on the temperature of hot electrons is out of the scope of this study, it is considered to from several dozens of eV to ~1000 eV, as mentioned in Subsubsection 1.2.5.1.

The thermal relaxation time of hot electrons (τ) can be expressed by combining the hot electron temperature (T_h), the core electron temperature (T_c), and the core electron density (n_c) (Equation [5.1]). The Coulomb logarithm (λ) in Equation (5.1) can be expressed by Equation (5.2) (Huba, 2009).

$$\tau = 5.6 \times 10^{18} \times \frac{m_e^{1/2}(T_c+T_h)^{3/2}}{n_c\lambda}. \quad (5.1)$$

$$\lambda = 23.5 - \ln(n_c^{1/2}T_c^{-5/4}) - [10^{-5} + (\ln T_c - 2)^2/16]^{1/2}. \quad (5.2)$$

The relationship between the hot electron temperature and the relaxation time at a distance of 6.1 R_J from Jupiter on DOY 91 in 2015 can be calculated using the derived density and temperature (Figure 5.6). It can be seen that the relaxation time is ~100 hours or less when the hot electron temperature is ~1000 eV or less, as shown in the red dotted line. Notably, as shown in the blue dotted line, the hot electrons with temperature less than ~100 eV are thermally relaxed within 5 hours, in which they corotate from the dusk/dawn side to the dawn/dusk side.

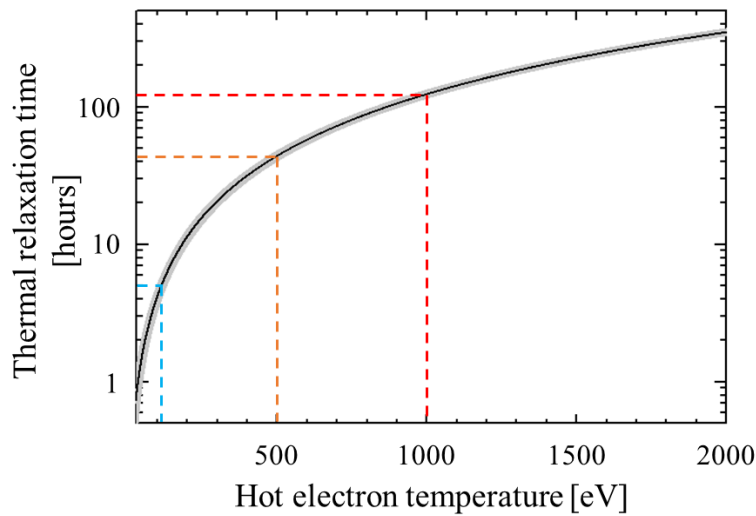


Figure 5.6. Thermal relaxation time of hot electrons at a distance of 6.1 R_J from Jupiter on the dusk side on DOY 91 in 2015. The horizontal blue dotted line indicates thermal relaxation times of 5 hours, while the vertical blue dotted line indicates the corresponding hot electron temperature. The vertical orange and red dotted lines indicate hot-electron temperatures of 500 eV and 1000 eV, while the horizontal orange and red dotted lines indicate the corresponding relaxation time. The gray area indicates the range of \pm one sigma derived by considering the propagation of error of plasma diagnosis.

Then, the possibility that the density and temperature of the core electron lead to the dawn-dusk asymmetry of the thermal relaxation time, which lead to the dawn-dusk asymmetry of the hot electron density after Events 2 and 4, will be discussed. Figure 5.7 shows the temporal variation in the thermal relaxation time of the hot electron, which was calculated from the derived density and temperature of the core electron using Equation (5.1). The temperature of the hot electron was set to 200 eV. In Figure 5.7, no significant dawn-dusk asymmetry was observed for the period when the dawn-dusk asymmetry of the hot electron density was confirmed after Event 2 (DOY 47–132). Regarding the period when the dawn-dusk asymmetry of the hot electron density was confirmed after Event 4 (DOY 508–554), the thermal relaxation time on the dawn side tends to be slightly longer than that on the dusk side; that is, the hot electron is more difficult to be thermalized on the dawn side than on the dusk side. These signatures indicate that the confirmed dawn-dusk asymmetry of hot electron density was not due to the asymmetry of the core component.

Let me discuss the possibility that the density and temperature of the core electron was the reason why the dawn-dusk asymmetry was not confirmed for the period involving Events 3 and 5. Regarding the period involving Event 3 (DOY 393–439), the thermal relaxation time on the dawn side tends to be longer than that on the dusk side. Therefore, the core component does not seem to be the reason why the dawn-dusk asymmetry of the hot electron density was not confirmed. On the contrary, no significant dawn-dusk asymmetry was confirmed for the period involving Event 5 (DOY 591–701); therefore, the core component might be the reason why the dawn-dusk asymmetry of hot electron density was not confirmed.

It should be noted that the possible presence of the dawn-dusk asymmetry of hot electron temperature could not be discussed in this study. It is possible that the dawn-dusk asymmetry of the transport path or heating causes the asymmetry of the hot electron temperature, resulting in the asymmetry of the thermal relaxation time. To evaluate it, future observations, which will be described in Subsection 5.3.4, are required.

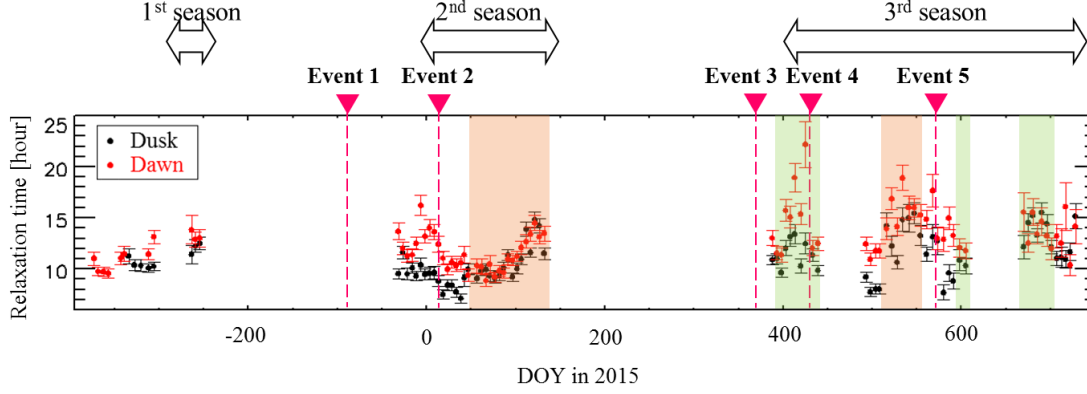


Figure 5.7. Temporal variation in thermal relaxation time of the hot electron at a distance of $6.1 R_J$ from Jupiter. The hot electron temperature was set to 200 eV. The black and red dots indicate the values for the dusk and dawn sides, respectively. The areas shaded in orange indicate periods when there are significant dawn-dusk asymmetries of the hot electron density. The areas shaded in green indicate periods when not significant dawn-dusk asymmetries of the hot electron density but the increases of the hot electron density were confirmed. The error bars represent the one-sigma values.

5. 3. 1. 2. Estimation of the minimum value of timescale of loss via pitch angle scattering of hot electrons inside the IPT

Another possible mechanism for the loss of the hot electrons supplied to the IPT is the loss to Jupiter's atmosphere via the pitch angle scattering. The minimum value of the loss timescale via the pitch angle scattering will be estimated in this section.

Under the assumption of a strong diffusion limit (Kennel, 1969), that is, with the isotropic scattering due to waves at maximum efficiency, the minimum value of the timescale of loss via the pitch angle scattering was evaluated. A dipole magnetic field was assumed. When the loss cone angle of the magnetic equator is α_{eq} , the solid angle of the cone formed by the loss cone angle, Ω , is expressed by Equation (5.3). The bounce period, T_{bounce} , is expressed as Equation (5.4) (Obayashi, 1970). ϕ_m , L , v , R_E represent the latitude at the bounce point, the L value, the particle velocity, and the Earth radius, respectively.

$$\Omega = 2\pi(1 - \cos \alpha_{eq}) \quad (5.3)$$

$$T_{bounce} = 4 \int_0^{\phi_m} \frac{ds}{v_{\parallel}} \simeq \frac{3.4 \times 10^4 \times L}{v} \times \frac{R_J}{R_E} \quad (5.4)$$

It was assumed that hot electrons with pitch angles within Ω would be lost after T_{loss} ($T_{bounce}/4$) (the strong diffusion limit assumption). Let N be the hot electron density at

the magnetic equator and τ be the minimum timescale of loss to the atmosphere due to pitch angle scattering. The following formula holds:

$$\frac{dN}{dt} = N \times \frac{\Omega}{4\pi} \times \frac{1}{T_{loss}} = \frac{N}{\tau}. \quad (5.5)$$

By transforming the formula, the following equation is obtained.

$$\tau = \frac{4\pi}{\Omega} \times T_{loss} = \frac{\pi}{\Omega} \times T_{bounce}. \quad (5.6)$$

From Equations (5.3), (5.4), and (5.6), when T_h was set to 100 eV and 500 eV, τ was estimated to be ~23 hours and ~10 hours, respectively. According to Figure 5.6, when T_h was set to 100 eV and 500 eV, the timescale of thermal relaxation due to the Coulomb collision was ~5 hours and ~40 hours, as shown in the blue and orange dotted lines, respectively. Therefore, when the hot electron temperature is low, the thermal relaxation is more prominent as a loss mechanism. Still, it can be said that the loss via the pitch angle scattering may be effective at high temperature.

It should be noted that it is possible that there is a dawn-dusk asymmetry of the timescale of loss via pitch angle scattering. To evaluate it, future observations, which will be described in Subsection 5.3.4, are needed.

5. 3. 2. Evaluation of the effect of local heating

In this section, the possibility that the local heating is responsible for the increase in the hot electron density and its dawn-dusk asymmetry will be discussed. The candidates for the local heating mechanism are as follows, which are described in Subsubsection 1.2.5.2.

- (1) The interaction with Alfvén waves generated by Io's passage through Jupiter's magnetosphere (Hess et al., 2011)
- (2) The interaction with ion cyclotron waves excited by pickup molecular ions (Russell et al., 2001)
- (3) The interaction with Alfvén waves generated by the radial motion of magnetic flux tubes (Hess et al., 2011; Copper et al., 2016)

The mechanisms of (1) and (2) cause the heating near Io, and the mechanism of (3) causes the heating not limited to the vicinity of Io. As the evaluation of the heating near Io was shown in Section 5.2, I will discuss the local heating by Alfvén waves generated by the motion of the magnetic flux tube.

As described in Chapter 4, in the period involving Event 2, when the mass density gradient was significantly changed, the time taken from the volcanic activation (DOY ~10) to the

decrease in the mass density gradient (DOY ~42) was found to be ~30 days. In comparison, the time taken to increase the hot electron density on the dusk side (from DOY ~47, shown in Table 3.3) was found to be ~40 days during the same period. This meant that it took approximately ten days from the increase in the amount of plasma transported outward, that is to say, from the enhancement of the radial motion of flux tubes, to increase the density of hot electrons.

Then, let me estimate the growth timescale of the interchange instability. The growth rate of the instability can be expressed as the ratio between the external force and the gradient scale length (L) as shown in Equation (5.7) (Treumann and Baumjohann, 1997). r and ω represent the distance from Jupiter and the angular velocity of corotation, respectively. L can be obtained from the mass density (ρ) and the mass density gradient, as shown in Equation (5.8).

$$\gamma = \sqrt{r\omega^2/L}. \quad (5.7)$$

$$L = \rho \left(\frac{d\rho}{dr} \right)^{-1}. \quad (5.8)$$

Using the mass density and their radial-gradient values obtained in this study shown in Section 4.2, the typical growth time of the instability was estimated to be several hours at most. For example, by substituting the values in DOY 42 in 2015 ($\rho = 4.5 \times 10^{-23} \text{ kg/cm}^3$, $\frac{d\rho}{dr} = 2.9 \times 10^{-33} \text{ kg/cm}^4$), the typical growth time was estimated to be approximately one hour. Based on this estimation, the timing gap mentioned above cannot be explained by the growth time of the instability. Therefore, it can be said that the heating by Alfvén waves excited by the radial motion of the magnetic flux tube was revealed not to be the dominant mechanism responsible for the increase in the hot electron density and its dawn-dusk asymmetry.

Note that its effect other than Event 2 could not be grasped due to the discontinuity of the observations and the scale of volcanic activity as indicated in Section 4.2.

5. 3. 3. Possibility for transport to be asymmetric

It is possible that the dawn-dusk asymmetry of the hot electron density during the periods involving Events 2 and 4 was caused by the effect of the dawn-dusk asymmetry of transport other than the loss timescales, which were discussed in Section 5.3.1. In other words, there is a possibility that, due to some mechanism, more hot electrons were transported to the dusk side than the dawn side, and the hot electrons supplied to the dusk side were lost within 5 hours (half of Jupiter's rotation period) before they corotated to the dawn side inside the IPT, resulting in the dawn-dusk asymmetry of the hot electron density. However, this is equivalent to assuming a special situation that there is a dawn-dusk asymmetry in the transient transport such as interchange motions. To verify this possibility, I look forward to future observations, which will be indicated in the next section.

It should be noted that the signature of the brightening phenomena of Jupiter’s aurora and the IPT, which was introduced in Subsubsection 1.1.2.2, is consistent with the above possibility that more hot electrons are supplied to the dusk side by some mechanism. It was revealed by the Hisaki observation that the frequency of the IPT brightening with the auroral brightening was higher on the dusk side than on the dawn side in the first and second seasons. For example, the temporal variations in the auroral and IPT radiations during the second season is shown in Figure 5.8. It can be seen that the IPT brightening on the dusk side was more often than on the dawn side. The event numbers of the brightening are listed in Table 5.4, which are divided according to the start position of brightening. In the volcanically quiet and active periods, the event number of the brightening on the dusk side is nearly twice and three times that on the dawn side, respectively. This suggests that the difference in activity of inward transport between dusk and dawn sides is greater in the volcanically active period than it is in the quiet period. The same analysis for the third season is future work.

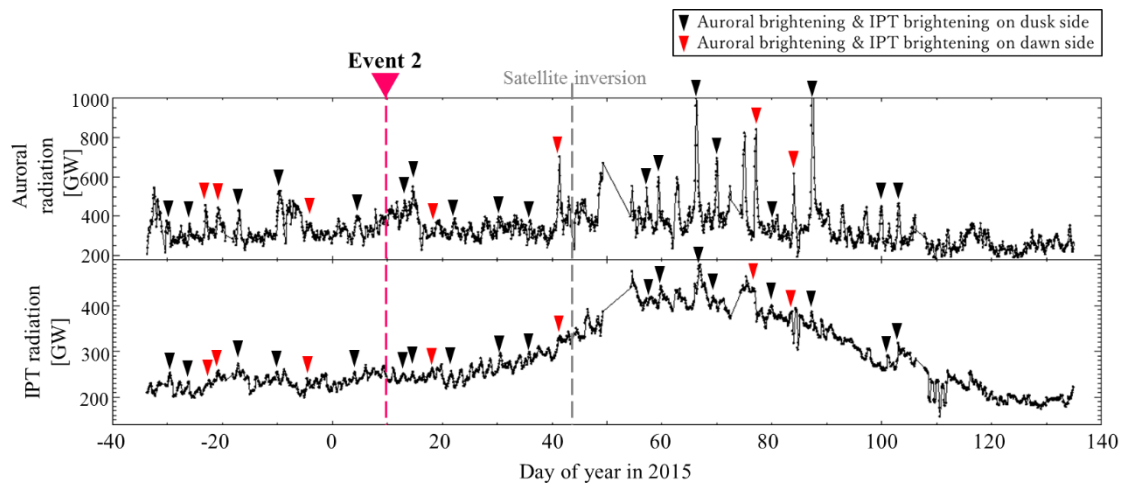


Figure 5.8. Temporal variations in the auroral and IPT radiations during the second season. The starting point of the auroral and IPT brightenings detected by the method of Suzuki et al. (2018) are indicated by triangles. The black and red triangles indicate the peak timings of the IPT brightening on the dusk and dawn sides, respectively. The approximate timing of volcanic activation indicated by the ground-based observations is indicated by the magenta dotted line. Note that events when the IPT on both the dusk and dawn sides brightened simultaneously, which is labeled as “N/A” in Table 5.4, are not shown in this figure.

Table 5.4. List of the event numbers of the transient brightening in the volcanically quiet and active periods. “N/A” represents the events when the IPT on both the dusk and dawn sides brightened simultaneously.

	In the volcanically quiet period (from DOY -364 to DOY 10)	In the volcanically active period (from DOY 10 to DOY 132)
Dusk	13	13
Dawn	7	4
N/A	3	7
Total	23	24

5. 3. 4. Future work

The following three would be useful for evaluating the dawn-dusk asymmetry of the loss timescales. The first is to monitor the electron density and temperature inside the IPT by the direct observation of the Juno satellite and to evaluate the dawn-dusk asymmetry of the thermal relaxation time. The second is to monitor the number of electrons precipitating into the atmosphere due to pitch angle scattering by direct observation and evaluate the dawn-dusk asymmetry of the amount of loss from IPT. The third is to develop a new mass-energy balance model, which is a renewal version of Delamere & Bagenal (2003), which was introduced in Subsection 1.2.6, in that it considers the local time dependence and to investigate whether the timescale of loss from the system depends on the local time.

Besides, to investigate the dawn-dusk asymmetry of heating by Alfvén waves generated by the radial motion of magnetic flux tubes, which was discussed in Section 5.3.2, is needed. To discuss it, the observations of the electric field, magnetic field, and energy spectrum of electrons are useful as Alfvén waves cause the broadband electron acceleration (Frank & Paterson, 2000a).

To clarify the mechanism of the increase in the efficiency of radial transport and verify the possibility that the radial transport is responsible for the dawn-dusk asymmetry during the volcanically active period, the following four studies would be useful. The first is to analyze the Juno/Waves data and to investigate the occurrence rate and position of burst events of narrow-band kilometric radiation (nKOM), which comes from the external part of Io’s torus (~8–9 R_J). It was shown by Galileo/PWS and Galileo/EPD that bursts of nKOM radio emission are correlated with energetic electron injections (Louarn et al., 2014). By observing nKOM radio emission, it might be possible to detect the smaller-scale injection events than by the HISAKI observation. By using ground-based and Hisaki observations, the relationship between volcanic activity and injection events can be discussed. The second is to use the image of Jupiter’s aurora and to investigate where the patch-like aurora on the low latitude appears and

how it moves. It would make it possible to discuss the occurrence rate of injection events, the location of occurrence, and the location of arrival at the IPT. The third is to explore the dawn-dusk asymmetry of the transient IPT brightening, which was shown in Figure 5.8, using the Hisaki data in 2016 (the period involving Events 3–5). This allows us to discuss the occurrence rate of injection events and where they reach in the IPT more generally. The fourth is to perform a global MHD simulation with a high spatial resolution (e.g. Fukazawa et al., 2010) and to discuss the dawn-dusk asymmetry of the transport path when the transient events occur.

Finally, the comparison between the plasma parameters derived from the spectroscopic observation by the Hisaki satellite and parameters obtained by the direct observation of the Juno satellite is a future task in order to evaluate the validity of the analysis method of this study.




5. 4. Conclusion

In this study, the dawn-dusk asymmetry of the hot electron density was found for the first time. After two volcanic events (Events 2 and 4), the increases were confirmed only on the dusk side. As described in Section 5.2, from the dependence on the Io phase angle of the hot electron density, it was clarified that heating near Io was not the dominant mechanism responsible for the increases in the hot electron density and the dawn-dusk asymmetries. Also, based on the temporal variation in the mass density gradient, the heating by Alfvén waves excited by the radial motion of the magnetic flux tube was revealed not to be the dominant mechanism responsible for the increase in the hot electron density and its dawn-dusk asymmetry for the period involving the greatest volcanic event (Event 2) as described in Subsection 5.3.2. Therefore, as for Event 2, the local heating was excluded as the dominant causes of the increase in the hot electron density and its dawn-dusk asymmetry. As for the cause of the dawn-dusk asymmetry of the hot electron density during the period involving Events 2 and 4, both loss and transport can be listed. Also, the cause of the difference of the dawn-dusk asymmetry between events, which may suggest that the strength of the dawn-dusk asymmetry of loss or transport depends on the event, could not be clarified. Future observations by the Juno satellite are required to identify them.

6. General conclusion

The temporal variation in plasma densities and temperature was explored by using the data obtained by the Hisaki satellite with the widest slit from Dec. 2013 to Apr. 2014, from Nov. 2014 to May 2015, and from Jan. 2016 to Dec. 2016, which are mentioned as the first season, the second season, and the third season in this study. From the observation by the ground-based telescopes, five volcanic events, which are mentioned as Events 1–5 in this study, are indicated to occur before and during the above periods. The temporal variation in the radiation from the IPT showed that the volcanic event in 2015 (Event 2) had the greatest impact on the IPT of the five events. The properties obtained so far regarding the response of the magnetosphere at each volcanic event are summarized in Table 6.1. The main findings in this study and discussions are summarized as follows.

Table 6.1. Summary of the properties obtained so far regarding the response of the magnetosphere at each volcanic event.

Event number	1	2	3	4	5
Data continuity	△	○	△	△	△
Increase in plasma density on dusk or dawn side (Section 3.1)	○	○	○	○	○
Increase in hot electron density on dusk or dawn side (Section 3.1)	×	○	○	○	○
Significant temporal variation in the mass density gradient (Section 4.2)	×	○	×	×	×
Dawn-dusk asymmetry of hot electron density (Section 5.1)		○	×	○	×
Influence of local heating associated with I _o on temporal variation in hot electron density (Subsection 5.2.2)		×	×	×	×
Influence of local heating by the motion of magnetic flux tube on temporal variation in hot electron density (Subsection 5.3.2)		×	?	?	?

- The temporal variation in the hot electron density was explored (Chapter 3). The increases in the hot electron density were confirmed after four of the five volcanic activation events (Events 2–5). The reason why no increase was confirmed after Event 1 might be the timing gaps of the observation periods, as discussed in Section 3.3.

- The temporal variation in the mass density distribution in the IPT in the radial direction was clarified for the first time (Chapter 4). Although only during the second season, when the greatest volcanic event (Event 2) occurred, there was a noticeable temporal change in the mass density gradient, and it was revealed that ~30 days after the volcanic activation, the amount of outward plasma transport with magnetic flux tube increased. The reason why its response to other volcanic events was not clear might be the timing gaps of the observation periods and the difference in the scale of volcanic activity, as discussed in Section 4.2.
- The dawn-dusk asymmetry of the hot electron density was confirmed for the first time (Chapter 5). After two volcanic events (Events 2 and 4), the increases were confirmed only on the dusk side.
- From the timing of the change in the mass density gradient and the dependence of hot electron density on the Io phase angle, the local heating was revealed not to be the dominant mechanism responsible for the increase in the hot electron density and its dawn-dusk asymmetry for the period involving Event 2.
- From the above evaluation of local heating effects, it can be concluded that transport is the cause of the increase in the hot electron density after Event 2. This suggests that increased mass loading increased the efficiency of radial transport. As for other events (Event 3–5), though they could not be fully verified due to data discontinuities as indicated in Subsection 5.3.2, there is no contradiction in considering that the transport is responsible for the increase in the hot electron density.
- Based on the lengths of the periods from the occurrence of volcanic eruptions to the increases in hot electron density, the timescale of plasma transport associated with volcanic activation was suggested to be 20–80 days, as indicated in Section 3.3. This timescale is considered to reflect the timescale to change the magnetospheric situation from (0) to (5) as below. Note that it is not clear whether (3), (4), and (5) hold for Events 1 and 3–5 due to the data discontinuities as mentioned above.
 - (0) Volcanic activation
 - (1) Increase in the amount of plasma supply to the IPT (the inner magnetosphere)
 - (2) Increase in plasma density in the inner magnetosphere
 - (3) Increase in mass transport from the inner magnetosphere to outside the IPT
 - (4) Increase in plasma density outside the IPT dozens of days later the activation of the volcano
 - (5) Increase in hot electron density in the inner magnetosphere (IPT region) due to inward transport
- As for the cause of the dawn-dusk asymmetry of the hot electron density during the periods involving Events 2 and 4, both loss and transport can be listed. Also, the cause of the difference of the dawn-dusk asymmetry between events, which suggests that the strength of the dawn-dusk asymmetry of loss or transport depends on the event, could not be clarified. To identify them, future observations by the Juno satellite would be useful.

In this way, the response of dynamics of Jupiter's magnetosphere to the increase in the plasma supply rate could be discussed; that is, the timescale of the plasma transport and its spatial structure were discussed for the first time by deriving the temporal variations of the plasma density after the volcanic activations on timescales of several tens of days.

Appendix

A. Identification of emission lines

A1. Methods

To identify spectral features as a preparation for the plasma diagnosis analysis, I used the high-resolution data with a resolution of $\sim 0.3\text{--}0.4$ nm, which is acquired by the observation with the narrowest slit (the slit of 10 arc seconds), shown in Figure 2.3(a). While the IPT was observed mainly with the widest slit, several days were devoted to observation with the narrowest slit. The observation dates and integration time with the narrowest slit are listed in Table A.1. I used the data obtained between Feb. 18, 2015 and Feb. 23, 2015 for two reasons. (1) The total observation time was the longest. (2) The IPT in Feb. 2015 was significantly brighter than that in the four other periods because of the volcanic activity on Io. The faint features can be seen in this period.

Table A.1. List of observations with the narrowest slit.

Observation period			Total observation time [min.]
Nov. 29, 2013	to	Nov. 30, 2013	623
Nov. 10, 2014	to	Nov. 16, 2014	2465
Feb. 18, 2015	to	Feb. 23, 2015	2494
May. 16, 2015	to	May. 17, 2015	557
Dec. 3, 2015	to	Dec. 24, 2015	1645

In this study, the level-2 data provided by the data pipeline system were used (Kimura et al., 2019). The photon counts were reduced to spectrum by integration for 2494 min. Spectra were spatially integrated from 2 to 8 R_J at dusk because the dusk side is brighter than the dawn side. This is interpreted as the effect of a large-scale dawn-to-dusk electric field in the IPT (Barbosa and Kivelson, 1983; Ip and Goertz, 1983; Murakami et al. 2016). The geocoronal contamination can be eliminated by screening out the data with the satellite local time, as shown in Yoshioka et al. 2017. However, in this analysis, I did not eliminate it to obtain a long integration time.

A2. Results

The resultant spectra from 63.8 to 146.5 nm are shown in Figures A.1–A.4. The spectral features were identified with the use of the National Institute of Standards and Technology (NIST) database (Kramida et al., 2017) and study on geocoronal emissions (Meier, 1991). No

emission lines were detected below 63.8 nm and above 146.5 nm except for He I (58.4 nm), which is mainly a geocoronal emission. The error bar was estimated based on Poisson statistics of the photon counts and the sensitivity error (Yoshioka et al., 2013). The shaded areas in Figures A.3 and A.4 indicate data with large errors due to the low sensitivity of detector around H I 121.6 nm, which were excluded from the identification of emission lines.

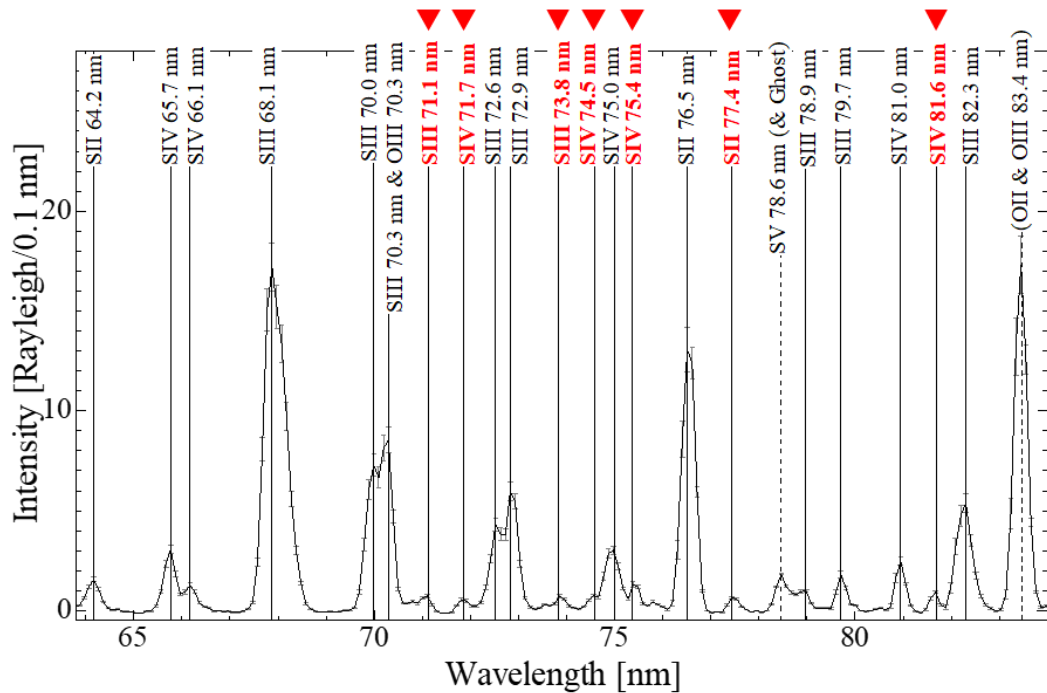


Figure A.1. Spectrum (63.8–84.0 nm) extracted from 2–8 R_J in the projected radial distance. I used the wavelength labels from the NIST database. The red characters and triangles indicate spectral lines detected for the first time. The dotted lines and brackets indicate geocoronal emission, narcissistic ghost, or second-order diffracted light. The error bars represent the one-sigma values.

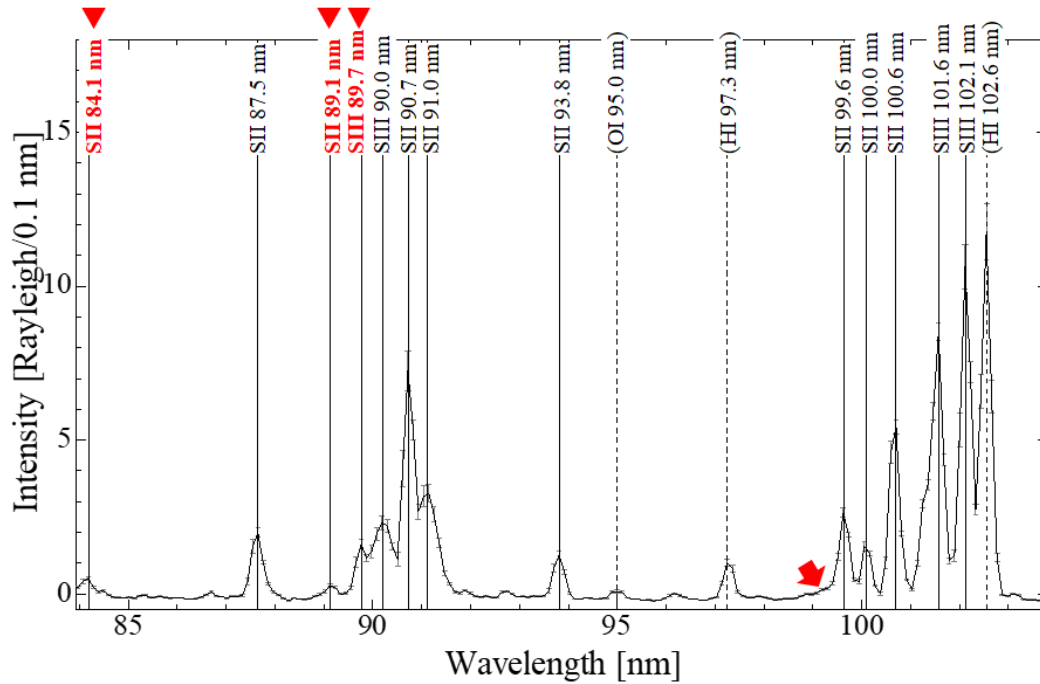


Figure A.2. Spectrum (84.0–103.8 nm). Same as Figure A.1, except for red arrow indicating the unidentified feature near 99.0 nm.

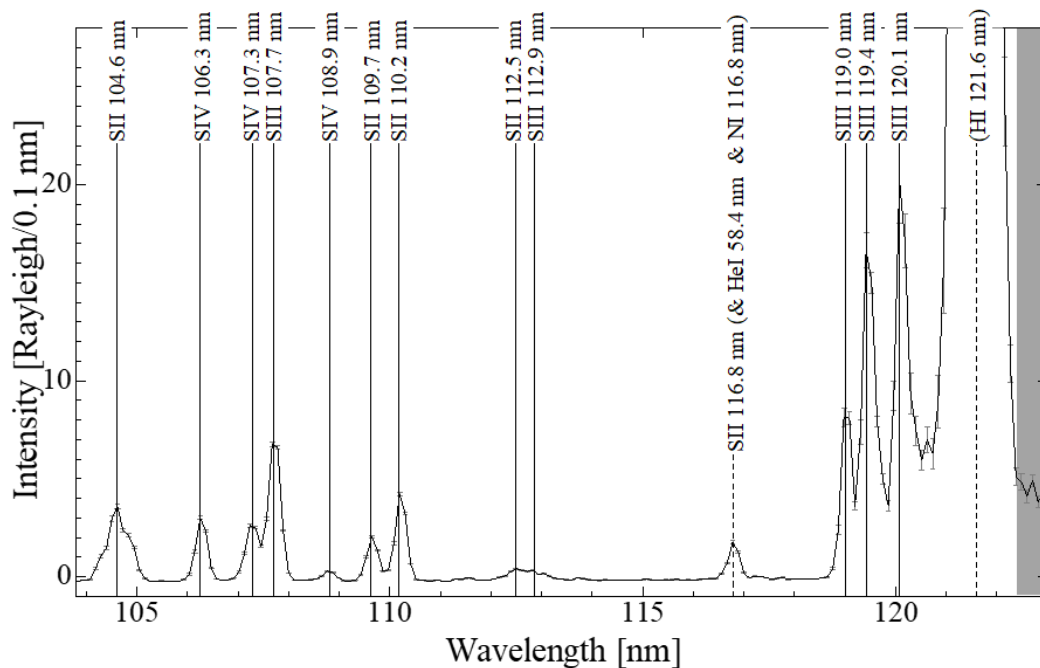


Figure A.3. Spectrum (103.8–123.0 nm). Same as Figure A.1, except for shaded area indicating data with large errors and excluded from spectral identification.

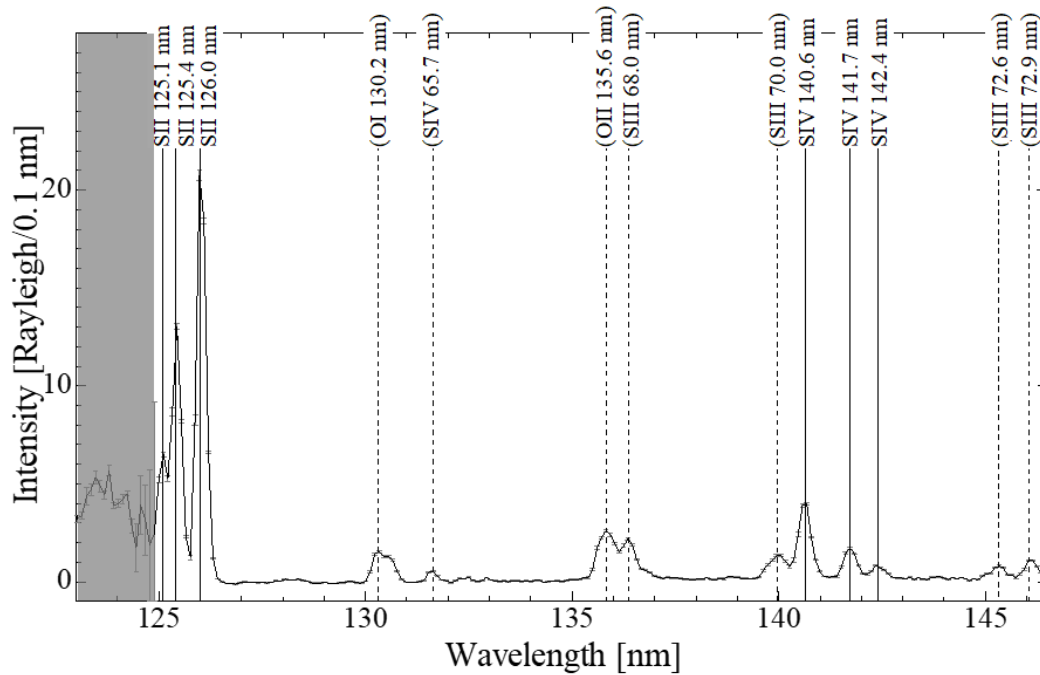


Figure A.4. Spectrum (123.0–146.5 nm). Same as Figure A.3.

The spectral lines labeled with red characters and triangles are emissions that are detected for the first time in the IPT observation. There are mainly three reasons why these emission lines could be detected for the first time by the Hisaki observation. (1) High wavelength resolution. (2) High sensitivity. (3) Long integration time. Here, focusing on the above points, I will compare the performance in the wavelength range from 70.0 to 90.0 nm of spectrographs on HUT, EUVE, Cassini, and Hisaki, which conducted the IPT observations recently. Firstly, the HUT spectrograph has a limiting spectral resolution of ~ 0.15 nm, which is almost comparable to the performance of EXCEED. Still, the integration time was only 1274 sec, which is two orders of magnitude shorter (Moos et al., 1991). Secondly, the spectrograph on EUVE has an FWHM of 0.25–0.35 nm, which is comparable to EXCEED, but the effective area was only ~ 0.1 cm², which is one order of magnitude smaller (Hall et al., 1994b; Sirk et al., 1997). The integration time was 62196 sec. Thirdly, the spectrograph on Cassini had a lower spectral resolution than that of EXCEED in the IPT observations. It was reported that the wavelength resolution of Cassini, as measured by the point spread function was an FWHM of ~ 0.3 nm (Steffl et al., 2004a), but the emission from the IPT is not a point source. The integration time was 17000 sec. For the reasons stated above, EXCEED was able to detect new emission lines from the IPT.

Feldman et al. (2004) used the spectroscopic data obtained by the FUSE and reported the existence of features from 99.1 to 99.5 nm, though they could not identify the emitters and configurations. The spectral resolution of EXCEED is not sufficient to resolve those unidentified lines.

Three types of features which contaminate the data are indicated by dotted lines and

brackets in Figures A.1, A.2, A.3, and A.4. One is geocoronal emissions (O II 83.4 nm, O I 95.0 nm, H I 97.2 nm, H I 102.5 nm, N I 116.8 nm, H I 121.6 nm, O I 130.2 nm, and O II 135.6 nm). Another type is the so-called narcissistic ghost (McCandliss et al., 1998). The ghost of H I 121.6 nm appears approximately at the wavelength of 80.0 nm. The third type is the second-order diffracted light. The features at 131.4, 136.0, 140.0, 145.2, and 145.8 nm are ascribed to the second-order diffracted light of S IV 65.7 nm, S III 68.0 nm, S III 70.0 nm, S III 72.6 nm, and S III 72.9 nm, respectively. The feature at 116.8 nm includes contributions from three types of emissions: S II 116.8 nm, geocoronal N I 116.8 nm, and the second-order diffracted light of He I 58.4 nm.

By summarizing past observations and using the results obtained by EXCEED, I updated the term diagrams for S II, S III, and S IV emissions from the IPT in Figures A.5, A.6, and A.7, respectively. The energy levels of the same term are shown vertically. Some minor lines were omitted from the diagram. I identified configurations of energy levels with the use of the NIST database. The emission lines detected for the first time are underlined and shown in red.

S II

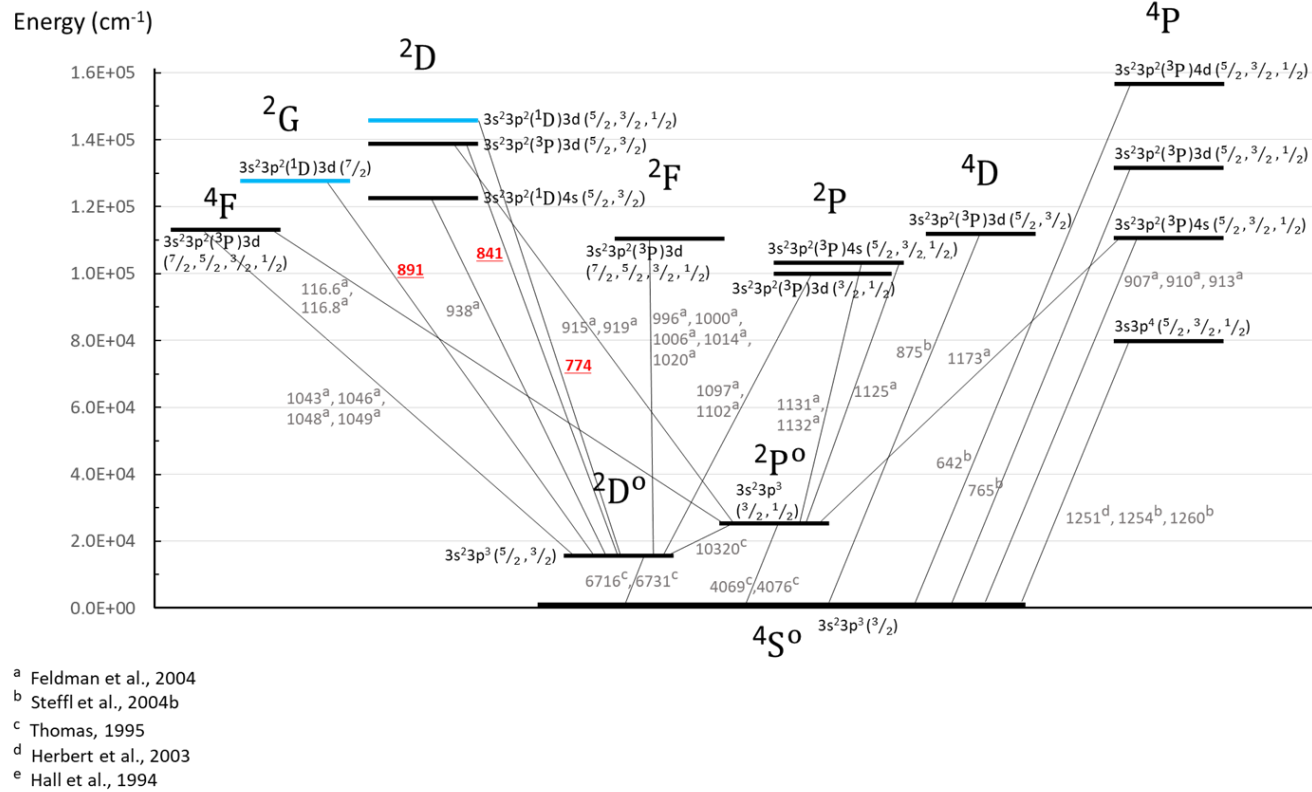
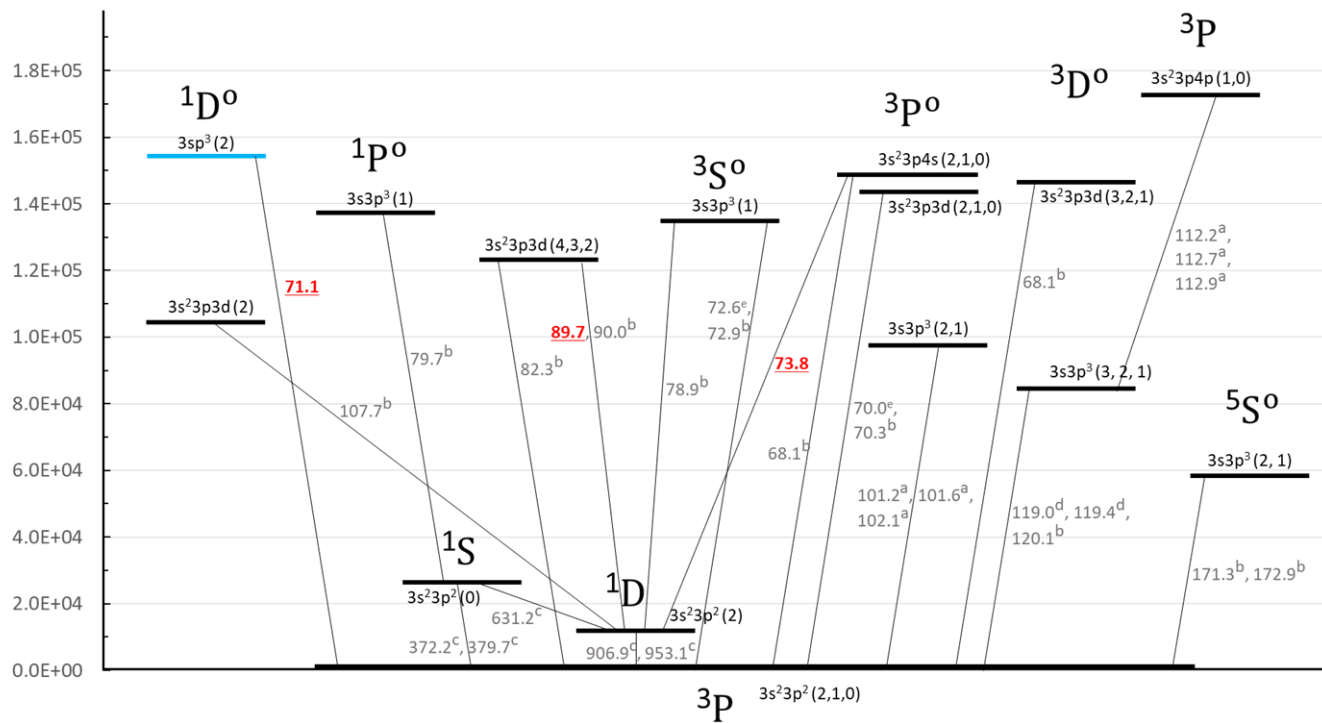


Figure A.5. Term diagram for S II. Levels of the same term are shown vertically. Transitions detected by IPT observations are shown. Some minor lines are omitted from the diagram. Emission lines detected for the first time are underlined and shown in red. Energy levels detected for the first time are shown in blue.

S III

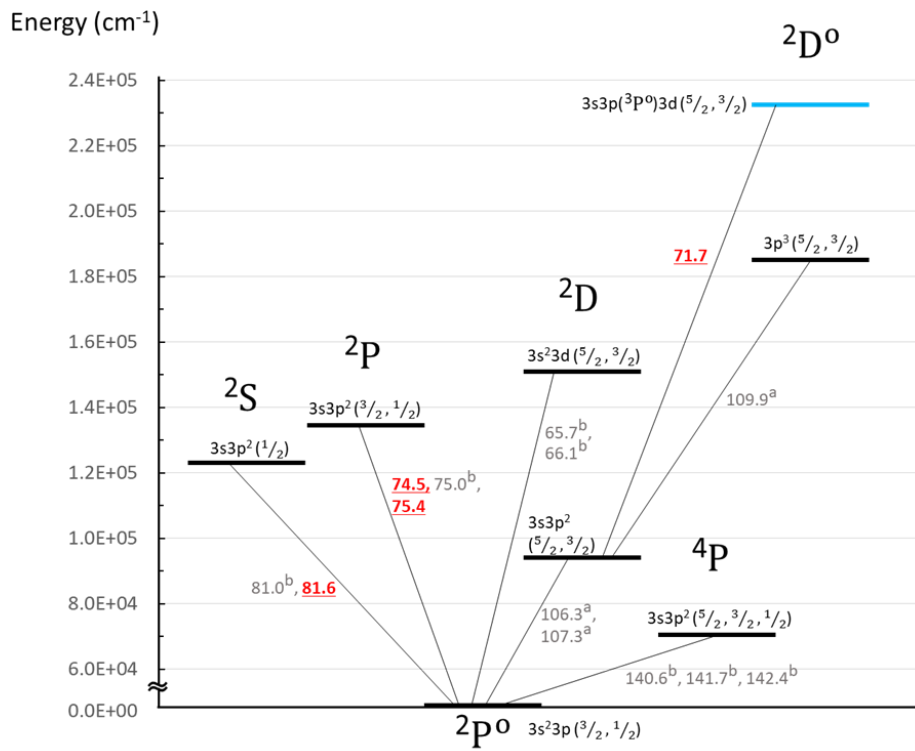
Energy (cm⁻¹)



- ^a Feldman et al., 2004
- ^b Steffl et al., 2004b
- ^c Thomas, 1995
- ^d Herbert et al., 2003
- ^e Hall et al., 1994

Figure A.6. Term diagram for S III. Same as Figure A.5.

S IV



- ^a Feldman et al., 2004
- ^b Steffl et al., 2004b
- ^c Thomas, 1995
- ^d Herbert et al., 2003
- ^e Hall et al., 1994

Figure A.7. Term diagram for S IV. Same as Figure A.5.

There are two caveats about the term diagrams. (1) As shown in Figure A.6, the transitions emitting 68.1 nm are identified as the transitions of S III from 3P_0 to 3P and from 3D_0 to 3P . However, the former (3P_0 - 3P) had not been confirmed in the past IPT observations because of overlap with the latter, more intense transition (3D_0 - 3P), and low spectral resolution. Here I assumed that the transition from 3P_0 to 3P also contributes to S III 68.1 nm to some extent because S III 73.8 nm, which upper level is 3P_0 , was detected. (2) S IV 108.8 nm is not listed in Figure A.7 because the configuration of S IV 108.8 nm has been a controversial issue, as mentioned in Feldman et al. (2004). Whereas the NIST database (Kramida et al., 2017) lists the S IV transition at 108.8 nm between the 4D_0 and 4F states, some studies list it between the 2D and 2D_0 states (Kelly, 1987; Mendoza et al., 1995).

The transitions detected for the first time can be classified into two types, as listed in Table A.2. One is transitions between energy levels, which have the same configuration as levels detected in the past IPT observations except for the spin state (Type A). S III 73.8 nm, S IV 74.5 nm, S IV 75.4 nm, S IV 81.6 nm, S II 84.1 nm, and S III 89.7 nm are attributed to this type. The other type is transitions whose upper levels were not identified in the past IPT observations (Type B). S III 71.1 nm, S IV 71.7 nm, S II 77.4 nm, and S II 89.1 nm are attributed to this type. Their four upper levels, which are detected for the first time in the IPT, are shown in blue in Figures A.5, A.6, and A.7. In particular, the excited level of S IV 71.7 nm has the highest energy among the levels so far.

Table A.2. Classification of the emission lines detected for the first time

Type A	Type B
S III 73.8 nm	S III 71.1 nm
S IV 74.5 nm	S IV 71.7 nm
S IV 75.4 nm	S II 77.4 nm
S IV 81.6 nm	S II 89.1 nm
S II 84.1 nm	
S III 89.7 nm	

(Type A) Emission lines attributed to transitions between energy levels, which have the same configuration as levels detected in the past IPT observations except for the spin state. (Type B) Emission lines attributed to transitions whose upper levels were not identified in the past IPT observations.

Ten emission lines from the IPT in the wavelength range 71.1–89.7 nm are detected and identified for the first time. These identifications can be used for improving the derivation accuracy of plasma parameters, especially the fraction of hot electron density. Consider S IV lines as an example. Figure A.8 shows the dependence of volume emissivity of S IV lines on the fraction of hot electron density. The vertical axis is the ratio of the emissivity to the typical

parameters in the IPT (T_h (hot electron temperature) = 200 eV, F_h (hot electron fraction) = 2%, N_e (electron density) = 2500 cm⁻³, and T_c (core electron temperature) = 5 eV). I used the CHIANTI atomic database version 8.0.7 for the calculation (Dere et al. 1997; Del Zanna et al. 2015). The main emission lines (65.7 nm, 75.0 nm, 106.3 nm, and 141.7 nm) and the newly detected lines (71.7 nm, 75.4 nm, and 81.6 nm) are color-coded according to the legend. The larger slope means that the volume emissivity is more sensitive to the fraction of hot electron density. As shown in Figure A.8, the transitions at wavelengths shorter than 90.0 nm are more sensitive to the fraction of the hot electron density than those at longer wavelengths. Therefore, detecting those lines may increase constraints on the fraction of hot electron density, though their intensities are weak. Using these lines in the plasma diagnosis analysis is one of the future tasks.

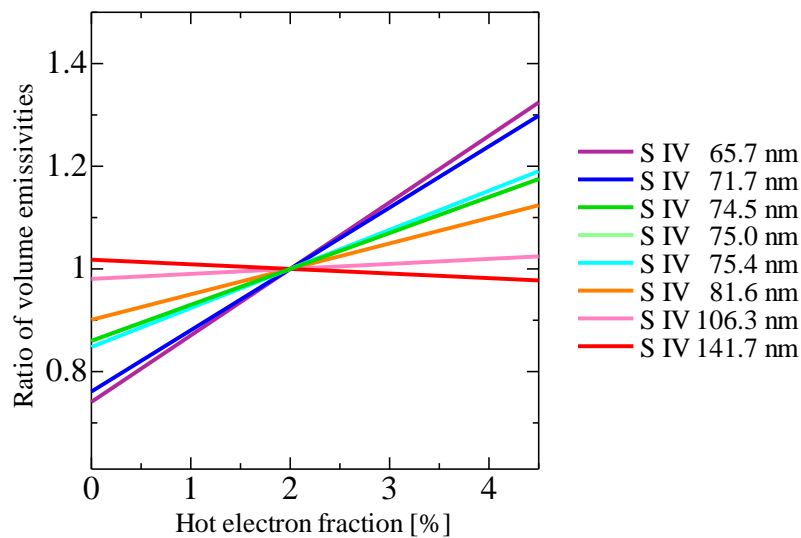


Figure A.8. Dependence of volume emissivity of bright lines of S IV on the fraction of hot electron density to core electron density. The horizontal axis is the fraction of the hot electron density. The vertical axis is the ratio of the emissivity to the emissivity with typical electron parameters in the IPT ($T_h = 200$ eV, $F_h = 2\%$, $N_e = 2500$ cm⁻³, and $T_c = 5$ eV). I used the CHIANTI atomic database version 8.0.7 for the calculation (Dere et al., 1997; Del Zanna et al., 2015). Note that SIV 75.0 nm overlaps S IV 74.5 nm and is not visible on the plot.

B. Evaluation of the effect of satellite inversion

To prevent sunlight from entering the optical system, the Hisaki satellite is inverted around the equatorial plane, as shown in Figure B.1, mainly when the observation target is changed or when the planetary opposition occurs. In this study, the dawn-dusk asymmetry of parameters obtained by plasma diagnosis was discussed. Before and after the inversion, the relationship between the upper/lower side of the detector and the dusk/dawn side are reversed. Then, it is necessary to evaluate the spatial dependence of the sensitivity of the detector. It is also necessary to evaluate changes in the relationship between Jupiter's position and the field of view.

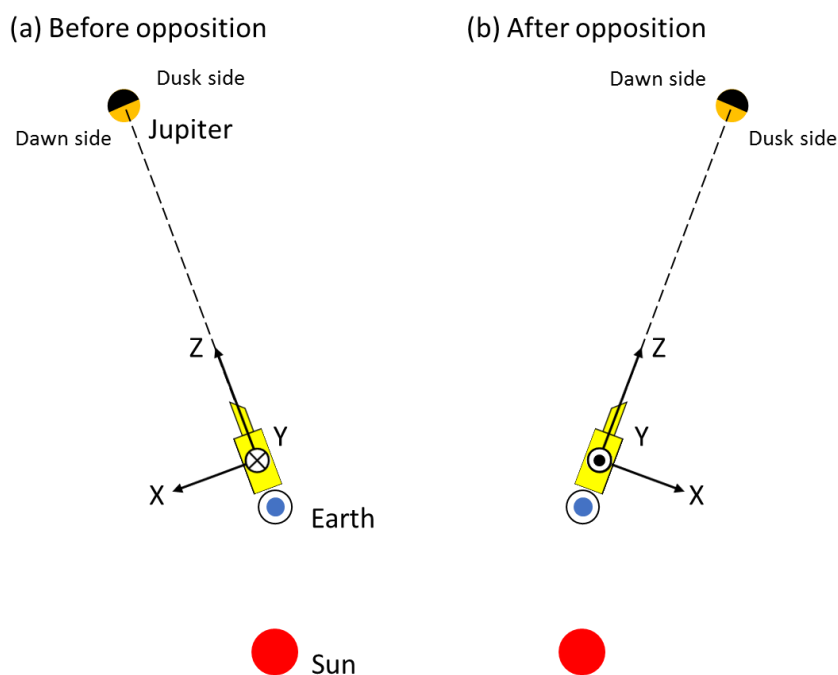


Figure B.1. Schematic of the attitude of the Hisaki satellite before and after the opposition of Jupiter as seen from above the north pole. This figure is not to scale.

B1. Evaluation of spatial dependence of sensitivity

The spatial dependence of the sensitivity was evaluated using the spectroscopic images of geocoronal emissions, which are almost uniform over the entire field of view. The data before the inversion (DOY -30 to 42 in 2015) and after the inversion (DOY 43 to 135 in 2015) were integrated, respectively, as shown in Figure B.2. Figure B.3 shows the ratios of count rates in the lower areas to those of upper areas of He I 58.4 nm, O II & O III 83.3 nm, HI 97.2 nm, HI 102.4 nm, NI 116.8 nm, and OI 130.4 nm. The average value of the ratio of count rates was 0.996, and it can be concluded that the spatial dependence of sensitivity was negligible. Note

that the characteristic pattern of each emission shown in Figure B.2 is not inverted before and after the satellite inversion. Therefore, it can be said that the ratio of each emission line is associated with the unevenness of sensitivity before reaching the detector (in the spectroscopic section).

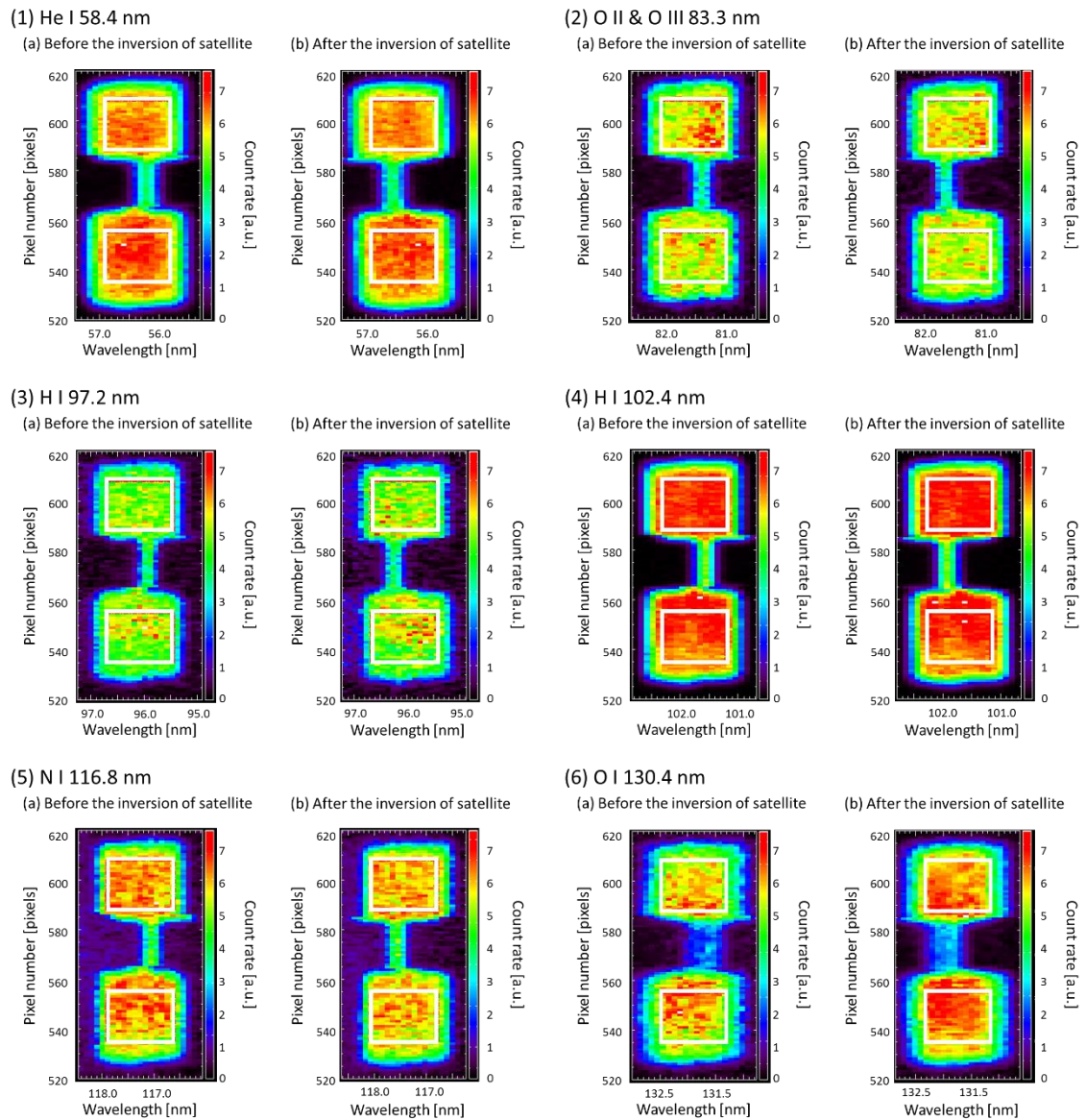


Figure B.2. Spectral images of geocoronal emissions of (1) He I 58.4 nm, (2) O II & O III 83.3 nm, (3) H I 97.2 nm, (4) H I 102.4 nm, (5) N I 116.8 nm, and (6) O I 130.4 nm. The areas enclosed by white lines indicate regions of interest used for analysis.

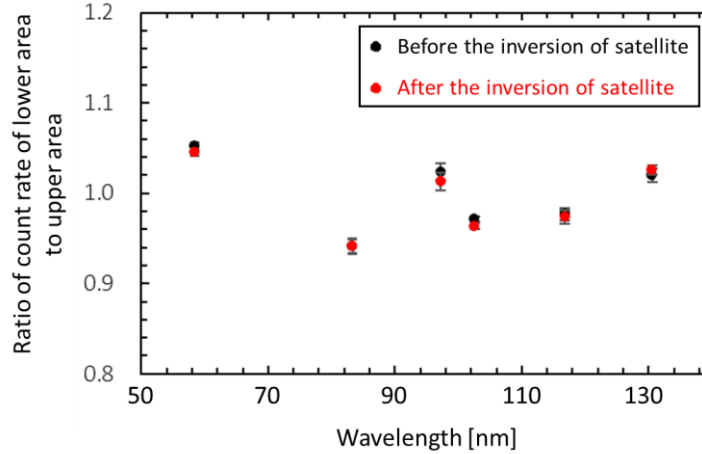


Figure B.3. Ratios of count rate in the lower area of the detector to the upper area. The black and red dots indicate values before and after the inversion of the satellite, respectively.

B2. Evaluation of variation in the field of view

The radial variation in the field of view, which corresponds to the variation in the vertical axis of the spectral image, was evaluated by detecting Jupiter's radial position using the auroral emission. In the following, the variation in the horizontal axis in the field of view, in the north-south direction, was evaluated. The images of Jupiter and the shadow of the slit, as shown in Figure B.4, obtained with the Field-Of-View (FOV) camera on the Hisaki satellite were used. Details on the FOV camera are shown in Yamazaki et al. (2014).

The center position of Jupiter was detected by the following procedure. (1) The image was smoothed with ± 2 pixels in the x and y directions. (2) The Gaussian fit was performed on the cross-sectional profile along the y -coordinate using the data in the center of the image, which is shown in the upper panel in Figure B.4(1a) and (1b). This determined the x -coordinate of Jupiter's center position. (3) The y -coordinate at which the cross-sectional profile at the x coordinate takes the maximum value was determined as the y coordinate of Jupiter's center, which is shown on the right side of the panel in Figure B.4(1a) and (1b). In this procedure, the data before smoothing was used. As a result, the y -coordinates before and after satellite inversion were found to be 107 and 140.

The position of the end of the slit was detected as follows. (1) The data of the area inside and outside the shadow of the slit were averaged, respectively. (2) The data enclosed by the white chain line were averaged along the x -direction to obtain the cross-sectional profile, which is shown on the right side of the panel in Figure B.4 (2a) and (2b). (3) The pixels closest to the median value inside and outside the shadow of the slit was determined. As a result, the y -coordinates of the end of the slit before the satellite inversion were determined as 117 and 136. After the inversion, they were 118 and 137.

From the above results, the distances from Jupiter's center position to the slit edge were

10 (=117–107) pixels and 3 (=140–137) pixels before and after the satellite inversion, respectively. There was a gap of 7 pixels before and after the inversion. Since the plate scale of the FOV camera is ~ 1.09 arcsec/pixel, the above gap corresponds to $\sim 0.4 R_J$. This is sufficiently small compared to the width of the 140 arc seconds slit in the north-south direction, but it may have a slight effect on the results of the analysis.

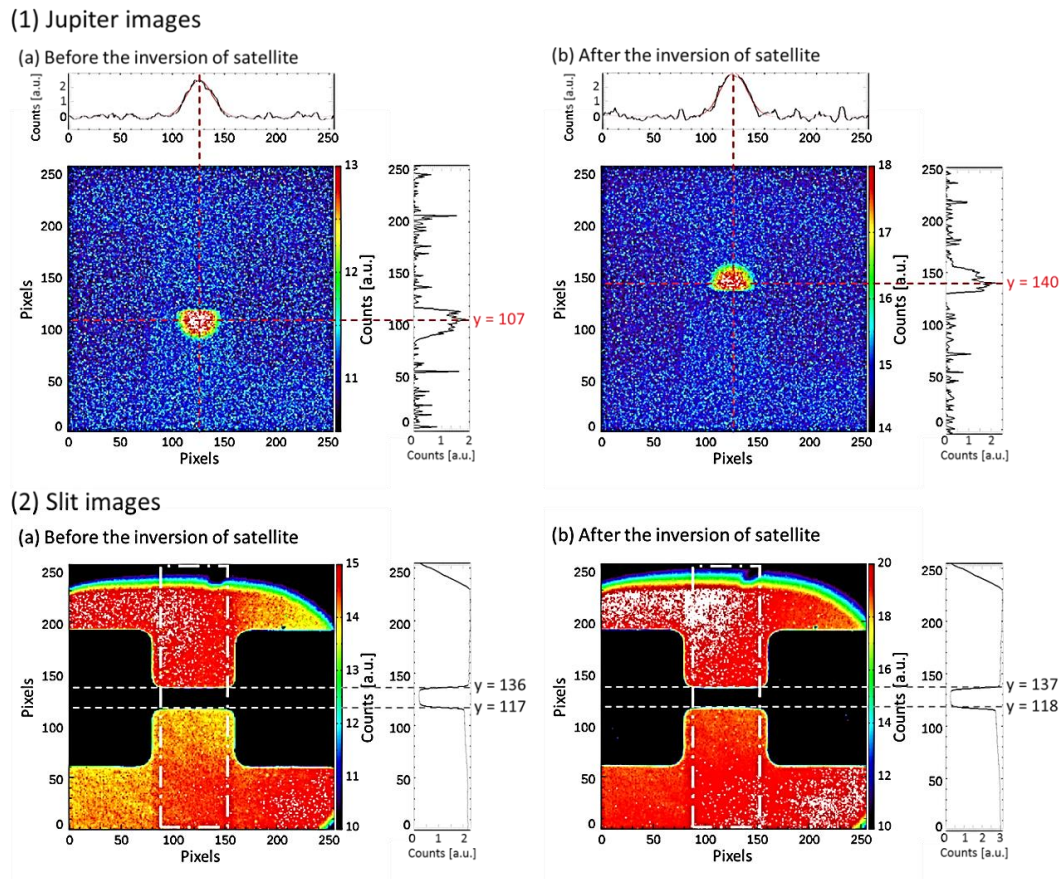


Figure B.4. Estimation of the position of Jupiter and dumbbell slit using images obtained by the Field-Of-View camera. (1) Jupiter images obtained by integrating images (a) before the inversion of the satellite and (b) after the inversion. Plots at the top of panels indicate examples of smoothed cross-sectional views in the x -axis direction. Vertical red dotted lines show the estimated x coordinate center position of Jupiter. Plots at the right panels indicate cross-sectional views in the y -axis direction with the x coordinate center position of Jupiter. Horizontal red dotted lines show the determined y -coordinate center positions of Jupiter. (2) Slit images obtained by integrating images (a) before the inversion of the satellite and (b) after the inversion. Plots at the right panels indicate cross-sectional views in the y -axis direction obtained by integrating data enclosed by white chain lines. Horizontal red dotted lines show determined y -coordinate positions of the edge of the slit.

C. How to convert light intensity to brightness

C1. Estimation of torus emission width

As mentioned in Subsection 2.2.2, the equivalent width of torus emission was used in calculating the line brightness from data with the 140 arc seconds slit, which is wider than the apparent width of the torus. In this section, the method for estimation of torus width will be shown. The shape of the spectrum acquired by Hisaki (f_{Hisaki}) is determined not only by the spatial structure of torus (f_{torus}) but also by the line blending (f_{λ}) and instrumental function (f_{inst}), as shown in Equation (C.1).

$$f_{\text{Hisaki}} = f_{\text{torus}} * f_{\lambda} * f_{\text{inst}}. \quad (\text{C.1})$$

In this study, the spatial structure of the torus, f_{torus} , was determined by subtracting their effects as follows. (1) By assuming the distribution along the north-south direction to be described by the Gaussian function, the width including all effects, f_{Hisaki} , was estimated. (2) The instrumental function of Hisaki/EXCEED, or f_{inst} , was estimated by using data with the 10 arc seconds slit. At this time, it was assumed that the slit width is sufficiently narrow, and the light intensity in the slit can be regarded as to be uniform. The obtained spectral resolution was roughly consistent with Yoshioka et al. (2013), which showed the results of laboratory calibration. (3) The relationship between f_{Hisaki} and f_{torus} was derived for each line by using the CHIANTI atomic database and the instrumental function. The convolutions of emission lines around S II 76.5 nm with the Gaussian width of torus emission (H_{torus}), which is σ in Equation (2.4), of 0.1 nm, 0.3 nm, 0.5 nm, and 0.7 nm are shown in Figure C.1. As a result, the relationships between the Gaussian width including all effects (H_{Hisaki}) and H_{torus} are obtained as shown in Figure C.2. (4) The spatial structure of torus, f_{torus} , can be estimated from (3) and f_{Hisaki} derived in (1). Then, H_{torus} is obtained, as shown in Figure C.3. It is thought that these temporal fluctuations in the thickness of torus emissions in the north-south direction represent changes in the scale height due to variation in ion temperatures with the volcanic activity on Io.

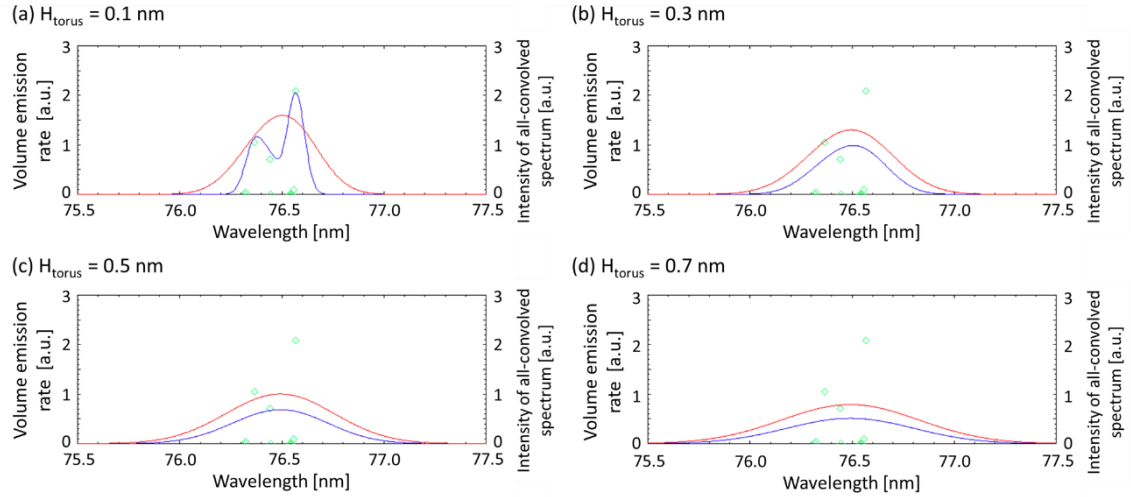


Figure C.1. Convolution of emission lines around S II 76.5 nm. The dots indicate the volume emission rate of each adjacent spectrum, which exists around the target wavelength. The blue lines show the convolved spectra with the instrumental function. The red lines express the convolved spectra with the Gaussian width of torus emission. The four panels show the spectra with the different width of torus emission of (a) 0.1 nm, (b) 0.3 nm, (c) 0.5 nm, and (d) 0.7 nm. Note that the vertical axis of all-convolved spectra shown by the red lines is indicated on the right.

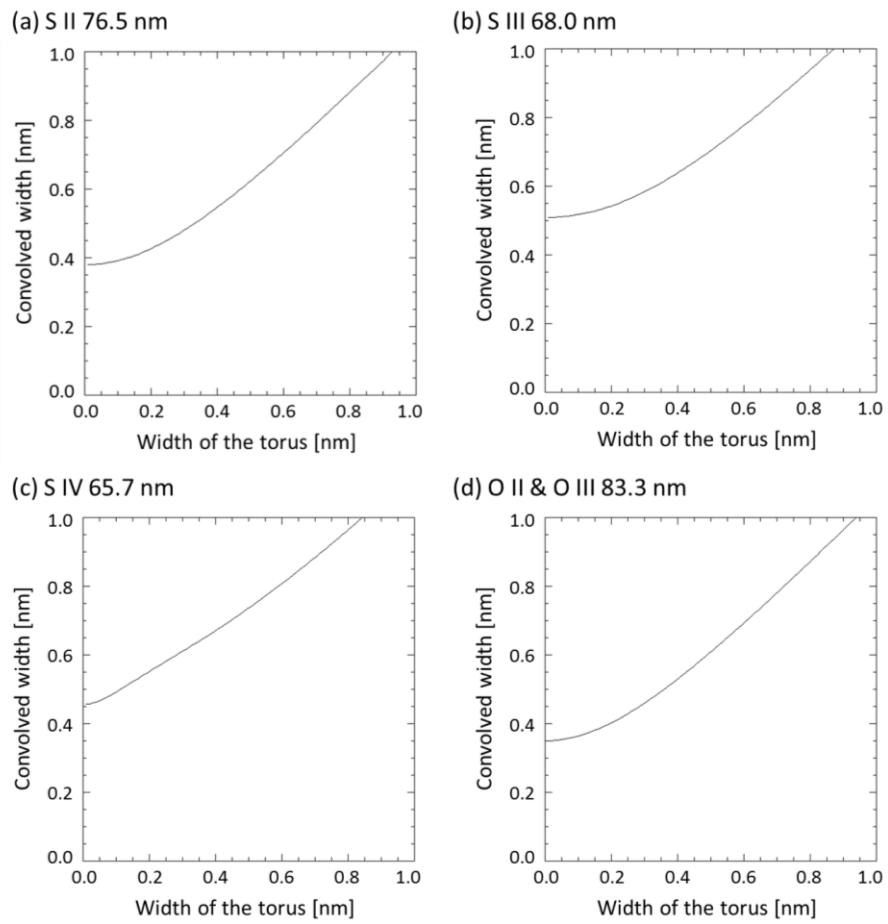


Figure C.2. Relationship between torus width and convolved width in the case of (a) S II 76.5 nm, (b) S III 68.0 nm, (c) S IV 65.7 nm, and (d) O II & O III 83.3 nm calculated by CHIANTI atomic database ver. 8.0.7.

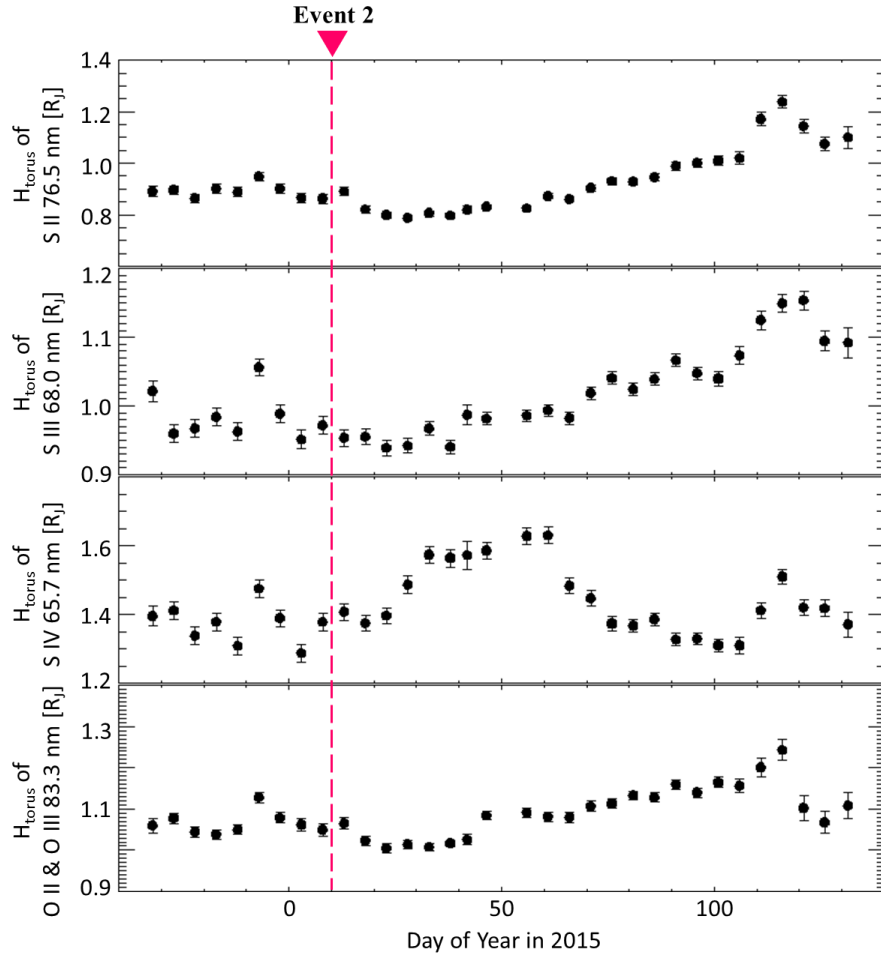


Figure C.3. Temporal variation in Gaussian width of torus emission of S II 76.5 nm, S III 68.0 nm, S IV 65.7 nm, and O II & O III 83.3 nm from DOY -32 to DOY 132 in 2015.

C2. Conversion factor to brightness

The conversion factor from light intensity to brightness, β in Equation (2.4), is obtained, as shown in Figure C.4. These values reflect the width of torus emission and distance from Jupiter to Earth, which is shown in Figure C.5.

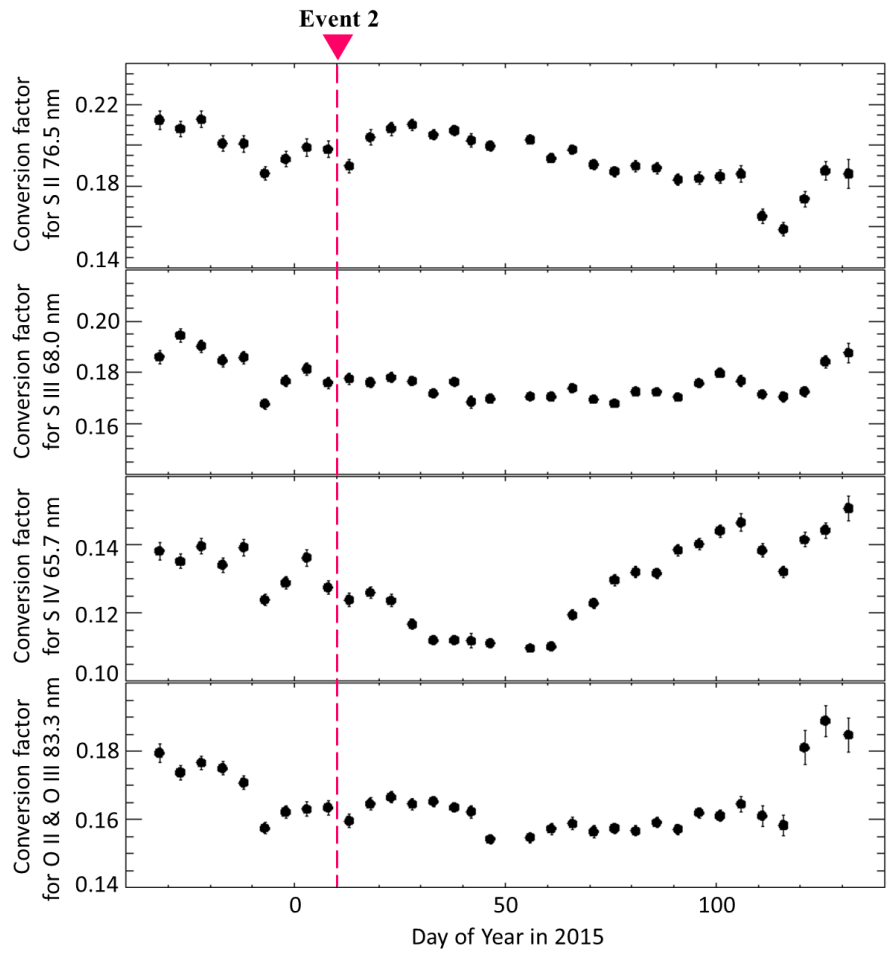


Figure C.4. Temporal variation in conversion factor for S II 76.5 nm, S III 68.0 nm, S IV 65.7 nm, and O II & O III 83.3 nm from DOY -32 to DOY 132 in 2015.

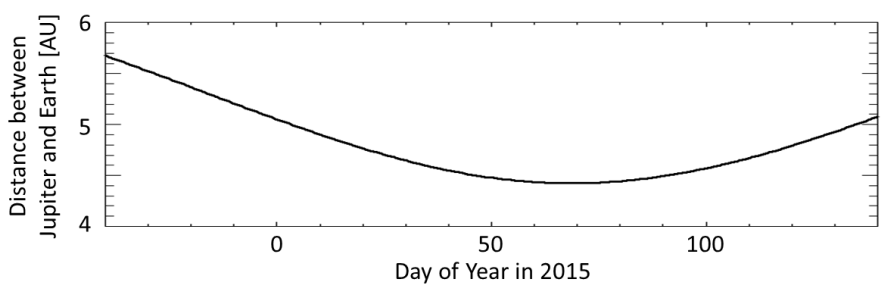


Figure C.5. Temporal variation in distance between Jupiter and Earth.

D. Verifying the validity of assumptions

In this chapter, the validity of the assumptions made in Subsubsection 2.2.2.3 will be verified.

D1. Verification of solution dependence on the hot electron temperature and the mixing ratios of proton and doubly ionized oxygen

In this section, let me focus on the results from DOY -32 to DOY 132 in 2015, when the response of the IPT to the volcanic activation was comprehensively observed.

I used assumptions in estimating plasma densities and temperature; (1) $[H^+]/[e^-] = 0.1$, (2) $[O^{2+}]/[O^+] = 0.1$, and (3) T_h (hot electron temperature) = 200 eV. The effect on parameter derivation of changing assumptions, as shown in Table D.1, was examined for 6.1 R_J , as shown in Figure D.1. The temporal variations in parameters in the IPT with the assumptions of No.1–No.9, No.10–No.18, No.19–No.27, and No.28–No.36, which correspond to the cases with the hot electron temperature of 50 eV, 100 eV, 200 eV, and 1000 eV, respectively, are shown in Figures D.2–D.5. The temporal variations with the assumptions of No.37–No.45, which corresponds to the case that there is a radial gradient of the hot electron temperature, are shown in Figure D.6. The radial distribution of the hot electron temperature was assumed by the linear fitting to the temperatures obtained by the Voyager spacecraft, which are 100 eV at 5.9 R_J and 400 eV at 8.0 R_J (Bagenal, 1994). Though the derived parameters vary slightly, it was found that the conclusion that the hot electron fraction increased only on the dusk side was significant. As shown in Figures D.7–D.12, I also evaluated the effect on the mass density and its radial gradient, which were shown in Section 4.2. Though the absolute values vary depending on the assumptions, it was revealed that a noticeable temporal change in the mass density gradient ~30 days after the volcanic activation was significant regardless of the assumption.

Table D.1. List of assumption set.

The assumption set of No.23 is used in the analysis method shown in Chapter 2.

	$[H^+]/[e^-]$	$[O^{2+}]/[O^+]$	Hot electron temperature (T_h)
No. 1	0.01	0.01	50 eV
No. 2	0.01	0.10	50 eV
No. 3	0.01	0.30	50 eV
No. 4	0.10	0.01	50 eV
No. 5	0.10	0.10	50 eV
No. 6	0.10	0.30	50 eV
No. 7	0.30	0.01	50 eV
No. 8	0.30	0.10	50 eV
No. 9	0.30	0.30	50 eV

No. 10	0.01	0.01	100 eV
No. 11	0.01	0.10	100 eV
No. 12	0.01	0.30	100 eV
No. 13	0.10	0.01	100 eV
No. 14	0.10	0.10	100 eV
No. 15	0.10	0.30	100 eV
No. 16	0.30	0.01	100 eV
No. 17	0.30	0.10	100 eV
No. 18	0.30	0.30	100 eV
No. 19	0.01	0.01	200 eV
No. 20	0.01	0.10	200 eV
No. 21	0.01	0.30	200 eV
No. 22	0.10	0.01	200 eV
No. 23	0.10	0.10	200 eV
No. 24	0.10	0.30	200 eV
No. 25	0.30	0.01	200 eV
No. 26	0.30	0.10	200 eV
No. 27	0.30	0.30	200 eV
No. 28	0.01	0.01	1000 eV
No. 29	0.01	0.10	1000 eV
No. 30	0.01	0.30	1000 eV
No. 31	0.10	0.01	1000 eV
No. 32	0.10	0.10	1000 eV
No. 33	0.10	0.30	1000 eV
No. 34	0.30	0.01	1000 eV
No. 35	0.30	0.10	1000 eV
No. 36	0.30	0.30	1000 eV
No. 37	0.01	0.01	With radial gradient
No. 38	0.01	0.10	With radial gradient
No. 39	0.01	0.30	With radial gradient
No. 40	0.10	0.01	With radial gradient
No. 41	0.10	0.10	With radial gradient
No. 42	0.10	0.30	With radial gradient
No. 43	0.30	0.01	With radial gradient
No. 44	0.30	0.10	With radial gradient
No. 45	0.30	0.30	With radial gradient

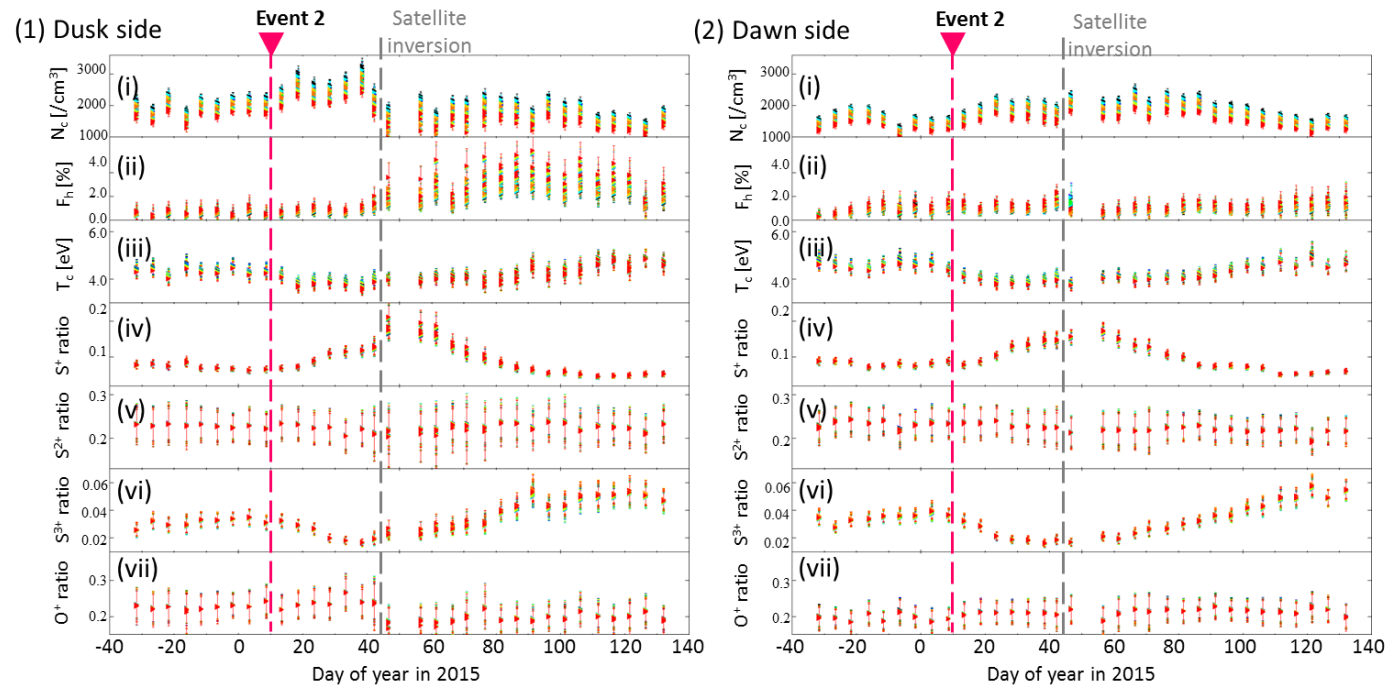
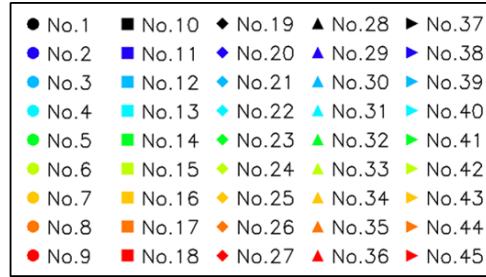


Figure D.1. Dependence of derived parameters at 6.1 R_J on assumptions. Same as Figure 3.8, except for the seven assumptions color-coded according to the legend and listed in Table D.1.

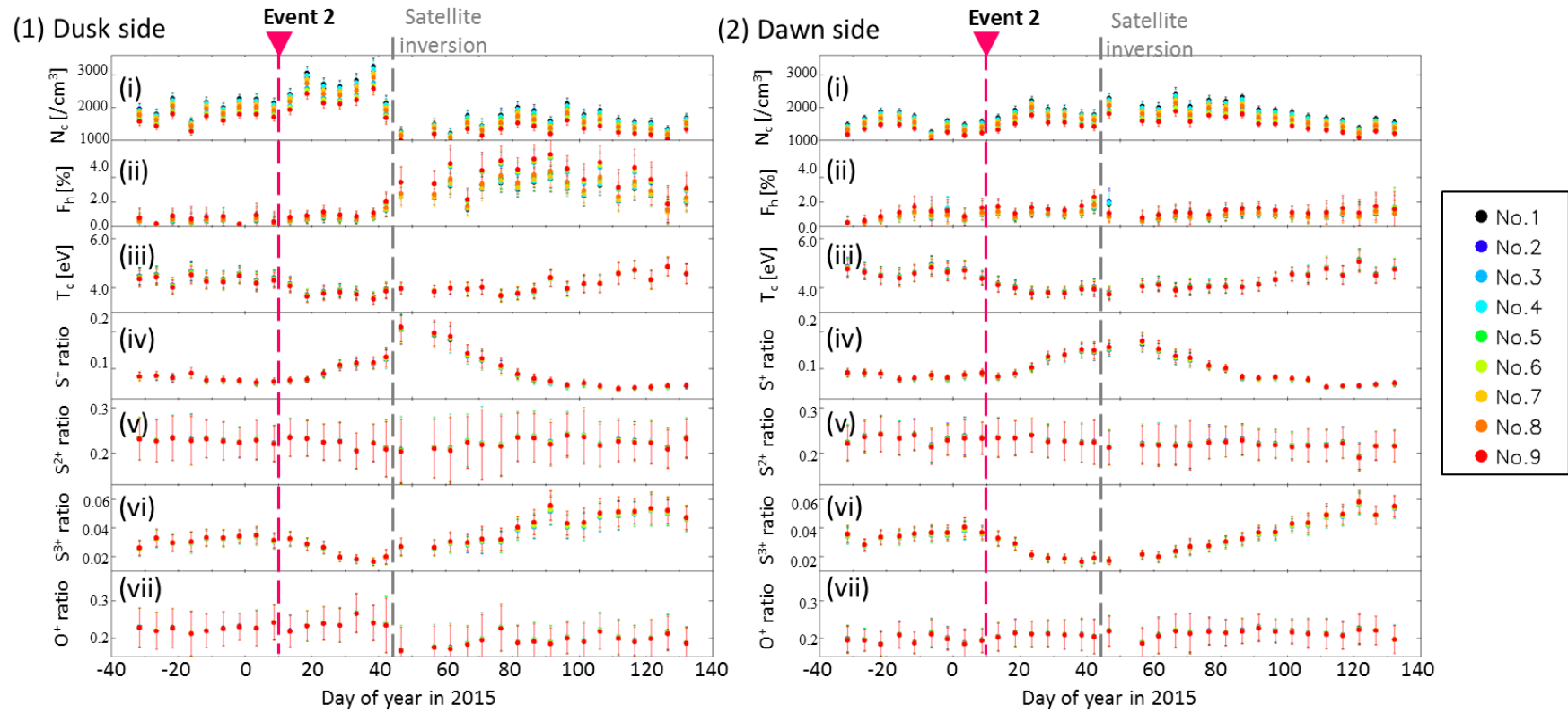


Figure D.2. Same as Figure D.1, except for assumptions color-coded according to the legend ($T_h = 50$ eV).

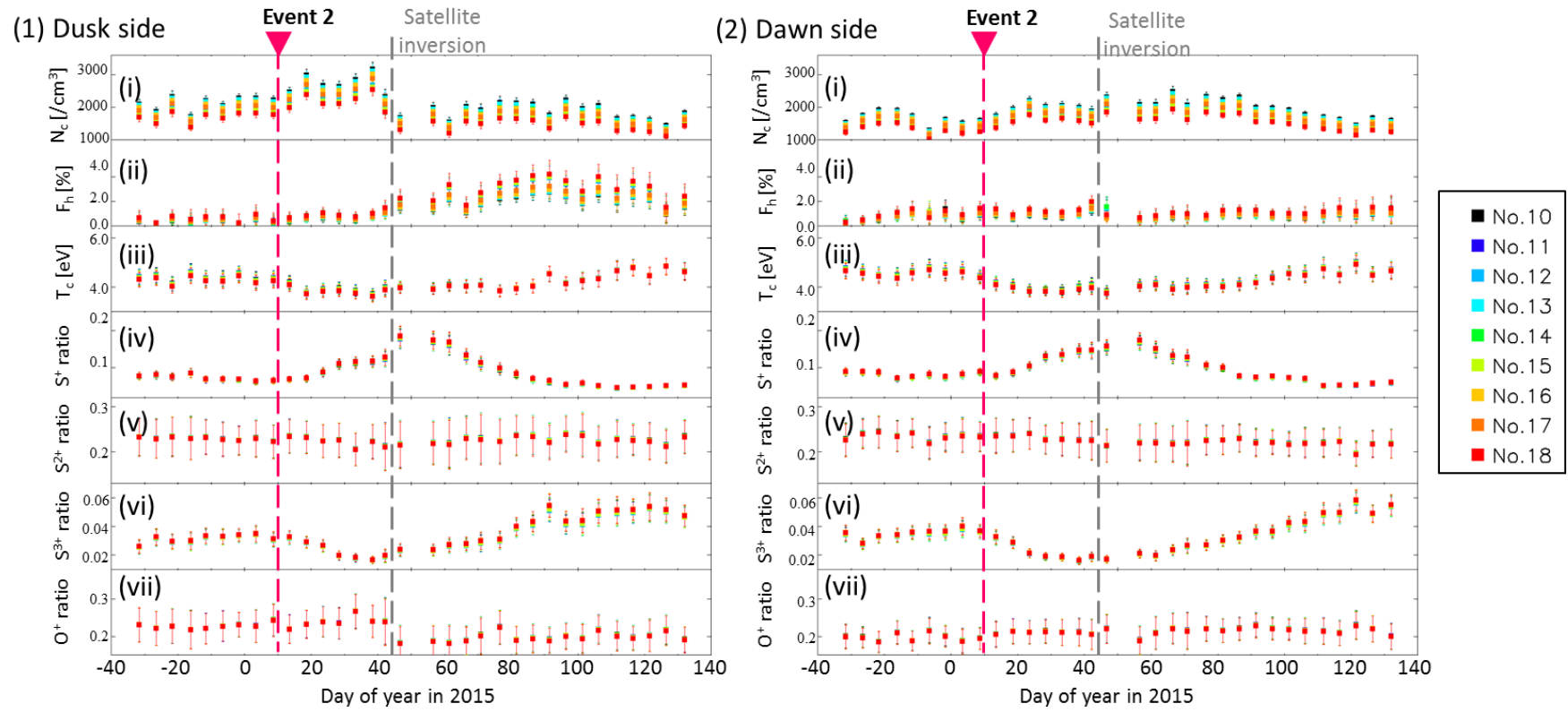


Figure D.3. Same as Figure D.1, except for assumptions color-coded according to the legend ($T_h = 100$ eV).

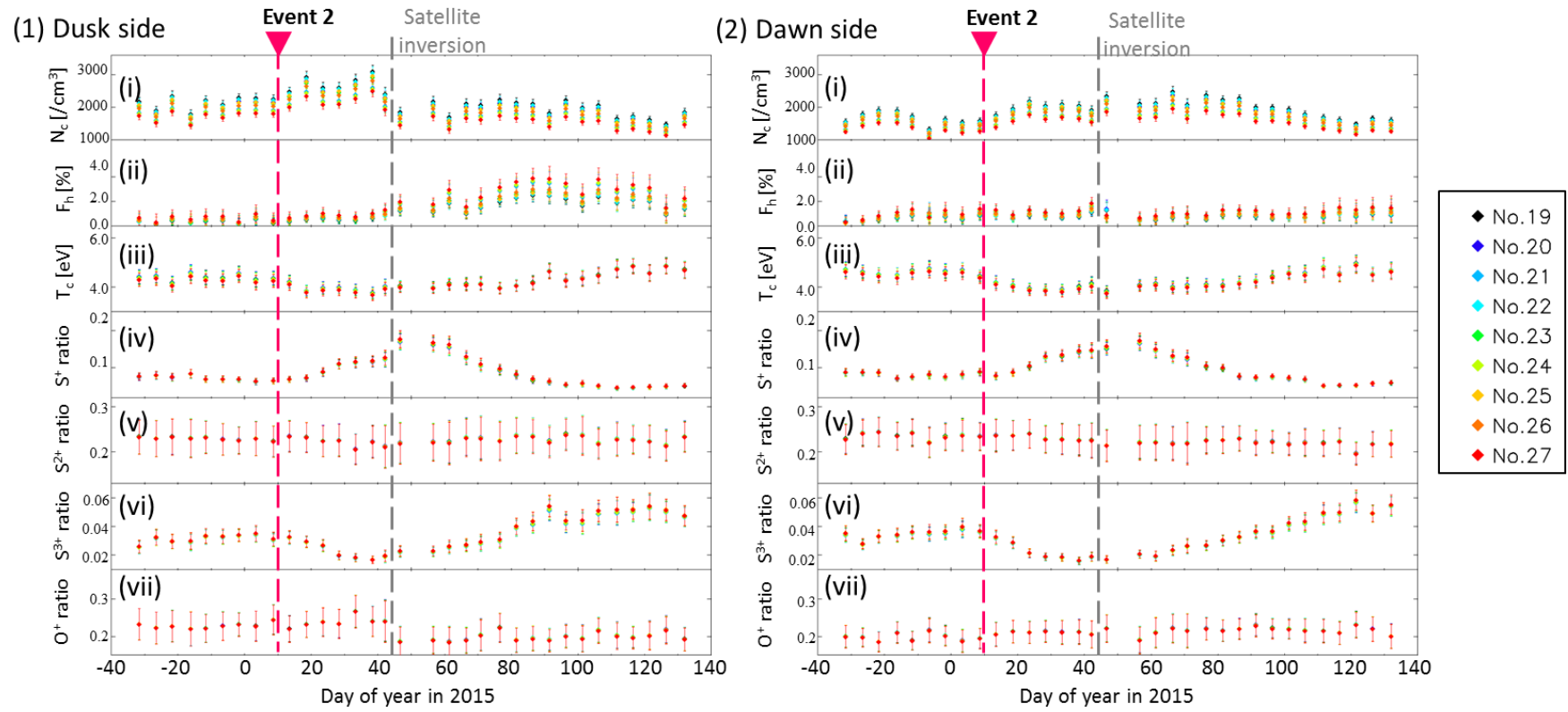


Figure D.4. Same as Figure D.1, except for assumptions color-coded according to the legend ($T_h = 200$ eV).

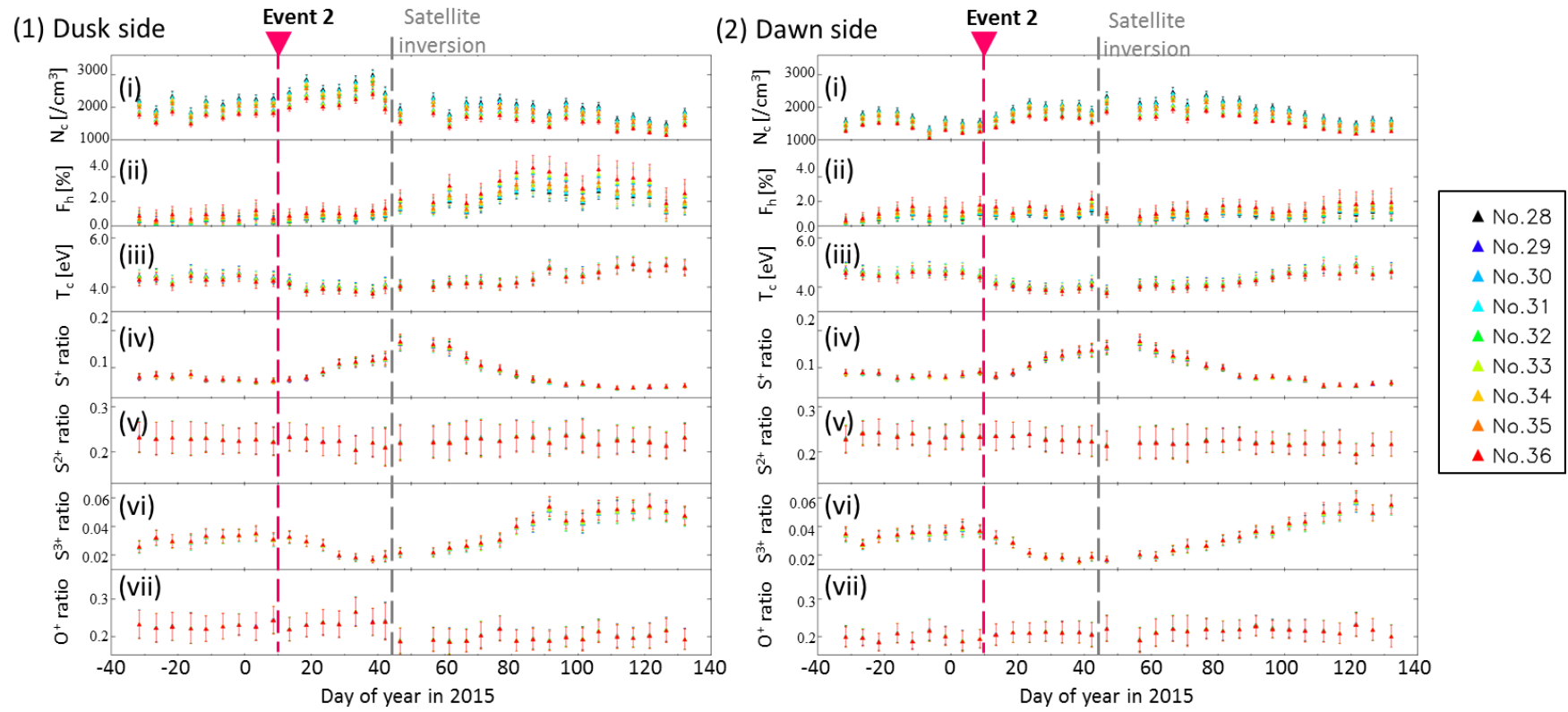


Figure D.5. Same as Figure D.1, except for assumptions color-coded according to the legend ($T_h = 1000$ eV).

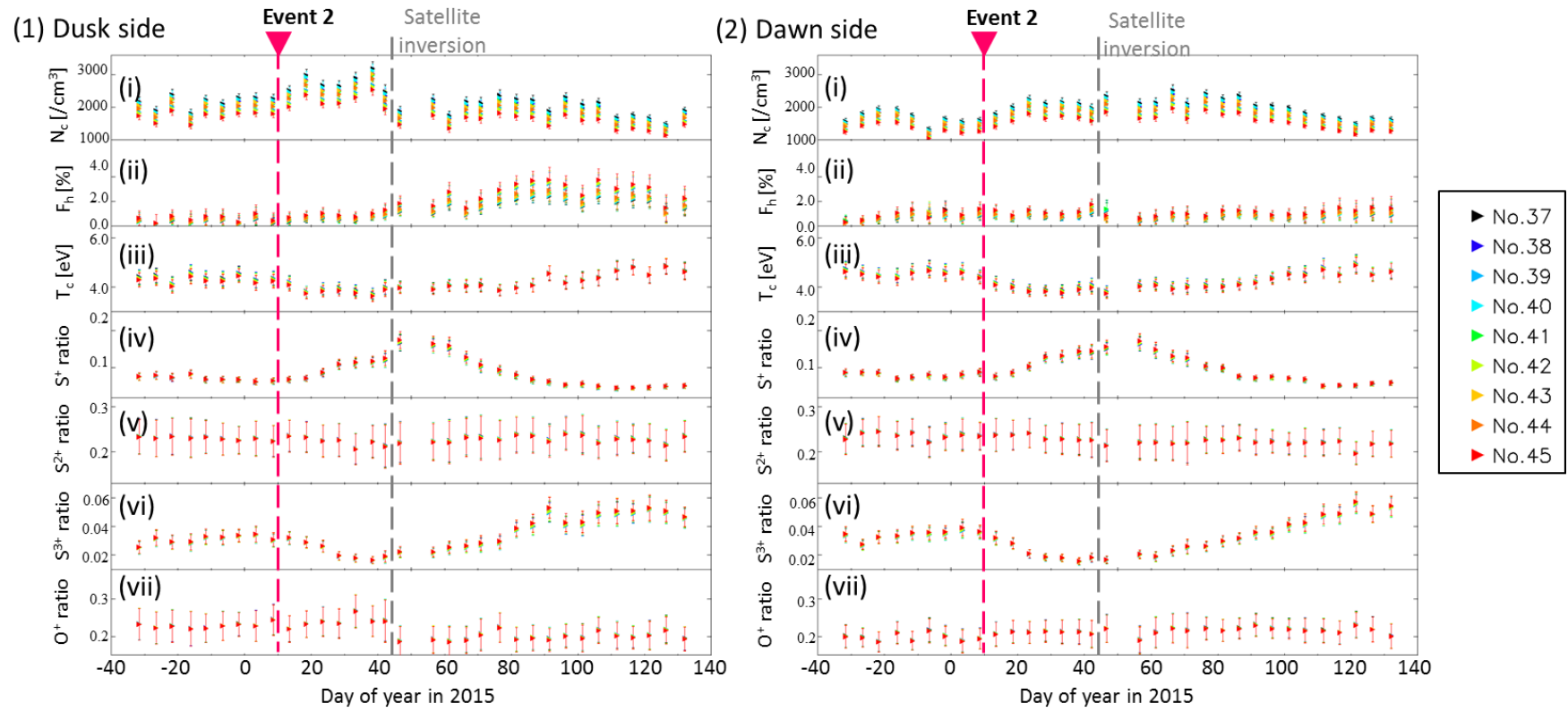


Figure D.6. Same as Figure D.1, except for assumptions color-coded according to the legend (with the radial gradient of T_h).

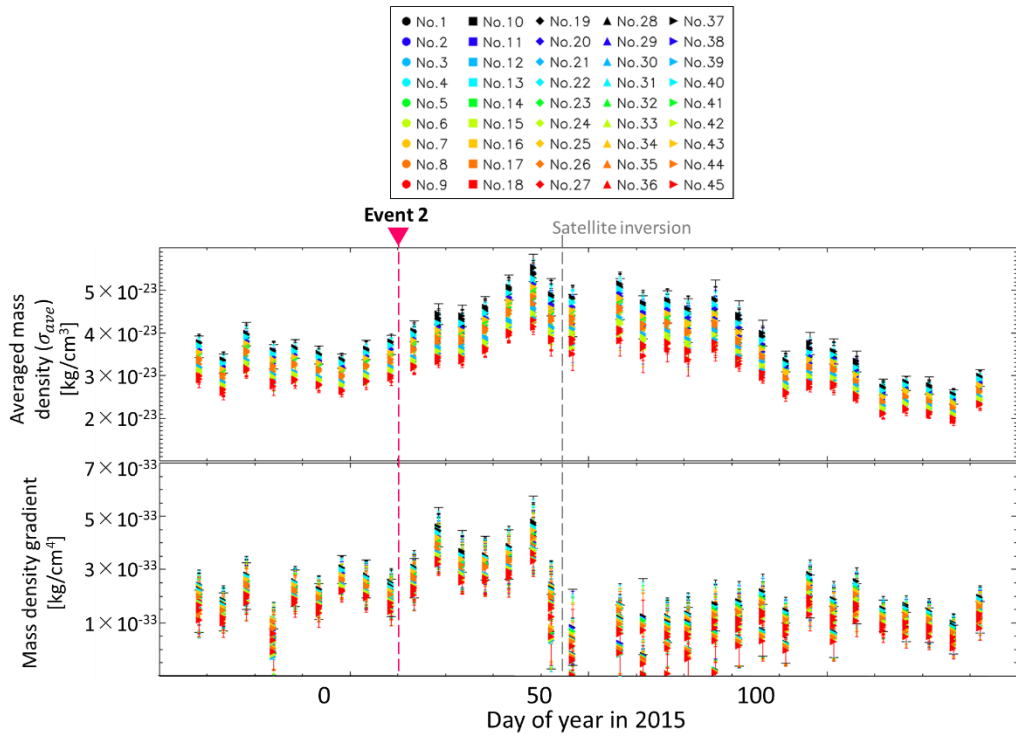


Figure D.7. Dependence of the averaged mass density and radial gradient for the dusk side on assumptions. Same as Figure 4.3, except for the assumptions color-coded according to the legend and listed in Table D.1.

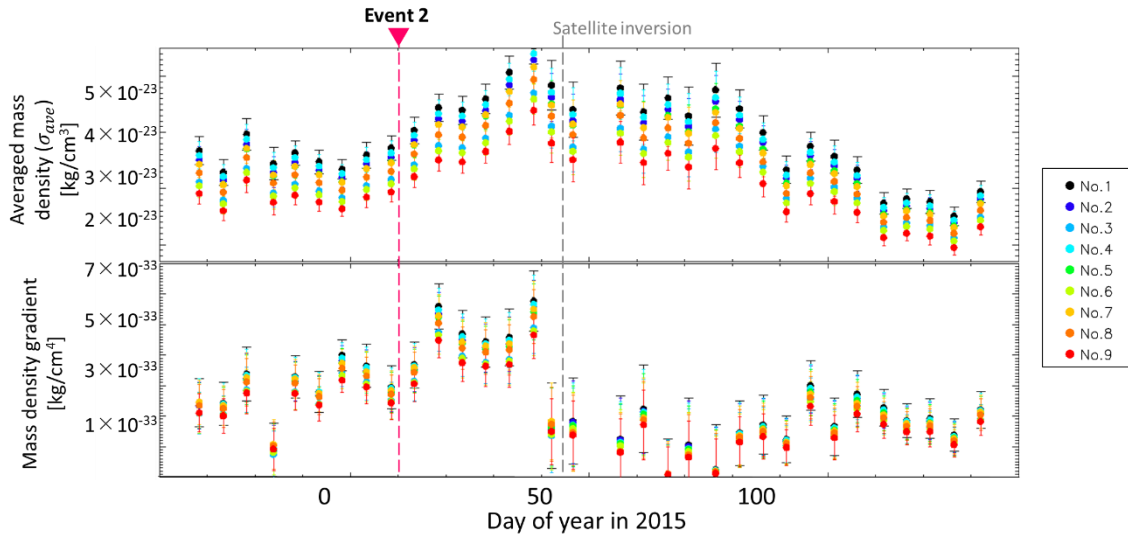


Figure D.8. Same as Figure D.7, except for assumptions color-coded according to the legend ($T_h=50$ eV).

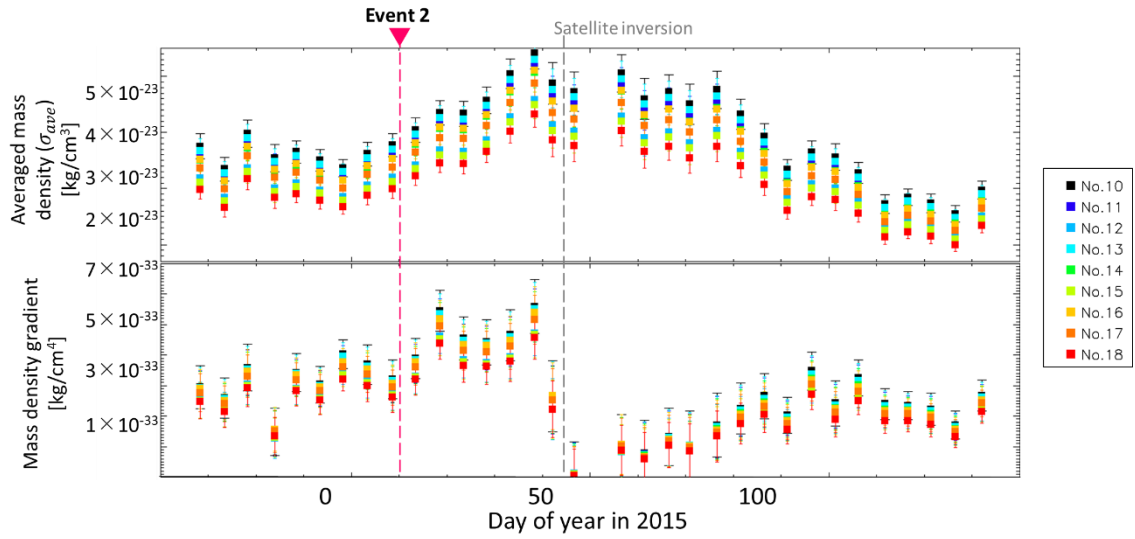


Figure D.9. Same as Figure D.7, except for assumptions color-coded according to the legend ($T_h=100$ eV).

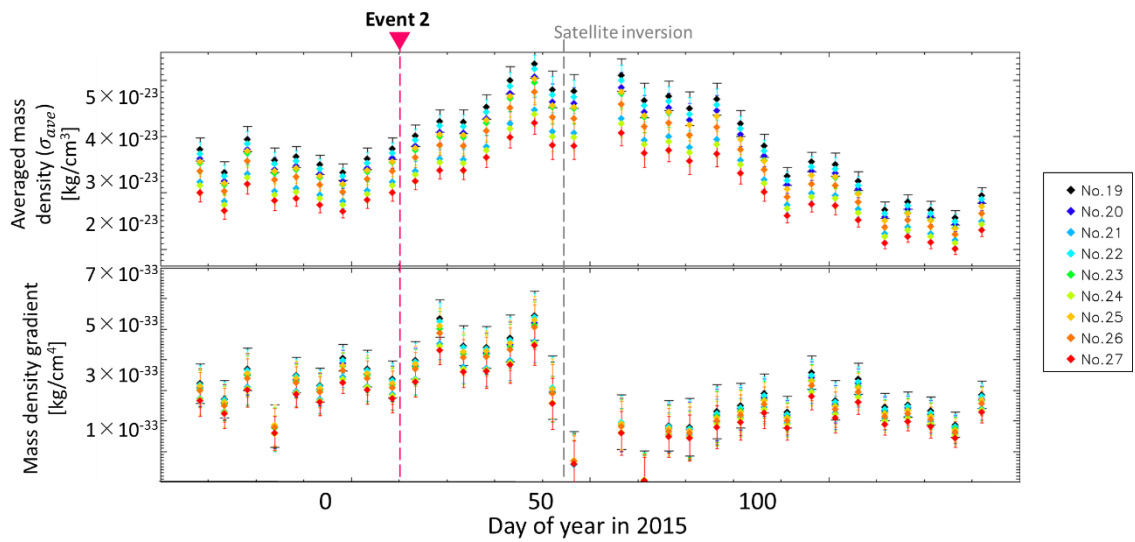


Figure D.10. Same as Figure D.7, except for assumptions color-coded according to the legend ($T_h=200$ eV).

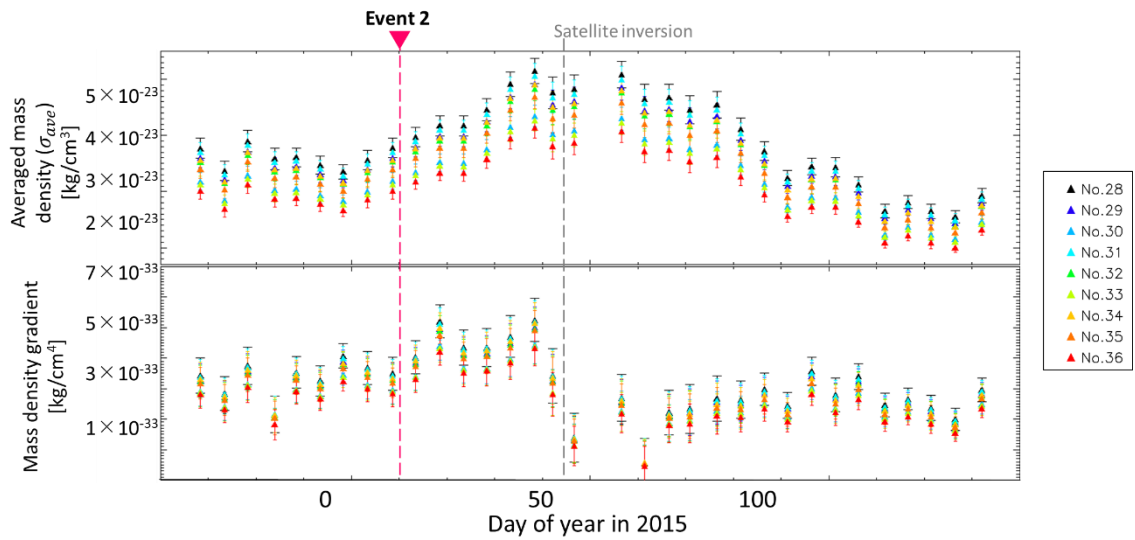


Figure D.11. Same as Figure D.7, except for assumptions color-coded according to the legend ($T_h=1000$ eV).

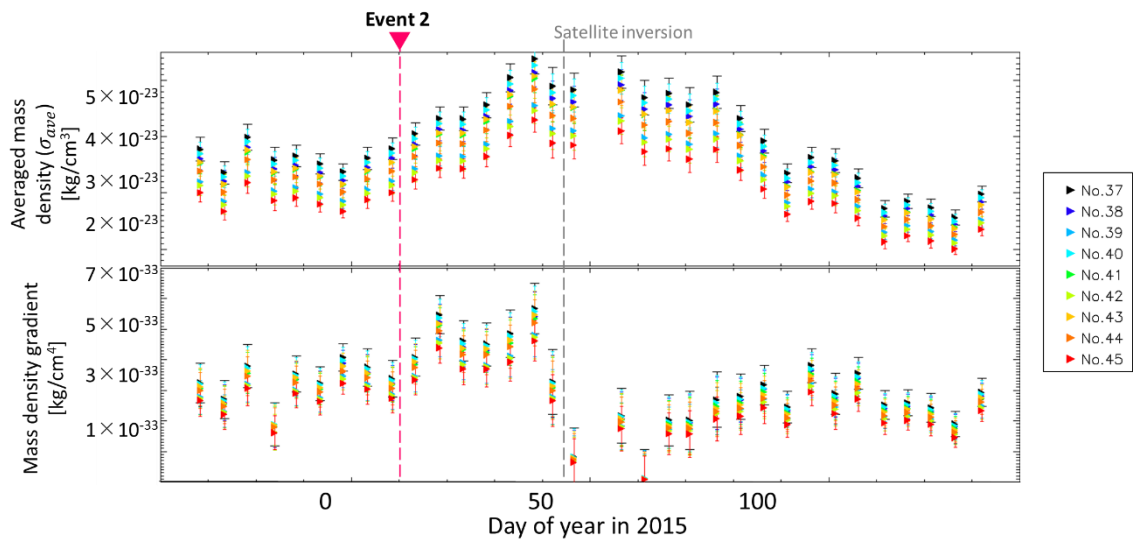


Figure D.12. Same as Figure D.7, except for assumptions color-coded according to the legend (with the radial gradient of T_h).

D2. Verification of the validity of the assumption of the mixing ratio of singly ionized oxygen in the third season

As described in 3.1.2.3, in this research, the ratio of $[O^+]$ to $[S^{2+}]$ was fixed to 1 in the analysis of the third season. This section will try to verify the validity of the assumption.

Figure D.13 shows the temporal variation in $[O^+]/[S^{2+}]$ in the first and second seasons. The largest volcanic activity occurred during the second season, but the $[O^+]/[S^{2+}]$ value did not fluctuate remarkably and was ~ 1 . Therefore, it is expected that it is also ~ 1 in the third season and the assumption used in this research is valid. It is one of the future works to re-analyze data in the third season screening out with the satellite local time to eliminate the geocoronal contamination in the same way as the analysis for the first and second seasons.

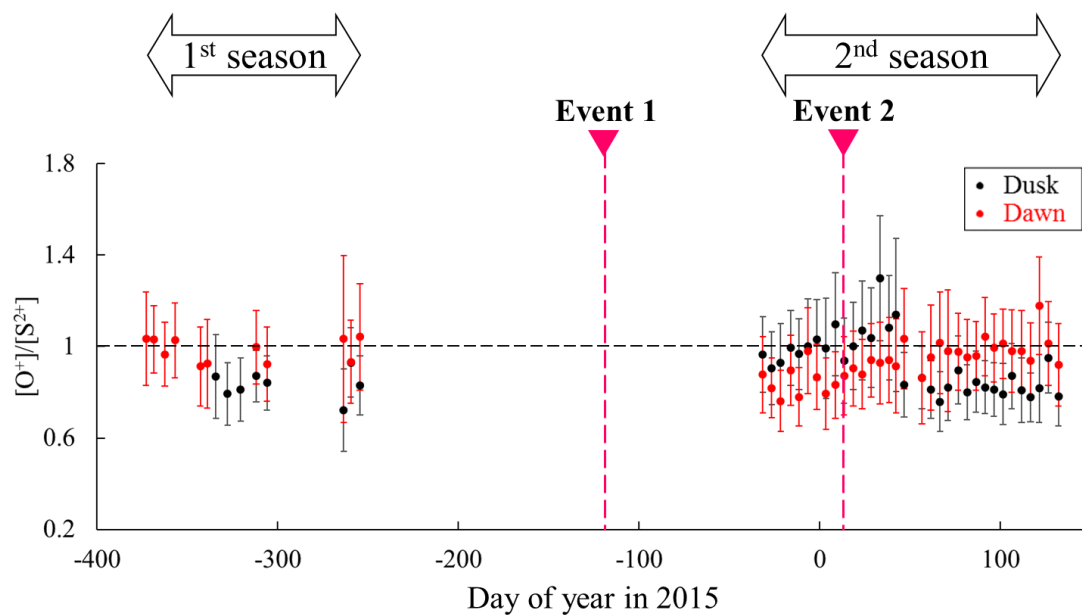


Figure D.13. Temporal variation in the ratio of $[O^+]$ to $[S^{2+}]$ obtained by plasma diagnosis in the first and second seasons.

E. Parameter determination uncertainties

In this section, let me focus on the results from DOY -32 to DOY 132 in 2015, when the response of the IPT to the volcanic activation was comprehensively observed.

E1. Comparison of line intensities and results of plasma diagnosis

The temporal variation in line intensities is shown in Figure E.1. The black and red bars represent observed and fitted intensities, respectively. Readers should note that they do not represent the shape of the spectrum but just line intensities. The line intensities on DOY 3, DOY 38, and DOY 91, which are indicated by orange-dotted lines in Figure 3.3, are shown. On DOY 38, when the plasma density reaches a maximum value, all of S II and S III lines without the wavelength dependence are brighter than those in the quiet period such as DOY 3. This fact is consistent with the dependence of volume emissivities on the electron density shown in Figure 2.5(a). It should be noted that, on the dusk side, the line intensities in the short wavelength range are significantly higher on DOY 91, when the hot electron fraction reaches the maximum value, than those in the other periods. This tendency is not confirmed on the dawn side. These facts are consistent with the dependence of emissivity on the hot electron fraction shown in Figure 2.5(c) and trend captured by the plasma diagnosis; the hot electron fraction increases on the dusk side.

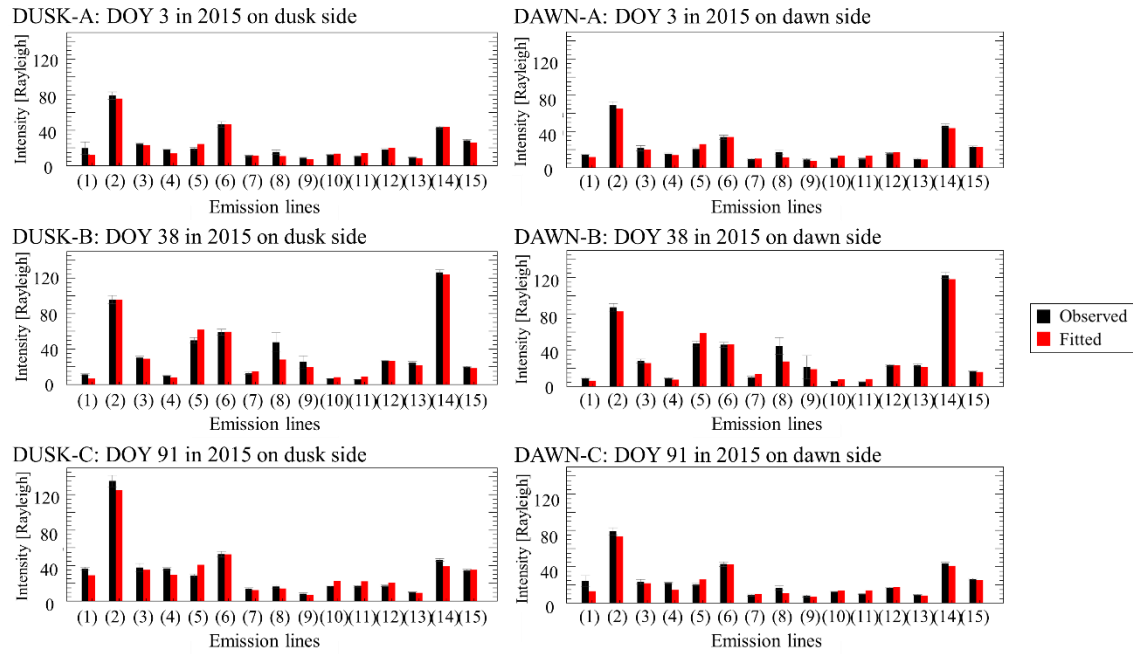


Figure E.1. Temporal variation in line intensities at $6.1 R_J$. The black and red bars represent observed and fitted intensities, respectively. The 15 numbered emission lines are listed in Table 3.2. Error bars show values estimated by sensitivity error and Poisson statistics of counts. (DUSK-A) Line intensities on the dusk side on DOY 3 in 2015: volcanic activity was relatively quiet. (DUSK-B) Line intensities on the dusk side on DOY38 in 2015: core electron density reached a maximum. (DUSK-C) Line intensities on the dusk side on DOY 91 in 2015: hot electron fraction reached a maximum. (DAWN-A) The same as (DUSK-A) on the dawn side. (DAWN-B) The same as (DUSK-B) on the dawn side. (DAWN-C) The same as (DUSK-C) on the dawn side.

E2. Dependences of confidence intervals and chi-square values on electron parameters

The 68.3%, 95.4%, and 99.7% confidence intervals, corresponding to one, two, and three sigma/sigmata, with two kinds of parameters set to be free are shown in Figure E.2. On the dusk side, it can be said that the hot electron column density on DOY 3 and DOY 38 and that on DOY 91, whose three-sigma levels do not overlap, are significantly different. The same applies to the core electron column density on DOY 3 and DOY 91 and that on DOY 38 on both sides, whose one sigma levels do not overlap. Also, the one sigma levels of the core electron column-averaged temperature on DOY 3 and DOY 91 and that on DOY 38 do not overlap on both sides. Therefore, it is reasonable to conclude that these modulations of electron parameters are significant. As can be seen in Figure E.2(2), in contrast to the dusk side, the hot electron column density at dawn side on DOY 3 and that on DOY 91 fall within the one sigma level, though the one sigma levels of that on DOY 38 and DOY 91 do not overlap. These facts indicate that the increase in the hot electron fraction at dawn is not as definite as that at dusk.

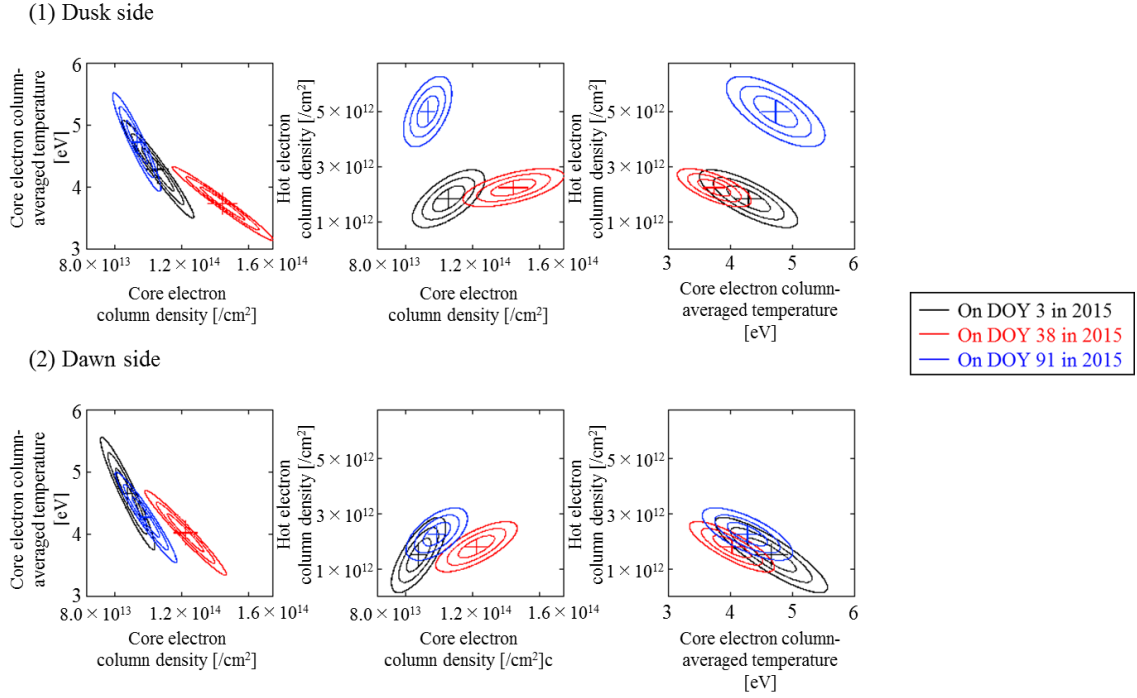
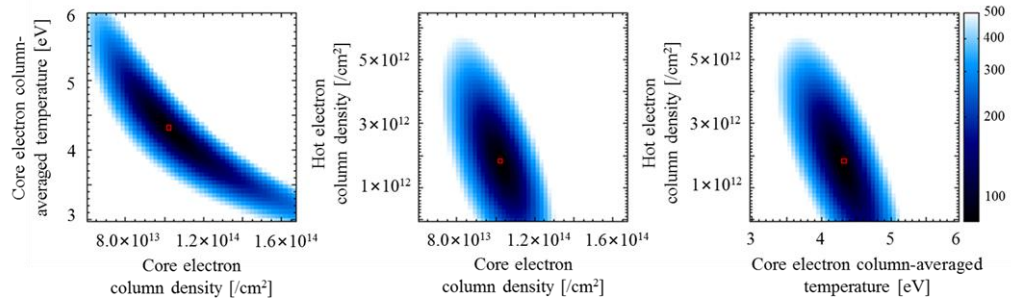


Figure E.2. Two-dimensional confidential interval maps at $6.1 R_J$ on (1) dusk side and (2) dawn side. The areas in contour lines give 68.3%, 95.4%, and 99.7% confidence levels (corresponding to one, two, and three sigmas). The black, red, and blue lines indicate contour lines on DOY 3, DOY 38, and DOY 91 in 2015, respectively. The intersection points of lines represent the best fit values. The length of lines indicates one-sigma confidence levels with other parameters fixed to the best-fitted parameters, shown as error bars in Figure 3.3.

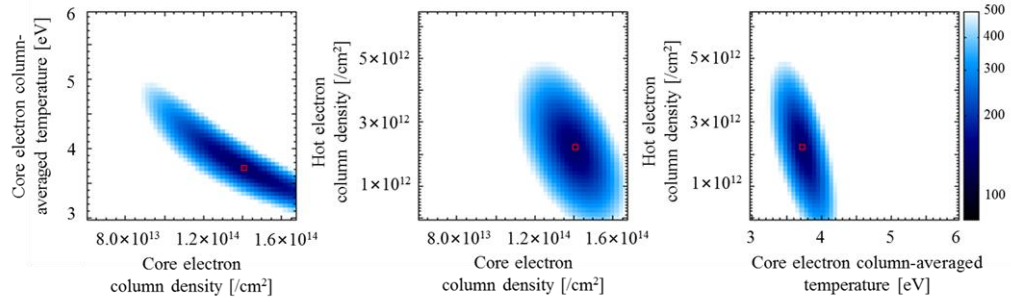
The parameter dependence of the chi-square value for the dusk and dawn sides are shown in Figures E.3 and E.4, respectively. When each parameter takes a value within the typical range in the IPT, shown in Figures E.3 and E.4, it can be said that the minimum value of the chi-square can be uniquely determined. As for the panel in the first and third columns, the shape of the distribution of chi-square values is almost the same as the shape of the contour lines in Figure E.2. However, the shape differs a lot as for the panel in the middle columns. This may be because the behavior is somewhat unstable when the parameters of the core electron density and hot electron density are moved.

The resolution of calculation was $2.1 \times 10^{12} \text{ cm}^{-3}$ for the core electron column density, 0.06 eV for the core electron temperature, and $1.3 \times 10^{11} \text{ cm}^{-3}$ for the hot electron column density.

DUSK-A: DOY 3 in 2015 on dusk side



DUSK-B: DOY 38 in 2015 on dusk side



DUSK-C: DOY 91 in 2015 on dusk side

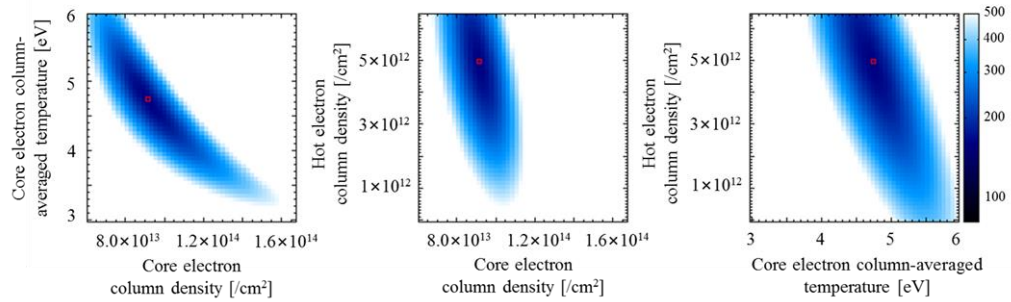
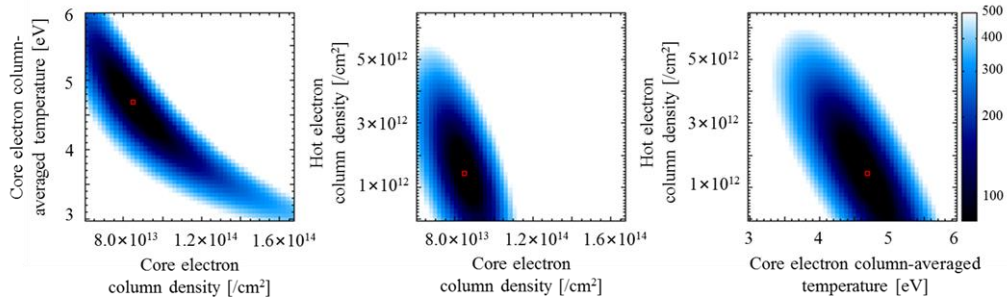
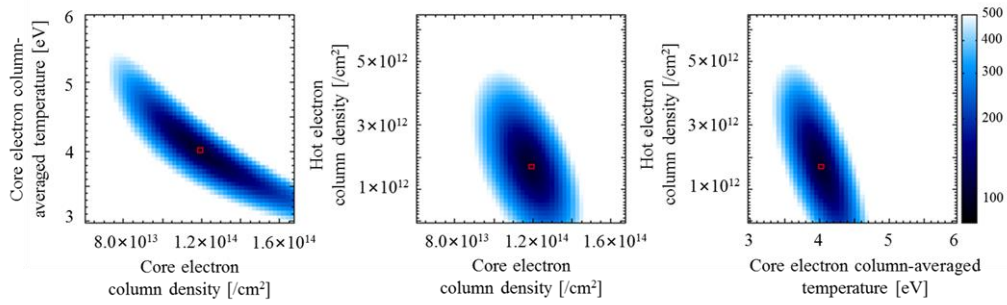


Figure E.3. Two-dimensional chi-parameter maps at 6.1 R_J on the dusk side. The red frame represents the best fit.

DAWN-A: DOY 3 in 2015 on dawn side



DAWN-B: DOY 38 in 2015 on dawn side



DAWN-C: DOY 91 in 2015 on dawn side

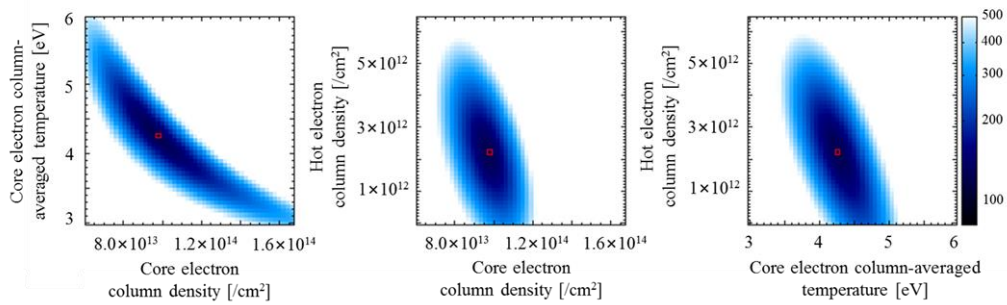


Figure E.4. Same as Figure E.3, except for the dawn side.

E3. Verification of solution plausibility in a multidimensional space

To consider whether the minimum value of the chi-square value is detected, the fitting with parameters outside the range of $\pm 3\sigma$ from the best-fitted parameters in a multidimensional space was conducted as shown in Figure E.5. All the parameters fitted outside the range of $\pm 3\sigma$, which is shown in red, is close to the best-fitted parameters: the values are just outside the $\pm 3\sigma$ range. From this, it is highly probable that not local minima of the chi-square value, but actual minima are detected.

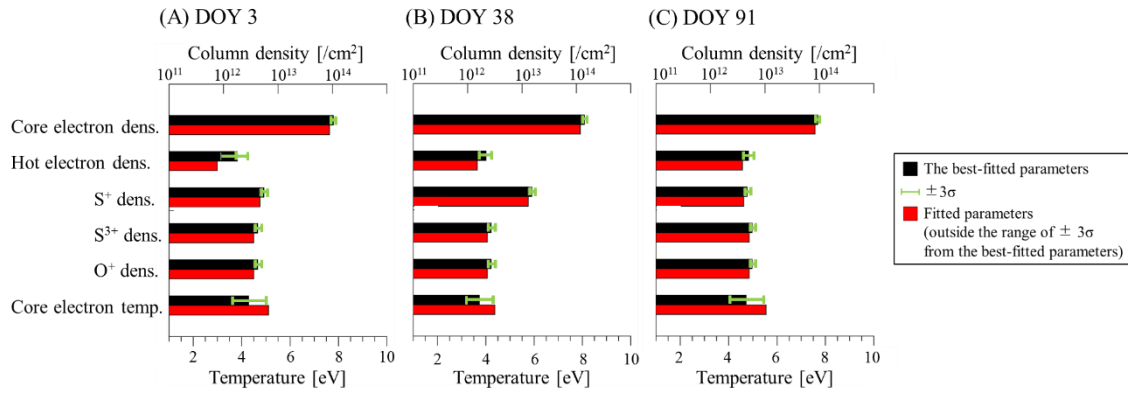


Figure E.5. Best-fitted parameters (shown in black) and parameters fitted outside the range of $\pm 3\sigma$ from the best-fitted parameters (shown in red). Results on the dusk side at a distance of $6.1 R_J$ from Jupiter on (A) DOY 3 in 2015, (B) on DOY 38, and (C) on DOY 91 are shown.

F. Shift of streamlines due to dawn-to-dusk electric field

Here, a supplementary explanation regarding the possible process of the shift of plasma streamlines due to the dawn-to-dusk electric field produced by the magnetotail flow will be given (Thomas et al. 2004). Note that the strength of the dawn-to-dusk electric field is $\sim 1/100$ compared to that of the corotation electric field in the inner magnetosphere. Since the dawn-to-dusk electric field weakens the corotation electric field on the dawn side and strengthens it on the dusk side, the corotating plasmas are decelerated on the dawn side and accelerated on the dusk side. Then, with the conservation of angular momentum, the plasma streamlines shift to the dawn side. The observation of images of the S^+ torus at 673.1 nm by Schneider and Trauger (1995) have shown that the emission region of the IPT is shifted actually to the dawn side by $\sim 0.2\text{--}0.3 R_J$ (Figure F.1).

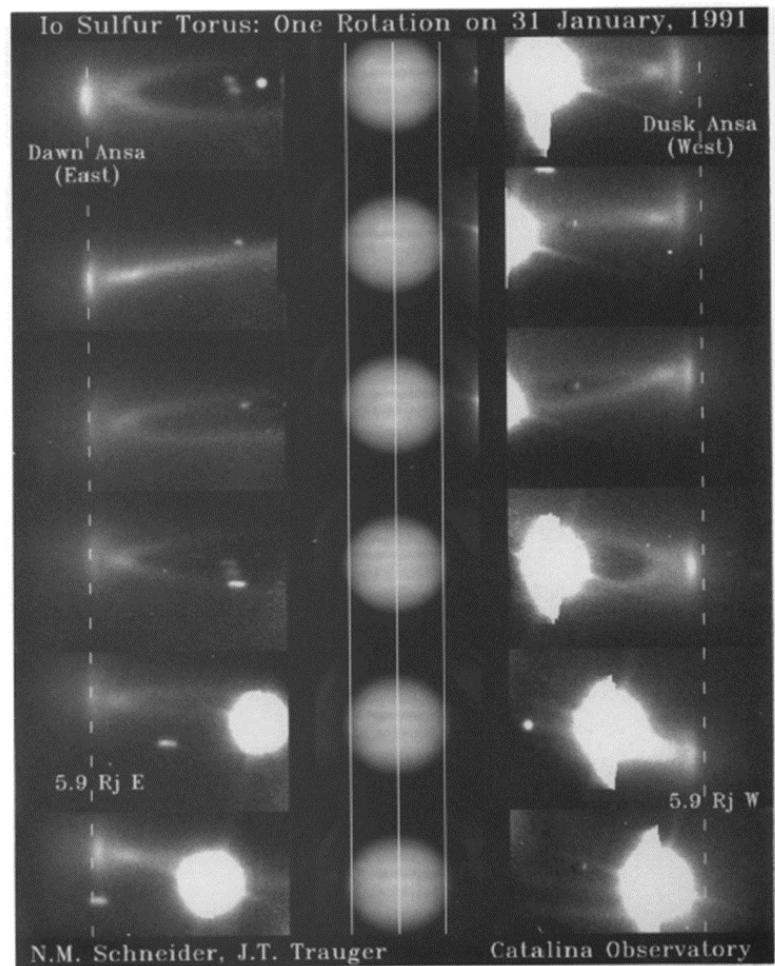


Figure F.1. Images of the S^+ torus on Jan. 31, 1991 in ~ 8 hours at 673.1 nm (Schneider and Trauger, 1995). Images of Galilean Satellites are saturated. Dashed lines show the position of Io's orbit ($5.91 R_J$).

References

- Acuna, M. H., K. W. Behannon, and J. E. P. Connerney (1983). Jupiter's magnetic field and magnetosphere, in *Physics of the Jovian magnetosphere*, edited by A. J. Dessler, pp. 2, Cambridge Univ. Press, Cambridge.
- Anderson J. D. and Schubert G. (2007). Saturn's Gravitational Field, Internal Rotation, and Interior Structure. *Science*: 317, 5843, 1384–1387.
- Arridge, C.S., André, N., McAndrews, H.J. et al. (2011). Mapping Magnetospheric Equatorial Regions at Saturn from Cassini Prime Mission Observations. *Space Sci. Rev.*, 164: 1. <https://doi.org/10.1007/s11214-011-9850-4>
- Azari, A. R., Liemohn, M. W., Jia, X., Thomsen, M. F., Mitchell, D. G., Sergis, N., et al. (2018). Interchange injections at Saturn: Statistical survey of energetic H⁺ sudden flux intensifications. *Journal of Geophysical Research: Space Physics*, 123, 4692–4711. <https://doi.org/10.1029/2018JA025391>
- Azari, A. R., X. Jia, M. W. Liemohn, G. B. Hospodarsky, G. Provan, S. -Y. Ye, S. W. H. Cowley, C. Paranicas, N. Sergis, A. M. Rymer, M. F. Thomsen, and D. G. Mitchell (2019). Are Saturn's Interchange Injections Organized by Rotational Longitude? *Journal of Geophysical Research: Space Physics*. <https://doi.org/10.1029/2018JA026196>
- Badman SV, Bonfond B, Fujimoto M, Gray RL, Kasaba Y, Kasahara S, Kimura T, Melin H, Nichols JD, Steffl AJ, Tao C, Tsuchiya F, Yamazaki A, Yoneda M, Yoshikawa I, Yoshioka K (2016) Weakening of Jupiter's main auroral emission during January 2014. *Geophys Res Lett* 43:988–997. doi:10.1002/2015GL067366
- Bagenal, F. (1994). Empirical model of the Io plasma torus: Voyager measurements. *Journal of Geophysical Research*, 99(A6), 11,043–11,062. doi:10.1029/93JA02908
- Bagenal, F., & P. A. Delamere (2011), Flow of mass and energy in the magnetospheres of Jupiter and Saturn, *Journal of Geophysical Research*, 116, A05209, doi:10.1029/2010JA016294.
- Barbosa, D. D., & Kivelson, M. G. (1983). Dawn-dusk electric field asymmetry of the Io plasma torus. *Geophysical Research Letters*, 10, 210-213. doi:10.1029/GL010i003p00210
- Book, D. L., (1990). *NRL Plasma Formulary*, Naval Res. Lab., Washington, D. C.

Broadfoot, A. L., Belton, M. J., Takacs, P. Z., Sandel, B. R., Shemansky, D. E., Holberg, J. B., Ajello, J. M., Moos, H. W., Atreya, S. K., Donahue, T. M., Bertaux, J. L., Blamont, J. E., Strobel, D. F., McConnell, J. C., Goody, R., Dalgarno, A., and McElroy, M. B. (1979). Extreme ultraviolet observations from Voyager 1 encounter with Jupiter. *Science*, 204: 979–982. doi: 1126/science.204.4396.979

Brown, R. A. (1976). A model of Jupiter's sulfur nebula. *The Astrophysical Journal*, 206:L179–L183.

Brown, M. E., and Bouchez, A. H. (1997). The response of Jupiter's magnetosphere to an outburst on Io. *Science*, 278, 268–271.

Clarke, J. T., et al. (1998), Hubble Space Telescope imaging of Jupiter's UV aurora during the Galileo orbiter mission, *J. Geophys. Res.*, 103(E9), 20217– 20236, doi:10.1029/98JE01130

Clarke J. T., D. Grodent, S. W. H. Cowley, E. J. Bunce, P. Zarka, J. E. P. Connerney, and T. Satoh (2005). Jupiter's aurora, in *Jupiter: The Planet, Satellites, and Magnetosphere*, edited by F. Bagenal, T. E. Dowling, and W. B. McKinnon, pp. 639–670, Cambridge Univ. Press, New York.

Copper, M., P. A. Delamere, and K. Overcast-Howe (2016), Modeling physical chemistry of the Io plasma torus in two dimensions, *Journal of Geophysical Research*, 121, 6602–6619, doi:10.1002/2016JA022767.

Connerney, J. E. P., Acuña, M. H., and Ness, N. F. (1982), Voyager 1 assessment of Jupiter's planetary magnetic field, *J. Geophys. Res.*, 87(A5), 3623– 3627, doi:10.1029/JA087iA05p03623

de Kleer, K., & de Pater, I. (2016a). Time variability of Io's volcanic activity from near-IR adaptive optics observations on 100 nights in 2013–2015. *Icarus*, 280, 378–404. <https://doi.org/10.1016/j.icarus.2016.06.019>

de Kleer, K., Nimmo, F., & Kite, E. (2019). Variability in Io's volcanism on timescales of periodic orbital changes. *Geophysical Research Letters*, 46, 6327–6332. <https://doi.org/10.1029/2019GL082691>

Delamere, P. A., & Bagenal, F. (2003). Modeling variability of plasma conditions in the Io torus. *Journal of Geophysical Research*, 108(A7), 1276. <https://doi.org/10.1029/2002JA009706>

Delamere, P. A., Steffl, A., & Bagenal, F. (2004). Modeling temporal variability of plasma conditions in the Io torus during the Cassini era. *Journal of Geophysical Research*, 109, A10216. <https://doi.org/10.1029/2003JA010354>

Delamere, P. A., Bagenal, F., & Steffl, A. (2005). Radial variations in the Io plasma torus during the Cassini era. *Journal of Geophysical Research*, 110, A12223. <https://doi.org/10.1029/2005JA011251>

Delamere, P. A., and Bagenal, F. (2010), Solar wind interaction with Jupiter's magnetosphere, *J. Geophys. Res.*, 115, A10201, doi:10.1029/2010JA015347.

Delamere, P. A., Otto, A., Ma, X., Bagenal, F., & Wilson, R. J. (2015). Magnetic flux circulation in the rotationally driven giant magnetosphere. *Journal of Geophysical Research*, 120, 4229–4245. <https://doi.org/10.1002/2015JA021036>

Del Zanna, G., Dere, K.P., Young, P. R., Landi, E., and Mason, H. E. (2015). CHIANTI - An atomic database for Emission Lines. Version 8, *Astronomy & Astrophysics*, 582, A56. doi:10.1051/0004-6361/201526827

Dere, K. P., Landi, E., Mason, H. E., Monsignori Fossi, B. C., and Young, P. R. (1997). CHIANTI—An atomic database for emission lines—Paper I: Wavelengths greater than 50 Å (version 1). *Astronomy and Astrophysics Supplement Series*, 125, 149–173. doi:10.1051/aas:1997368

Divine, N., and Garrett, H. B. (1983), Charged particle distributions in Jupiter's magnetosphere, *J. Geophys. Res.*, 88(A9), 6889– 6903, doi:10.1029/JA088iA09p06889.

Durrance, S. T., Feldman, P. D., and Weaver H. A. (1983). Rocket detection of ultraviolet emission from neutral oxygen and sulfur in the Io torus. *The Astrophysical Journal*, 267: L125–L129.

Feldman P. D., B. A. Thomas, A. F. Berman, H. W. Moos, D. J. Sahnou, D. F. Strobel, and H. A. Weaver (2001). Detection of chlorine ions in the far ultraviolet spectroscopic explorer spectrum of the Io plasma torus. *The Astrophysical Journal*, 554:123–126.

Feldman, P. D., Strobel, D. F., Moos, H. W., and Weaver H. A. (2004). The Far Ultraviolet Spectrum of the Io Plasma Torus. *The Astrophysical Journal*, 601:583–591.

Frank, L. A., and Paterson, W. R. (2000a). Observations of plasmas in the Io torus with the Galileo spacecraft. *Journal of Geophysical Research*, 105(A7), 16,017–16,034. doi:10.1029/1999JA000250

Fukazawa, K., T. Ogino, and R. J. Walker (2010), A simulation study of dynamics in the distant Jovian magnetotail, *Journal of Geophysical Research*, 115, A09219, doi:10.1029/2009JA015228.

Geissler, P., McEwen, A., Phillips, C., Keszthelyi, L., and Spencer, J. (2004). Surface changes on Io during the Galileo mission. *Icarus*, 169, 29-64. doi:10.1016/j.icarus.2003.09.024

Grodent, D. A. (2015) Brief Review of Ultraviolet Auroral Emissions on Giant Planets. *Space Sci Rev* 187, 23–50. doi:10.1007/s11214-014-0052-8

Hall, D. T., Bednar C. J., Durrance S. T., Feldman P. D., McGrath M. A., Moos H. W., and Strobel D. F. (1994a). Hopkins Ultraviolet Telescope determination of the Io torus electron temperature. *The Astrophysical Journal*, 426, L51–L54. doi:10.1086/187159

Hall, D. T., Gladstone, G. R., Moos, H. W., Bagenal, F., Clarke, J. T., Feldman, P. D., McGrath, M. A., Schneider, N. M., Shemansky, D. E., Strobel, D. F., and Waite, J. H. (1994b). Extreme Ultraviolet Explorer satellite observation of Jupiter's Io plasma torus. *The Astrophysical Journal*, 420, L45–L48. doi:10.1086/187337

Herbert, F & Sandel, B. R. (2000). Azimuthal variation in ion density and electron temperature in the Io plasma torus. *Journal of Geophysical Research*, 105(A7), 16,035-16,052, 10.1029/1998JA000259

Herbert, F., Schneider, N. M., Hendrix, A. R., and Bagenal, F. (2003). Hubble Space Telescope observations of sulfur ions in the Io plasma torus: New constraints on the plasma distribution. *Journal of Geophysical Research*, 108(A5), 1167. doi:10.1029/2002JA009510

Hess, S. L. G., Delamere, P., Bagenal, F., Schneider, N., & Steffl, A. J. (2011). Longitudinal modulation of hot electrons in the Io plasma torus. *Journal of Geophysical Research*, 116, A11215. <https://doi.org/10.1029/2011JA016918>

S.L.G. Hess, B. Bonfond, V. Chantry, J.-C. Gérard, D. Grodent, S. Jacobsen, A. Radioti. (2013). Evolution of the Io footprint brightness II: Modeling, *Planetary and Space Science*, Volume 88, 76-85, doi:10.1016/j.pss.2013.08.005.

- Hikida, R., Yoshioka, K., Murakami, G., Kimura, T., Tsuchiya, F., Yamazaki, A., Yoshikawa I., & Iwagami N (2018). Identification of extreme ultraviolet emission lines of the Io plasma torus observed by Hisaki/EXCEED. *Journal of Geophysical Research: Planets*, 123. <https://doi.org/10.1029/2018JE005629>
- Hill, T. W. (1976). Interchange stability of a rapidly rotating magnetosphere. *Planetary and Space Science*, 24, 1,151-1,154. doi:10.1016/0032-0633(76)90152-5
- Hill, T. W., Dessler, A. J., and Maher, L. J. (1981). Corotating magnetospheric convection. *Journal of Geophysical Research*, 86(A11), 9,020-9,028. doi:10.1029/JA086iA11p09020
- Hiraki, Y., Tsuchiya, F., & Katoh, Y. (2012). Io torus plasma transport under interchange instability and flow shears. *Planetary and Space Science*, 62(1), 41–47. <https://doi.org/10.1016/j.pss.2011.11.014>
- Huba, J. D. (2009). NRL Plasma Formulary, tech. Rep. NRL/PU6790-09-523, (p. 71). Washington, DC: Nav. Res. Lab.
- Ip, W. H. & Goertz, C. K. (1983). An interpretation of the dawn-dusk asymmetry of UV emission from the Io plasma torus, *Nature*, 302, 232-233. doi:10.1038/302232a0
- Jackman, C.M., Arridge, C.S., André, N. et al. Large-Scale Structure and Dynamics of the Magnetotails of Mercury, Earth, Jupiter and Saturn. *Space Sci Rev* 182, 85–154 (2014) doi:10.1007/s11214-014-0060-8
- Judge, D. L., and Carlson, R. W. (1974). Pioneer 10 Observations of the Ultraviolet Glow in the Vicinity of Jupiter. *Science*, 183 (4122), 317–318. doi:10.1126/science.183.4122.317
- Kasahara, S., Kronberg, E. A., Kimura, T., Tao, C., Badman, S. V., Masters, A., Retinò, A., Krupp, N., and Fujimoto, M. (2013), Asymmetric distribution of reconnection jet fronts in the Jovian nightside magnetosphere, *J. Geophys. Res. Space Physics*, 118, 375– 384, doi:10.1029/2012JA018130.
- Kelly, R. L. (1987). Atomic and Ionic Spectrum Lines below 2000 Angstroms: Hydrogen through Krypton Part I (H–Cr). *Journal of Physical and Chemical Reference Data*, 16.
- Kennel, C. F. (1969), Consequences of a magnetospheric plasma, *Rev. Geophys.*, 7 (1, 2), 379–419, doi:10.1029/RG007i001p00379.

Khurana K. K., M. G. Kivelson, V. M. Vasyliunas, N. Krupp, J. Woch, A. Lagg, B. H. Mauk, W. S. Kurth (2005). The Configuration of Jupiter's Magnetosphere, in *Jupiter: The Planet, Satellites, and Magnetosphere*, edited by F. Bagenal, T. E. Dowling, and W. B. McKinnon, pp. 593–616, Cambridge Univ. Press, New York.

Kimura, T., Kimura, T., Hiraki, Y., Tao, C., Tsuchiya, F., Delamere, P. A., et al. (2018). Response of Jupiter's aurora to plasma mass loading rate monitored by the Hisaki satellite during volcanic eruptions at Io. *Journal of Geophysical Research*, 123. <https://doi.org/10.1002/2017JA025029>

Kimura, T., et al. (2015), Transient internally driven aurora at Jupiter discovered by Hisaki and the Hubble Space Telescope, *Geophys. Res. Lett.*, 42, 1662–1668, doi:10.1002/2015GL063272.

Kimura, T., Yamazaki, A., Yoshioka, K., Murakami, G., Tsuchiya, F. et al. (2019). Development of ground pipeline system for high-level scientific data products of the Hisaki satellite mission and its application to planetary space weather. *J. Space Weather Space Clim.* 9, A8.

Koga R, Tsuchiya, F., Kagitani, M., Sakanoi, T., Yoneda, M., Yoshioka, K., Kimura, T., Murakami, G., Yamazaki, A., Yoshikawa, I., and Smith, T. (2018a). The temporal variation in atomic oxygen emission around Io during a volcanic event observed with Hisaki/EXCEED. *Icarus*, 299, 300-307. doi:10.1016/j.icarus.2017.07.024

Kramida, A., Ralchenko, Y., Reader, J. and NIST ASD Team (2018). NIST Atomic Spectra Database (version 5.5.2), [Online]. Available: <https://physics.nist.gov/asd> [Sun Feb 18 2018]. National Institute of Standards and Technology, Gaithersburg, MD.

Krüger, H., Geissler, P., Horányi, M., Graps, A. L., Kempf, S., Srama, R., Moragas - Klostermeyer, G., Moissl, R., Johnson, T. V., and Grün, E. (2003), Jovian dust streams: A monitor of Io's volcanic plume activity, *Geophys. Res. Lett.*, 30, 2101, doi:10.1029/2003GL017827, 21.

Krupp N., V. M. Vasyliunas, J. Woch, A. Lagg, K. K. Khurana, M. G. Kivelson, B. H. Mauk, E. C. Roelof, D. J. Williams, S. M. Krimigis, W. S. Kurth, L. A. Frank, and W. R. Paterson (2005). Dynamics of the Jovian Magnetosphere, in *Jupiter: The Planet, Satellites, and Magnetosphere*, edited by F. Bagenal, T. E. Dowling, and W. B. McKinnon, pp. 617–638, Cambridge Univ. Press, New York.

Kupo, I., Mekler, Y., and Eviatar, A. (1976). Detection of ionized sulfur in the Jovian magnetosphere, *The Astrophysical Journal*, 205, L51–L53.

Kuwabara, M., Yoshioka, K., Murakami, G., Tsuchiya, F., Kimura, T., Yamazaki, A., and Yoshikawa, I. (2017). The geocoronal responses to the geomagnetic disturbances. *Journal of Geophysical Research*, 122, 1269–1276. doi:10.1002/2016JA023247

Lichtenberg, G., and Thomas, N., and Fouchet, T. (2001). Detection of S (IV) 10.51 μm emission from the Io plasma torus, *Journal of Geophysical Research*, 106, A12, 29899–29910.

Louarn, P., C. P. Paranicas, and W. S. Kurth (2014), Global magnetodisk disturbances and energetic particle injections at Jupiter, *J. Geophys. Res. Space Physics*, 119, 4495–4511, doi:10.1002/2014JA019846.

Ma, X., Delamere, P. A., Thomsen, M. F., Otto, A., Neupane, B., Burkholder, B. L., & Nykyri, K. (2019). Flux tube entropy and specific entropy in Saturn's magnetosphere. *Journal of Geophysical Research: Space Physics*, 124, 1593–1611. <https://doi.org/10.1029/2018JA026150>

Marchis, F., Prangé, R., Christou, J., (2000). Adaptive optics mapping of Io's volcanism in the thermal IR (3.8 μm). *Icarus* 148, 384–396.

Mason, H.E., Monsignor Fossi, B.C. Spectroscopic diagnostics in the VUV for solar and stellar plasmas. *The Astron Astrophys Rev* 6, 123–179 (1994) doi:10.1007/BF01208253

Mauk, B. H. et al. Storm-like dynamics of Jupiter's inner magnetosphere. *J. Geophys. Res.* 104, 22759–22778 (1999). doi:10.1029/1999JA900097

Mauk, B., Clarke, J., Grodent, D. et al. Transient aurora on Jupiter from injections of magnetospheric electrons. *Nature* 415, 1003–1005 (2002) doi:10.1038/4151003a

Mauk, B. H., Mitchell, D. G., McEntire, R. W., Paranicas, C. P., Roelof, E. C., Williams, D. J., Krimigis, S. M., and Lagg, A. (2004), Energetic ion characteristics and neutral gas interactions in Jupiter's magnetosphere, *J. Geophys. Res.*, 109, A09S12, doi:10.1029/2003JA010270.

May J., T.D. Carr, M.D. Desch. (1979). Decametric radio measurement of Jupiter's rotation period, *Icarus*, Volume 40, Issue 1, Pages 87-93, doi:10.1016/0019-1035(79)90055-1.

McCandliss, R. S., McPhate, J. B., and Feldman, P. D. (1998). Narcissistic ghosts in Rowland-mounted concave gratings with: $\beta = 0^\circ$ a cautionary note. *Applied Optics*. 37, 5070–5074. doi:10.1364/AO.37.005070

Meier, R. R. (1991). Ultraviolet spectroscopy and remote sensing of the upper atmosphere. *Space Science Reviews*, 58, 1–185. doi:10.1007/BF01206000

Mendillo, M., Wilson, J., Spencer, J., and Stansberry, J. (2004). Io's volcanic control of Jupiter's extended neutral clouds, *Icarus*, 170, 430–442. doi:10.1016/j.icarus.2004.03.009

Mendoza, C., Eissner, W., Dourneuf, M. Le., and Zeippen, C. J. (1995). Atomic data for opacity calculations. XXIII. The aluminium isoelectronic sequence, *Journal of Physics B: Atomic, Molecular and Optical Physics*, 28, 3485.

Mewe, R. X-ray spectroscopy of stellar coronae. *The Astron Astrophys Rev* 3, 127–168 (1991) doi:10.1007/BF00873539

Meyer-Vernet, N., M. Moncuquet, and S. Hoang (1995), Temperature inversion in the Io plasma torus, *Icarus*, 116, 202–213. doi:10.1006/icar.1995.1121.

Moncuquet, M., F. Bagenal, and N. Meyer-Vernet, Latitudinal structure of outer Io plasma torus, *Journal of Geophysical Research*, 107(A9), 1260, doi:10.1029/2001JA900124, 2002

Moos, H. W. and Clarke, J. T. (1981). Ultraviolet observations of the Io torus from earth orbit using the IUE Observatory. *The Astrophysical Journal*, 247, 354–361.

Moos, H. W., Feldman, P. D., Durrance, S. T., Blair, W. P., Bowers, C. W., Davidsen, A. F., Dixon, W. V., Ferguson, H. C., Henry, R. C., Kimble, R. A., Kriss, G. A., Kruk, J. W., Long, K. S., and Vancura O. (1991). Determination of ionic abundances in the Io torus using the Hopkins Ultraviolet Telescope. *The Astrophysical Journal*, 382, L105–L108.

Morgenthaler J. P., J. A. Rathbun, C. A. Schmidt, J. Baumgardner, and N. M. Schneider (2019) Large Volcanic Event on Io Inferred from Jovian Sodium Nebula Brightening. *The Astrophysical Journal*, 871, L23. doi: 10.3847/2041-8213/aafdb7

Murakami, G., Yoshioka, K., Yamazaki, A., Tsuchiya, F., Kimura, T., Tao, C., Kita, H., Kagitani, M., Sakanoi, T., Uemizu, K., Kasaba, Y., Yoshikawa, I., & Fujimoto, M. (2016). Response of Jupiter's inner magnetosphere to the solar wind derived from extreme ultraviolet monitoring of the Io plasma tours. *Geophysical Research Letters*, 43, 12308-12316. doi:10.1002/2016GL071675

Nerney, E. G., Bagenal, F., & Steffl, A. J. (2017). Io plasma torus ion composition: Voyager,

Galileo, and Cassini. *Journal of Geophysical Research*, 122, 727–744. <https://doi.org/10.1002/2016JA023306>

Nichols, J. & Cowley, S. (2004). Magnetosphere-ionosphere coupling currents in Jupiter's middle magnetosphere: Effect of precipitation-induced enhancement of the ionospheric Pedersen conductivity. *Annales Geophysicae*. 22. 10.5194/angeo-22-1799-2004.

Nozawa, H., Misawa, H., Takahashi, S., Morioka, A., Okano, S., and Sood, R. (2004). Long-term variability of [SII] emissions from the Io plasma torus between 1997 and 2000, *Journal of Geophysical Research*, 109, A07209. doi:10.1029/2003JA010241

Oza A. V., R. E. Johnson et al. (2019). Sodium and Potassium Signatures of Volcanic Satellites Orbiting Close-in Gas Giant Exoplanets. *The Astrophysical Journal*, 885, Number 2. doi:10.3847/1538-4357/ab40cc

Peale, S., Cassen, P., Reynolds, R., (1979). Melting of Io by tidal dissipation. *Science* 203, 892–894. (Rathbun 2006 Loki).

Russell, C. & Wang, YL & Blanco-Cano, X. & Strangeway, R. (2001). The Io mass-loading disk: Constraints provided by ion cyclotron wave observations. *Journal of Geophysical Research*. 106. 26233-26242. 10.1029/2001JA900029.

Russell, C. T., Kivelson, M. G. and Khurana K. K. (2005). Statistics of depleted flux tubes in the Jovian magnetosphere, *Planetary and Space Science*, 53, 937–943, doi:10.1016/j.pss.2005.04.007.

Sandel, B. R., and Broadfoot, A. L. (1982a). Discovery of an Io-correlated energy source for Io's hot plasma torus, *Journal of Geophysical Research*, 87(A4), 2231–2240. doi:10.1029/JA087iA04p02231

Schneider, N. and Trauger, J. (1995). The Structure of the Io Torus. *The Astrophysical Journal*. 450. 450. doi:10.1086/176155.

Scudder, J. D., Sittler, E. C., and Bridge, H. S. (1981), A survey of the plasma electron environment of Jupiter: A view from Voyager, *J. Geophys. Res.*, 86(A10), 8157– 8179, doi:10.1029/JA086iA10p08157.

Shemansky, D. E. (1980). Radiative cooling efficiencies and predicted spectra of species of the Io plasma torus. *The Astrophysical Journal*, 236, 1043–1054. <https://doi.org/10.1086/157832>

Shemansky, D. E., and Smith, G. R. (1981). The Voyager 1 EUV spectrum of the Io plasma torus, *Journal of Geophysical Research*, 86, 9179–9192.

Shemansky, D. E. (1987). Ratio of oxygen to sulfur in the Io plasma torus. *Journal of Geophysical Research*, 92, 6141–6146. <https://doi.org/10.1029/JA092iA06p06141>

Shemansky, D. E. (1988), Energy branching in the Io plasma torus: The failure of Neutral cloud theory, *Journal of Geophysical Research*, 93(A3), 1773–1784, doi:10.1029/JA093iA03p01773.

Sirk, M. M., Vallerga, J. V., Finley, D. S., Jelinsky, P., and Malina, R. F. (1997). Performance of the extreme ultraviolet explorer imaging telescopes. *The Astrophysical Journal*, 110:347E356.

Siscoe, G. L. (1978), Jovian plasmaspheres, *Journal of Geophysical Research*, 83(A5), 2118–2126, doi:10.1029/JA083iA05p02118.

Siscoe, G. L. and Summers D. (1981). Centrifugally driven diffusion of iogenic plasma. *Journal of Geophysical Research*, 86(A10), 8,471-8,479. doi:10.1029/JA086iA10p08471

Sittler, E. C., Jr., and Strobel, D. F. (1987). Io plasma torus electrons: Voyager 1, *Journal of Geophysical Research*, 92(A6), 5741–5762. doi:10.1029/JA092iA06p05741

Steffl, A. J., Ian, A., Stewart, F. and Bagenal F. (2004a). Cassini UVIS observations of the Io plasma torus: I. Initial results, *Icarus*, 172(1), 78–90. doi:10.1016/j.icarus.2003.12.027.

Steffl, A. J., Bagenal F., Ian A., and Stewart F. (2004b). Cassini UVIS observations of the Io plasma torus: II. Radial variations, *Icarus*, 172(1), 91–103. doi:10.1016/j.icarus.2004.04.016

Steffl et al., (2008). Cassini UVIS observations of the Io plasma torus IV. Modeling temporal and azimuthal variability. *Icarus*, 194, 153-165, doi:10.1016/j.icarus.2007.09.019

Strobel D. F. and J. Davis (1980) Properties of the Io plasma torus inferred from Voyager EUV data. *The Astrophysical Journal*, 238, L49. doi:10.1086/183256

Suzuki, F., Yoshioka, K., Hikida, R., Murakami, G., Tsuchiya, F., Kimura, T., & Yoshikawa, I. (2018). Corotation of bright features in the Io plasma torus. *Journal of Geophysical Research: Space Physics*, 123, 9420–9429. <https://doi.org/10.1029/2018JA025363>

Tao C, Kataoka R, Fukunishi H, Takahashi Y, Yokoyama T (2005) Magnetic field variations in the Jovian magnetotail induced by solar wind dynamic pressure enhancements. *J Geophys Res* 110:A11208. doi:10.1029/2004JA010959

Tao, C., Kimura, T., Tsuchiya, F., Muirakami, G., Yoshioka, K., Yamazaki, A., Fujimoto, M. et al. (2018). Variation in Jupiter's aurora observed by Hisaki/EXCEED: 3. Volcanic control of Jupiter's aurora. *Geophysical Research Letters*, 45. <https://doi.org/10.1002/2017GL075814>

Thomas, N. (1995). Ion temperatures in the Io plasma torus, *Journal of Geophysical Research*, 100, 7925–7935.

Thomas, N., F. Bagenal, T. W. Hill, and J. K. Wilson (2004). The Io neutral clouds and plasma torus, in *Jupiter: The Planet, Satellites, and Magnetosphere*, edited by F. Bagenal, T. E. Dowling, and W. B. McKinnon, pp. 561–591, Cambridge Univ. Press, New York.

Thorne, R. M., Armstrong, T. P., Stone, S., Williams, D. J., McEntire, R. W., Bolton, S. J., et al. (1997). Galileo evidence for rapid interchange transport in the Io torus. *Geophysical Research Letters*, 24(17), 2131–2134. <https://doi.org/10.1029/97GL01788>

Treumann, R. A. and Baumjohann, W. (1997). *Advanced space plasma physics*. Imperial College Press, London. doi: 10.1142/p020

Tsuchiya, F., Kagitani, M., Yoshioka, K., Kimura, T., Murakami, G., Yamazaki, A., Nozawa, H., Kasaba, Y., Sakanoi, T., Uemizu, K., and Yoshikawa, I. (2015). Local electron heating in the Io plasma torus associated with Io from HISAKI satellite observation. *Journal of Geophysical Research*, 120, 10317–10333. doi:10.1002/2015JE004849

Tsuchiya, F., Yoshioka, K., Kimura, T., Koga, R., Murakami, G., Yamazaki, A., et al. (2018). Enhancement of the Jovian magnetospheric plasma circulation caused by the change in plasma supply from the satellite Io. *Journal of Geophysical Research: Space Physics*, 123, 6514–6532. <https://doi.org/10.1029/2018JA025316>

Tsuchiya, F., R. Arakawa, H. Misawa, M. Kagitani, R. Koga, F. Suzuki, R. Hikida, K. Yoshioka, A. Steffl, F. Bagenal, P. Delamere, T. Kimura, Y. Kasaba, G. Murakami, I. Yoshikawa, A. Yamazaki, and M. Yoneda (2019). Azimuthal variation in the Io plasma torus observed by the Hisaki satellite from 2013 to 2016. *Journal of Geophysical Research*, 120, 10317–10333. doi:10.1029/2018JA026038

Vasyliunas, V. M. (1983). In A. J. Dessler (Ed.), *Plasma distribution and flow, in physics of the*

Jovian magnetosphere, (pp. 395–453). Cambridge, U. K.: Cambridge Univ. Press. <https://doi.org/10.1029/CBO9780511564574.005>

Watanabe, T., T. Kato, I. Murakami, and M. Yamamoto. (2007) Solar and LHD Plasma Diagnostics. AIP Conference Proceedings 901, 215. doi:10.1063/1.2727371

Woch, J., Krupp, N., and Lagg, A. (2002) Particle bursts in the Jovian magnetosphere: Evidence for a near - Jupiter neutral line, *Geophys. Res. Lett.*, 29 (7), doi:10.1029/2001GL014080.

Yamazaki, A., Tsuchiya, F., Sakanoi, T., Uemizu, K., Yoshioka, K., Murakami, G., Kagitani, M., Kasaba, Y., Yoshikawa, I., Terada, N., Kimura, T., Sakai, S., Nakaya, K., Fukuda, S., and Sawai, S. (2014). Field-Of-View guiding camera on the HISAKI (SPRINT-A) satellite. *Space Science Reviews*, 184, 259–274. doi:10.1007/s11214-014-0106-y

Yoneda, M., Nozawa, H., Misawa, H., Kagitani, M., and Okano, S. (2010). Jupiter's magnetospheric change by Io's volcanoes, *Geophysical Research Letters*, 37, L11202. doi:10.1029/2010GL043656

Yoneda, M., Kagitani M., Tsuchiya, F., Sakanoi, T., and Okano, S. (2015). Brightening event seen in observations of Jupiter's extended sodium nebula, *Icarus*, 261, 31–33. doi:10.1016/j.icarus.2015.07.037

Yoshikawa, I., Yoshioka, K., Murakami, G., Yamazaki, A., Tsuchiya, F., Kagitani, M., Sakanoi, T., Terada, N., Kimura, T., Kuwabara, M., Fujiwara, K., Hamaguchi, T., and Tadokoro, H. (2014). Extreme Ultraviolet Radiation measurement for planetary atmospheres/magnetospheres from the Earth-orbiting spacecraft (Extreme Ultraviolet Spectroscopy for Exospheric Dynamics: EXCEED). *Space Science Reviews*, 184, 237–258. doi:10.1007/s11214-014-0077-z

Yoshikawa, I., Yoshioka, K., Murakami, G., Suzuki, F., Hikida, R., Yamazaki, A., et al. (2016). Properties of hot electrons in the Jovian inner magnetosphere deduced from extended observations of the Io plasma torus. *Geophysical Research Letters*, 43, 11,552–11,557. <https://doi.org/10.1002/2016GL070706>

Yoshikawa, I., Suzuki, F., Hikida, R., Yoshioka, K., Murakami, G., Tsuchiya, F., Tao, C., Yamazaki, A., Kimura, T., Kita, H., Nozawa, H., & Fujimoto, M. (2017). Volcanic activity on Io and its influence on the dynamics of the Jovian magnetosphere observed by EXCEED/Hisaki in 2015. *Earth, Planets and Space*, 69:110. doi:10.1186/s40623-017-0700-9m

Yoshioka, K., I. Yoshikawa, F. Tsuchiya, M. Kagitani, and G. Murakami (2011), Hot electron component in the Io plasma torus confirmed through EUV spectral analysis, *Journal of Geophysical Research*, 116, A09204, doi:10.1029/2011JA016583.

Yoshioka, K., Murakami, G., Yamazaki, A., Tsuchiya, F., Kagitani, M., Sakanoi, T., Kimura, T., Uemizu, K., Uji, K., and Yoshikawa, I. (2013). The extreme ultraviolet spectroscopy for planetary science, EXCEED. *Planetary and Space Science*, 85, 250–260. doi:10.1016/j.pss.2013.06.021

Yoshioka, K., Murakami, G., Yamazaki, A., Tsuchiya, F., Kimura, T., Kagitani, M., Sakanoi, T., Uemizu, K., Kasaba, Y., Yoshikawa, I., & Fujimoto, M. (2014), Evidence for global electron transportation into the Jovian inner magnetosphere. *Science*, 345(6204), 1581–1584. doi:10.1126/science.1256259

Yoshioka, K., Tsuchiya, F., Kimura, T., Kagitani, M., Murakami, G., Yamazaki, A., Kuwabara, M., Suzuki, F., Hikida, R., Yoshikawa, I., Bagenal, F., and Fujimoto, M. (2017). Radial variation in sulfur and oxygen ions in the Io plasma torus as deduced from remote observations by Hisaki. *Journal of Geophysical Research*, 122, 2999–3012. doi:10.1002/2016JA023691

Yoshioka, K., Tsuchiya, F., Kagitani, M., Kimura, T., Murakami, G., Fukuyama, D., et al. (2018). The influence of Io's 2015 volcanic activity on Jupiter's magnetospheric dynamics. *Geophysical Research Letters*, 45, 10,193–10,199. <https://doi.org/10.1029/2018GL079264>

Zhou, Q., F. Xiao, C. Yang, Y. He, and L. Tang (2013), Observation and modeling of magnetospheric cold electron heating by electromagnetic ion cyclotron waves, *Journal of Geophysical Research*, 118, 6907–6914, doi:10.1002/2013JA019263

大林辰蔵(1970),「宇宙空間物理学(物理科学選書 (5))」, 978-4-7853-2405-6